Université Paris 13, Sorbonne Paris Cité

ÉCOLE DOCTORALE GALILÉE

Thèse

présentée par

Egor Evlyukhin

Pour obtenir le titre de

Docteur de l'Université Paris 13

Synthèse avancée de matériaux hybrides pHEMA-TiO_2 par méthode sol-gel et polymérisation induite par hautes pressions, analyse de leurs propriétés optiques.

Directeur de these:	
Luc Museur	Professeur, Université Paris 13
Rapporteurs:	
Laurence Rozes	Professeur, Université Paris 6
Benoit Loppinet	Chercheur principal, IESL-FORTH
Examinateurs:	
Vincent Lorent	Professeur, Université Paris 13
Christian Perruchot	MCF, Université Paris 7
Andrei Kanaev	Directeur de Recherche CNRS

Résumé

Les propriétés fonctionnelles spécifiques des matériaux hybrides organique-inorganique dépendent de leur structure à l'échelle microscopique ainsi que de la nature de l'interface entre leurs composantes organique et inorganique. L'une des voies principales pour synthétiser ces matériaux, consiste à incorporer des blocs inorganiques à l'intérieur d'un polymère. En pratique les applications des matériaux hybrides sont souvent limitées par leur comportement mécanique. En effet, l'augmentation de la concentration de la composante inorganique, à priori souhaitable pour améliorer les propriétés fonctionnelles du matériau, entraine généralement une dégradation des propriétés mécaniques en limitant l'étendue de la polymérisation de la phase organique. La fabrication de matériaux hybrides offrant une combinaison optimale des propriétés mécaniques et fonctionnelles est un problème important auquel nous apportons quelques éléments de réponses dans cette thèse. Pour cela nous démontrons et étudions une nouvelle approche pour la synthèse de matériaux hybrides photosensibles pHEMA-TiO_2 (pHEMA=poly-(2-hydroxyéthyl)méthacrylate) dans lesquels des nanoparticules inorganiques sont dispersées dans un polymère. Le procédé que nous proposons est basé sur l'utilisation de hautes pressions (HP) pour provoquer la polymérisation de la phase organique en l'absence de tout initiateur chimique.

Nous avons d'abord observé la polymérisation spontanée du HEMA sous pression statique. La réaction se produit dans un domaine de pression limitée 0.1-1.6 GPa, en dessous du seuil de transition vitreuse, et est très peu efficace puisque le taux de conversion des monomères n'excède pas 28 % après 41 jours. La réaction peut cependant être considérablement accélérée lorsque l'échantillon sous pression est irradié dans le domaine UV. Nous avons montré que cela résultait de l'excitation à un photon de l'état triplet HEMA (T1) rendue possible par la modification de la structure électronique du HEMA sous HP. Cette méthode ne pouvant être utilisée pour la synthèse de matériaux photosensibles dans le domaine UV, nous avons développé une approche originale basée un cycle de compression-décompression. Lors de la phase de compression (> 6.5 GPa) des biradicaux $(HEMA)_2^{\bullet\bullet}$ sont formés à partir de monomères excités HEMA(T1). À cette pression les contraintes stériques empêchent la formation de plus longs oligomères. La polymérisation ne se produit que dans une seconde étape lorsque l'échantillon, décompressé entre 0.1 et 2 GPa, est en phase liquide. Le taux de conversion des monomères dépasse alors 90 % en moins de 5 min. Les mesures de chromatographie d'exclusion stérique montrent la formation de longues chaines polymère (45000g/mol) et soulignent l'absence des dimères $(HEMA)_2$ ayant servis d'initiateurs de polymérisation. Cette seconde méthode de polymérisation s'est révélée extrêmement efficace pour synthétiser des hybrides pHEMA-TiO_2. Par rapport aux hybrides obtenus par voie classique à pression atmosphérique en utilisant des initiateurs de polymérisation thermique ou photonique, l'approche HP mise au point dans cette thèse permet de multiplier par un facteur trois la concentration de nanoparticules sans détériorer l'état de polymérisation de matériau. La sensibilité photonique des hybrides est ainsi augmentée sans dégradation des propriétés mécaniques. L'étude des propriétés photochromiques des hybrides montre que le rendement quantique de séparation des charges photo-induites et la capacité de stockage des électrons atteignent respectivement 15 % et 50%.

Acknowledgements

Firstly, I would like to thank Prof. Luc Museur and Dr. Andrei Kanaev for giving me the opportunity to do this thesis. Their advice, guidance, stimulation and furthermore their patience throughout the years was invaluable.

A huge thanks to Dr. Andreas Zerr for teaching me about High Pressure techniques and for our important discussions. Without his guidelines this work could not be carried out.

Special thanks to Dr. Mamadou Traore for his assistance in chemical experiments. Moreover for his selfless help in administrative paper work, I have lost count of how often you got me out of trouble.

A huge thanks to Dr. Christian Perruchot at the University Paris 7 for his invaluable experience in polymer science and for his help and assistance with GPC analysis.

To Sana, Paola, Benoit and all my colleagues at the University Paris 13 thanks for your help and support in my PhD work.

Finally, I would like to thank Prof. Laurence Rozes and Dr. Benoit Loppinet for examination of my PhD work and for their important comments and suggestions. I am also very grateful to Prof. Vincent Lorent for his kindness, support and useful advice during my work.

Table of contents

Introduction

Hybrid organic-inorganic materials allow combining the useful properties of their constituent components. The specific properties of hybrids materials depend on their micro- and nanostructures as well as on the nature and extent of the organic-inorganic interface. The unlimited variety, unique structure–properties control, and the compositional and shaping flexibility open a large field of applications to these materials [1, 2]. Many routes exist to fabricate hybrid materials. One of the most prominent is the incorporation of inorganic building blocks in organic polymers in order to combine the advantages of organic polymers (flexibility, lightweight, process ability, etc.) with those of the inorganic component (high mechanical strength, good chemical resistance, thermal stability, optical sensitivity, etc.). The remarkable changes in properties of the obtained hybrids compared to pure organic materials, have stirred up a large interest [3, 4]. These hybrids are today used in optics, electronics, optoelectronics, protective coatings, sensors, etc. Nevertheless, the development of applications for these hybrid materials is often limited by their mechanical behavior. Basically, mechanical properties of polymers are mainly determined by the extent and nature of the polymer network and can be reinforced by the insertion of inorganic blocks at the nanoscale level. The complex relation between the nature and the size of the inorganic blocks, the hybrid interface and the nature of the interactions between the organic and inorganic components, are then key factors influencing mechanical properties [5]. While an increase of the inorganic component concentration can be required to improve the hybrid's functional properties, it can simultaneously leads to a degradation of the mechanical properties by limiting the extent of the polymer network [3, 5, 6]. Therefore, a balance exists between the concentration of the inorganic component and the mechanical properties of the hybrids. The elaboration of organic-inorganic hybrid materials with optimal combination of stable mechanical properties and highest functional response (i.e. optical sensitivity) is still a challenge in hybrid materials science.

In this PhD thesis we address this issue by proposing a new approach, based on high pressures (HPs) chemistry, for the fabrication of organic-inorganic hybrid materials. High pressure (HP) technologies are very important tool in material science widely used to transform an initial material in a new material exhibiting properties of high technological interest. One of the most important benefits of HP chemistry is the possibility to initiate chemical reactions without the use of catalysts or initiators thereby obtaining pure materials [7-9]. We show that the HP assisted elaboration process presented in this PhD is powerful approach for fabrication of organic-inorganic hybrid materials with improved optical and mechanical properties. This new approach appears to be an appealing alternative to the earlier developed elaboration methods [1, 2]. As a model system we consider the photosensitive nanoparticulate pHEMA-TiO_2 hybrid

materials elaborated by the NINO team at LSPM (Laboratoire de Science des Procédés et des Matériaux).

New elaboration processes of photosensitive TiO_2-based hybrid materials have been developing in this team for several years. These hybrids materials are photochromic systems and exhibit a large capacity of electrons storage. Among them TiO_2 wet-gels offer a high efficiency towards photo-induced charge separation and long-term storage of electrons in form of small polarons [10-13]. A high photonic sensitivity has also been reported in TiO_2 hybrid materials including two macroscopic interpenetrating (i) inorganic oxo-titanate, and (ii) organic poly(hydroxyethyl methacrylate) pHEMA, networks [14, 15]. A detailed investigation [16] of these hybrids has emphasized the role of the organic-inorganic interface morphology, in their optical properties. Many parameters influence this interface: inorganic blocks size, nature of the organic component, nature of chemical bonding between organic and inorganic components, gelation of the inorganic component. All these parameters can be affected by the material chemistry and processing [17], what has motivated new investigations in order to elaborate hybrids with more well defined organic-inorganic interface. In TiO_2 based hybrid materials produced from sol-gel process [18], the manual control of hydrolysis reaction precursor does not permit to obtain a gel with a well-defined morphology of TiO_2 chains. Gorbovyi *et al*. [6] solved this problem by replacing the titanium hydroxide precursor by TiO_2 nanoparticles monodispersed in size. The obtained TiO_2-pHEMA hybrids present a well-defined inorganic blocks and conserve the photosensitive properties of gels based hybrids. Nevertheless, in these hybrids the concentration in nanoparticles is limited. Indeed, at high nanoparticles concentration, the polymerization of the organic phase becomes inefficient and hybrids with poor macroscopic aspect and crumbling structure are obtained. In this PhD we demonstrate that the HP induced polymerization of HEMA, allows multiplying by at least a factor two the concentration in TiO_2 nanoparticles without degrading the conversion yield of polymerization of the organic component. The manuscript is organized as follow.

The chapter I presents a short bibliographic review of relevant results concerning both TiO_2-based hybrid materials and HP induced polymerization. In section I a special attention is given to the elaboration method proposed by Kameneva *et al.* [18] for pHEMA-TiO_2 gel-based hybrid materials (section I.1.3.3) and the investigation of their optical properties by Kuznetsov *et al.* [16] (section I.1.4.1). The process proposed by Gorbovyi *et al*. [6] to fabricate nanoparticulate pHEMA-TiO_2 hybrid materials is then discussed in section I.1.3.4. as well as, the photorefractive properties of theses hybrids investigated by Uklein *et al.* [19] (section I.1.4.2). In these hybrids, based on titanium gels or nanoparticles, the organic component (HEMA) is always polymerized from the thermal excitation of initiating molecules, usually AIBN [6, 18]. The influence of TiO_2

nanoparticles concentration on the polymerization of HEMA was carefully studied by Gorbovyi *et al.* They reported a degradation of the mechanical properties of hybrids with increasing nanoparticles concentration, and determined a critical titanium concentration (C_{Ti} = 3.0 M with respect to C_{HEMA} = 8.0 M) above which only powder like samples were obtained. The second part of the chapter I (section I.2) presents some aspects of high pressure chemistry. Basically, the high pressure leads to large modifications of intermolecular interactions and electronic structure, making the system thermodynamically unstable. On the other hand, the stress induced by HP results in significant potential energy barriers which can lead to selectivity in the reaction pathways. The main factors controlling the chemical reactions induced by HP are discussed in section I.2.2. Examples of irreversible or reversible HP-induced chemical reactions are considered in section I.2.4. A particular attention is paid to HP induced polymerization processes. Several examples of HP induced polymerization of unsaturated hydrocarbons molecules in liquid or crystalline phases are also considered in section I.2.4.3.

The chapter II is devoted to a detail presentation of the characterization methods and experimental setups used to fabricate and analyze the HP elaborated hybrids materials. The first part of the chapter (section II.1) describes the "standard" fabrication process of nanoparticulate pHEMA-TiO_2 hybrid materials proposed by Gorbovyi *et al* [6], as well as the HP cells used to press the samples in order to induce the polymerization (section II.2). The second part of the chapter (section II.3) focused on characterization methods: Gel Permeation Chromatography, Raman spectroscopy and mainly the pump-probe photodarkenning experiment developed to analyze and measure the optical properties of TiO_2-pHEMA hybrids produced by HP assisted process.

The next three chapters are devoted to the results obtained during this PhD. The chapter III describes the polymerization of HEMA at static pressure. The process is extremely long (more than 41 days), poorly efficient and limited to a small range of pressure ranging from 0.1 to 1.6 GPa (section III.4.1). In section III.4.2 we report on the laser-assisted HP induced polymerization of HEMA and show that the polymerization reaction rate is increased by a factor ~10 and 30 under action of laser irradiation with wavelengths of 488 nm and 355 nm, respectively. Finally, the catalytic effect of light on polymerization process is explained. Due to the photosensitivity of TiO_2-pHEMA hybrids materials in the UV range, the laser assisted HP induced polymerization presented in this chapter is not suitable to produce hybrids.

The chapter IV describes an alternative approach, so called High Pressure Ramp process (HPR), and based only on high pressures without laser assistance. HEMA is efficiently polymerized in two steps of compression and decompression (section IV.4). The process is fast, few minutes, and leads to the formation of long polymers chains. A model based on the

influence of HP on electronic structure of HEMA and steric factors is proposed to explain the effectiveness of the process (section IV.5).

In the fifth (last chapter) of this manuscript we discuss the optical properties of nanoparticulate pHEMA-TiO_2 hybrid materials elaborated using HPR induced polymerization. After a description of the elaboration process, the first part of this chapter compares the polymerization yield of hybrids polymerized by HPR process or by conventional polymerization using a thermal initiator (section V.3). We report on that the use of HP assisted process allows multiplying at least by two the concentration in nanoparticles without degrading the polymerization state of HEMA. The second part of the chapter is devoted to the investigation of the optical properties of hybrids from a pump-probe photodarkening experiment (section V.4). We demonstrate that (i) the quantum yield of photo-induced charges separation process is independent of the TiO_2 nanoparticles concentration and (ii) the electron loading capacity, $[Ti^{3+}]/[Ti^{4+}]_{0,}$ is proportional to the TiO_2 nanoparticles concentration. The electron loading capacity exceeds 40% far higher than capacities usually observed in other TiO_2-based materials. Finally we analyze the UV induced Ti^{+3} center kinetics in the frame of a theoretical model developed by Kuznetsov *et al.* [16] (section V.4.2.4). We show that this model is in disagreement with our observations for high UV irradiation dose and that it requires some major modifications.

The conclusions section at the end of the manuscript summarizes the main results obtained in this PhD.

Chapter I: Bibliography

I. Bibliography

I.1. Hybrid materials

I.1.1. Introduction

Throughout the entire development of science and technology there always has been a demand for new materials. Many of well-established materials such as ceramics, metals, or plastics could not completely filled all technological requirements for new applications. Scientists realized early on that mixture of materials can show unique novel properties compared with their pure components. One of the most successful examples is nanocomposite materials based on the mixture of organic and inorganic components. These materials are called hybrid materials. Nowadays organic–inorganic hybrid materials do not represent only a creative alternative to design new materials and compounds for academic research, their improved or unusual features allow the development of innovative industrial applications. Many functional systems include hybrid materials in their development process [20]:

- optical systems (photochromic and laser dyes, sensors, luminescent solar concentrators);
- microelectronics (resistors and molding compounds, multilayer dielectric, planarization applications,…);
- micro-optics (free-standing micro-optical elements, such as diffractive lenses or arrays of refractive lenses, dielectric mirrors,…);
- electrochemical devices (batteries, photovoltaic and fuel cell application,…);
- bioactive hybrids (biosensors, dental applications, delivery of drugs and medicaments,…).

I.1.2. Classification of hybrid materials.

The term hybrid material is used for many various systems spanning a wide area of different materials (see Table I.1.1). Basically, a hybrid material is defined as a system that includes two moieties blended on the molecular scale [2]. Commonly one of these compounds is inorganic and the other one is organic in nature.

Table I.1.1 Different possibilities of composition and structure of hybrid materials (Table from ref. [2]).

Matrix	crystalline ↔ amorphous organic ↔ inorganic
Building blocks	molecules ↔ macromolecules ↔ particles ↔ fibers
Interactions between components	strong ↔ weak

The particular nanostructure, the degree of organization and the properties that can be obtained for hybrid materials depend on the chemical nature of their components and also heavily influenced by the interaction between these components [1]. Therefore, hybrid materials are classified depending on the nature of interactions between organic and inorganic components. Two different classes of hybrid materials are defined in this way.

Class I includes hybrids systems where one of the component (organic, biologic or inorganic), which can be molecules, oligomers or polymers is entrapped within a network of the other component. In that case there are only weak-type interactions between the hosting network and the entrapped species. This kind of systems is essentially based on Van der Walls, Hydrogen bonding or electrostatic interactions.

Conversely, ***class II*** gathers hybrids where the inorganic and organic parts are chemically bonded by a covalent or iono-covalent bond. Actually the frontier between both classes is not always simple and hybrids systems can eventually have class I and class II characteristics. A Typical example is hybrids materials for optical applications made by encapsulation of organic chromophores within hybrid matrix which belongs to class II. Although the dye interacts with the hybrid host via Van der Waals or Hydrogen bonding forces, the strong chemical bonds between organic and inorganic parts which make the host material has a significant impact on the overall properties of the system and therefore this kind of hybrids will be also classified as class II [20]. The Table I.1.2 classifies the different kinds of chemical interactions as function of their binding energies and gives some of their mains characteristics.

Table I.1.2 Different chemical interaction and their respective strength. (Table from ref. [2])

Type of interaction	Strength (kJ mol^{-1})	Strength (eV)	Range	Character
Van der Waals	ca. 50	ca. 0.52	Short	Nonselective, nondirectional
H-bonding	5-65	0.052-0.67	Short	Selective, directional
Coordination bonding	50-200	0.52	Short	Directional
Ionic	50-250	0.52-2.6	Long	Nonselective
Covalent	350	3.6	Short	Predominantly irreversible

This classification is illustrated in Figure I.1.1 in the case of a typical hybrid material formed by polymeric chains (monomer molecules, covalently bonded with each other) as organic part and inorganic building blocks (nanoparticles, clusters, networks, etc.) [2]. According to this model of classification, four different cases of inter-component behavior are observed (Figure I.1.1).

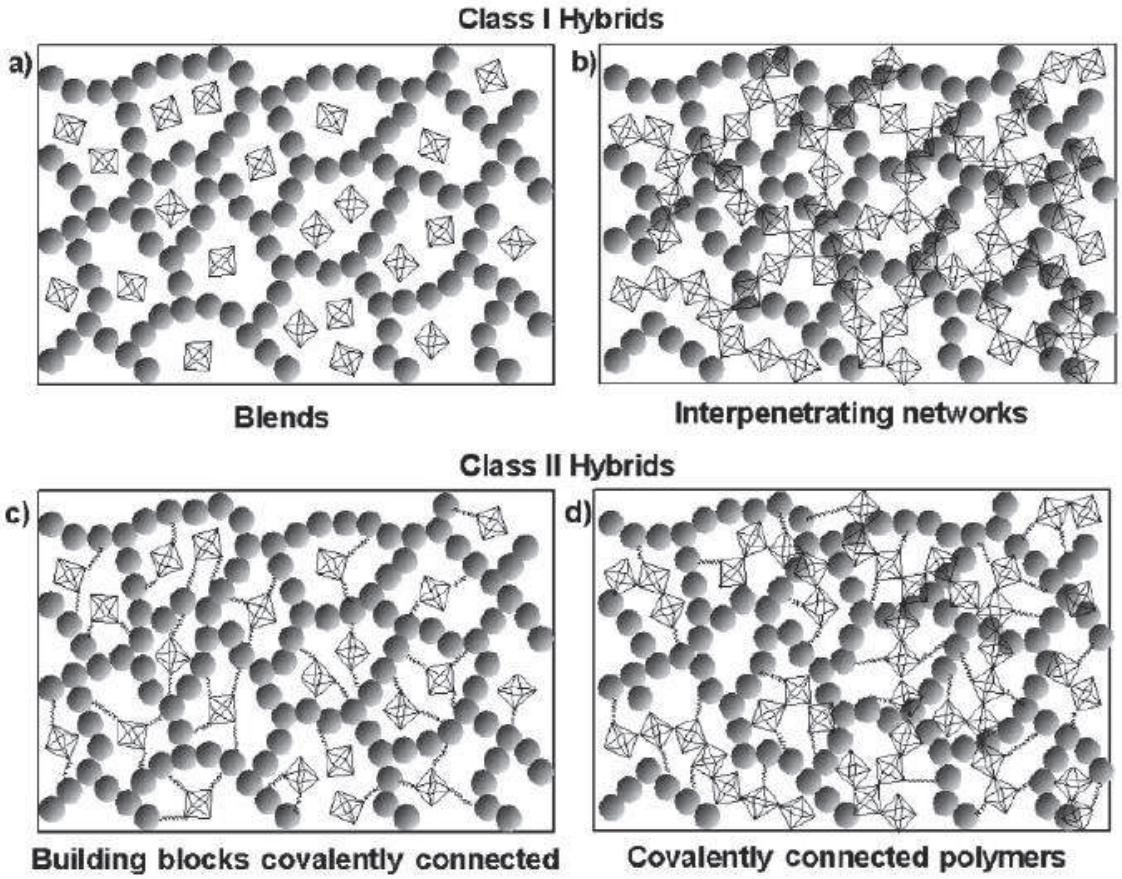

Figure I.1.1 Examples of hybrid materials composed of Nano-building blocks. ● and ◊ represent respectively organic and inorganic building units. (Redraw form ref. [2]).

Blends are formed if no strong chemical interactions exist between the inorganic and organic building blocks. One example for such a material is the combination of inorganic clusters or particles with organic polymers lacking a strong interaction between the components (Figure I.1.1a). If an inorganic and an organic network interpenetrate each other without strong chemical interactions, so called interpenetrating networks (IPNs) are formed (Figure I.1.1b). Both described examples belong to class I hybrids. Class II hybrids are formed when the discrete inorganic building blocks, are covalently bonded to the organic polymers (Figure I.1.1c) or inorganic networks and organic polymers are covalently connected with each other (Figure I.1.1d).

I.1.3. Hybrid materials based on TiO_2 and poly(2-hydroxyethyl)methacrylate)

The TiO_2-based materials can be found in different forms, such as polymorphs of crystalline solid TiO_2 (rutile, anatase, brookite), wet sols and gels, powders with different presence of crystalline and amorphous phases and hybrid materials. Titanium dioxide hybrids attract particular interest mainly due to a high refractive index, biocompatibility, charge storage and electron transport properties. Original photochromic TiO_2-based hybrids were proposed for photochemical conversion and storage of solar energy [21]. Electronic properties of these hybrids are related to TiO_2 (inorganic part), in which the electron-hole separation under UV illumination result in visible darkening due to the absorption of visible light by trapped electrons. In this work our attention has been focused on advanced fabrication and investigation of electronic and optical properties of hybrid materials based on poly(2-(hydroxyethyl)methacrylate) (pHEMA) and titanium oxide TiO_2.

In this section we present separately the basic properties of TiO_2 and pHEMA. Then we review the previous results obtained in the NINO team at LSPM regarding pHEMA-TiO_2 hybrids. We will present synthesis methods proposed by Kameneva *et al*. [18] and Gorbovyi *et al*. [6]. Eventually, we also discuss the optical and electronic properties of TiO_2-based hybrids investigated by Kuznetsov *et al*. [16] and Uklein *et al*. [19].

I.1.3.1. General information about titanium dioxide (TiO_2)

Titanium dioxide (TiO_2) is the amphoteric oxide of tetravalent titanium. It is the main product of the titanium industry. Although the TiO_2 is colorless, in large quantities it is a white pigment. TiO_2 hardly absorbs any incident light in the visible spectrum region. Under normal conditions TiO_2 is stable (the most stable of all known white pigments), non-volatile, and insoluble in acids, alkalis and other solutions. Titanium dioxide has a high reactional stability with different kind of compounds, including air toxic compounds. Because of its inert properties,

titanium dioxide is not toxic and it's generally considered as a very safe substance and biocompatible product.

There are several forms of titanium dioxide. The most common in nature, are crystals with tetragonal syngony (anatase, rutile). An orthorhombic syngony (brookite) is very rare and is only industrially produces (Figure I.1.2). Two high-pressure modifications: rhombic V and hexagonal IV are also known. Different characteristics of the crystal lattices of TiO_2 are shown in Table I.1.3.

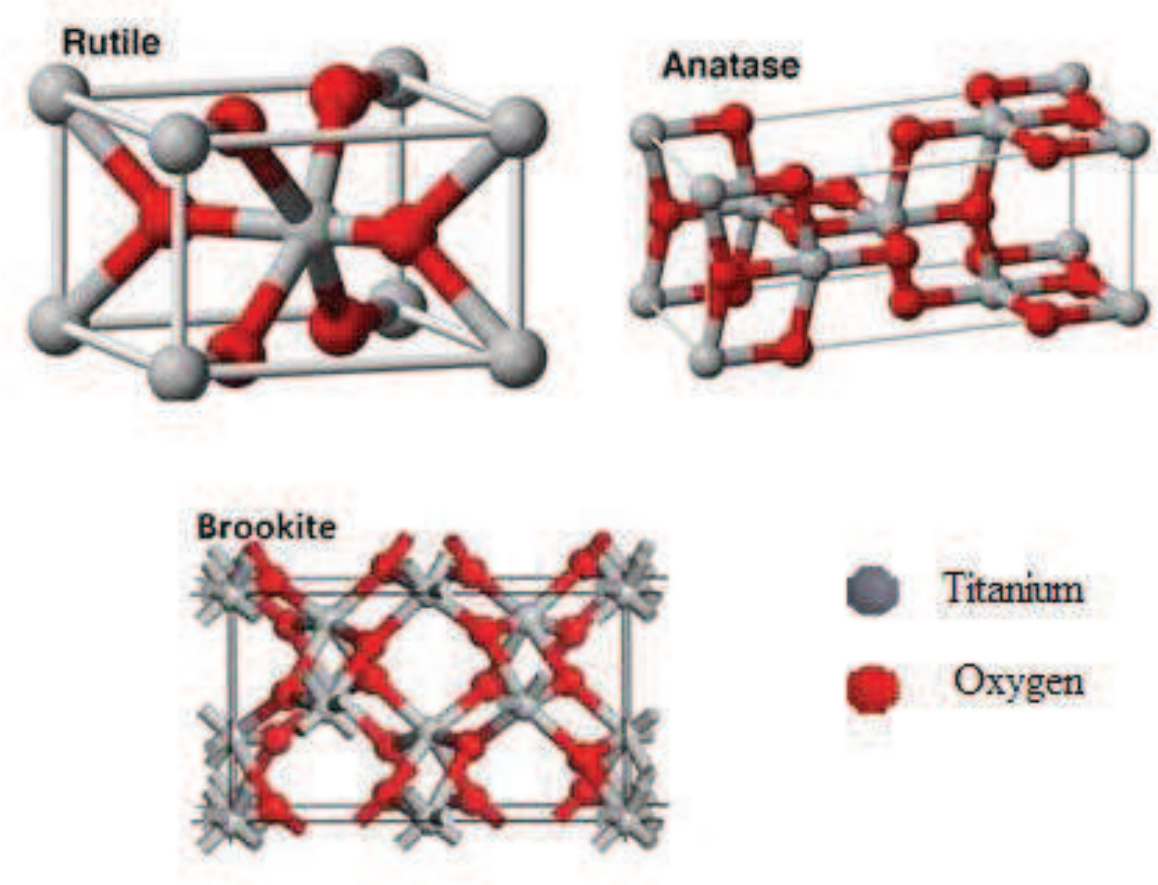

Figure I.1.2 Crystalline structure of the different titanium dioxide modifications. (Redraw form ref. [22])

Table I.1.3 Characteristics of the crystal lattices of TiO_2

Parameters/modifications		**rutile**	**anatase**	**brookite**	**rhombic V**	**hexagonal IV**
Parameters of the elementary lattice, nm	a	0,45929	0,3785	0,51447	0,4531	0,922
	b	-	-	0,9184	0,5498	-
	c	0,29591	0,9486	0,5145	0,4900	0,5685
Number of formula units in the cell		2	4	8	-	-

The titanium dioxide is also recognized for its semiconductor properties. Figure I.1.3 shows the scheme of electronic structure of titanium dioxide.

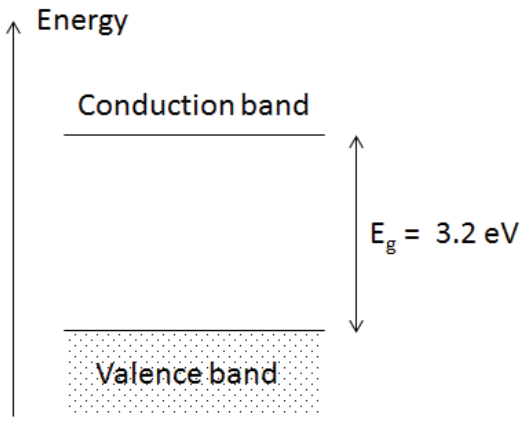

Figure I.1.3 Simple scheme of electronic band structure of titanium dioxide (anatase).

The "bandgap" energy for the titanium dioxide phase anatase is E_g = 3.2 eV. Numerical calculation of the electronic structure of titanium dioxide was carried out by Daude *et al.* [23] in 1977. Authors took simple tetragonal Brillouin zone (BZ) of the tetragonal unit cell which is the case of TiO_2 (Figure I.1.4). TiO_2 is known to be strongly ionic; therefore, the valence band is mainly composed of the *p* electrons of oxygen and the corresponding wave functions are considerably localized on O^{2-} sites. The lowest conduction band would be chiefly composed of the states of titanium ion Ti^{4+}.

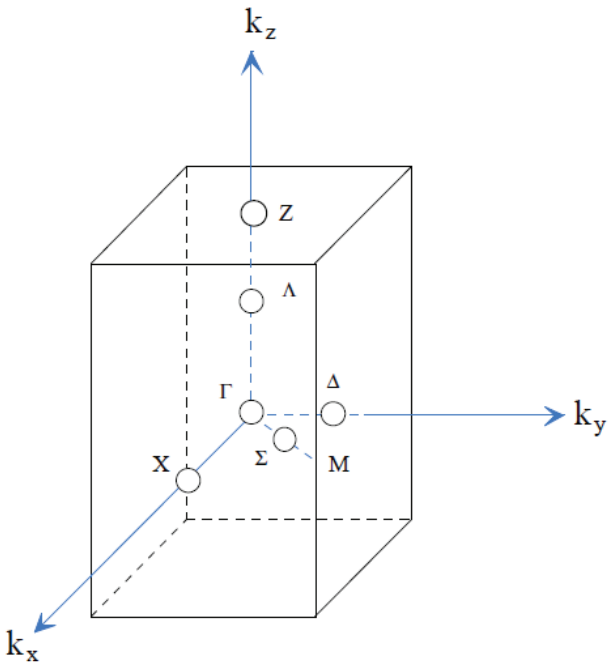

Figure I.1.4 Brillouin zone of simple tetragonal lattice. (Redraw form ref. [16]).

The maximum in the valence band is the state Γ_3 at the center of the BZ; its wave function is a mixing of p_x and p_y orbitals. It should be noted that the transition from that state towards Γ_1, the minimum of the conduction band, is forbidden. The first direct allowed transitions are at the X edge of the BZ: $X_1 \rightarrow X_1$ (3.45 eV with $\vec{E} \perp \vec{c}$) and $X_2 \rightarrow X_1$ (3.59 eV with $\vec{E} \parallel \vec{c}$). The lowest indirect transitions are: $X_1 \rightarrow \Gamma_1$ (2.91 eV with $\vec{E} \perp \vec{c}$) and $X_2 \rightarrow \Gamma_1$ (3.05 eV with $\vec{E} \parallel \vec{c}$). The scheme of direct and indirect transitions is shown in Figure I.1.5. The energies of the transitions are summarized in Table I.1.4.

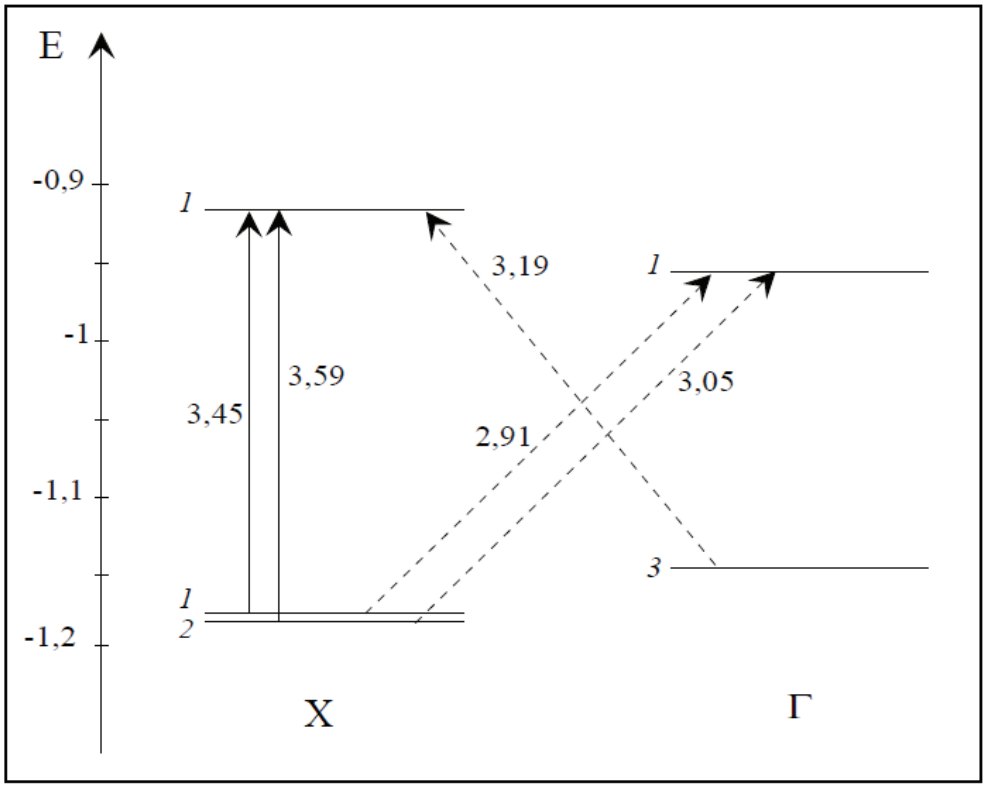

Figure I.1.5 Scheme of direct and indirect transitions (anatase). (Redraw from ref. [23]).

Table I.1.4 Theoretical values of the first transitions of TiO_2. (Table from ref. [23])

initial state → final state	Type of transition	E (eV)
X1 → Γ1	indirect	2.91
X2 → Γ1	indirect	3.05
Γ3 → X1	indirect	3.19
X1 → X1	direct	3.45
X2 → X1	direct	3.59
Γ2 → Γ1	direct	4.30
Γ3 → Γ5	direct	4.81

I.1.3.2. The poly(2-(hydroxyethyl)methacrylate)

Methacrylic polymers and copolymers are widely used for medical applications such as dentistry, bone cements and biomaterials [24, 25]. The 2-(hydroxyethyl)methacrylate or HEMA is the monomer used to synthesize the poly(2(hydroxyethyl)methacrylate) (pHEMA) (Figure I.1.6). The information about chemical and physical properties of HEMA is discussed in section II.1.1.

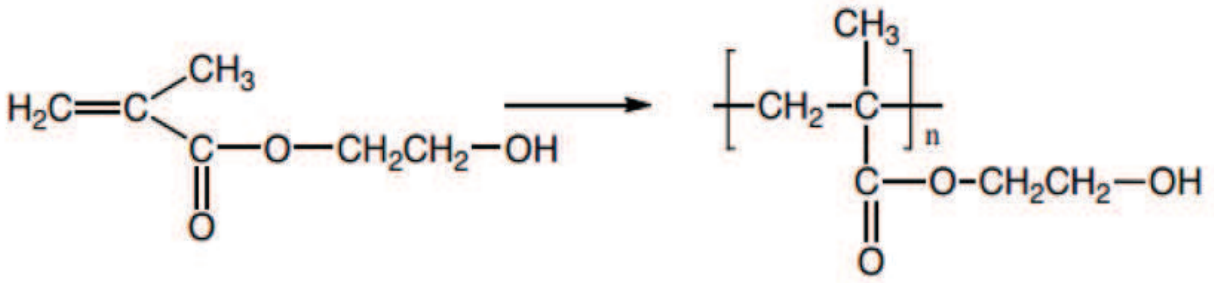

Figure I.1.6 The schematic representation of HEMA polymerization. (Redraw from ref. [6]).

The poly(2-(hydroxyethyl)methacrylate) (pHEMA) is the polymer favored for preparing microbeads for vascular embolization, immobilization of cells, enzymes or pharmacological drugs [26]. Because of its hydroxyethyl pendant groups, pHEMA can also be prepared in the form of hydrogel used to manufacture soft contact lenses [27]. The presence of a hydroxyl and carbonyl groups on each repeat unit in pHEMA makes this polymer compatible with water.

I.1.3.3. Synthesis of gel based pHEMA-TiO_2 hybrids

The preparation method of gel based pHEMA-TiO_2 hybrids has been developed by Kameneva *et al*. [18] from earlier studies by Novak *et al*. [28].

The synthesis of gel based pHEMA-TiO_2 hybrids was performed in three steps as shown in Figure I.1.7. The first step is the chemical modification of titanium tetra-isopropoxide ($Ti(OR)_x$, where $(OR)_x = (O^iPr)_4$) by HEMA was carried out at room temperature with a HEMA/Ti molar ratio between 4 and 20. During the reaction the released 2-propanol was gently pumped out. As a result, new precursors $Ti(OR')_z = Ti(OEMA)_{4-x}(O^iPr)_x$ (x = 1 or 0) in a solution of polymerizable HEMA are obtained:

$$Ti(OR)_x + xHEMA \rightarrow Ti(OR')_z + xROH$$

In the second step, the new solution was hydrolyzed in acidic conditions:

$$Ti(OR')_z + xH_2O \rightarrow Ti(OR')_{z-x}(OH)_x + xR'OH.$$

Hydrolyzed titanium precursor produce condensed titanium-oxo-alkoxy species, which can associate into the macroscopic inorganic gel via polycondensation:

$$N - OH + N - OH \rightarrow N - O - N + H_2O,$$

$$N - OH + M - OR' \rightarrow N - O - M + R' - OH\ ,$$

where $N = Ti(OR')_{z-x}(OH)_{x-1}$ and $M = Ti(OR')_{z-x-1}(OH)_x$ is hydrolyzed titanium prescursors.

In the last step, the free-radical polymerization of free HEMA monomers was carried out thermally in presence of azobisisobutyronitrile (AIBN) as radical initiator. The polymerization proceeded at 65 °C for 20 h and then at 120 °C for 3 h.

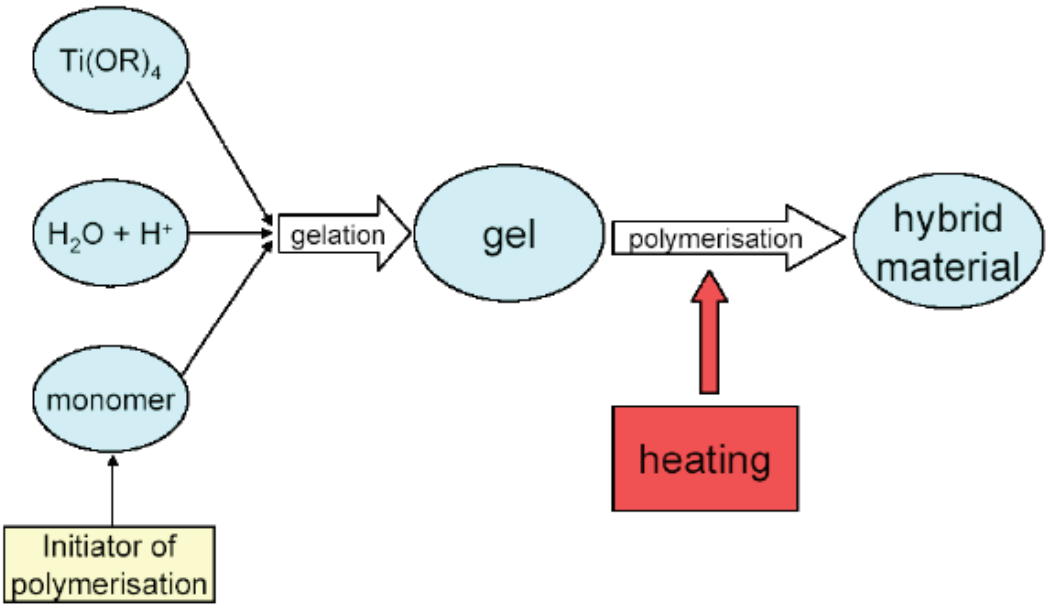

Figure I.1.7 The hybrid material elaboration scheme proposed by Kameneva at al. [18].

An example of the gel based pHEMA-TiO_2 organic–inorganic hybrid material is shown in Figure I.1.8. A very good homogeneity of the materials has been achieved, free of internal cracks and bubbles. According to the synthesis schema, the obtained materials belong to the class II hybrids consisting of covalently interacting organic and inorganic chains.

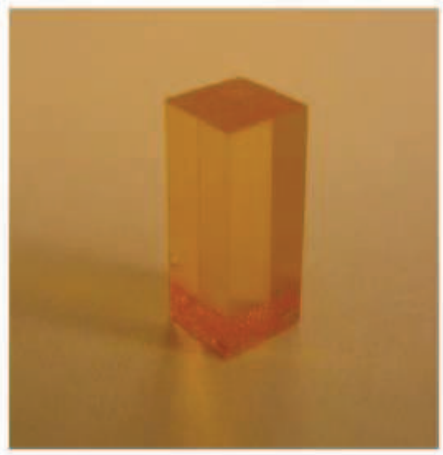

Figure I.1.8 Photo of organic–inorganic hybrid material containing titanium oxide gel network. The rectangular-tailored and optically polished parallelepiped is of 4 × 4 × 10 mm^3 size. (Redraw from ref. [14]).

Depending on ageing time, i.e. the delay time between gelation and polymerization processes, hybrids samples with different morphology of the inorganic network can be obtained as pictured in the Figure I.1.9. The first three samples were prepared in the same experimental conditions except for the delay time between gelation, observed after a time t_{gel}, and polymerization processes. This delay varies from 0, t_{gel} and 20 t_{gel} for sample #1, #2 and #3 respectively. A fourth hybrid based on titanium oxo-cluster as building blocks and HEMA [29] is also represented (sample #0 in Figure I.1.9).

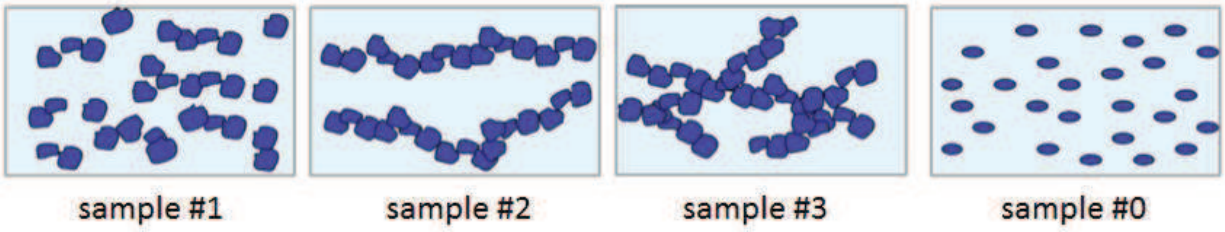

Figure I.1.9 The schematic representation of the microstructure of the four prepared hybrid samples. (Redraw form ref. [17])

The main difference between these samples is the microstructure of the inorganic component: sample #0 is made of titanium-oxo nano-domains well dispersed in the organic polymer, whereas samples #1, #2, and #3 possess bigger titanium-oxo blocks. Samples #1, #2 and #3 were prepared in the same experimental conditions except for the delay time between gelation and polymerization processes. Delay time varies from 0, t_{gel} and 20 t_{gel} for sample #1, #2 and #3 respectively. Thereby, sample #1 is composed of short chains, sample #2 is possessed of macroscopic chains of low fractal dimension and sample #3 has a bushy structure. Main characteristics of these hybrid materials are presented in Table I.1.5.

Table I.1.5 Four hybrid samples prepared for optical measurements (from ref. [16]).

samples	Microstructure of inorganic component	Thickness, mm	Titanium concentration, M	Preparation method
hybrid sample # 1	Isolated species + larger domains	0.4	2.0	Polymerization without gelation
hybrid sample # 2	Long chains formed by the association of small particles	0.4	2.0	1 t_{gel}* before polymerization
hybrid sample # 3	Macroscopic branched chains	0.4	2.0	20 t_{gel} before polymerization
hybrid sample # 0	Isolated species (inorganic nano-domains)	0.4	2.0	T_{16} clusters inside HEMA

*Where gelation time (t_{gel}) is 10 min.

Optical properties of these different kinds of pHEMA-TiO_2 gel-based hybrids have been extensively analyzed by Kunestsov *et. al* [16] and will be discussed in section I.1.4.1.

I.1.3.4. Synthesis of pHEMA-TiO_2 hybrid materials based on TiO_2 nanoparticles

The elaboration method proposed by Kameneva *et al*. [18] for pHEMA-TiO_2 gel based hybrid materials does not allow a precise control of the size of inorganic blocks created during the sol-gel process. To address this issue another approach has been proposed by Gorboviy *et al*. [6]. This new approach includes 3 stages (Figure I.1.10):

- preparation of size-selected TiO_2 nanoparticles,
- surface groups exchange,
- organic polymerization.

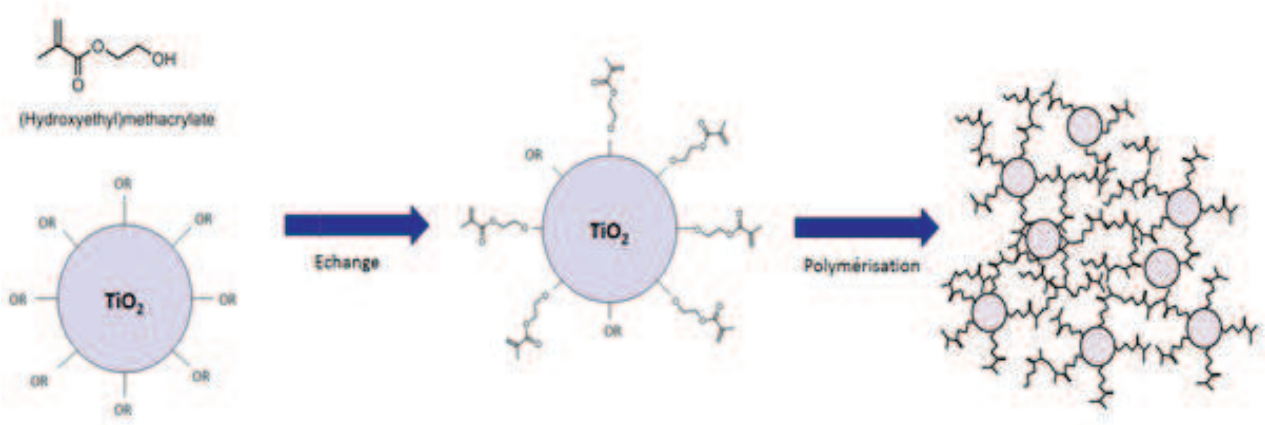

Figure I.1.10 Scheme of synthesizing of pHEMA-TiO_2 hybrid materials based on TiO_2 nanoparticles.

This method is discussed in more details in section II.1.2. Gorboviy *et al*. have shown that the hierarchical mechanism of TiO_2 oxo-units growth in sol-gel process allows selective nanoparticles generation in 2-propanol solution by applying a rapid (turbulent) fluid micromixing. For elaboration of the pHEMA-TiO_2 hybrids, the grafting of -OEMA groups on the particle surface has been realized by solvent exchange under vacuum pumping. This exchange reaction results in a stable nanoparticulate precursor in HEMA solution, which inorganic mass density can be adjusted. During the exchange reaction the particles radius (2.5 nm) does not change that signified the stability of the newly formed solution due to the protective role of the -OEMA groups.

I.1.4. Optical and electronic properties of pHEMA-TiO_2 hybrid materials

I.1.4.1. Light-induced darkening of pHEMA-TiO_2 gel-based hybrids

Kuznetsov *et al*. [16] have investigated the optical properties of the different kind of TiO_2 gel-based hybrid materials fabricated by Kameneva *et al*. [14, 16] (Figure I.1.9). These hybrids undergo a photodarkening effect under UV irradiation (380 nm $\geq \lambda \geq$ 300 nm) (Figure I.1.11). The studies carry out by Kuznetsov *et al*. [16] have permitted to reveal correlations between the morphology of organic and inorganic parts of hybrid materials and their photosensitivity.

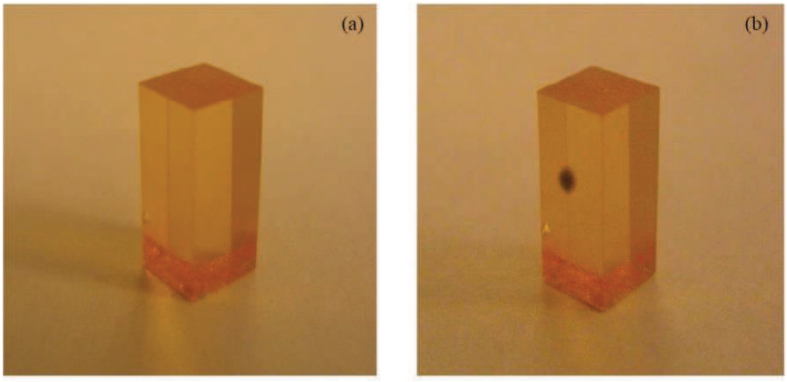

Figure I.1.11 Hybrid organic-inorganic materials based on titanium oxide gels: (a) before and (b) after UV laser irradiation (λ_{laser} = 355 nm). (Redraw from ref. [16]).

a) Optical and EPR spectra of UV light-induced darkening of TiO_2 gel-based hybrid materials.

The absorption of UV (λ_{laser} = 355 nm) irradiated part of the pHEMA-TiO_2 gel-based hybrid, the darkened zone, is very broad spanning over IR, visible and UV ranges (Figure I.1.12). The spectra of samples #1, #2 and #3 are rather similar with absorption band maximum at roughly 640 nm.

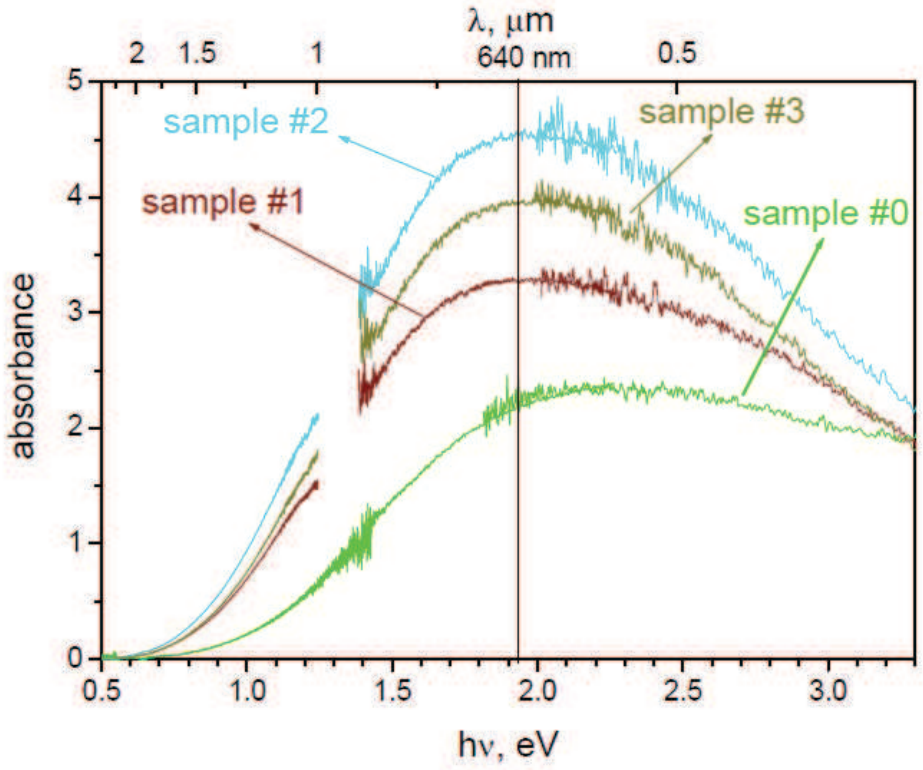

Figure I.1.12 Laser-induced absorption spectra of different pHEMA-TiO_2 hybrids (Redraw from ref. [16]).

Electron paramagnetic resonance (EPR) measurements have been carried out to get more insights about the chemical nature of the species involved in the absorption processes. Indeed, EPR measurements provide information about the nature and the quantity of paramagnetic species in a medium. In 1985 Howe R.F. and Grätzel M. [30] reported the EPR study of paramagnetic species formed under irradiation of colloidal TiO_2 solutions by near UV light. They have attributed the observed paramagnetic signal to the trapped electrons as Ti^{3+} centers located both at the surface and in the interior of TiO_2 particles, demonstrating that Ti^{3+} was responsible for a dark blue coloration of the colloid solution. The EPR spectrum recorded at

77 K on the UV-irradiated gel based pHEMA-TiO_2 hybrid is shown in Figure I.1.13. It exhibits the characteristic magnetic parameters of paramagnetic Ti^{3+} centers in a distorted rhombic oxygen ligand field (g_x = 1.973 ± 0.002, g_y = 1.919 ± 0.002 and g_z = 1.855 ± 0.002) [14].

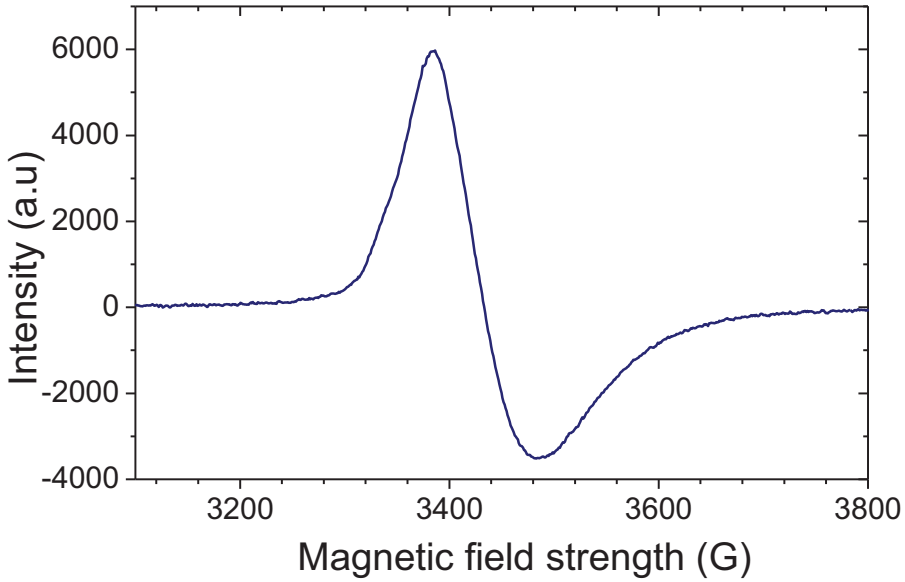

Figure I.1.13 EPR spectrum of irradiated (λ=355 nm) gel based pHEMA-TiO_2 hybrid sample. (Redraw form ref. [16]).

EPR measurements have shown that Ti^{3+} centers which are produced at irradiation of pHEMA-TiO_2 gel-based hybrids by light below 380 nm are responsible for laser-induced darkening effect.

b) Dark relaxation of Ti^{3+} centers in TiO_2 gel-based hybrid materials.

The lifetime of the laser-induced Ti^{3+} centers in the hybrid materials is extremely long and exceeds several months at room temperature and atmospheric pressure [16]. The relaxation is due to reactions with atmospheric oxygen diffused into the hybrid sample according to the reaction.

$$Ti^{3+} + O_2 \rightarrow Ti^{4+} + O_2^-$$

The bleaching of the dark spot in the solid sample begins at the surface, then penetrating inside the material (Figure I.1.14a). After long time when Ti^{3+} relaxation is complete, the hybrids recover their transparency.

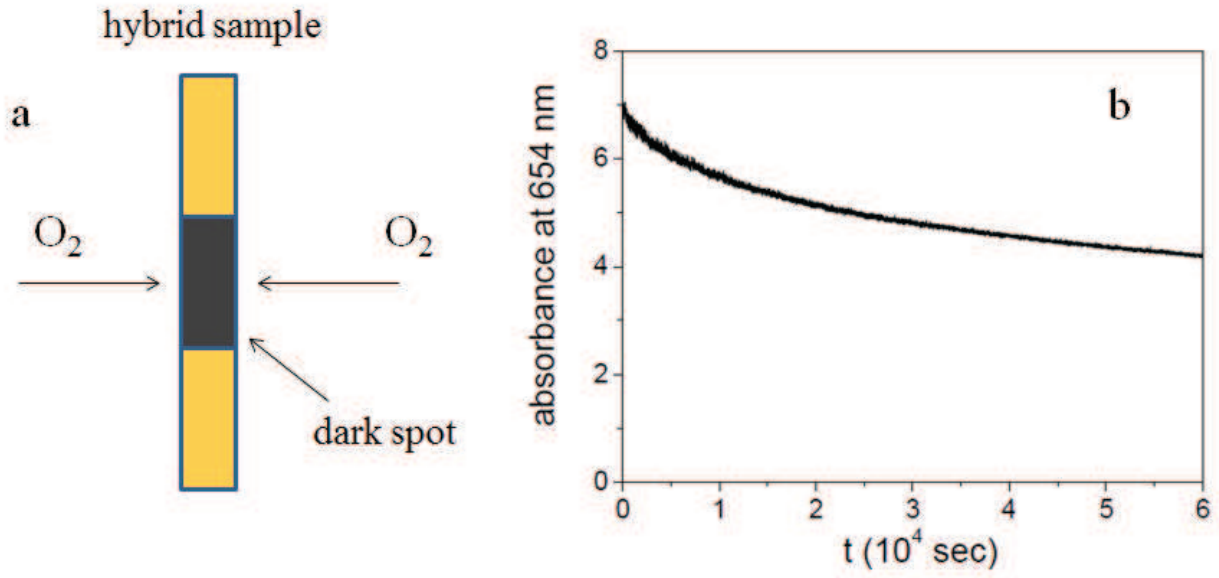

Figure I.1.14 Dark relaxation of the laser-induced (λ_L = 355 nm) visible absorption in the hybrid TiO_2 sample of width 1.4 mm. a) – picture of sample, b) – evolution of the sample absorbance with time. (Redraw form ref. [16]).

The typical relaxation of the laser-induced Ti^{3+} centers in the hybrid sample is shown in Figure I.1.14. The high relaxation rate at the beginning corresponds to the oxygen bleaching of the surface layers. Then the rate decreases that corresponding to the deeper layers bleaching.

c) Laser-induced Ti^{3+} center kinetics in TiO_2 gel-based hybrid materials.

Kuznetzov et all. [17] have investigated the laser-induced photodarkening kinetics in TiO_2 gel-based hybrid materials. The evolution of the absorbance at 430 nm as function of the UV irradiation dose at 355 nm is reported in Figure I.1.15 for the different samples under consideration. The photodarkening effect is less efficient in the sample possessing inorganic nano-domains (sample #0), than in samples based on bigger inorganic blocks (sample #1, #2 and #3) Moreover, the morphology of the inorganic phase also influence the kinetics of the photodarkening effect, since the absorbance of sample #1 is significantly lower than the one of samples #2 and # 3.

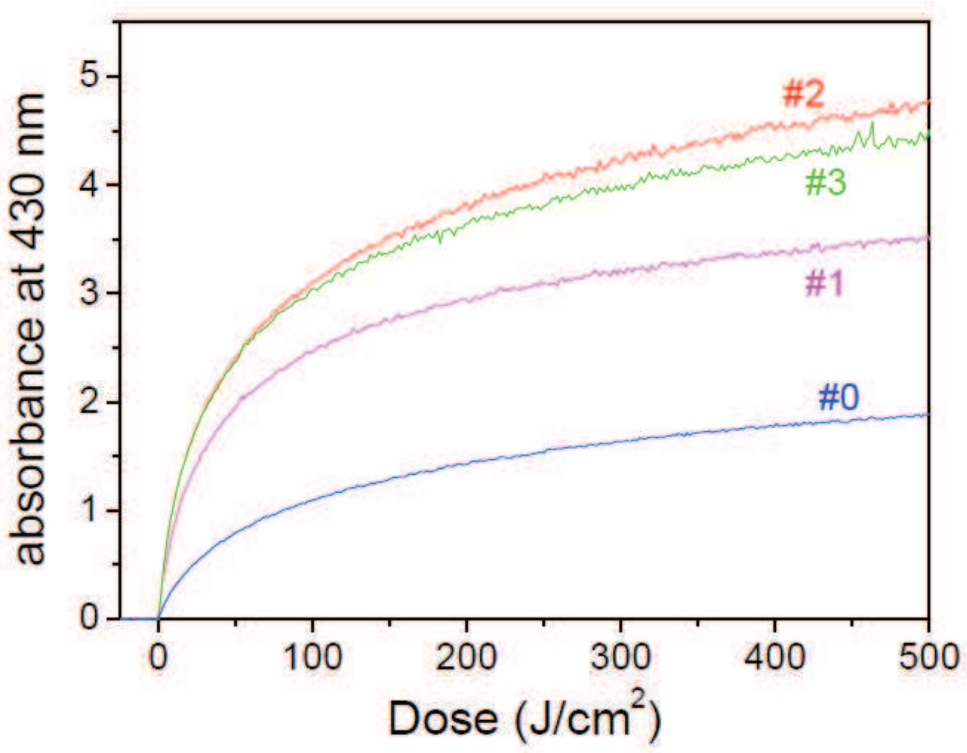

Figure I.1.15 Laser-induced darkening kinetics of hybrid samples (λ_{laser} = 355 nm, I = 0.36 W/cm^2). The numbers of the samples are shown in the figure. (Redraw from ref. [16]).

For a better understanding of the laser-induced darkening kinetics, Kuznetzov *et al*. [17] have proposed a model depicted in Figure I.1.16. The absorption of UV photons $h\nu_1$ (1) result in the electrons transition from the valence band due to O^{2-} 2p-orbital to the conduction band related to Ti^{4+} 3d-orbital. The excited electrons either can be trapped on Ti^{3+} centers (4) with a quantum efficiency η, either can recombine with the hole (2) with a probability 1-η. At the same time, light holes h^+ can escape into the organic pHEMA component where they are trapped as h_{tr}^+ (3). The Ti^{3+} centers have very long lifetime $\tau \geq 10^7$ s and their spontaneous (''dark'') relaxation (5) with trapped holes is slow. However, trapped electrons on Ti^{3+} can either recombine with "freshly" created holes (6), either can be reexcited in the CB by the absorption of a photon $h\nu_2$ (7). This last process is described by the absorption cross-section σ_b. Eventually, the successfully reexcited CB electrons can migrate to the trapped holes h_{tr}^+ and recombine with them (9) with quantum efficiency η_b, or be retrapped by a Ti^{3+} (8) center with the probability (1-η_b).

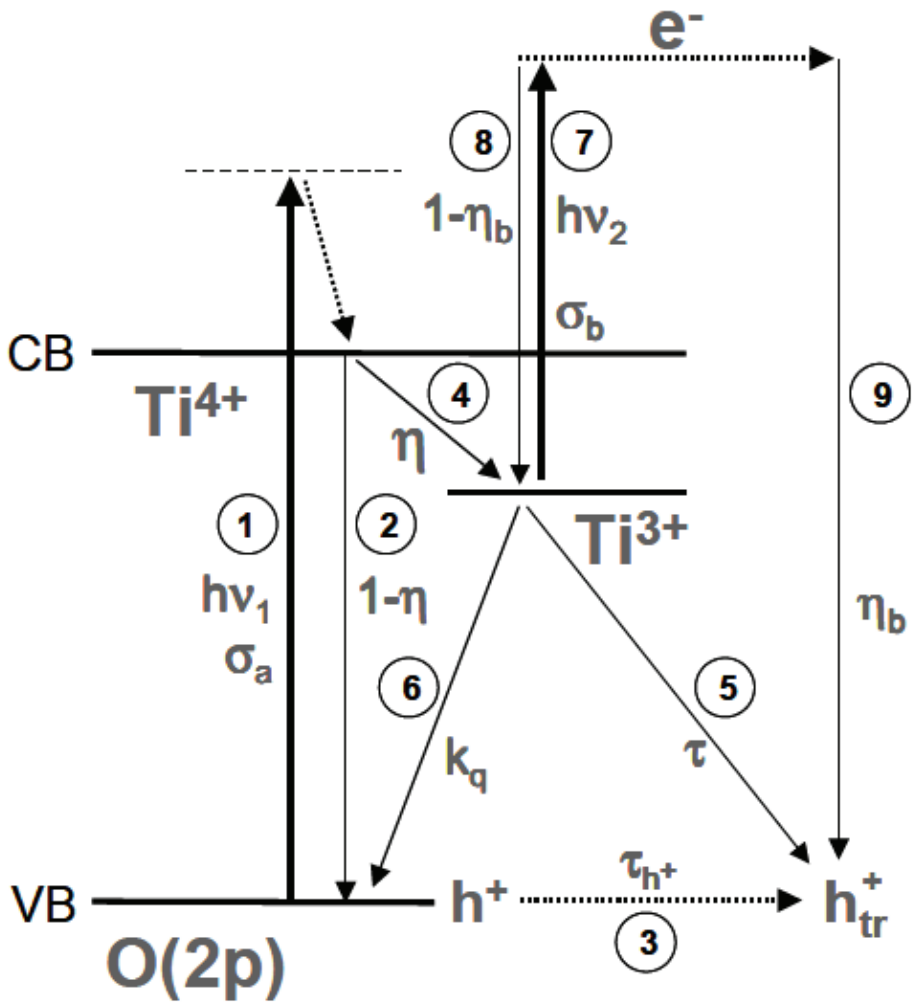

Figure I.1.16 Scheme of photoinduced processes in TiO_2 hybrid materials. (Redraw from ref. [17]).

According to this model the evolution of the trapped electrons density [Ti^{3+}] and UV laser intensity are described by the following coupled equations.

$$\partial[Ti^{3+}]/\partial t = \eta(1 + [Ti^{3+}]/b_c)^{-1}([Ti^{4+}]_0 - [Ti^{3+}])\sigma_a I - \eta_b[Ti^{3+}]\sigma_b I$$

$$\partial I/\partial x = -(\sigma_a[Ti^{4+}] + \sigma_b[Ti^{3+}])I$$

where $[Ti^{4+}]_0 = 1.2 * 10^{21}$ cm^{-3} is initial concentration of titanium, $b_c = (k_q t_{h+})^{-1}$ is a critical Ti^{3+} concentration, k_q is the rate constant for the recombination of trapped electrons on Ti^{3+} centers with ‘‘fast’’ holes (process 6 in Figure I.1.16). The laser intensity I on surface of the irradiated sample is expressed in photons per cm^2 s and both absorption cross-sections σ_a and σ_b are referred to the same wavelength (λ_{laser} = 355 nm), the indexes a and b are related to Ti^{4+} and Ti^{3+} centers, respectively. The terms $(1 + [Ti^{3+}]/b_c)^{-1}$ and $\eta_b[Ti^{3+}]\sigma_b I$ describe, respectively, the contributions from annihilation of photoexcited holes with already trapped electrons and inner

photoeffect. Neither of these terms affects the initial absorption growth, which is uniquely defined by the efficiency η.

The fits of the experimental data with the theoretical model for four hybrid samples are shown in Figure I.1.17. The obtained fit parameters are summarized in Table I.1.6 with estimated accuracy at ~10%.

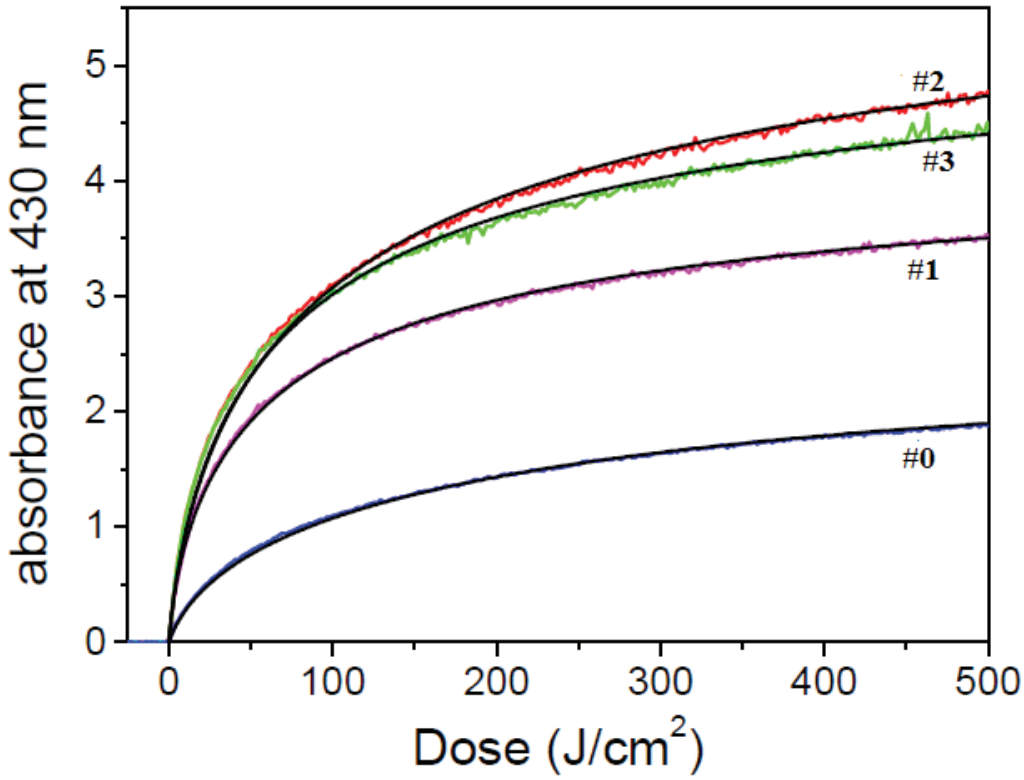

Figure I.1.17 Fitting of experimental data on dose dependence of laser-induced absorbance (The thickness of the samples is 0.4 mm, irradiation is performed at 355 nm (third harmonic of a Nd:YAG laser), repetition rate 10 Hz, average intensity I_{av} = 0.36 W/cm^2, absorbance is measured at the wavelength 430 nm). (Redraw from ref. [16]).

Table I.1.6 Parameters of fit of the laser-induced absorption kinetics in the hybrid materials by the theoretical model proposed by Kuznetsov et al [16].

Samples	Quantum yield (η), %	Maximum population Ti^{3+}/Ti^{4+} (%)	η_q, %	b_c/a_0
hybrid #0	6	4.6	0.16	0.0071
hybrid #1	12	8.2	1.65	0.0125
hybrid #2	12	13.9	1.3	0.025
hybrid #3	12	11.8	2.0	0.029

A comparison made of different pHEMA-TiO_2 hybrids allowed to evidence correlations between their nanoscale morphology and photonic sensitivity. Indeed, the hybrids prepared of inorganic nano-domains (hybrid #0) show the lowest charges separation efficiency and minimum charges loading between the considered samples. On the other hand, the hybrids composed of macroscopic chains of low fractal dimension (hybrid #2) demonstrate the maximum charges separation efficiency and maximum charge loading.

I.1.4.2. Photo-induced refraction of hybrid materials based on TiO_2 nanoparticles

Uklein *et al*. [19] have investigated the UV photo-induced refraction of nanoparticulate organic-inorganic TiO_2-pHEMA hybrids prepared according to the approach proposed by Gorbovyi *et al*. [6]. They developed an original approach, based on the well-known Z-scan method, to measure the photoinduced change of refractive index in the hybrid samples. The scheme of experimental setup is depicted in Figure I.1.18. A UV laser diode at 375 nm delivers a TEM_{00} beam. This beam interacts with the sample at normal incidence, and the transmitted beam is analyzed by two photodiodes (D1 and D2). The photodiode D1 monitors the total transmitted power whereas the photodiode D2 measures the transmitted power through a small diaphragm (r_a = 225µm) placed in far field (on-axis transmittance). Depending on the sample position, the increase or decrease of the on-axis transmittance measured by the photodiode D2 allows determining the sign of the photoinduced refractive index variations in the sample. The amplitude of the refractive change is obtained, in the framework of Gaussian optics, from the evolution of the on-axis transmittance power as function of the UV irradiation dose (Figure I.1.19).

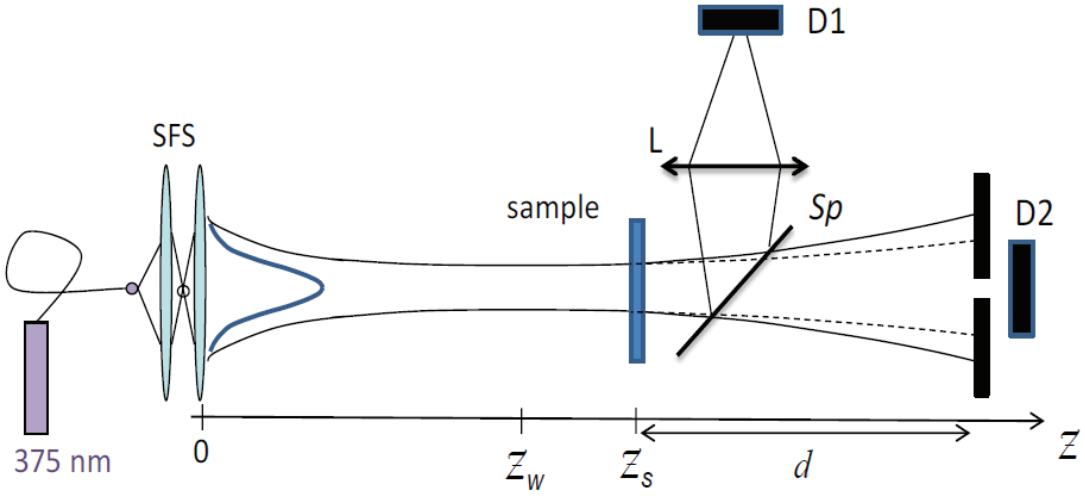

Figure I.1.18 Experimental setup: SFS – spatial filtering system, Sp is a beam splitter, D1 and D2 are photodiodes. The beam waist position is taken as the origin of the axis z. (Redraw from ref. [19]).

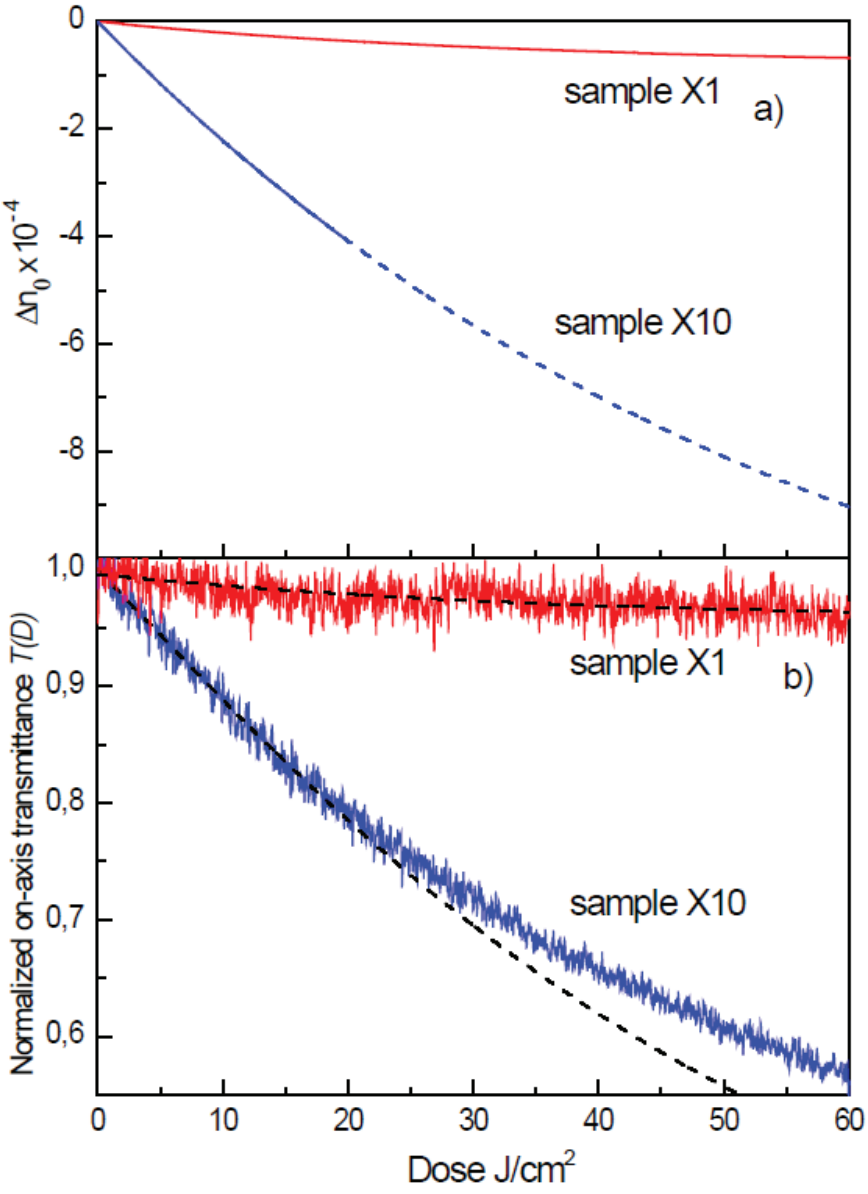

Figure I.1.19 Variations of refractive index Δn_0 (a) and normalized on-axis transmittance (b) of hybrid samples X1 and X10 versus the UV irradiation dose. On (b) the dashed lines represent the fits of on axis transmittance. (Redraw from ref. [19]).

Uklein *et al*. have found that refractive index of hybrid materials decrease with the increase on UV irradiation dose. It also has been shown that both organic and inorganic components of hybrids can contribute to the refractive changes. The strongest variation of $\Delta n = -5 \cdot 10^{-4}$ has been measured in the sample with highest concentration of TiO_2 nanoparticles. All the data obtained by Uklein *et al*. [19] is presented in Table I.1.7.

Table I.1.7 Hybrid samples characteristics: $[Ti^{4+}]$ concentration, thickness of samples (L), quantum yield η_a (section I.1.4.1), photoinduced refractive index change Δn_0, density of $[Ti^{3+}]$ centers and refractive index modification per Ti^{3+} center a_0*.

Name of samples	$[Ti^{4+}]$ 10^{20} cm^{-3}	L μm	η_a %	Δn_0 10^{-4}	$[Ti^{3+}]$ 10^{18} cm^{-3}	a_0 10^{-23} cm^3
X1	0.88	94.9	14.5	-0.23	0.90	-2.55
X2	1.76	78.1	13.4	-0.36	1.72	-2.13
X5	4.4	92.9	7.0	-0.48	2.59	-2.17
X10	8.8	98.6	16.5	-2.42	10.85	-2.23
X20	17.6	82.7	15.1	-5.64	19.01	-2.97

* All values are given for a reference irradiation dose equal to 10 J/cm^2.

I.1.5. Conclusions

In this section we have considered some hybrid materials. Firstly, a classification of hybrid materials has been presented highlighting two different classes. The hybrids with weak-type interactions (Van der Walls, hydrogen bonding or electrostatic interactions) between organic and inorganic parts belong to the class I, whereas the class II includes the hybrids with strong-type interactions (coordinative, ionic, or covalent interactions).

Especial attention has been paid to organic-inorganic pHEMA-TiO_2 hybrid materials belonging to the class II. Previous results obtained in the NINO team (LSPM) and concerning properties of pHEMA-TiO_2 hybrids have been reviewed. We have discussed the synthesis method of gel-based pHEMA-TiO_2 hybrids proposed by Kameneva *et al*. [18] and emphasized that delay time between gelation and polymerization processes strongly influence on the microstructure of the inorganic component.

The method to synthesize nanoparticulate pHEMA-TiO_2 hybrid materials proposed by Gorbovyi *et al.* [6] has also been considered. The difference with approach proposed by Kameneva *et al*. is the ability to precisely control the morphology of inorganic component.

Finally, the investigations of optical and electronic properties of TiO_2-based hybrids made by Kuznetsov *et al.* [16] and Uklein *et al.* [19] have been presented. Under UV irradiation the pHEMA-TiO_2 hybrid materials are subject to a reversible photo-stimulated darkening. This effect is a result of an efficient charges separation at the organic-inorganic interface, when the conduction-band (CB) electrons remain trapped in the inorganic component and the valence-band (VB) holes leave to the polymer component.

Uklein *et al.* [19] have shown that photosensitivity of nanoparticulate pHEMA-TiO_2 hybrid materials strongly depends on the concentration of TiO_2 nanoparticles demonstrating the

higher photosensitivity for higher concentration of TiO_2. However it has been found by Gorboviy *et al*. [6] that simultaneously with increase of the nanoparticle concentration the hybrids mechanical properties are deteriorated. For that reason, one of the main tasks of our work was to elaborate a fabrication method of pHEMA-TiO_2 hybrid materials allowing to increase concentration of nanoparticles without significant degradation of hybrids mechanical properties. To solve this problem we propose to use high-pressure chemistry. That's why, in the next sections we present some concepts of high pressure chemistry, and consider several examples of high pressure induced chemical reactions.

I.2. Chemical systems at high pressure

I.2.1. Introduction

Pressure is a thermodynamic parameter which strongly influences properties of a chemical system. Chemical equilibria and chemical kinetics of a system depend on pressure. Depending on the scientific field, pressure is conventionally divided into low, moderate, high and very high. The range of high pressures found in nature, is very broad. Pressure on the depths of the ocean caused by the gravitational field of the Earth reaches 100 MPa. Pressure in the center of the Earth is 360 GPa, on stars (white dwarfs) is 10^{10}-10^{12} GPa. In physics and chemistry, pressures exceeding 0.1 GPa (1000 atm) are considered as a high pressure.

The main effect of a pressure increase is to reduce the volume available for the system. For example in solid nitrogen in the β-phase compression from 0 to 1 GPa results in a volume reduction of 25% [31]. Liquids and solids are much less compressible than gases. Molecular systems are characterized by strong intramolecular interactions responsible for molecular bonding and weak intermolecular van der Waals interactions defining the aggregation state of the system. Under volume compression greater than 1 order of magnitude with respect to atmospheric pressure, intermolecular distances are reduced to such an extent that repulsive part of the intermolecular potential is explored. The relative weights of the strong intramolecular interactions and weaker intermolecular interactions are strongly altered. In these conditions, the system becomes thermodynamically unstable and the free energy (due to the pV term in the Gibbs free energy $G = E + pV - TS$) can be large enough to exceed the energy of the molecular bonds. The minimization of the free energy is then achieved through a full reorganization of the chemical bond connectivity leading to ionization, polymerization, formation of atomic lattices, metallization [32-35], etc.

I.2.2. Effect of pressure on molecular systems

I.2.2.1. Effect of pressure on electronic structure of molecular systems

The reactivity of molecular system at high pressure results from substantial changes of the electronic structure with the reduction of the available volume [36]. This include shifts and broadening of the electronic energy levels and subsequent mixing of ground and excited states leading to thermal population of higher electronic states. These effects have been discussed by Drickamer *et al.* on the basis of a harmonic model of the potential energy surfaces [37] and by others authors with more elaborated approaches [38-40]. Drickamer *et al.* described the influence of pressure on molecular systems in terms of different compressibility of the ground and excited states. According to their model the increase of pressure induces an increasing overlap of electronic orbitals of adjacent atoms or molecules resulting in, (i) a reduction of the difference in energy between the lower empty π^* (LUMO) and the higher occupied π (HOMO) orbitals (ΔE_{ex} and ΔE_{gr} on Figure I.2.1), (ii) a horizontal displacement of potential energy surfaces along the configuration coordinate Q (ΔQ_{ex} and ΔQ_{gr} on Figure I.2.1). Both together these effects lead to an efficient mixing of the ground and excited states (*i.e.* to a ground state strongly modified by configuration interaction) allowing the thermal population of excited states [37]. Moreover, the change of molecular energetic structure occurring at high pressure also modified the threshold for optical excitation of excited states (blue arrow on Figure I.2.1). These effect has been experimentally put in evidence by Citroni *et al.* [41]. Although the HP induced modification of electronic distribution and molecular geometry can trigger reaction with neighboring molecules [42], optical excitation of the molecule to suitable electronic states, is often used to speed up the reactions and lowers the pressure threshold required for the reaction to occur [32].

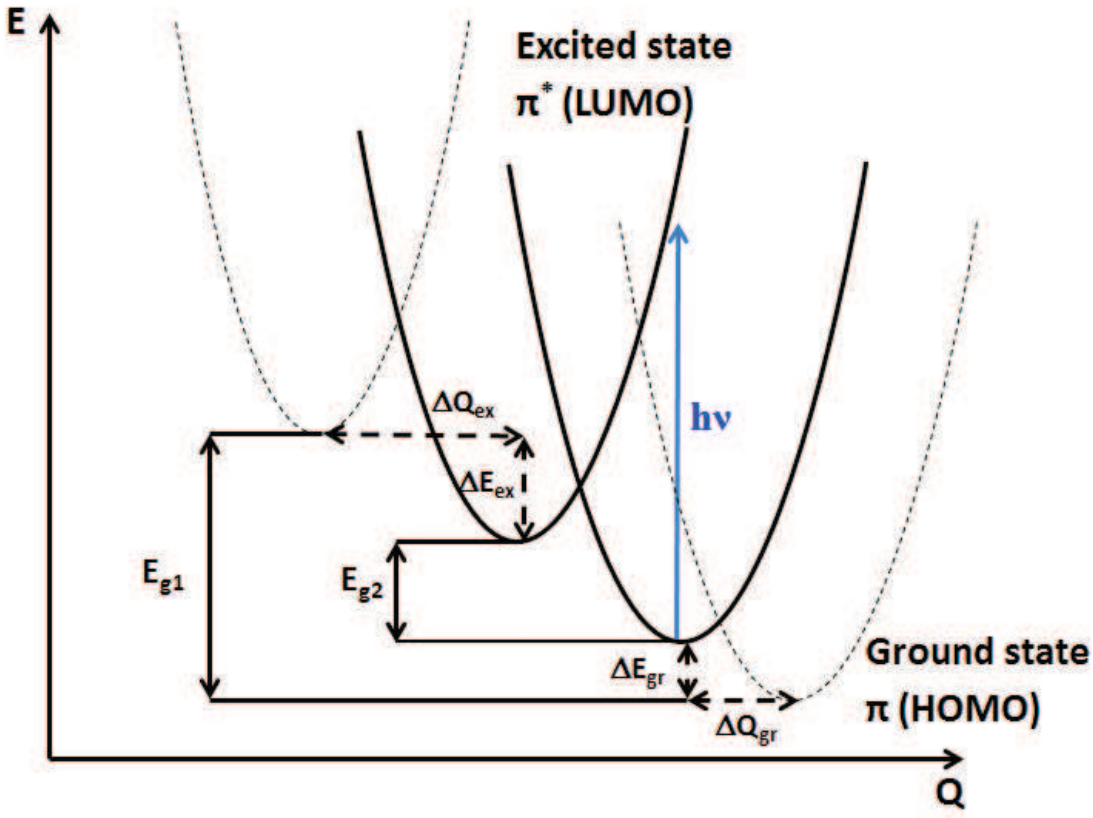

Figure I.2.1 Schematic configuration coordinate diagram (solids lines correspond to potential energy surfaces under pressure, dash lines correspond to the potential energy surfaces at atmospheric pressure).

Basically, the rearrangement of electronic clouds induced by compression leads to substantial changes in the electronic structure of reactants and, potentially, to modifications of chemical bonds. Compared with ambient conditions, new chemical reactions pathways become available and novel reaction products may be expected. Indeed, under high pressure, the interplay between energy surfaces of ground and excited states makes the thermal excitation of excited electronic states feasible. Consequently, the electronic structure of HP reactants is quite different from that of reactants at ambient pressure, and the role of excited state in the reaction has to be considered. This is why HP chemical reactions share common features with photochemical reactions, as reported in several experiments where an acceleration of the reaction by optical pumping of the reactants in a suitable excited state has been demonstrated to be equivalent to an increase in pressure [32].

I.2.2.2. Environmental and steric effects of molecular systems at high pressure

As it has been already mentioned, the electronic structure of reactants can change considerably with increasing pressure. There are, however, other relevant aspects of environmental and steric effects on molecular systems at high pressure that deserve a discussion.

The primary effect of compression on a system is the contraction of the volume and thus a decrease of the interatomic and intermolecular distances. Figure I.2.2 shows an example of evolution of the shortest intermolecular H•••H separation with pressure of silane (SiH_4) [43].

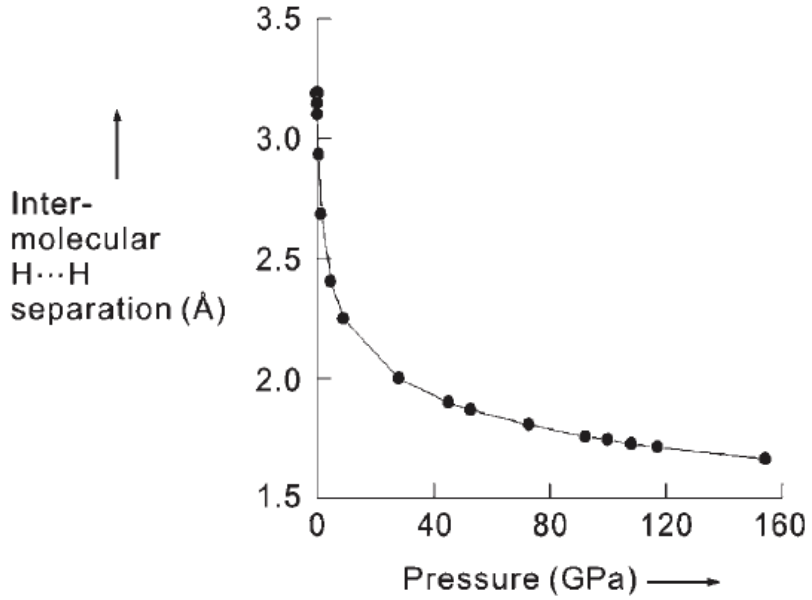

Figure I.2.2 The evolution of the shortest intermolecular H•••H separation with pressure in one hypothetical structure for SiH_4**.** Note the rapid diminution in the H•••H separation as pressure increase to 10 GPa. (Redraw from ref. [44]).

The compression can be as large as $V/V_0 = 0.5$ for pressures in the range of several GPa, which corresponds to a ~80% reduction of interatomic distances. In these conditions the energy density increase is comparable with energy of chemical bonds and therefore the physical and chemical properties of molecules are expected to differ from those at ambient conditions. The importance of the environment changes of molecular systems at high pressure is of particular relevance in solids, where the spatial arrangements of the molecules impose geometrical constraints that can play a basic role in determining the reaction pathway [45]. The reactivity of molecular materials at high pressures can, equivalently, be viewed considering that with the reduction of the available volume the electronic density greatly increases and the kinetic energy of the electrons involved in the chemical bonds predominates over the attractive interactions. At high pressure the molecular system will react by substituting the multiple bonds and the weak intermolecular bonds with a distribution of single bonds. Such distribution will correspond to a topology in accordance with the Le Chatelier's principle that favors the evolution of the system toward reduced volume products at high pressure [35].

I.2.3. High pressure technology

For the last 50 years progresses in high-pressure chemistry have been resulting from fast growing and significant improvements of high pressure generation techniques. Static pressure up to several hundreds of GPa can be generated by using diamond anvil cells (DACs), while higher pressure can be obtained dynamically by using shock-wave techniques [46]. The static approach with DAC is of particular interest because it allows a continuous tuning of pressure, a control of temperature and the possibility to use a large number of in situ characterizations methods (XRD, Raman and IR spectroscopies, etc.) [32]. The principle of the DAC operation is simple: two opposing brilliant-cut diamond anvils compress the sample contained inside a hole drilled in a metal gasket (see Figure I.2.3). The force applied on the large face of the diamond, and the ratio between the area of this face and that of the small culet face in contact with the sample, determine the pressure undergone by the sample. The principle of DAC operation is discussed In more detail in section II.2.

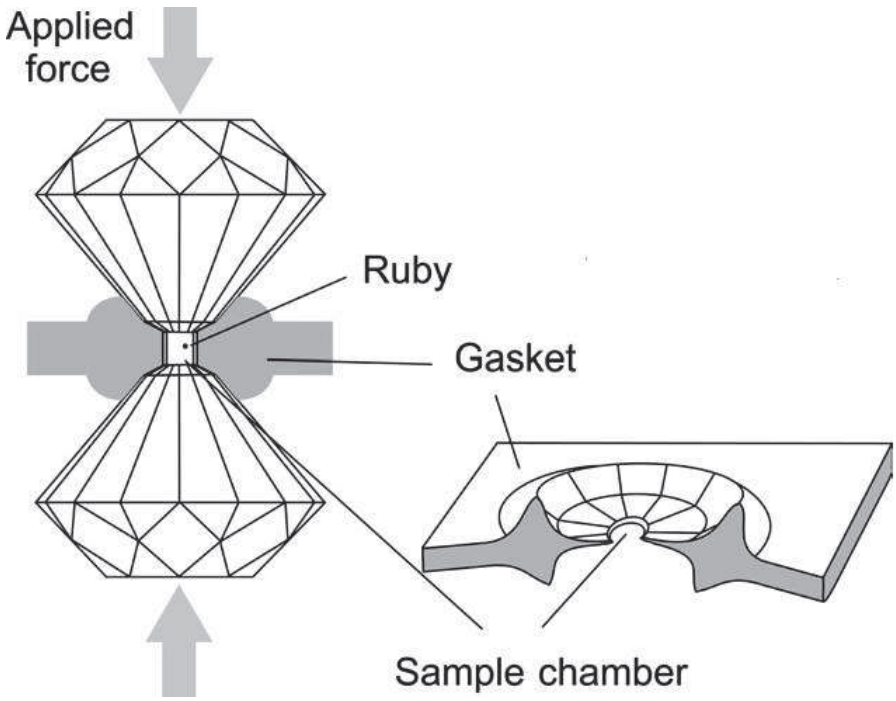

Figure I.2.3 The principle of diamond anvil cell (DAC). (Redraw form ref. [35]).

I.2.4. Chemical reactions at high pressure

In this section several chemical reactions occurring at high pressure will be discussed. Two cases of reversible reactions with diatomic and triatomic molecules (carbon dioxide and

molecular nitrogen) will be presented. After, we will consider a high pressure induced polymerization of cyanoacetylene and acrylic acid as examples of irreversible and reversible high pressure reactions. Finally, we will overview the laser-assisted high-pressure induced chemical reactions of hydrocarbons. Considering of several examples (ethylene, acetylene, butadiene, and benzene) we will show that combination of high pressure with laser irradiation specifically influence on the kinetics of the reaction and strongly modify the nature of the recovered product.

I.2.4.1. Diatomics and triatomics molecular systems

In condensed phases diatomic and triatomic molecules show an extremely high compressibility with a reduction of volume by a factor of up to 2 or 3. Two examples considered in this section (reactions of carbon dioxide and molecular nitrogen) are cases of reversible reactions where recovered products do not differ from the original reactants. Nevertheless the substantial rearrangements of chemical bonds are observed in both reactions. Moreover their simple molecular structures bring information on the electronic configuration changes induced by high pressures [45]. Therefore, it is useful to discuss these two examples, before considering high-pressure induced reactions of more complex systems.

HP induced transformations of Carbon Dioxide

CO_2 is an attractive solvent in organic synthesis. It has been shown that the solvent properties of carbon dioxide can be tuned by pressure [47]. Although CO_2 is a simple molecule, its high pressure phase diagram is rather complex, exhibiting up to six different solid phases [48]. Figure I.2.4 shows the thermodynamic and kinetic phase diagram of solid carbon dioxide. At room temperature CO_2 solidifies into cubic phase I, commonly known as dry ice. When CO_2 compressed between 12 and 22 GPa at room temperature phase I transfers into the orthorhombic phase III [49] which is a molecular crystal too. Actually, the view of a molecular solid for CO_2-III would seem to be challenged by a recent structural investigation [49], where it was suggested that phase III is a high strength and hard material with increased intermolecular bonds. At pressures above 30 GPa and 1800 K [50, 51] a CO_2-III transforms into a non-molecular phase (polymeric CO_2-V), where carbon atoms are tetrahedrally bounded by single bonds to oxygen atoms in a crystalline tridimensional array. Moreover, phase V was found to be ‘‘superhard’’, e.g. as hard as cubic BN that is the second hardest known material. The polymeric CO_2-V form is found to be metastable over a large pressure range (below 25 GPa). In fact it can be quenched at ambient temperature and to 1 GPa, when a back transformation to the (liquid) molecular form is observed [52].

Dissociation of solid CO_2 into diamond and molecular oxygen was found by heating this material at 30–80 GPa and 1500–3000 K [53]. Above 40 GPa the dissociation was preceded by the formation of a new non molecular phase, CO_2-VI, which was thought to be precursor of the dissociation itself.

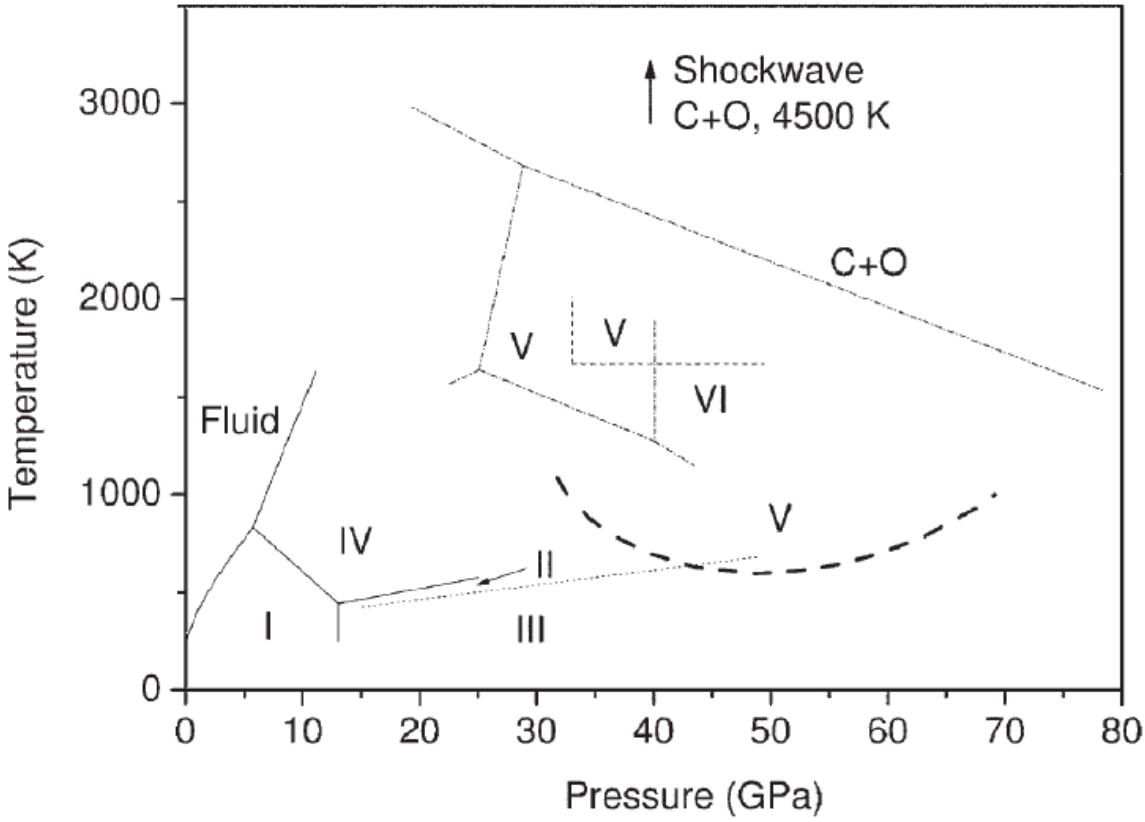

Figure I.2.4 Thermodynamic and kinetic phase diagram of solid carbon dioxide: continuous lines, phase boundaries delimiting CO_2-I, II, III, and IV [54, 55]; dotted line, kinetic transformation boundary from CO_2-III to CO_2-II [54, 55]; thick dashed line, kinetic transformation boundary from molecular to non-molecular CO_2 [51]; dashed [49] and dot-dashed [53] lines, approximate kinetic transformation boundaries from molecular CO_2 to the extended covalent phases V and VI, and to dissociation. (Redraw from ref. [48]).

After the discovery of crystalline non-molecular CO_2, two new solid phases, named IV and II, where reported to exist, close to the pressure–temperature range of CO_2-V. Phases II and IV can be obtained by heating CO_2-III in the pressure ranges 12-30 GPa [54] and above 20 GPa [56] respectively. It has been found that CO_2-IV and II show intermediate character between molecular solids and covalent bonded solids, thus playing the role of precursors to forming phase V.

HP induced transformations of Nitrogen

The dissociation energy of molecular nitrogen N_2 is ~950 kJ/mol, making the N≡N triple bond one of the stronger known chemical bond. Under high pressure (above 66 GPa) nitrogen form a tridimensional network of single bonded atoms [57, 58]. One of the interests of non-molecular nitrogen is that the dissociation energy of the N-N single bond (~160 kJ/mol) [59] is much lower than the one of the N≡N triple bond. Thus, a considerable amount of energy could be store in non-molecular nitrogen making this material appealing for applications in energetics. Reichlin *et al*. [60] carried out room temperature high pressure experiments of up to 130 GPa. They found that molecular nitrogen was stable in this range of pressure even if several phase transformations were observed. Later, a phase transformation, occurring above 150 GPa was observed by optical absorption and electrical resistance measurements [61, 62]. The absorption and electrical resistance measurements gave a clear evidence that new phase (named the η phase) corresponds to an amorphous semiconductor with an estimated optical gap in the range 0.6-0.7 eV [62]. In this phase, the Raman and infrared measurements showed the complete disappearance of both N_2 vibron bands and of the phonon modes [61]. The back transformation to the molecular form of nitrogen on releasing pressure is hindered by kinetics barriers and it was found that non-molecular form (η phase) can be stabilized and recovered at 10 K and at pressures of 10-20 GPa. Once recovered in these conditions the solid is stable on heating up to 175 K [62]. A crystalline form of non-molecular nitrogen has been obtained by Eremets and al. [63] by heating the amorphous η form at 1500 K. The obtained structure has been characterized by X-ray diffraction and Raman spectroscopy as a cubic gauche form (mixture of small clusters of bonded nitrogen atoms) and it has been found that it is metastable only down to 42 GPa. The nitrogen network in the cubic gauche structure is shown in Figure I.2.5.

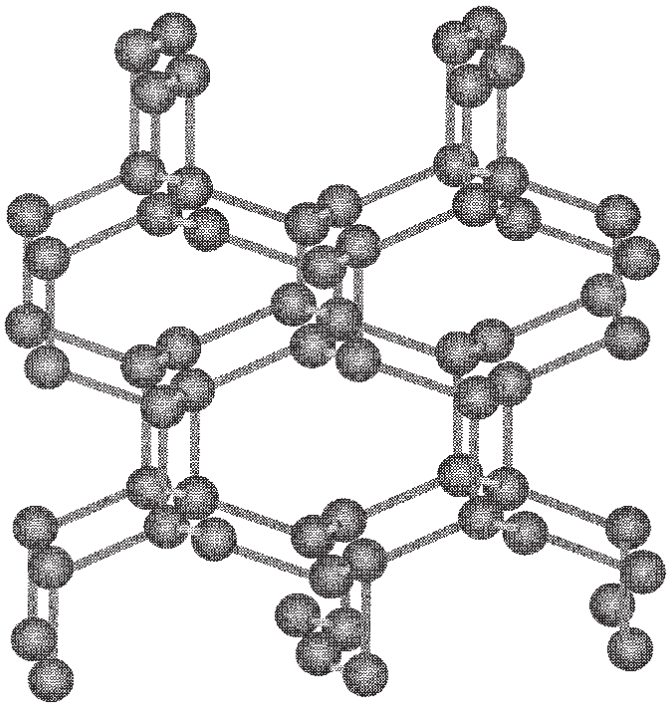

Figure I.2.5 Atoms arrangement in the cubic gauche form of non-molecular nitrogen (from Ref. [45]).

I.2.4.2. HP induced polymerization of Cyanoacetylene and Acrylic Acid

Pressure-induced polymerization is a chemical process pertaining to green chemistry since the reactions can be carried out in the absence of any solvent or catalysts, which implies a lesser environment impact. The application of pressure was found to have a significant impact on polymerization in initially liquid systems where monomers at high pressure may undergo structural transitions to phases that are favorable for polymerization. Here we present two different examples where high-pressure induced polymerization or oligomerization occur in HP induced crystalline state. First we consider the high pressure polymerization of cyanoacetylene. This is an example of irreversible reaction. We also discuss the high pressure polymerization/oligomerization of acrylic acid as an example of reversible reaction where recovered product slightly different from the initial reactant.

HP induced polymerization of Cyanoacetylene

In some solids the reduced molecular mobility and significant energy barriers for rotation, reorientation and translation of molecules dictates the reaction pathways that are possible at high pressure. The reaction of the high pressure induced polymerization of cyanoacetylene (H−C≡C−C≡N) have been studied by Aoki *et al.* [64]. The reaction has been studied in a single crystal where the presence of defects is minimized. At room temperature, cyanoacetylene

crystalizes at 70 MPa in the monoclinic $P2_1/m$ space group with two molecules per unit cell [65]. Because of strong dipole-dipole and hydrogen bonding interactions the molecules in crystal are aligned in chains parallel to one of the crystal axis *a*, as shown in Figure I.2.6(a). This arrangement determines a larger compressibility of the crystal in the directions perpendicular to the chain's axis. Aoki *et al*. have reported that at room temperature after few hours at pressure 1.5 GPa cyanoacetelene transfers to polycyanoacetylene. The reaction occurs through the opening of the C≡C triple bond and cross-linking of the hydrogen-bonded chains in a direction perpendicular to the *a* crystal axis (Figure I.2.6(b)). As can be seen from the Figure I.2.6, the polymerization requires a minimum rearrangement of the molecules once the compression has brought them to a sufficiently short separation. The polycyanoacetylene can be recovered at ambient pressure.

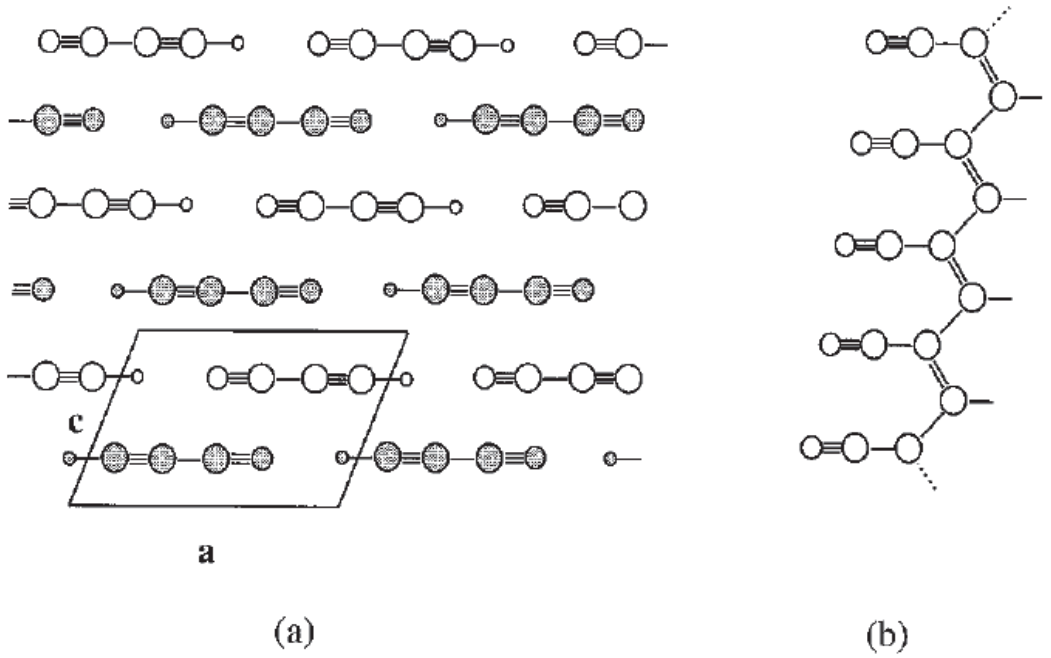

Figure I.2.6 (a) Projection along the *b* axis of the molecular arrangement in the monoclinic $P2_1/m$ crystal structure of cyanoacetylene. Hydrogen bonded molecules from infinite parallel chains arranged in the same *ac* plane (empty molecules). (b) The proposed mechanism of the high-pressure reaction. The molecules lying on the same *ac* plane react through the opening of the triple bond along a direction perpendicular to the *a* axis and not involving the cyano groups. (Redraw from ref. [64]).

HP induced polymerization (or oligomerization) of Acrylic Acid

In case of cyanoacetylene, the recovered polymer is stable at ambient pressure. A completely different picture is observed in the case of acrylic acid (CH_2=CH−COOH). HP induced polymerization of acrylic acid have been studied by Murli *et al.* [66]. It is the case of reversible HP chemical reaction. Murli *et al.* have investigated pressure-induced transformations

of acrylic acid up to 10 GPa. Two crystalline phases (I and II) are observed upon compression up to ~0.3 GPa and ~2.7 GPa respectively. The appearance of phase I corresponds to a liquid-to-solid transformation whereas the formation of phase II relates with a solid-to-solid transition. At pressures 8-10 GPa acrylic acid transforms into a disordered polymeric phase. To understand the transformation process (oligomerization or polymerization) and its reversibility, Murli *et al*. have investigated Raman spectra of acrylic acid on decompression from 10 GPa to ambient pressure (Figure I.2.7). They claimed that acrylic acid remained in the polymeric phase on decompression at pressures above 2.3 GPa. Below 2.3 GPa, some additional bands in the C−H stretching region (e.g., 3109, 3040, 2973, 1638, and 852 cm^{-1}) started to be recovered and were most clearly resolved when the sample was completely quenched to ambient pressure. Compared to the ambient-pressure Raman spectrum of acrylic acid before compression, the recovered substance exhibited similar Raman profiles with only minor differences in the CH_2 stretching region (2800-3200 cm^{-1}) and in the lattice region (200-800 cm^{-1}) indicating a substantial amount of recovered monomers (Figure I.2.7). Moreover, the observation of the additional CH bands and the missing of one of the C=C stretching modes (1638 cm^{-1}) suggest that the retrieved sample may have a structures comprising oligomers instead of initial pure monomers. The significant amount of recovered monomers/oligomers evidenced by Raman spectroscopy suggests that pressure-induced polymerization (or oligomerization) of acrylic acid is highly incomplete.

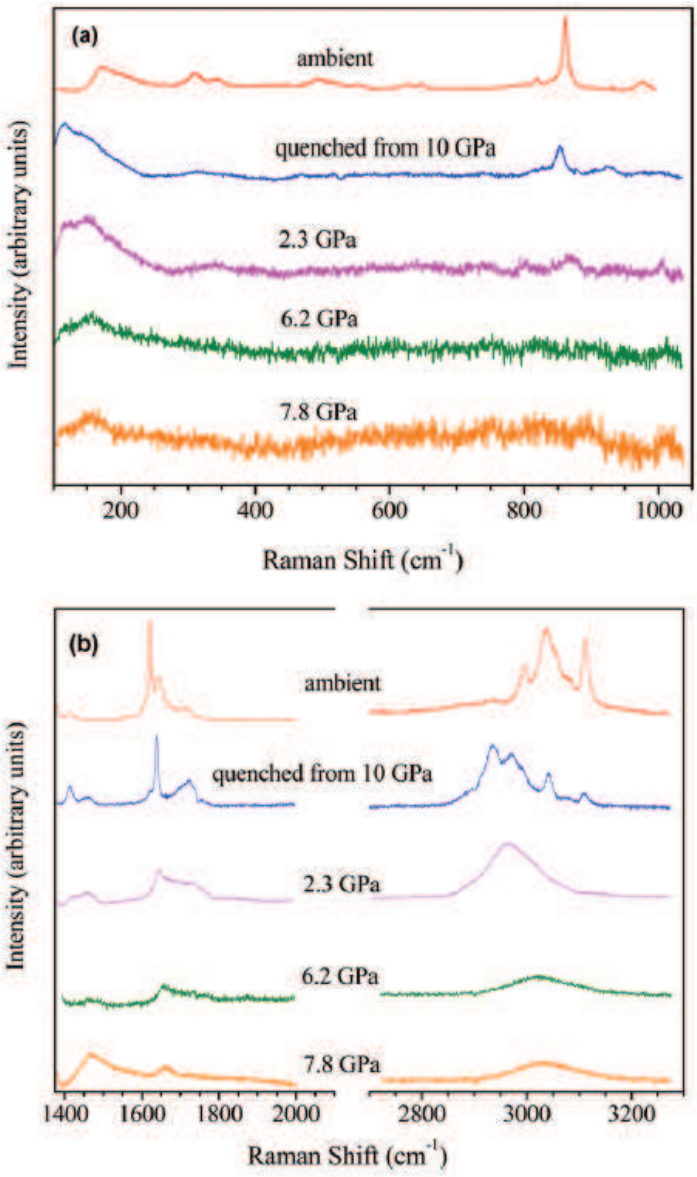

Figure I.2.7 Raman spectra of acrylic acid at selected pressures on decompression in the spectral region of (a) 100-1300 cm^{-1} and (b) 1400-3300 cm^{-1}. (Redraw from ref. [66]).

I.2.4.3. High-pressure induced chemical reactions of hydrocarbons

The effects of HP on hydrocarbon compounds have been attracting a large attention since the beginning of high-pressure research. For example, polymerization of isoprene and butyraldehyde at high pressure were studied by Conant and Tongberg in 1930 [67]. Under high pressures (10-20 GPa) and temperatures (1300-3000°K) hydrocarbons, in particular unsaturated hydrocarbons dissociate [68, 69]. However, dynamic and static high pressure experiments [68-70] and alternative modellings [71, 72] have shown that at high pressure/temperature, hydrocarbons exhibit a more complicated chemical behavior as a result of the balance between the effect of temperature (which favors the dissociation into the constituent

elements), and pressure (which favors condensation processes). There are more several interesting aspects of the hydrocarbons behavior at high pressure and temperature. In particular there is evidence that before complete dissociation, several intermediates (dimers, oligomers, polymers) are formed. Most of chemical reactions of hydrocarbons at high pressure have been investigated with laser assisting. Indeed the idea to combine high pressure and laser irradiation to accelerate chemical reactions derives from basic considerations concerning the pressure effects on electronic states discussed in section I.2.2.1. It has been discussed that an optical activation is extremely efficient in lowering the threshold pressure and increasing the rate of high-pressure reactions [32]. Moreover irradiation may also select a specific process among alternative reaction paths [73]. In this section we will consider laser-assisted high-pressure chemical reactions of unsaturated hydrocarbons including double bonds (ethylene), conjugated polyenes (butadiene), triple bonds (acetylene), and aromatic molecules (benzene).

HP and laser-assisted HP induced polymerization of acetylene.

Acetylene (H−C≡C−H) is an example where both high pressure and laser irradiation specifically influence on the kinetics of the reaction. Polyacetylene is generally prepared in solution using appropriate catalysts [74]. In the solid state, acetylene is found in two crystalline forms [75, 76]. At room temperature, C_2H_2 crystallizes at 0.7 GPa in the *Pa3* cubic structure and has a transition at 1 GPa to an orthorhombic *Cmca* structure stable up to 3.6 GPa. Above this pressure chemical reactions are observed. The first experimental investigation of the solid state pressure induced polymerization of acetylene was reported by Aoki *et al*. [77], by means of Raman spectroscopy. The experiment was performed at room temperature and polymerization was observed from 3.5 GPa. The reaction was also investigated by infrared spectroscopy by Sakashita *et al.* [78]. The pressure threshold of polymerization was confirmed and the reaction was studied in the pressure range 4-14 GPa. At 4.2 GPa the reaction proceeds very slowly (several hours) until a saturation occurs leaving a large amounts of unreacted monomer Upon further increase of pressure, the reaction starts again and come to completion at ~13 GPa. These experiments have raised several questions. Indeed, the identification of the obtained polymer as *trans*-polyacetylene with amounts of *cis* isomer was performed by Raman spectroscopy. However, this result has to be considered with caution because Raman spectra of polyacetylene are known to be very sensitive to resonance enhancement which can make the identification of the reaction products uncertain. Moreover, the kinetics and mechanism of the reaction were suspected to be influenced by laser irradiation used to collect Raman spectra or monitor the pressure from ruby luminescence (see section II.2.1.4). These issues have been addressed by

Ceppatelli *et al*. with a more accurate control of experimental conditions [79]. In these new experiments the polymerization reaction was probed by IR absorption and an infrared pressure sensor ($NaNO_2$/NaBr) was used in order to avoid any laser irradiation of the sample. The obtained results have confirmed that at pressures above 3.5 GPa, the reaction proceeds up to a saturation and can be restarted by a further increasing of pressure. The evolution of the reaction is illustrated in the lower panel of Figure I.2.8 (empty dots) which represents the growth in intensity an IR band related to the reaction products. If ruby fluorescence (and therefore laser irradiation) is used to measure the pressure a similar growing (as in case without laser irradiation) of product IR band is observed (full dots in lower panel of Figure I.2.8). Moreover, it was also found that the sample irradiation with a laser of appropriate wavelength at low power (1-5mW) accelerates the reaction. This effect is illustrated in the upper panel of Figure I.2.8 (full dots), clearly evidence of photoactivation of the HP induced polymerization of acetylene. When the laser irradiation is applied (arrows on in upper panel of Figure I.2.8) the reaction accelerates until the laser irradiation is off (arrows off in upper panel of Figure I.2.8).

A careful analysis of the infrared spectrum shows that the product is composed by *trans*-polyenic chains containing fragments with more than 12 C=C double bonds together with saturated sp^3 carbon atoms evidenced from the presence in the spectrum of saturated CH stretching and bending modes. The intensity of the bands corresponding to saturated sp^3 carbons greatly increases with the laser irradiation of the sample at the expenses of bands related to longer chains. This indicates that laser irradiation produces a substantial branching of the chains that give rise to an extended network. The process is interpreted on the basis of an efficient one-photon absorption to π^* antibonding states [80]. In the excited state, the torsional barrier around the C-C bonds of the chain is lowered, thus favoring the interaction with carbon atoms belonging to other polyenic chains or with acetylene molecules, thus inducing the polymer ramification [32].

These findings are in agreement with other experiments and with the results of calculations on acetylene polymerization. In *ab initio* molecular dynamics simulations [76, 81] it has been found that the reaction product is polyacetylene with some degree of cross-linking [81] and with a composition consisting of mixture *sp*, sp^2 and sp^3 carbons in ration 22:41:37.

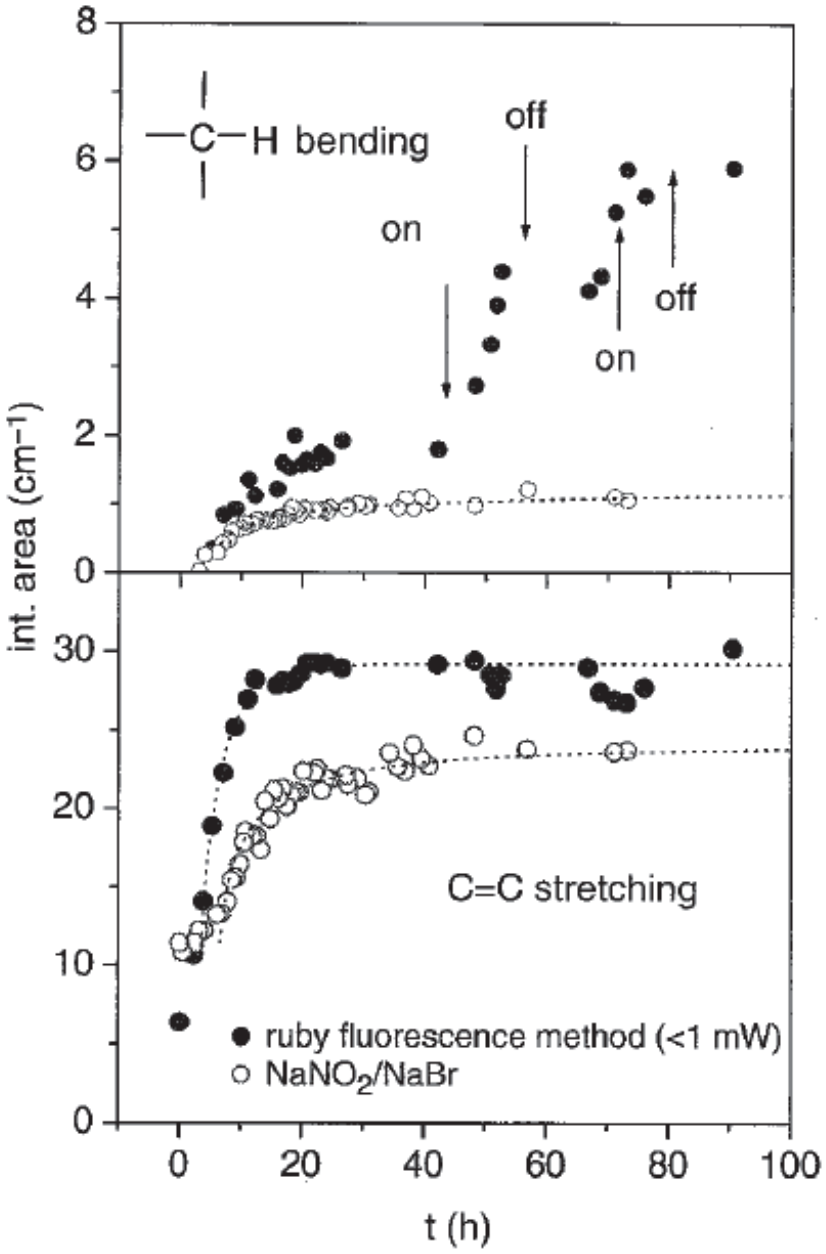

Figure I.2.8 *Lower panel*: Kinetics of the polymerization reaction measured through the time evolution of the IR absorption relative the C=C stretching modes. Full and empty dots correspond to experiments where the pressure calibration was performed by the ruby fluorescence and by infrared sensors, respectively. Differences in the early stages of the reaction reveal the effect of laser light in the activation of the reaction. *Upper panel*: Effect played by laser irradiation in the branching of the chains. The comparison between experiments where laser light is employed (full symbols) or is completely absent (empty symbols) shows that the absorption of the C-H stretching modes involving saturated C atoms sharply increase when the laser light is hitting the sample (irradiation cycles are delimited by the arrows *on* and *off*). (Redraw from ref. [45]).

From the experimental evidence [79, 82] and from the molecular dynamic simulations [76, 81] it has been found that the polymerization reaction develops along a precise crystal

direction (the diagonal of the *bc* plane) (see Figure I.2.9). In this direction the molecules are almost aligned and only a small reorientation is required to realize the polymer geometry.

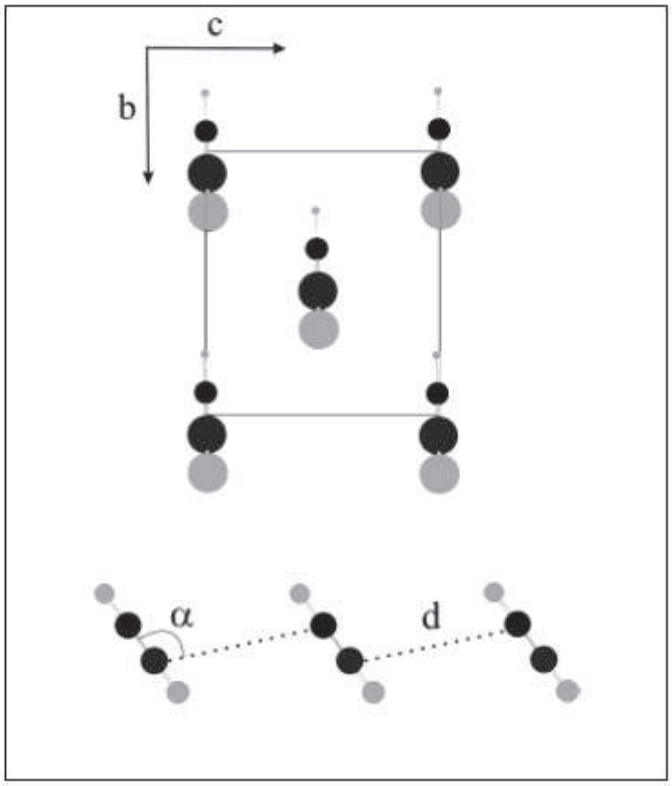

Figure I.2.9 (Top) Molecular arrangement on the *bc* face of the orthorhombic cell of acetylene. (Bottom) The molecules involved in the polymerization reaction lying on the plane containing the diagonal of the *bc* face and forming a 39.5° angle with the *b* axis (α = 109.1°, d = 3.05 Å). (Redraw from ref [32]).

HP and laser-assisted HP induced polymerization of Ethylene.

In the previous example of HP induced polymerization of acetylene we have shown that the reaction can be triggered by laser irradiation. The reaction product of both HP induced and laser-assisted HP induced polymerization of acetylene appeared to be similar. A different picture is observed in the case of ethylene ($H_2C{=}CH_2$). Actually laser irradiation of ethylene under pressure accelerate the reaction of polymerization, but also strongly modify the nature of the recovered product compared to the one obtained by HP alone.

Polyethylene is classified as (a) high-density polyethylene (HDPE) containing mainly linear chains or (b) low-density polyethylene (LDPE) corresponding to branched polymeric chains. The self-polymerization of ethylene under pressure has been widely analyzed both in solid and liquid phases.

The polymerization reaction of solid ethylene at room temperature has been studied in solid phase at 3.3 and 5.4 GPa by means of IR spectroscopy [8]. The first changes in the IR spectra, indicating the occurrence of the reaction, were observed after ~30 h at 3.6 GPa, while this induction time is reduced to ~10 h at 5.4 GPa. The pressure was kept constant during the entire experiment and the spectra were acquired for 289 h at 3.6 GPa and 719 h at 5.4 GPa. In both cases part of the monomer was still present in the cell when the experiment was stopped, indicating that the reaction was not complete. Nevertheless, a considerable amount of a white/transparent plastic solid was recovered at ambient condition, thus confirming the polymer formation. The new IR bands growing during the reaction are observed in the region between 2850 and 3000 cm^{-1}, assigned to CH stretching modes involving saturated C atoms, at 1482 cm^{-1} on the high-frequency side of the ν_{12} band, and in the C−H bending region at 720 cm^{-1} (see Figure I.2.10). The reaction product has been defined as a low-density form of polyethylene with a considerable degree of branching.

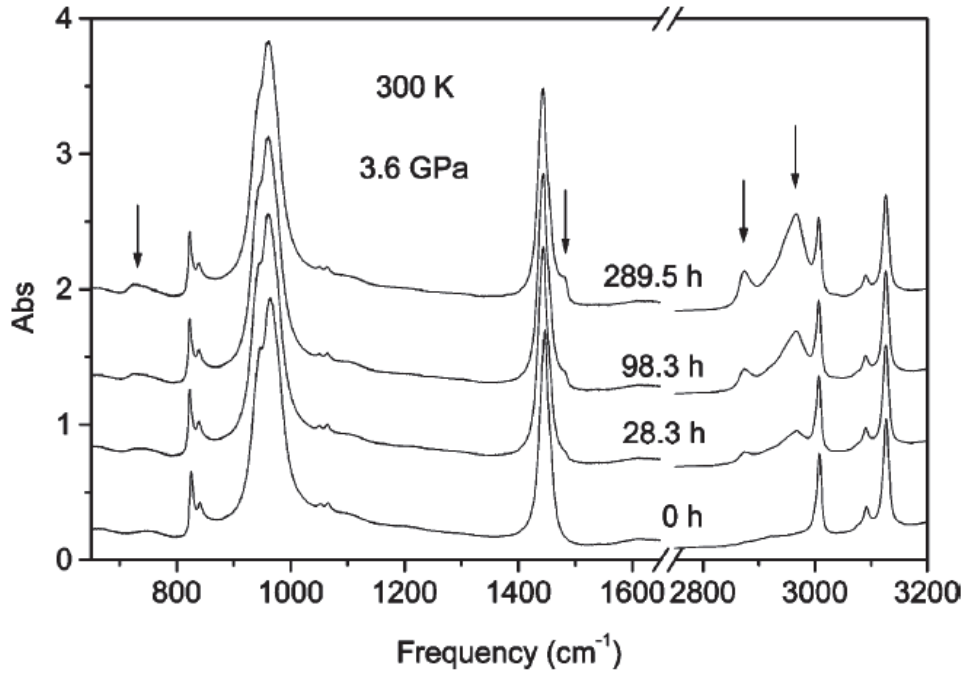

Figure I.2.10 Time evolution of the IR spectra during the reaction at 300 K and 3.6 GPa. Arrows indicate the polymer peaks forming during the reaction. (Redraw from ref. [8]).

The pressure-induced polymerization of ethylene in the liquid state has been studied by Chellazzi *et al*. [7, 8]. At room temperature no polymerization occurs in liquid ethylene under a pressure of 0.7 GPa. On the other hand, a polymerization is observed when the compressed liquid sample at 0.7 GPa is irradiated by a laser in visible or near-UV range. Figure I.2.11 shows comparison of the room temperature IR spectra measured on a freshly loaded ethylene sample after irradiation with different wavelengths at 0.7 GPa. The new IR bands growing during the

reaction are observed in the region between 2850 and 3000 cm^{-1}, assigned to CH stretching modes involving saturated C atoms. These new IR bands indicate that polymerization reaction can be triggered by light absorption. The efficiency of the process is greater as the excitation line shifts to the ultraviolet (UV) range. An almost complete conversion of monomers into polymer was reported in about six hours under UV multiline emission (mUV) - mainly 351 + 364 nm.

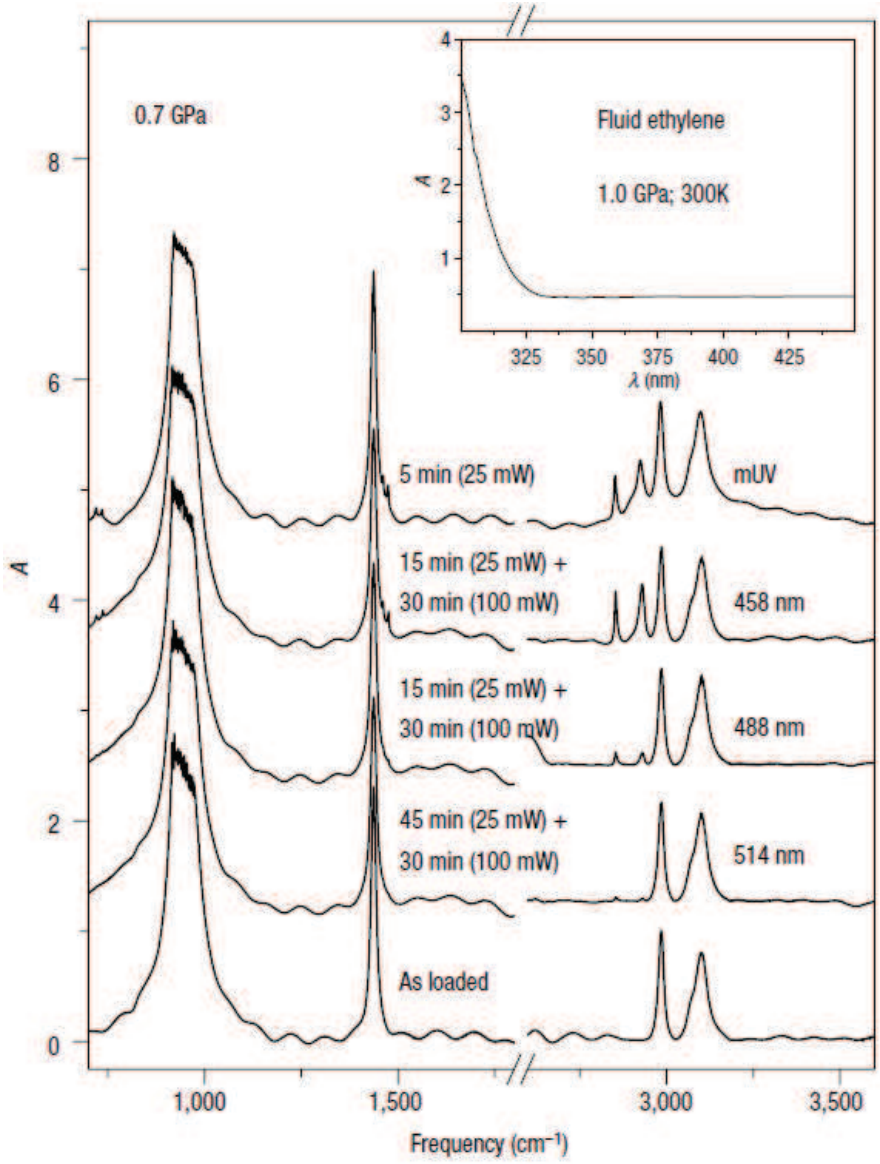

Figure I.2.11 The effect of the irradiation wavelength on liquid ethylene at high pressure. Comparison of the room-temperature infrared spectra measured on a freshly loaded ethylene sample after irradiation with different wavelengths at 0.7 GPa. For each spectrum the duration and the power of the irradiation are reported. The inset shows the UV-visible absorption spectrum measured at 1 GPa (well above the pressure where the reaction is optically induced). (Redraw from ref. [7]).

XRD analysis of the recovered polymer evidences a high degree of crystallinity of the obtained polyethylene. In addition, from infrared absorption, the recovered product was identified as a high-density polyethylene (high linearity polymer).

Chellazzi *et al*. [7] have proposed that photochemical activation of the high pressure reaction was due to a two-photon excitation of the $^1B_{3u}$ antibonding state with a twisted geometry. Because this state has a very short lifetime (20 ± 10 fs), the reaction is likely triggered by excited molecules after relaxation in the ground state and before rearrangement of the geometry in the planar structure.

The high-pressure reaction mechanism of ethylene has been studied in some details by *ab initio* molecular dynamic simulation [83]. The HP-induced polymerization has been found to be ionic in nature. The reactive system is characterized by a strong reduction of the HOMO–LUMO gap and a collapse of the higher occupied states in only one band. The molecules under high pressure are strongly deformed and show appreciable dipole moments supporting the electrostriction interpretation of the sample response to pressurization and an ionic reaction mechanism. In both disordered and crystal phases, the reaction products (linear chains in the disordered systems and branched chains in the crystal) are in qualitative agreement with the experiments.

HP induced chemical reaction of Butadiene: a photochemical switch for polymerization.

We now consider the reactions of liquid and solid butadiene ($H_2C{=}CH{-}CH{=}CH_2$) at high pressure with and without laser irradiation. According to the conditions of pressure and irradiation the reactions proceed along specific and very selective pathways leading to different kinds of recovered products. We first discuss the laser-assisted high-pressure induced polymerization in liquid butadiene, and then reactions in solid butadiene at high pressure with and without laser irradiation.

In gas phase butadiene is an unstable species. At ambient conditions it easily reacts to give a mixture of several dimers (vinylcyclohexen, cyclooctadiene and divinylcyclobutane) obtained through different reaction mechanisms. As a result of the competition between the different reaction mechanisms, vinylcyclohexen is the most abundant produced dimer [84]. The polymerization of butadiene is generally carried out in liquid with presence of appropriate catalysts [85]. The obtained polybutadiene is usually as a mixture of the *trans* and *cis* isomers.

Under pressure at room temperature, butadiene is stable in liquid phase up to 0.7 GPa. Above this pressure a reaction starts revealed by the growth of new infrared absorption bands (see Figure I.2.12 A) [73, 86-88].

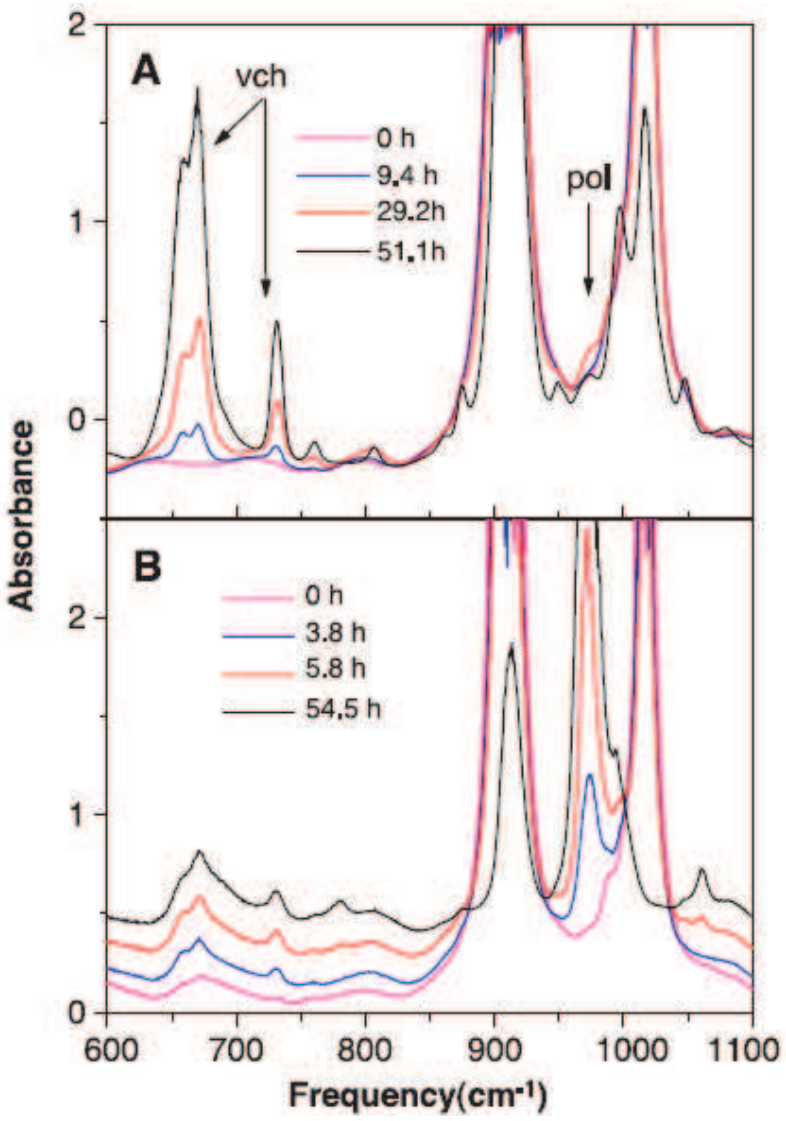

Figure I.2.12 IR spectra showing the kinetic evolution of pressure induced reaction in liquid butadiene at 0.8 GPa and 300 K (A) without laser irradiation and (B) while the sample was irradiated at 488 nm. Vch and pol refer to the characteristic absorption bands of vinylcyclohexen and polybutadiene, respectively. (Redraw from ref. [73]).

After several days, the initial butadiene is completely transformed in a recoverable liquid product identified as pure 4-vinylcyclohexene. No traces of the other dimers are detected, and only traces of a polybutadiene are presented. The reaction is strongly modified when the pressurized (0.7 GPa) liquid is irradiated at 488 or 458 nm by a CW Ar^+ laser (10 - 20 mW). Indeed the dimerization is fully inhibited and in a few hours the initial liquid sample is transformed in a transparent solid product identified as pure *trans*-polybutadiene (see Figure I.2.12 B) in which the *cis* isomers is completely absent. Citroni *et al*. [73] have also shown that laser irradiation at 514.5 nm is not effective for polymerization reaction demonstrating that there is an energy threshold for the photochemical activation of the reaction.

The kinetics of the polymerization reactions has been studied within the framework of the Avrami model [89] (Figure I.2.13). The Avrami model was originally proposed to describe the crystal growth from a liquid phase. According to this model the fraction of products at time t is given by:

$$A_t = A_\infty(1 - \exp(-k(t - t_0)^n)),$$

where A_t and A_∞ are the fraction of product at time t and at the end of the process, k is the reaction rate and n is a parameter related on the geometry of the polymer chain. In original Avrami's model, where only the growth step is taken into account, the n value increases with the dimensionality of the process ranging between 1-2, 2-3 and larger than 3 in the linear, bi- and three-dimensional growth cases, respectively.

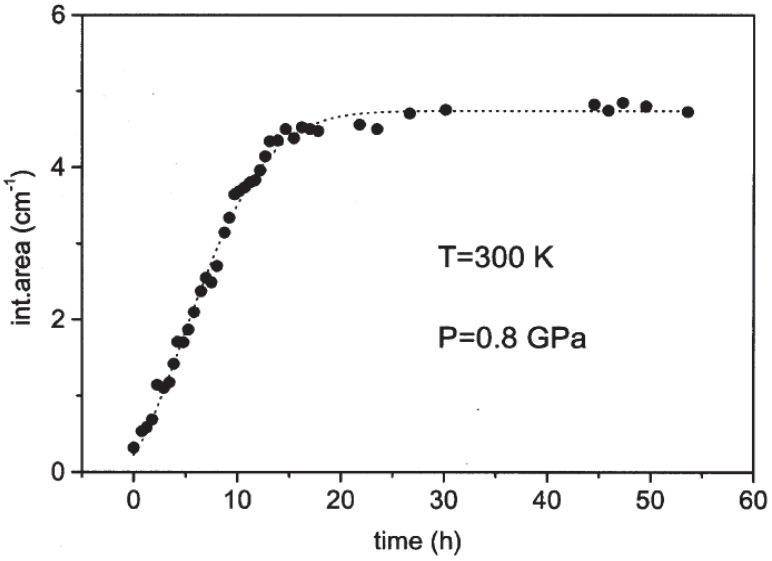

Figure I.2.13 Time evolution of the integrated area of the polybutadiene band at 1643 cm^{-1} (C=C stretching mode). The evolution has been reproduced (dotted line) by the Avrami law (eq. 1.1) with n = 1.86. (Redraw from ref. [35]).

The results agree with the Avrami model even in the early stages of the reaction (nucleation step). An Avrami parameter of n = 1.87 is obtained confirming a linear propagation of the polymer chain.

A two-photon excitation of the $S_1(2^1A_g)$ state has been proposed to explain the photochemical activation of the polymerization reaction [73]. In this antibonding π^* (LUMO) state, the molecule is stretched (~7%) (Figure I.2.14). The long S_1 lifetime together with its antibonding character, that lowers the rotational barrier around C=C bonds, favor the nearest neighbor molecules head-to-tail approach to develop the polymerization, while at the same time prevents the π electron clouds overlap necessary for the dimerization [35].

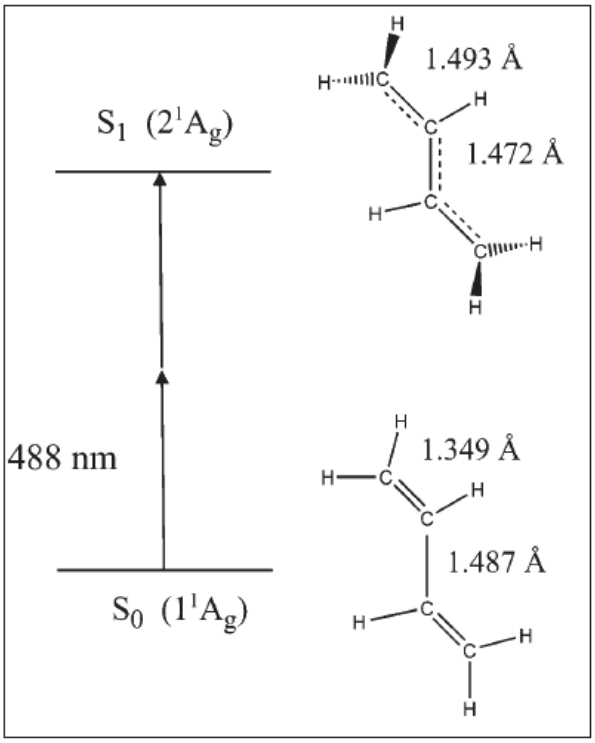

Figure I.2.14 Two-photon excitation to the $S_1(2^1A_g)$ state and the corresponding change of the butadiene molecular geometry. (Redraw from ref. [32]) .

The butadiene reaction at high pressure has also been studied in solid phase under pressures ranging from 2 to 6.6 GPa [88]. At pressure lower than 4 GPa only vinylcyclohexene is formed during the reaction with negligible amount of the polymer. Above this threshold, the amount of polymer increases rapidly with pressure.

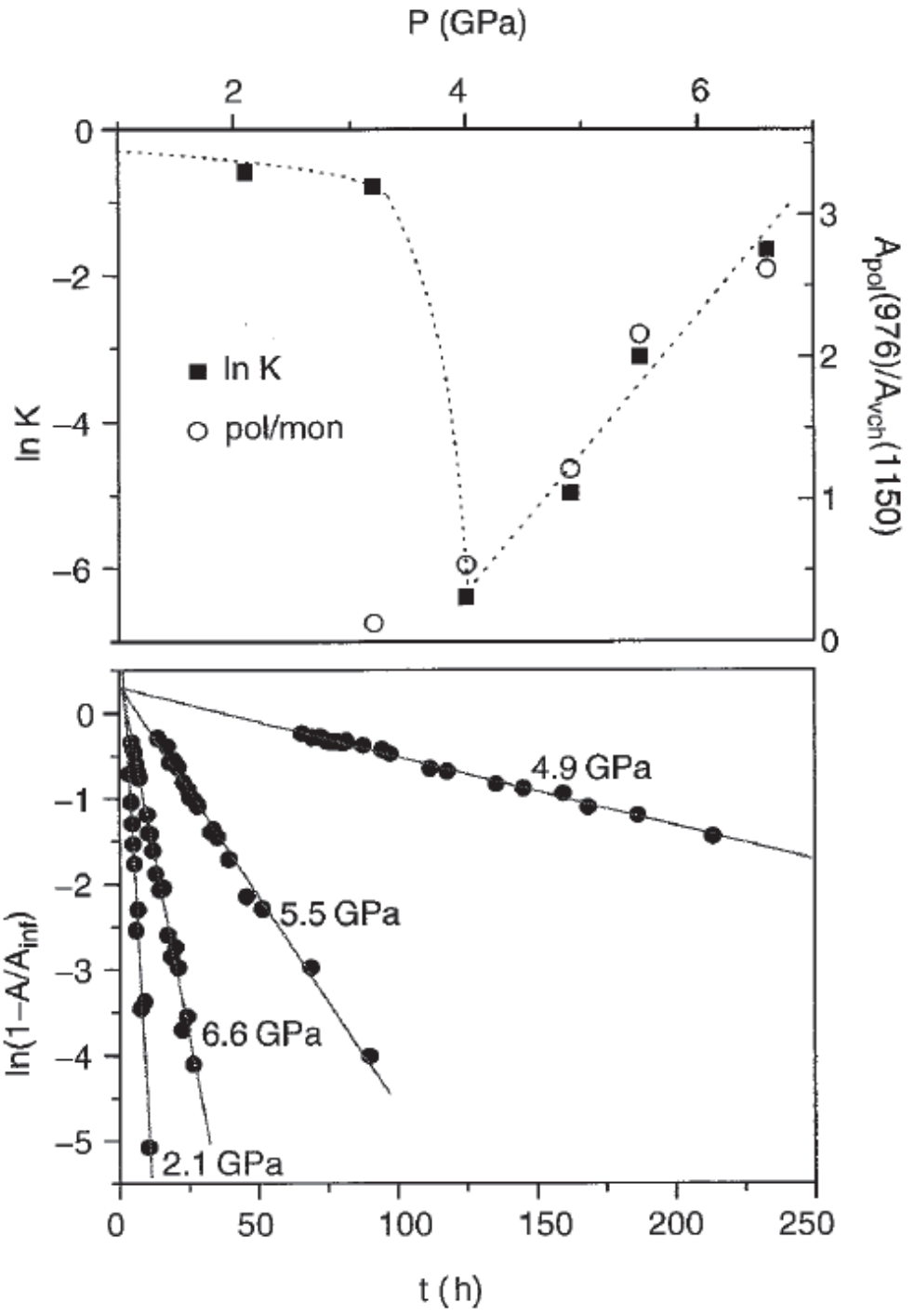

Figure I.2.15 Dimerization of butadiene in the crystalline phase. Lower panel: Logarithmic plots of the room-temperature evolution of the integrated absorption of characteristic vinylcyclohexene absorption bands at different pressures. The linear evolution unambiguously demonstrates the first-order kinetics of the reaction. Upper panel: Evolution of the natural logarithm of the dimerization rate constant as a function of pressure (full squares, left axis; the dotted line is intended as a guide for the eye) and evolution of the intensity ratio between selected polymer and dimer (vinylcyclohexene) bands (empty dots, right axis). (Redraw from ref. [45]).

The rate constants for the dimerization have been determined as a function of pressure (upper panel in Figure I.2.15). Up to 3.5 GPa the dimerization rate constant decreases smoothly while above 4 GPa the rate constant increases and recovers the measured low pressure value at 7 GPa. Moreover the reaction follows a first-order law over all the pressure range under consideration (lower panel in Figure I.2.15). Assuming that the two inequivalent molecules in the hypothesized unit cell are almost perpendicular to each over, the following three-step reaction mechanism has been proposed. The mechanism is depicted in Figure I.2.16. In first stage, two molecules in the unit cell interact and give a diradical species. This step is governed by the orientation and translational displacement of the molecules and gives rise to the observed temperature dependence of the rate constant. The second step is characterized by a rearrangement of the diradicals favored by the reduction of the rotational barrier. In the final step a fast closure of cyclohexene ring occurs.

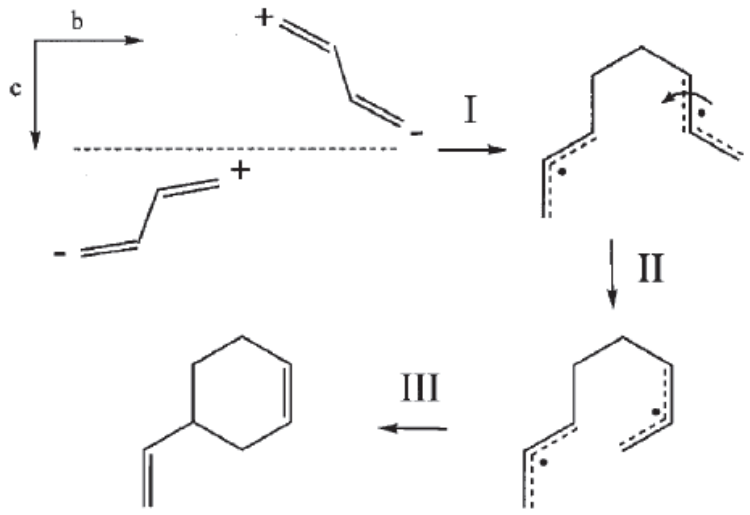

Figure I.2.16 Mechanism suggested for the butadiene dimerization to vinylcyclohexene in the crystal phase. The two molecules contained in the monoclinic unit cell react, driven by the lattice phonos, to give a diradical (step I). The rate limiting step of the reaction is the inertial rearrangement (step II) that is followed by the rapid ring closure (step III). (Redraw from ref.[35]).

The geometrical constrains of the crystal lattice suggest that while dimerization involves nonequivalent molecules of different unit cell, the polymerization occurs among equivalent molecules of different unit cells [45].

When the crystal under pressure (4 GPa) is laser irradiated (458 and 488 nm), different effects are observed. During the irradiation both the dimerization and polymerization processes are activated, but when the irradiation is suspended only the dimerization proceeds. The result of polymerization process can be explained by considering that the laser irradiation is absorbed

through a two-photon process, like in the liquid phase and the molecules of monomer excited to the $S_1(2^1A_g)$ state are stretched (~7%), making the intermolecular distance shorter. Therefore, the effect of the laser absorption reproduces the situation met at high pressure when both dimerization and polymerization processes are observed.

HP induced transformations of Benzene

In general aromatic molecules are characterized by a different high-pressure reactivity with respect to linear unsaturated hydrocarbons discussed above, because the stability of the aromatic ring makes the pressure threshold for the reaction much higher. In this section we consider a high pressure induced amorphization of crystalline benzene (C_6H_6). It is an example of acceleration of the reaction when the pressure is released. The chemical reaction of benzene at high pressure and temperature has been investigated both with shock waves [90, 91] and under static [92, 93] high pressures. The chemical transformation of crystalline benzene into an amorphous solid occurs at room temperature above 23 GPa and it is partial whatever the pressure [94, 95]. Indeed, infrared absorption bands of crystalline benzene are still detected when the sample is pressurized at 50 GPa [94]. Interestingly, the reaction of amorphization accelerates during the decompression [94, 95], as shown in Figure I.2.17 which represents the evolution of the benzene IR absorption during the compression and decompression steps. The X-ray diffraction spectrum confirms that the recovered sample is fully amorphous [94].

To clarify the reaction mechanism, in particular the ring opening mechanism, some specific experiments were carried out [94]. Ciabini *et al.* have shown that at high pressure a progressive mixing of the ground $^1A_{1g}$ (S_0) and first excited singlet state $^1B_{2u}$ (S_1) occurs. According to the molecular arrangement in the crystal at pressure close to the onset of the reaction, an effective overlap of the π clouds of neighboring molecules takes place. The high ring flexibility favors the interaction with the nearest neighbor molecules and the electronic charge density transfers toward the intermolecular region. Therefore, at high pressure the sample behaves as a network of strongly interacting distorted rings. This explains the persistence of the benzene vibrational modes even at the highest pressure. In these conditions differences between intra and intermolecular interactions are extremely reduced and new bonds between carbon atoms of different molecules start to be formed. However, the high density of the pressurized sample, i.e., the small available molecular volume, prevents an extended reconstruction of the chemical bonds. When the pressure is released, and the molecular volume available increases, the intramolecular bonds can break down and the ring opening produces radical species which rapidly propagate the formation of an extended network of saturated carbon–carbon bonds.

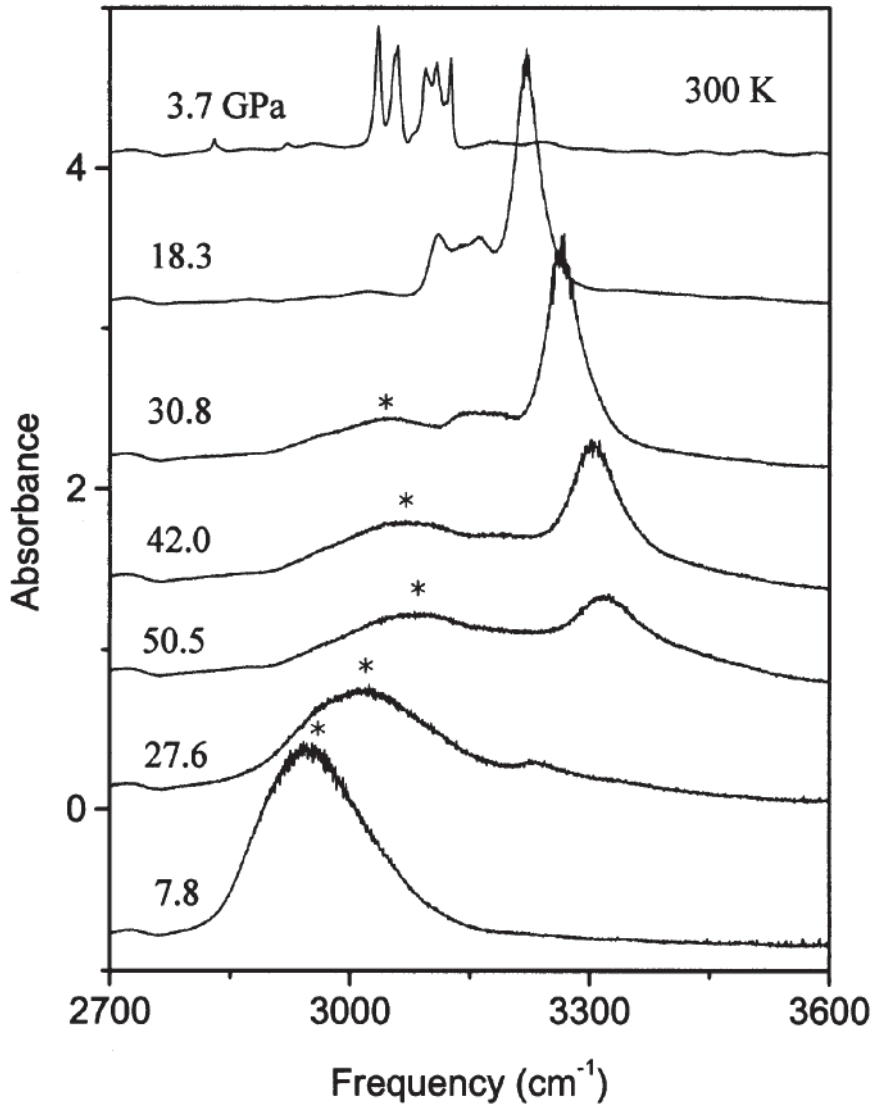

Figure I.2.17 IR absorption spectra of C-H stretching region of benzene during the compression and decompression steps. The band indicated by an asterisk is due to the sp^3 carbon atoms forming during the benzene transformation to an amorphous hydrogenated carbon. (Redraw from ref [35]).

Ciabini *et al.* [96] have also found that when benzene is pressurized at room temperature at 16 GPa (a less value than the high-pressure reaction threshold of 23 GPa) and irradiated with laser lines falling on the edge of the first excited singlet state ($\lambda < 550$ nm), the reaction rapidly proceeds. The reaction stopped when the laser irradiation was turned off and it was accelerated again when the pressure was released. Experiments have shown that a mixing of the ground state and the first singlet excited state, induced by the thermal fluctuations and favored by the usual lowering and broadening of the energy levels at high pressure plays a key role in the activation of the reaction. Indeed, the laser irradiation allows to considerably reducing the pressure threshold for the reaction. And it is remarkable that the laser induced reaction gives the same product as the purely pressure induced reaction.

I.2.5. Conclusions

In this section we have considered several examples of chemical reactions occurring under high pressure. The important feature emerging from these examples is that high pressure chemistry can differ in many significant ways from the chemistry at ambient conditions as far as the kinetics, the reaction mechanisms and the reaction output are concerned. The pressure cannot be considered only as a regulatory tool for the chemical equilibrium and the chemical kinetics. It has been shown that at high pressure, novel reaction pathways become possible. At high pressure the changes of the electronic structure of the reactants induced by intermolecular interactions can be substantial. These effects, with changes of geometrical constraints (molecule orientations, limited molecular mobility, volume constraints and high potential energy barriers) turn the reaction pathway along novel directions. This is most clearly illustrated by the results of the high pressure transformations of benzene that lead to quite specific product.

The high-pressure chemical reactions of simple hydrocarbons with laser assistance have been considered as well. Indeed laser irradiation is an important tool in high pressure chemistry. High-pressure chemical reactions occur when specific orientations and distances among molecules of the corresponding fluid or solid are realized. Under these conditions, the effect of producing excited molecules through light absorption corresponds to altering of the molecular and electronic structure and can result in activation or acceleration of the reaction. From high-pressure chemical reactions of ethylene, butadiene and benzene, it has been demonstrated that the laser light absorption is very powerful for lowering the reaction threshold. Moreover by modifying the molecular and electronic structure, new reaction channels can be opened or alternatively, a specific path can be selected among competitive reactive processes, as clearly demonstrated in the case of dimerization/polymerization of butadiene. In a number of experiments described in this chapter, the macroscopic threshold conditions (of pressure and temperature, but also of laser irradiation) to be overcome to induce chemical reactions have been reported. Indeed the knowledge of macroscopic threshold conditions of chemical reaction plays an important role in high-pressure chemistry. By appropriate selection of overall reaction conditions, high pressure reactivity can be tuned to obtain products that are of high interest (a highly crystalline polymer from liquid ethylene; a pure dimer, or, alternatively, a completely *trans*-polybutadiene from butadiene; an amorphous hydrogenated carbon from benzene).

In this PhD work, we have investigated chemical reactions of 2-hydroxyethyl-methacrylate (HEMA) at high pressure. We have shown that high pressure chemistry can be used for fabricating of pHEMA-TiO_2 hybrid materials with determined properties. All these tasks are discussed in next sections.

Chapter II: Experimental setups and methods of investigation

II. Experimental setups and methods of investigation.

In this chapter we present the general information about materials, characterization methods and equipment that has been used in this work. High pressure technique for the preparation of hybrid materials including the main principle of Diamond Anvil Cell and high pressure system equipped with Brigman Anvils will be considered. Gel Permeation Chromatography method for characterization of the synthetized pHEMA samples will be presented as well. Raman spectroscopy and pump-probe photodarkenning experiment as main characterization methods of the properties of TiO_2 hybrids materials will be discussed.

II.1. HEMA and pHEMA-TiO_2 hybrid materials.

In this work our attention has been focused on the studying of advanced fabrication and optical properties of TiO_2 hybrid materials. These hybrid materials consist of two parts: an organic part in poly-(hydroxyethyl)methacrylate (pHEMA) and an inorganic part in TiO_2 nanoparticles.

II.1.1. The 2-(hydroxyethyl)methacrylate

The 2-(hydroxyethyl)methacrylate or HEMA (Figure II.1) is the monomer used to synthesize the poly-(hydroxyethyl)methacrylate (pHEMA).

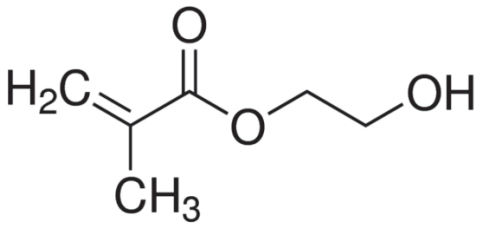

Figure II.1 Chemical formula of HEMA.

The basic information about HEMA provide by Sigma Aldrich and used in this work are presented in the Table II.1.

Table II.1 Basic information about HEMA.

Formula	$C_6H_{10}O_3$
Formula Weight:	130.14 g/mol
Appearance(color)	Colorless
Appearance(form)	Liquid
vapor density	5 (vs air)
vapor pressure	0.01 mmHg (25 °C)
assay	≥99%
contains	≤50 ppm monomethyl ether hydroquinone as inhibitor
refractive index	*n*20/D 1.453(lit.)
bp	67 °C/3.5 mmHg(lit.)
density	1.073 g/mL at 25 °C(lit.)
storage temp.	2-8°C

The initial solution of HEMA contains less than 50 ppm of monomethyl ether hydroquinone used as inhibitor of polymerization (MEHQ). The HEMA has been purified to avoid the yellow coloration of the TiO2-pHEMA hybrids samples due to the formation of unwanted complexes MEQH-Ti with Ti atoms [18].

For that, we have distilled HEMA solution at reduced pressure (1-2 mm Hg) in a 100 ml glass flask. A liquid nitrogen trap has been used to protect the monomer from contamination by oil vapors. The obtained solution of distillated monomer has been stored at low temperature (2-5 °C) and has been consumed in one week.

II.1.2. pHEMA-TiO_2 hybrid materials

The preparation method of the pHEMA-TiO_2 hybrid materials has been developed by Kameneva *et al*. [18], based on earlier studies by Novak *et al*. [28] and later improved by Gorbovyi *et al*. [6]. The process consists in several steps:

- preparation of the TiO_2 nanoparticles as a suspension in isopropanol;
- solvent exchange (isopropanol-monomer)
- polymerization of the organic component

II.1.2.1. Preparation of the TiO_2 nanoparticles as a suspension in isopropanol

The sol-gel reactor with fast micro-mixing developed by Rivallin [97] and Azouani [98] was used to produce a suspension of TiO_2 nanoparticles. The scheme of the reactor is shown in the Figure II.2.

The solutions of titanium tetraisopropoxide (TTIP) in 2-propanol and water in 2-propanol were prepared in a glove-box (MBraun), equipped with a Labstar detector system. These solutions were transferred into double-wall inox containers (1 and 2) thermostated with cryostat (HAAKE, DC10k15). Distillated water was used as a coolant. A flow of nitrogen was used to avoid the contamination of the solutions in the containers by air humidity. The reaction between TTIP and water was started in the mixing point: T-mixer. At the end of hydrolysis reaction all 100 ml of TiO_2 nanoparticle suspension were obtained in the thermostated reactor (3).

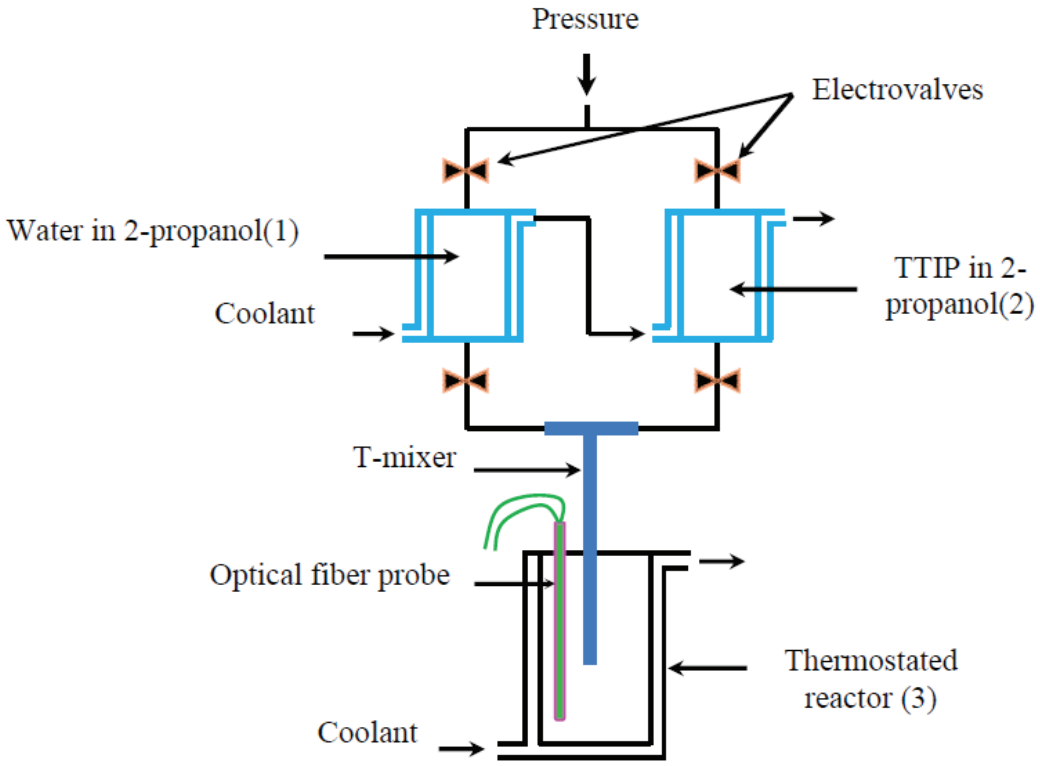

Figure II.2 Scheme of the sol-gel reactor. (Redraw form ref. [6]).

The main experimental parameters used to produce a solution of monodisperse TiO_2 nanoparticles in suspension have been determined by Gorbovyi [6] and are described in the Table II.2.

Table II.2 Main parameters for preparation of the TiO_2 nanoparticles suspension.

Parametrs		
Pressure of injection	P (bars)	4
Temperature	T (°C)	20
Concentration of TTIP	C_{TTIP}(M)	0.146
Hydrolysis ratio	H	2

These experimental conditions of fast micro-mixing allow obtaining size selected nanoparticles with the size (radius) of 2.5 nm.

II.1.2.2. Solvent exchange (isopropanol-monomer) phase

The freshly prepared suspension of TiO_2 nanoparticles in 2-propanol is mixed in glove box with HEMA in a proportion of X and 5ml correspondingly. Where X is the amount in ml of the TiO_2 nanoparticles solution depending on the required concentration of nanoparticles in the final product. The information about component's concentration in the final hybrid material after the solvent exchange phase are presented in the Table II.3.

Table II.3 The information about component's concentration in the final hybrid material.

Name of the sample	Volume of initial TiO_2 suspension, used in synthesis, ml	TiO_2 concentration in the final hybrid material, M	HEMA concentration in the final hybrid material, M	HEMA:TiO_2 molar ratio
1x	5	0.146	8.0	54.8: 1
2x	10	0.292	8.0	27.3: 1
5x	25	0.73	8.0	11: 1
10x	50	1.46	8.0	5.5: 1
20x	100	2.92	8.0	2.7: 1
40x	200	5.84	8.0	1.4:1

After mixing, the solution of TiO_2 nanoparticles in 2 propanol and HEMA was put in round flask with a vacuum valve. A single stage membrane pump (supplier: KNF N 840.3FT.18) was used for pressure reducing (10 mbars). A liquid nitrogen trap was used to condensate the 2-propanol vapors. As the solvent exchange phase is based on the relatively high difference in the boiling temperatures of solvents [6]. The boiling temperature of monomer (HEMA) is 207 °C, for the 2-propanol it's 82 °C. Thus the difference in temperatures is 125 °C and it allows expecting that a loss of monomer is negligible. The 2-propanol elimination was controlled by the

volume decrease of the total amount of TiO_2-HEMA solution. Usually, in case of elaboration the hybrid with the highest concentration of TiO_2 nanoparticles the solvent exchange reaction lasts 10-15 hours.

When the solution of TiO_2-HEMA is ready, it can be used for preparation of pHEMA-TiO_2 hybrid materials.

II.1.2.3. Polymerization

In this work we have used two different methods of polymerization of HEMA and HEMA-TiO_2 hybrid materials.

Thermally initiated polymerization

The thermally induced free radical polymerization is widely used for synthesizing the polymer materials. The basic principle consists in producing free radicals from the thermal excitation of an initiator. In our group this method has been previously used by Gorbovyi [6] to polymerize HEMA and hybrid materials using 2,2-Azobis(2-methylpropionitrile) (AIBN) as initiator. The process requires heating samples at 90 °C during 12 hours. Note that AIBN is the often used compound, as a radical initiator, for polymerization processes. Basic properties of AIBN are presented in the Table II.4.

Table II.4 Basic characteristics of 2,2-Azobis(2-methylpropionitrile).

Molar mass:	164.21 g/mol
Appearence:	white crystalline
Density:	0.858 g*cm^{-3}
Melting point:	103-105 °C
Decomposition point:	> 65 °C
Supplier:	Acros Organics

It has been experimentally shown by Gorboviy that 0.1 mol. % of initiator, dissolved in monomer's medium (1.35 mg of AIBN for a 1ml of HEMA), was the most suitable concentration of AIBN for polymerization process.

In our work we have successfully applied the thermally induced polymerization to synthesize large solid hybrid samples (Figure II.3) or thin samples between two glasses plates.

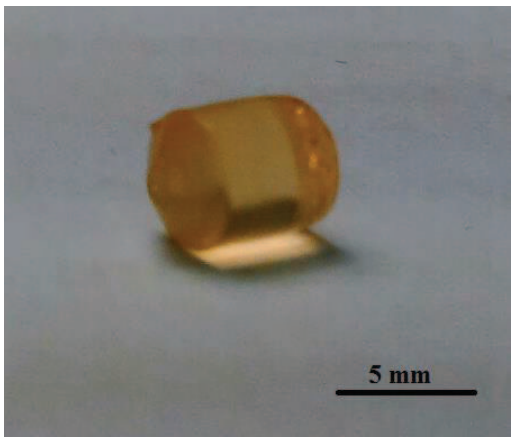

Figure II.3 Example of hybrid material (C_{Ti} = 1.46 M) thermally polymerized using the AIBN initiator.

High pressure induced polymerization

In this PhD we demonstrated that the polymerization can be efficiently induced without initiator by applying a high pressure on the sample. These results will be presented and discussed in details in the sections III and IV.

II.2. High pressure technology

In this part we present some basic principles about high pressure technology. The discussion is focused on Diamond Anvil Cell (DAC) and high pressure system equipped with pair of Bridgman anvils which are the HP cells used in this thesis.

II.2.1. Diamond Anvil Cell

Nowadays there are a lot of various devices in use to generate a high compression. The choice of a specific device depends of the pressure required and of applications targeted. One can distinguish between large volume opposed anvils (Bridgman anvils) and multianvils systems [99] which allow to achieve pressures up to 10-15GPa and on the other hand diamond anvil cells (DACs) that may create a much higher compression up to 500GPa [100] on the small volumes. The DAC technology was introduced by Dirckhamer in the early 50's and since has been strongly improved. Actual DAC's work in temperatures ranging from mK [101, 102] up to 5000K [103] at pressures up to 500 GPa. Compare with other high pressure systems, the main advantage of DAC is the transparency of diamond windows over a large range of the electromagnetic spectrum. The DAC are therefore particularly well suited for in situ spectroscopic analysis as : IR, Raman or Mössbauer spectroscopy, but also X-ray diffraction and NMR [104, 105]. The disadvantages of DAC's are the small dimensions of the sample under compression, the small acceptance angle and the high refractive index of diamond. Indeed the refractive index of diamond goes from 2.4 at 700 nm to 2.7 at 200 nm and increases up to 4.5 at 0.1 µm, then decrease to become 1 at wavelengths ≤ 62nm). We have used DAC equipped with

diamonds with a low degree of impurities to ensure low levels photoluminescence and low IR absorption.

II.2.1.1. DAC : description and utilization

The Diamond Anvil Cell (DAC) can generate a continues static pressure from less than 1kbar up to several hundreds of GPa. The scheme of DAC is shown on Figure II.4. The sample is placed in a small hole drilled in a preindented metallic gasket. It is squeezed between culets of two diamonds by pushing one against the other.

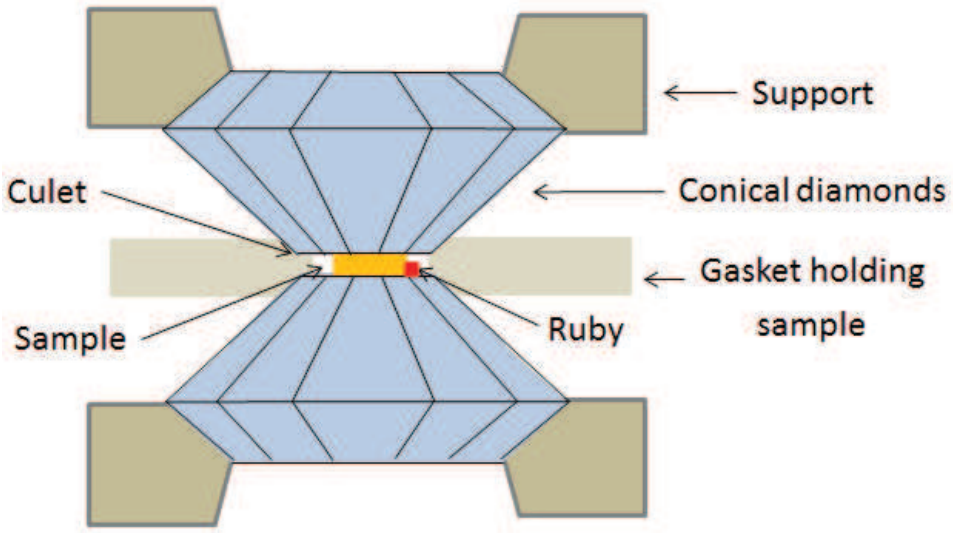

Figure II.4 The scheme of DAC.

The maximum pressure which can be reached depends on several factors (i) the applied force, (ii) the size of the drilled hole, (iii) the dimension of the small faces and (iv) gasket material. The Figure II.5 shows the photo of DAC which have been used in our experiments.

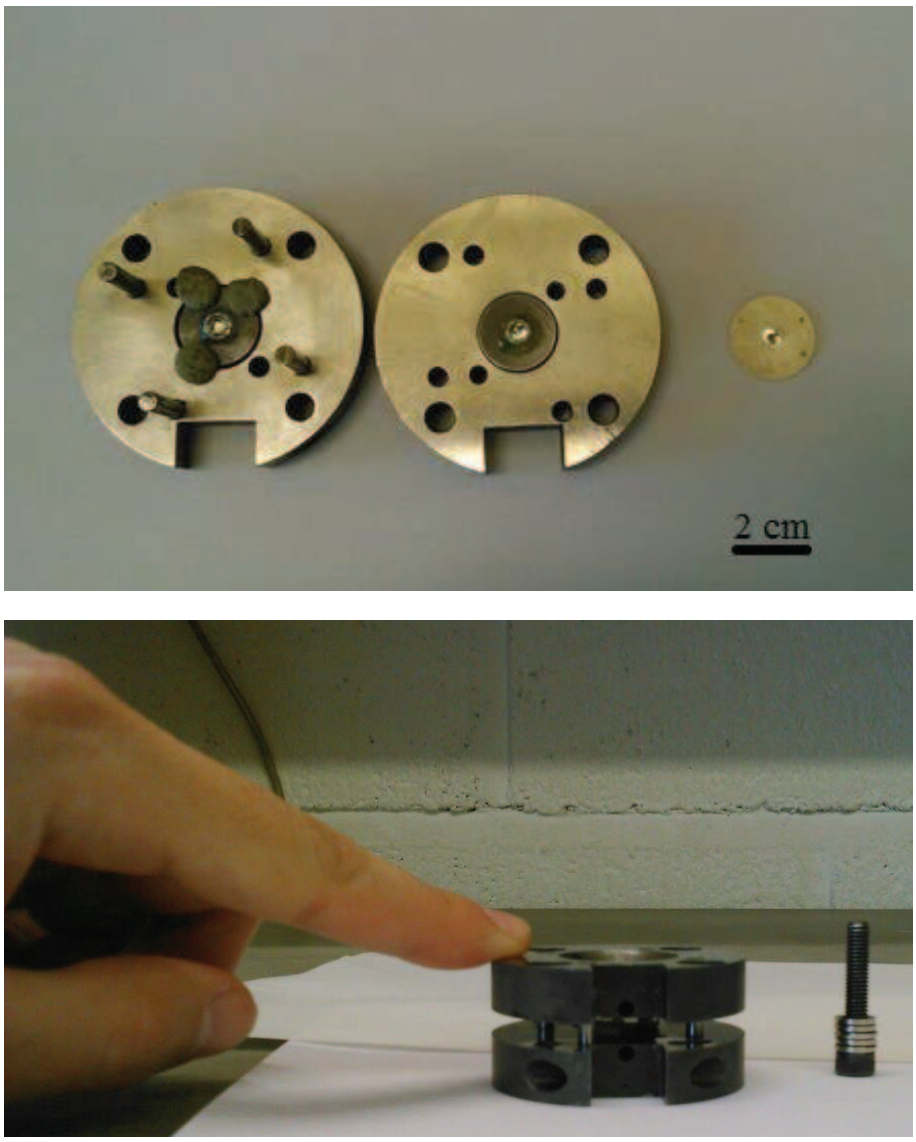

Figure II.5 Photos of DAC: a) open cell with gasket, b) closed cell.

II.2.1.2. Diamond windows

In situ measurements by means of Raman and UV/VIS spectroscopy require low fluorescence diamonds. The characteristic parameters of the diamonds used in this work (see Figure II.6) are presented in the Table II.5.

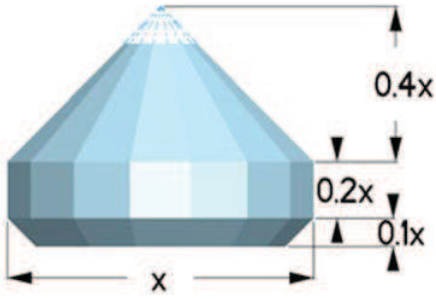

Figure II.6 The basic parameters of diamonds (Table II.5). (Redraw form ref. [106]).

Table II.5 The basic parameters of diamonds

Type of diamonds	Ia
Nitrogen impurities contain	0.3% (3000 ppm)
Inner face	400µm
Large face (x)	2.5mm
Crown height	0.1x
Girdle thickness	0.2x
Pavillion depth	0.4x

The fluorescence of diamond under visible excitation (390-700 nm) results in strong first and second order Raman bands respectively around 1350 and 2500 cm^{-1}. The use of diamonds with low impurities content allows reducing these unwanted Raman bands. In our measurements we have used the diamonds of type Ia.

Since the pressure is a force per unit area, it is evident that very high pressure can be obtained either by a considerable increasing of force acting on the sample, or by decreasing the sample size. According to the second approach the working face of the diamond is chosen as small as possible depending on the range of pressure required. Usually the diameter of the smaller (inner) face of the diamond anvil is in the range 50-600 µm whereas the diameter of the larger (outer) face is 4 mm. For generation the high pressure a higher ratio between big and small faces of diamond is required. In all experiments presented we have used diamonds with inner face dimension of 400 µm allowing to reach pressures up to 20 GPa.

II.2.1.3. Preparation of the gasket

The metallic gasket is an essential component in DAC's high pressure technology. The gasket contains the sample in a limited volume, and protects the inner surface of the diamonds

from potential damages when the pressure is applied. We have used stainless steel circular gaskets. The preparation of the gasket consists of two steps. First step is previous indenting of gasket with diamonds in DAC and the second step is drilling the circular hole (sample chamber) in the centre of preindented part (see Figure II.7). The holes have been drilled using the Spark erosion technique. Typically dimensions of hole are ranging from 5 to 300 µm depending on maximum pressure requires. For pressures not exceeding 15 GPa holes with diameter ranging from 150 to 250 µm holes can been used.

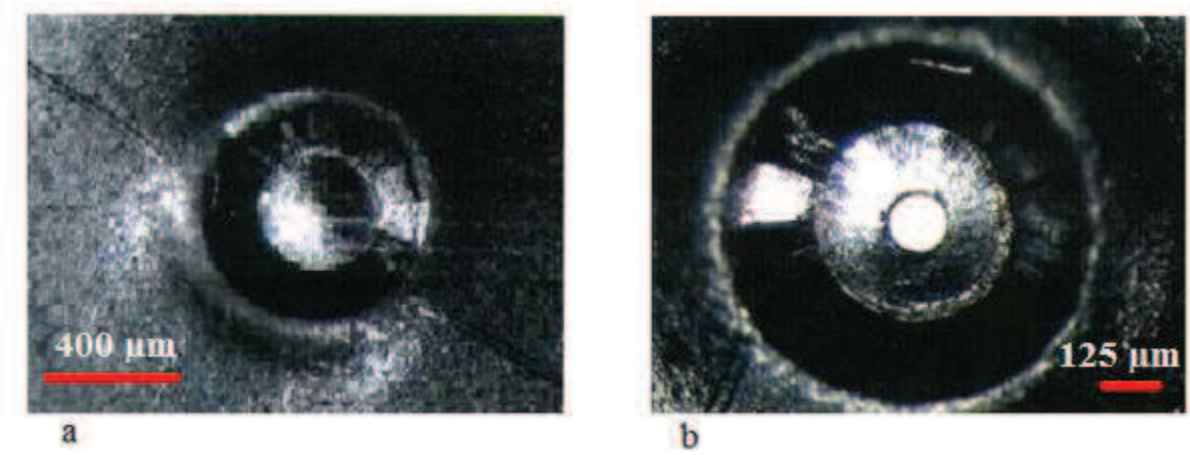

Figure II.7 Photo of the gasket: a) indent of diamond in gasket; b) after sample hole is drilled. (Redraw form ref. [107]).

The drilled gasket is placed in the DAC between two diamonds. Then, the samples and pressure sensors (small ruby pieces) are inserted in the hole by steel needle.

II.2.1.4. Pressure measurement by the ruby fluorescence approach

The most common method of determining the pressure in a diamond anvil cell is using a scale based on the shift of ruby fluorescence line. The Doped chromium ruby has two very strong fluorescence lines (R1 and R2) which undergo a red shift when the pressure is increased. The usual linear calibration of the ruby fluorescence emission is based on the equation of state of sodium chloride [108-110] obtained for quasi-hydrostatic environments in the pressure range up to 30 GPa. Mao and Bell [111] extended this calibration up to 80 GPa and proposed another ruby fluorescence scale which is used in our measurements. The Figure II.8 shows the ruby fluorescence emission spectrum excited by the 633 nm laser irradiation at ambient pressure condition.

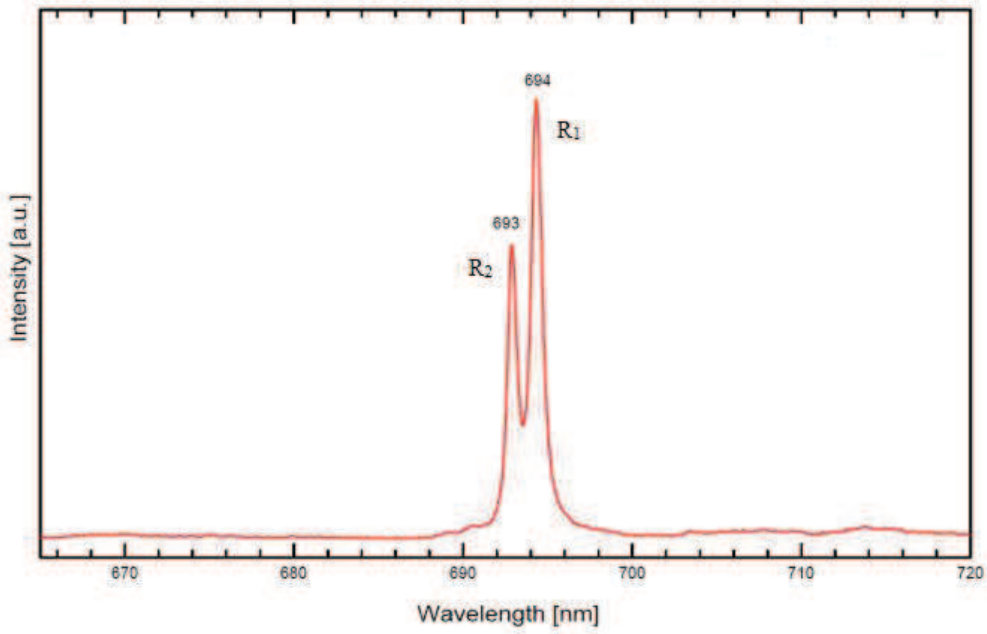

Figure II.8 Ruby fluorescence emission lines at 295 K and ambient pressure. (Redraw form ref. [112]).

In hydrostatic conditions, the ruby lines remain tight and very apparent. The relation equation between pressure and ruby fluorescence wavelength in quasi-hydrostatic conditions is

$$P = \frac{1904}{B}\left(\left[1 + \left(\frac{\Delta\lambda}{\lambda_0}\right)\right]^B - 1\right), \qquad (2.1)$$

where P is the pressure in GPa, B is the dimensionless parameter equal to 7.665, λ_0 is the wavelength of the R_1 ruby fluorescence line at ambient pressure and room temperature. $\Delta\lambda$ is the ruby shift with respect to the ambient pressure. The Figure II.9 shows the Ruby fluorescence emission at 295 K at ambient pressure and at 10 GPa respectively.

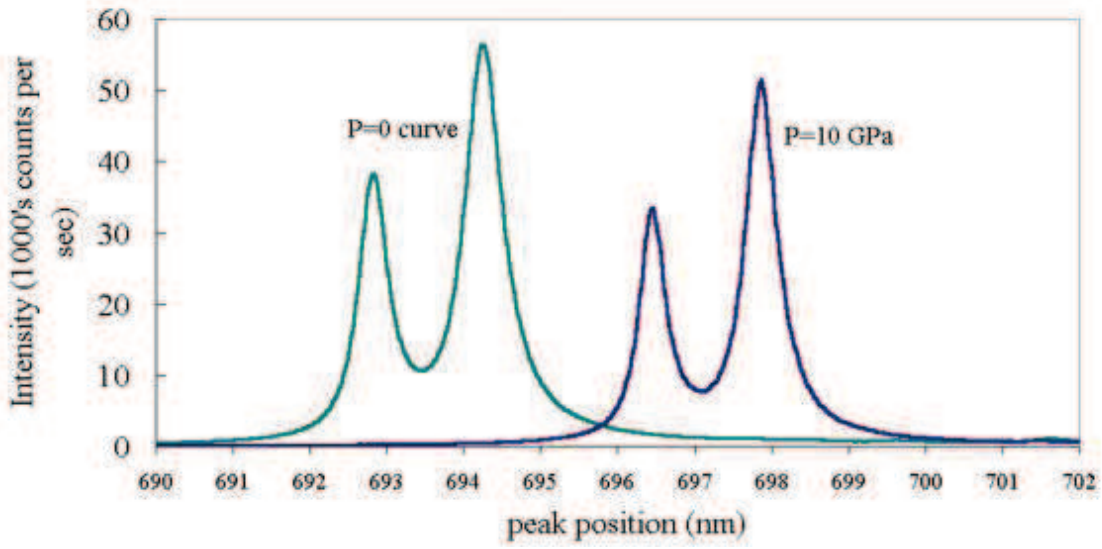

Figure II.9 Ruby fluorescence emission at 295 K at ambient pressure and at 10 GPa respectively (excitation wavelength is 633 nm). (Redraw form ref. [113]).

To measure in situ the pressure applied on our samples we have excited the ruby with a laser at 633 nm and analyzed the resulting luminescence by using the Raman spectrometer described in paragraph II.3.2. In this manner pressures ranging from 0.1 to 20 GPa have been measured with a precision of ± 0.05 GPa.

II.2.2. Bridgman anvil cell

Due to the small size of the working faces of diamond, the obtained samples in DAC are extremely small (diameter is 100-250 µm). Thus for producing bigger samples whose diameters range from 0.5 to 1 mm another kind of high pressure cell has to be used as for example the Bridgman opposed anvils [114-116].

Opposed anvils introduced by Bridgman (Figure II.10) are the simplest and most widely used form of high-pressure. The sample is compressed between the two flat tips of the anvils made from a hard materials as tungsten carbide [117] or sintered diamond [118]. In these anvils, the gasket is made from pyrophyllite, catlinite, clay mineral, oxides or metals, depending on the type of measurement [119].

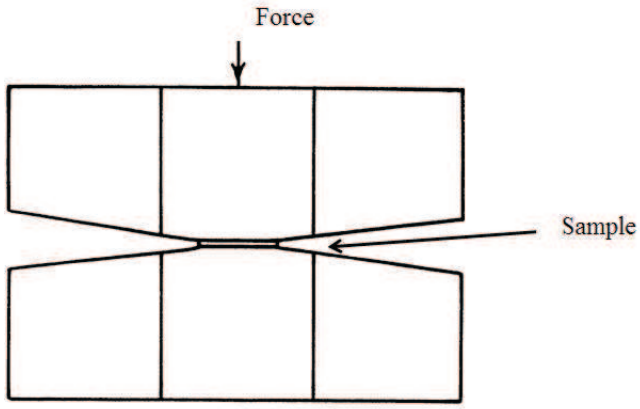

Figure II.10 Brigman anvils.

The technique of opposite anvil is based on principle of massive support [120]. According to this principle if a pair of truncated cones (Figure II.10) is designed so that the small circular faces have an area that is considerably smaller than the area of the cone bases, any axial thrust imposed on the abutting faces will transfer to the small faces and due to the large difference of faces areas, high pressures can be reached.

Bridgman anvils are commonly used to produce pressures in the range from 0 to 25 GPa. They have been used for low-temperature transport [117], electric and specific heat measurements [121]. Due to their low costs and large sample volume, Bridgman anvils are an attractive alternative to DAC in this range of pressure.

In our work we have used a high-pressure system (provided by Dr. Andreas Zerr) equipped with pair of Bridgman anvils for producing samples with the diameter of 800 μm and thickness of 120 μm. The Figure II.11 shows the scheme of the high-pressure system. Samples have been loaded in a hole of 1 mm in diameter drilled in a stainless steel gasket (thickness is 250 μm). Pressure has been generated in a gasket between anvils made of tungsten carbide and 12% of cobalt (WC+12%Co) with a culet diameter of 3 mm. The gasket was supported by a cooper ring, which keeps the gasket from going away and enables the pressure in the pressure chamber to be more than 5 GPa. The pressure to the opposed anvil system has been applied by the commercial tensile and compression press (Instron 1195). The Figure II.12 shows the photo of high pressure system equipped with pair of Bridgman anvils which have been used in our experiments.

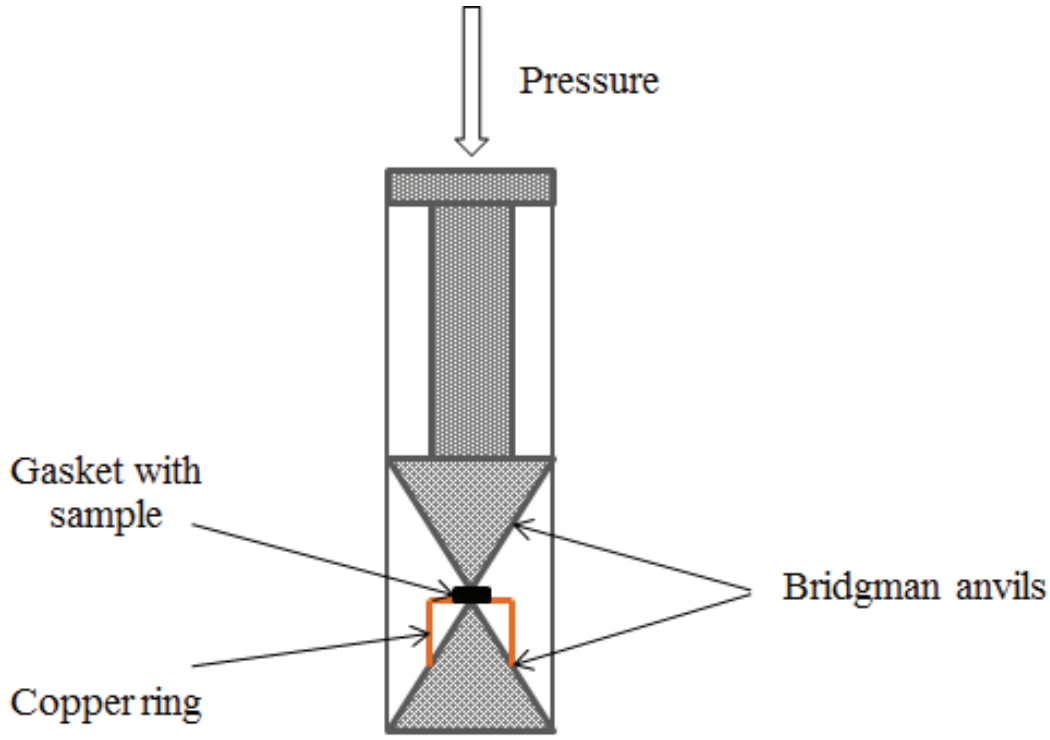

Figure II.11 High-pressure system equipped with pair of Bridgman anvils.

Figure II.12 Photo of high pressure system equipped with pair of Bridgman anvils.

II.3. Characterization of chemical and optical properties of HEMA and TiO_2-pHEMA

In this part three main characterization methods of material properties are considered. First of all, the Gel Permeation Chromatography which allows measuring the polymers chain length. Secondly the Raman spectroscopy we have used to monitor and characterize the polymerization process of HEMA and hybrid materials. Finally, the laser induced photodarkening experiment used to characterize and analyze the photosensitivity of the pHEMA-TiO_2 hybrid materials.

II.3.1. Gel Permeation Chromatography

We have used Gel Permeation Chromatography (GPC) method to measure molecular weight distribution of the HP induced polymerized HEMA. GPC is a type of size exclusion chromatography (SEC), in which molecules in solution are separated by their "effective size in solution" as they pass through a chromatographic column. Usually the sample is first dissolved in an appropriate solvent and then injected into a continually flowing stream of solvent (mobile phase). The mobile phase flows through millions of highly porous, rigid particles (stationary phase) tightly packed together in a column. Depending on their size, different components of the dissolved sample can or cannot enter the pores. Thereby the smaller components enter the pores more easily and therefore spend more time passing through the column. Conversely, larger components spend little if any time in the pores and are removed quickly. The concentration of polymer in the mobile phase is monitored continuously at the exit of the column by UV absorption.

We have used Dionex Ultimate 3000 GPC apparatus equipped with a Polymer Laboratories MesoPore 3 μm column (300*7.5 mm) located in an isothermal oven (35 °C) in series with a UV-Visible detector (wavelength of detection λ=210 nm). The flow rate of eluent (HPLC grade tetrahydrofuran, THF) was set to 1.0 mL/min. The polymerized samples were dissolved in THF in an ultrasonic bath for 2 hours. Each analysed solution (1 mg polymer dissolved in 2 ml of THF) was introduced via a manual injector loop (injected volume 20 μL). Data acquisition and analysis were performed with Chromeleon V 6.80 software supplied by Dionex.

We have paid a particular attention to the column calibration in the range of low masses corresponding to short HEMA oligomers. The column calibration was performed using a set of standard molecules:

- polystyrene oligomers with masses ranging from 268 to 788 g/mol with a maximum at 580 g/mol (EasiCal PS-2 Polymer Laboratories, Mp = 580-20650 g/mol range) (black line on the Figure II.13),
- 2-hydroxyethyl methacrylate (molar mass 130.14 g/mol) (red line on the Figure II.13),

The correspondence between measured retention times and molecular weights are presented in the Table II.6.

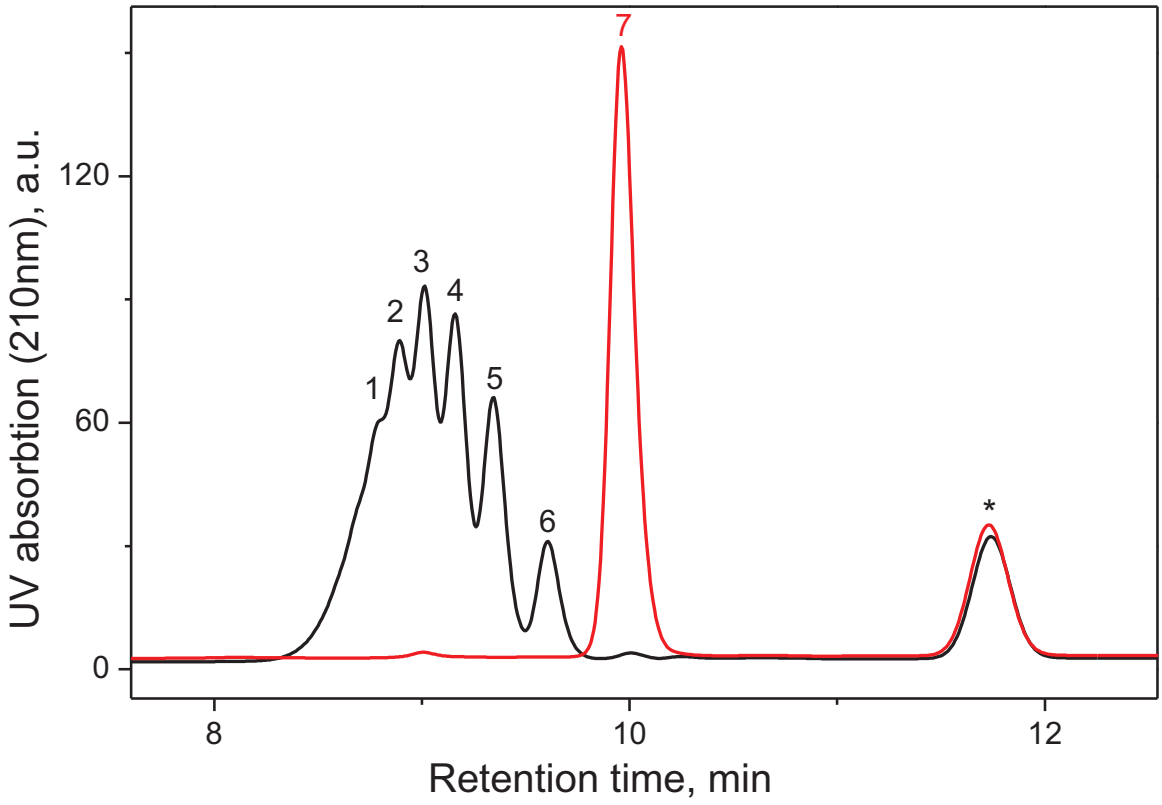

Figure II.13 GPC calibration of the column: black line corresponds to Polystyrene standard 580, red line corresponds to HEMA monomers. The relations between retention time and molecular mass are given in the Table II.6. The peaks marked by symbol * correspond to THF impurities.

Table II.6 The relations between retention time and molecular masse (see Figure II.13).

Name of material	№ of peak	Retention time, min	Molecular weight, g/mol	Name of the corresponding species
Polystyrene standard 580	1	8.81	788	Oligomers formed of 2, 3, 4, 5, 6, 7 monomers of Styrene
	2	8.89	684	
	3	9.01	580	
	4	9.16	476	
	5	9.35	372	
	6	9.61	268	
2-hydroxyethyl methacrylate	7	9.96	130.14	Monomers of HEMA

II.3.2. Raman spectroscopy

Vibrational, rotational, and other low-frequency modes spectra are good sources of information to analyze materials. In particular, these methods allow analyzing the kinetics of chemical reactions by monitoring the evolution of the spectroscopic signatures of reactants and products. We have used in-situ Raman spectroscopy to monitor the kinetics of the high pressure induced polymerization and laser assisted high pressure induced polymerization reaction of HEMA and pHEMA-TiO_2 hybrid materials. Raman spectroscopy is based on the scattering of the light. From a general point of view, there are two types of light scattering processes: elastics (Rayleigh) scattering and inelastic (Raman) scattering. In Rayleigh scattering incident and scattered irradiations are at the same frequency and the photon energy and molecular energy are both separately conserved. In Raman scattering incident and scattered irradiations are at the different frequencies and as this scattering consists in the fact that the laser beam interacts with the molecular vibrations or other excitations in the system the energy of the laser photons is shifted up or down. This shift in the energy gives information about the vibrational modes in the system. When the incident radiation is shifted to a lower energy, the scattered light is called Stokes scattering, the energy is transferred to the vibrational mode of the molecule which ends up in a higher vibrational energy state. When the incident radiation is shifted to a higher energy, the scattered light is called anti-Stokes, scattering the energy is transferred from a vibrational excited molecule, which ends up in a lower vibrational state after the scattering event (see Figure II.14) [122].

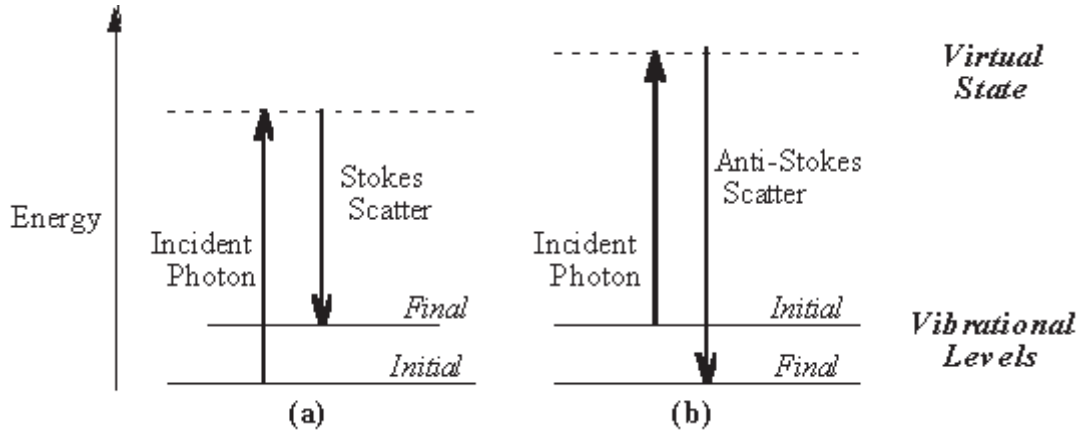

Figure II.14 Scheme of energy transfer model of Stokes Raman and anti- Stokes Raman scattering. (Redraw form ref. [123]).

To understand the origin of the scattering, the interactions processes between molecules and incident radiation have to be considered. When the electromagnetic field $\vec{E}$ interacts with the electrons in a molecule, a dipole moment $\vec{\mu}$ is induced in the molecule

$$\vec{\mu} = \alpha\vec{E} = \alpha\vec{E}_0 cos(2\pi\nu_0 t) \ , \qquad (2.2)$$

where α is the polarizability of the molecule, which measures how effective an electromagnetic field will be at inducing a dipole moment, $\vec{E}_0$ and ν_0 are the amplitude and the frequency of electromagnetic field correspondingly. According to the equation (2.2) the intensity of the dipole moment will oscillate with a frequency ν_0 which produce an electromagnetic field with a frequency ν_0. This electromagnetic field is the source of the elastic scattering (Rayleigh scattering).

Therefore, the polarizability of a molecule can be modulated by a molecule vibration [124]. Consequently, the induced dipole moment and therefore also the amplitude of the emitted field are modulated by the frequency of the vibration. The modulation of the polarizability of a molecule by a vibration with the frequency ν_k, can be expressed to first order as

$$\alpha_k = \alpha_0 + \left(\frac{\partial\alpha}{\partial q_k}\right)_0 q_k^0 \, cos(2\pi\nu_k t) \ . \qquad (2.3)$$

Where $(\partial\alpha / (\partial q_k)_0$ is a measure of how the polarizability of the molecule changes as the atoms in a molecule vibrate from their equilibrium position, q_k is a normal mode coordinate.

From the equations (2.2) and (2.3) obtain the a dipole moment $\vec{\mu}$ is

$$\vec{\mu} = \alpha_0 \vec{E}_0 cos(2\pi\nu_0 t) + \left(\frac{\partial\alpha}{\partial q_k}\right)_0 q_k^0 \vec{E}_0 cos(2\pi\nu_0 t)\, cos(2\pi\nu_k t) = \alpha_0 \vec{E}_0 cos(2\pi\nu_0 t) +$$

$$+\frac{1}{2}\left(\frac{\partial\alpha}{\partial q_k}\right)_0 q_k^0 \vec{E}_0 [cos(2\pi(\nu_0 + \nu_k)t) + cos(2\pi(\nu_0 - \nu_k)t)] \ . \quad (2.4)$$

Where the first term corresponds to the Raleigh scattering, the second term to anti-Stokes Raman scattering (at frequency $\nu_0 + \nu_k$) and the third term to Stokes Raman scattering (at frequency $\nu_0 - \nu_k$).

Typically experimental technique for obtaining Raman spectra are based on the collecting of scattering light from the illuminated sample. The light from the illuminated spot is collected by a lens in one beam and passed through a monochromator to separate the weak (0.001 % intensity) Raman scattering from the more intensive (99.999 %) Rayleigh scattering.

We have carried out Raman measurements in two different ways: in situ inside the DAC for the samples under compression and ex situ for recovered samples. All Raman spectra have been obtained at RT using a HR800 spectrometer equipped with a Peltier-cooled CCD detector (Horiba JobinIvon). In the Table II.7 general characteristics about Raman spectrometer are presented.

Table II.7 Characteristics of Raman spectrometer HR800.

Configuration	Backscattering
Spectral resolution	0.25 cm^{-1}
Spatial resolution	5 µm
Focal length spectrograph	800 mm
Confocal hole	0-1000 µm
CCD detector	1024x256 pixels
Objectives	10x, 20x, 40x, 100x
Lasers	HeNe, 20 mW, 632.817 nm
	Ar+, 488nm

II.3.3. Pump-Probe photodarkenning experiment.

To obtain some insights about photoinduced elementary processes and electronics properties of TiO_2-pHEMA hybrids, we carried out pump-probe photodarkening experiments. These experiments are based on the measurement of the absorption of the sample at 640 nm as function of the UV (355 nm) irradiation dose received by the sample. The Figure II.15 represents

the general scheme of the experimental setup. Basically, a UV pump beam delivered by a pulsed laser is superposed with a visible probe beam on the sample inside the DAC. The absorption of the visible beam is measured by a photodiode and the UV irradiation dose is carefully measured from a thermostated power meter. The different parts of the experiment are described below.

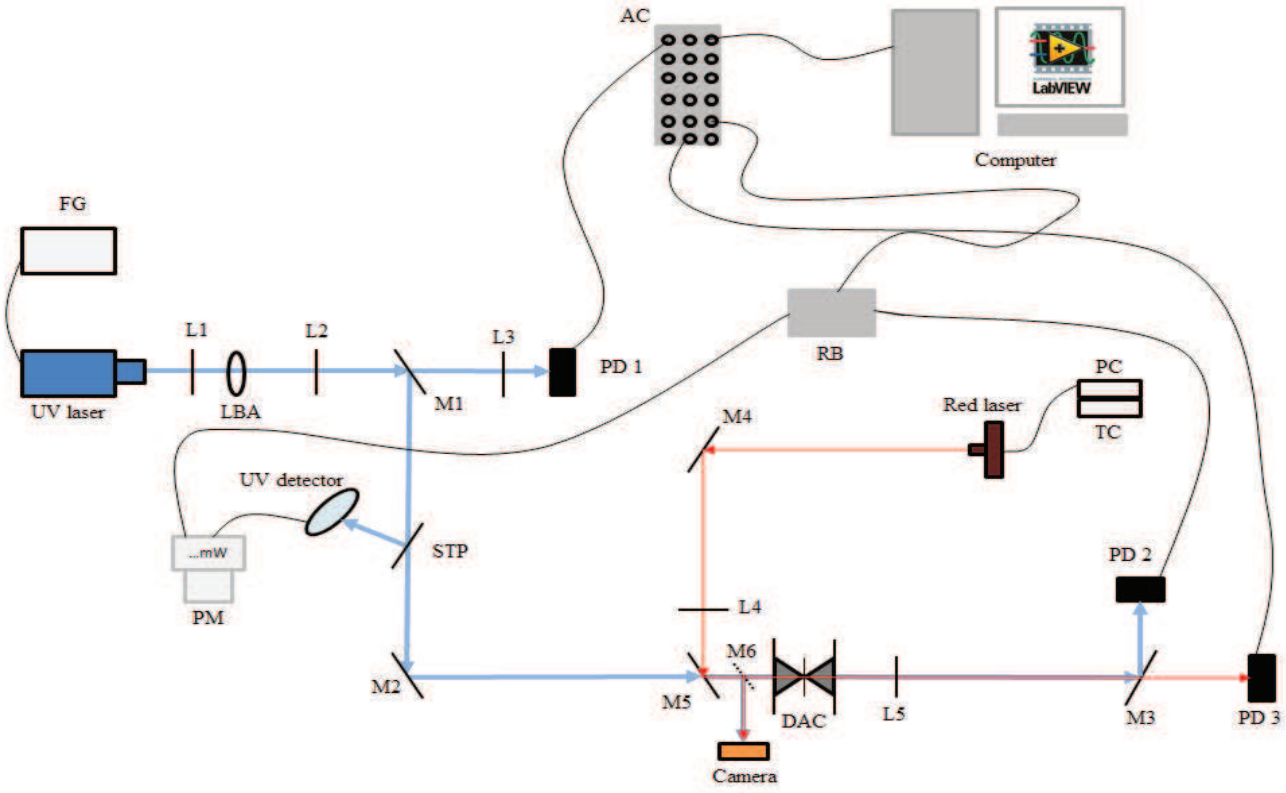

Figure II.15 Experimental setup for investigation of optical properties of hybrid materials (Table II.8 presents all characteristics of the devices).

Table II.8 Characteristics of the devices in experimental setup showed on the Figure II.15.

UV laser	LD pumped all-solid-state UV laser MPL-355-10-STD10 CNI
Red laser	CW Diode Fiber-Pigtailed laser LP 642-3F20 Thor labs
PC	Power controller of the 640 nm laser
TC	Temperature controller of the 640 nm laser
PD 1	Si photodiode Thor labs DET 10 A/M
PD 2	Si photodiode Thor labs PDA 36A-EC
PD 3	Si photodiode New Focus 2032
UV detector	UV detector Power max PS10Q Coherent
PM	Power meter Field Max II Coherent
Camera	USB Silicon CCD Camera Spiricon
FG	8111A pulse/function generator 20 MHz Hewlett Packard
RB	Reset box
AC	Acquisition card NI USB-6218 BNC
DAC	Diamond Anvill Cell
L1	Lens with the focal length 20 cm
L2	Lens with the focal length 75 cm
L3	Lens with the focal length 10 cm
L4	Lens with the focal length 4.5 cm
L5	Lens with the focal length 2 cm
STP	UV semitransparent plate
M1, M2, M3	UV mirrors
M4, M6	Mirrors
M5	Transparent mirror in the UV and 50% reflection in the visible
LBA	Laser Beam Attenuator Standa 031139

II.3.3.1. Pump UV laser

A high repetition rate diode pump solid state (DPSS) UV laser delivers pulses of 7 ns at 355 nm with a maximum mean power of 10 mW. The repletion rate can be adjusted from 1 to 7 kHz using an external function generator (FG on the Figure II.15). The UV beam is collimated by a first lens (L1 on the Figure II.15) and focused on the sample thought a second long focal lens (L2 on the Figure II.15). This combination of lenses ensures a Gaussian shape of the UV beam on the sample (Figure II.16a) with a radius equal to ~30 µm. A variable attenuator (LBA on the Figure II.15) designed for linearly polarized laser beam is placed between lenses L1 and L2 in order to adjust the laser power on the sample. The UV power is carefully controlled by a power meter (PM).

II.3.3.2. Probe beam at 640 nm.

The probe beam at 640 nm is delivered by a CW fibred-diode laser (Red laser on the Figure II.15). To provide stable operation conditions of the laser, power and temperature controllers (PC and TC) has been used. The laser is focused on a spot with a radius of ~10 µm on the sample inside the DAC (Figure II.16 b) by a short focal lens (L4 on the Figure II.15). The transmitted beam is collimated by a short focal lens (L5) and analyzed by Si photodiode (PD3).

II.3.3.3. Superposition of both laser beams on the surface of the sample

The superposition of UV and 640 nm laser beams on the sample is a critical parameter to ensure reliable measurements of the sample absorption. Due to the small sizes of beams a mere "eyes alignment" of UV and visible beams is not sufficient. For that reason, we have developed a very strict protocol to check the superposition of both beams before each experiment. Practically a removable metallic mirror (M6 on the Figure II.15) is placed in front of the DAC to reflect at right angle both UV and visible beams. The reflected beams are observed by a CCD camera placed on the focal point of the visible beam (Figure II.16 a, b). The UV mirrors M1 and M2 are then used to superpose the UV beam with the visible one (Figure II.16 c). Then the metallic mirror is removed and the DAC is placed on the focal point of the visible beam. This step is made easier by the small dimension of the hole drilled in the gasket which allows the observation of the diffraction rings produced by the red laser. The DAC is placed in a position where no diffraction rings are observed which corresponds to the focal point of the visible beam. We have used an ocular system to observe the position of the visible beam on the sample and to place the DAC in the right position.

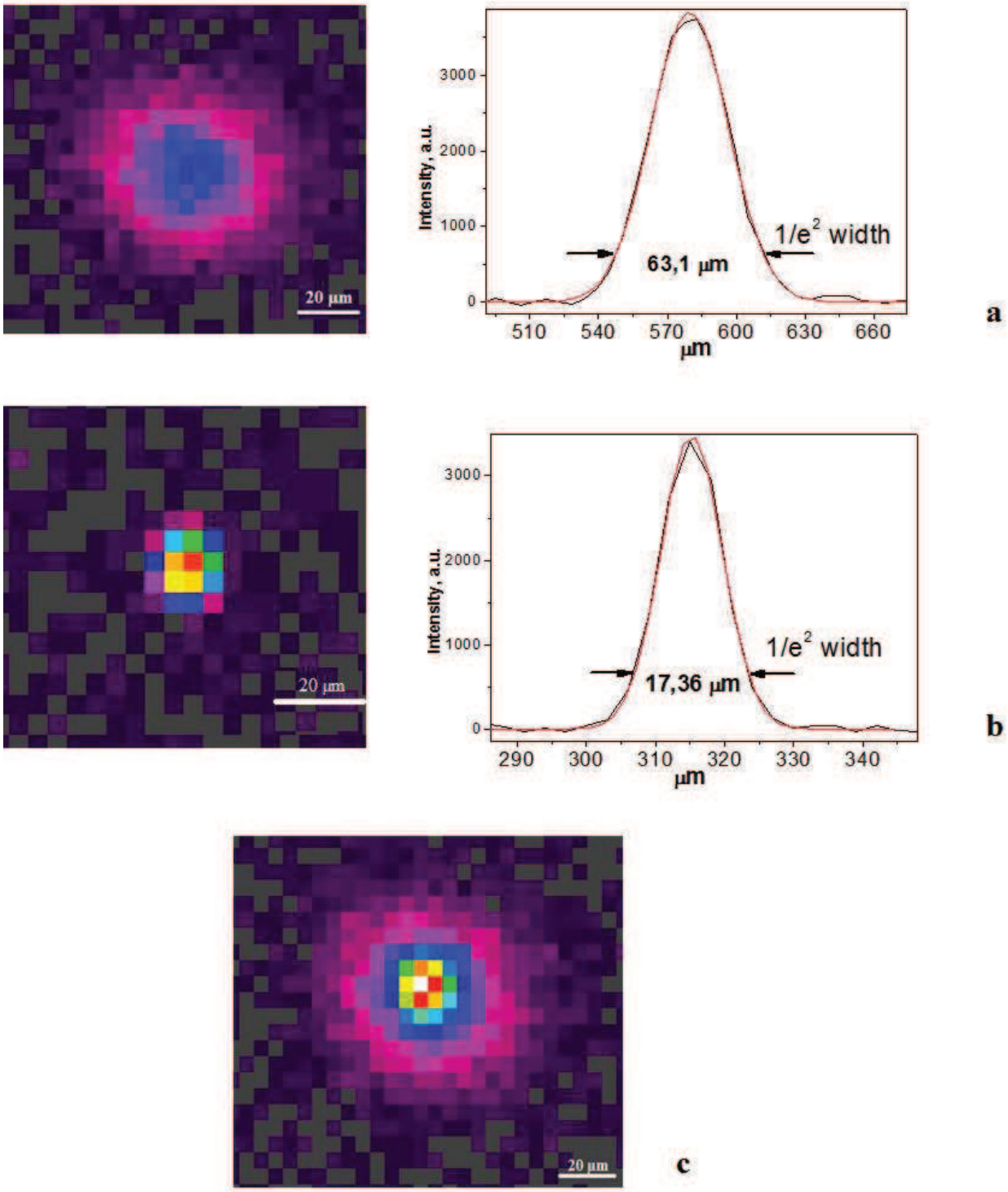

Figure II.16 UV laser beam and profile (a); 640 nm laser beam profile (b); superposition of both laser beams (c).

II.3.3.4. Measurement of the UV irradiation dose.

One of the key parameter in this experiment is the measurement of the UV irradiation dose. The dose received by the sample is defined by

$$Dose = \sum_i Fluence = \sum_i \frac{E_i}{S}, \qquad (2.5)$$

where E_i is energy by pulse and S the area of the laser spot. Since the pulse to pulse energy variation is less than 10 % on the time scale of the experiments, we have equated the energy per pulse E_i with the mean energy calculated from the mean power P and the laser repetition rate $Freq$. Thereby the dose is experimentally measured by

$$Dose = \frac{P}{S*Freq} * N_{pulses}. \qquad (2.6)$$

Experimentally a part of the UV beam is reflected on the power meter (PM) by a semitransparent plate (STP on the Figure II.15). The relation between the power measured on the power meter PM and the real power on the sample has been established thanks to a second power meter (Si photodiode Thor Labs S120VC) placed at the position of the sample. The resulting calibration curve is given on the Figure II.17.

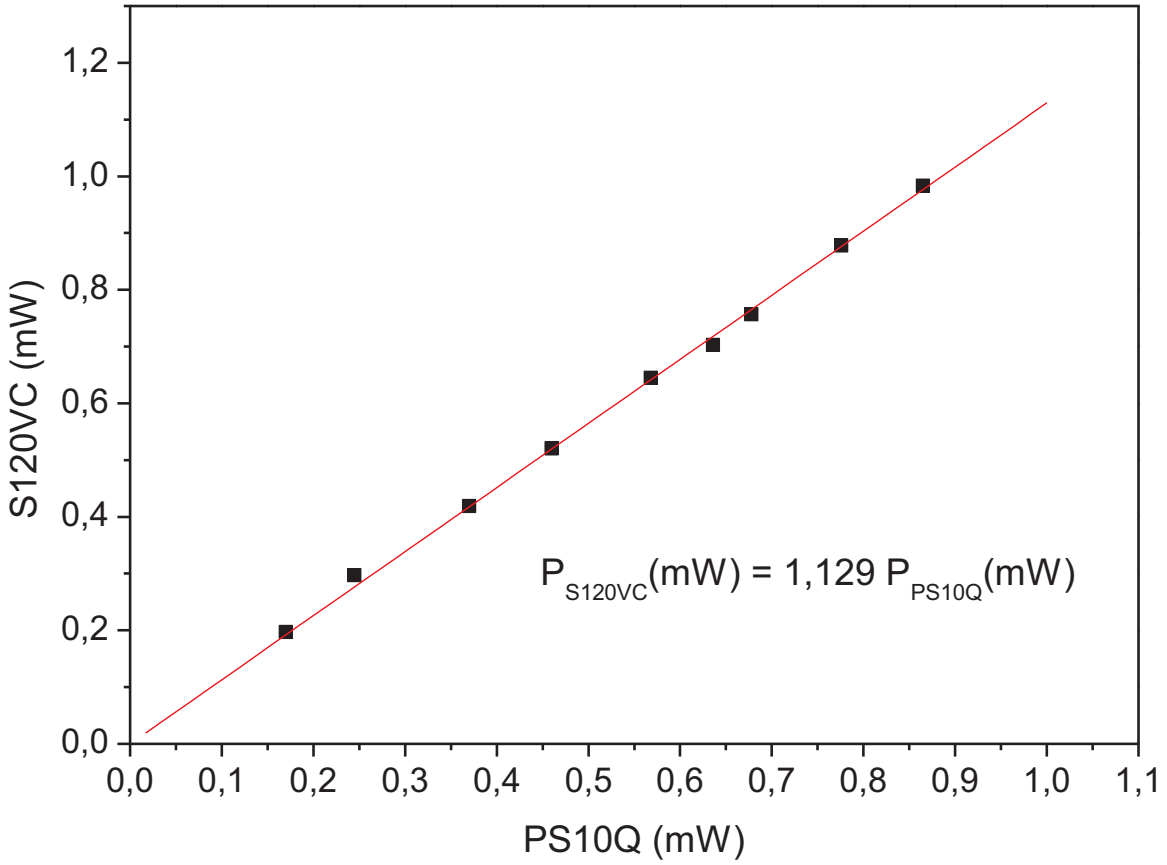

Figure II.17 Calibration curve of the UV power measurements.

Since the sample is placed inside the DAC, the UV absorption of the entrance diamond window has to be taken into account. The Figure II.18 shows the UV signal measured by the photodiode PD2 with or without the entrance diamond window. The measurements have been carried out with different UV powers to ensure that the absorption is linear. Moreover the UV absorption of the lens L5 also has been taken into account.

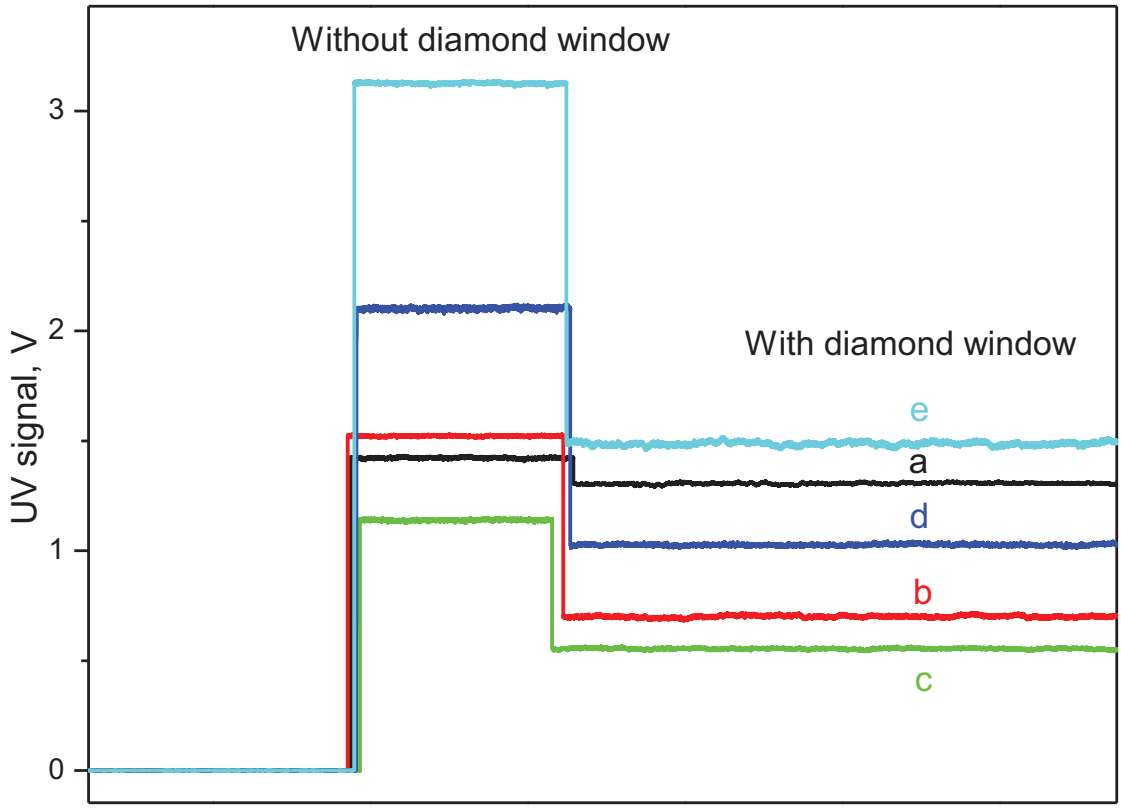

Figure II.18 UV Signal measured on the photodiode PD2 with or without diamond window: b) P = 0.288 mW, c) P = 0.2 mW, d) P = 0.385 mW, e) P = 0.6 mW. The transmission of the lens L5 is also indicated as a black line: a) P = 0.26 mW.

On the Figure II.18 the second (upper) plateau corresponds to the UV signal detected by PD2 without diamond window. The third plateau corresponds to the UV signal of beam passed through the diamond window. In the Table II.9 are presented the obtained values of the transmission of the diamond window and lens (L5).

Table II.9 Transmission of the diamond window and lens (L5) at 355 nm irradiation

Name of curves on the Figure II.18	UV power, mW	Transmission of the diamond window and lens (L5), %
a	0.26	92.1
b	0.288	45.85
c	0.2	48.51
d	0.385	48.84
e	0.6	47.72

Using the values from the Table II.9 we have calculated the transmission coefficient (T_{dw}) of one diamond window at 355 nm:

$$T_{dw} = \frac{0.48}{0.921} = 0.52. \qquad (2.7)$$

II.3.3.5. Data acquisition

In the photodarkenning experiment two signals are of particular interest (i) the power of the visible laser after the sample, measured by the photodiode PD3 and (ii) the UV power measured by the power meter (PM). These signals are acquired through a National Instrument acquisition card (AC on the Figure II.15) and then transferred to a computer. Although the repetition rate of the UV laser is rather high (few kHz), the acquisition system is conceived to measure the transmission of the visible probe beam after each UV pulse. Moreover, in order to improve the signal to noise ratio, the signal on photodiode PD3 is averaged on 10 measurements at each UV laser pulse. The time sequence of the measurements is shown the on oscilloscope screen represented on the Figure II.19.

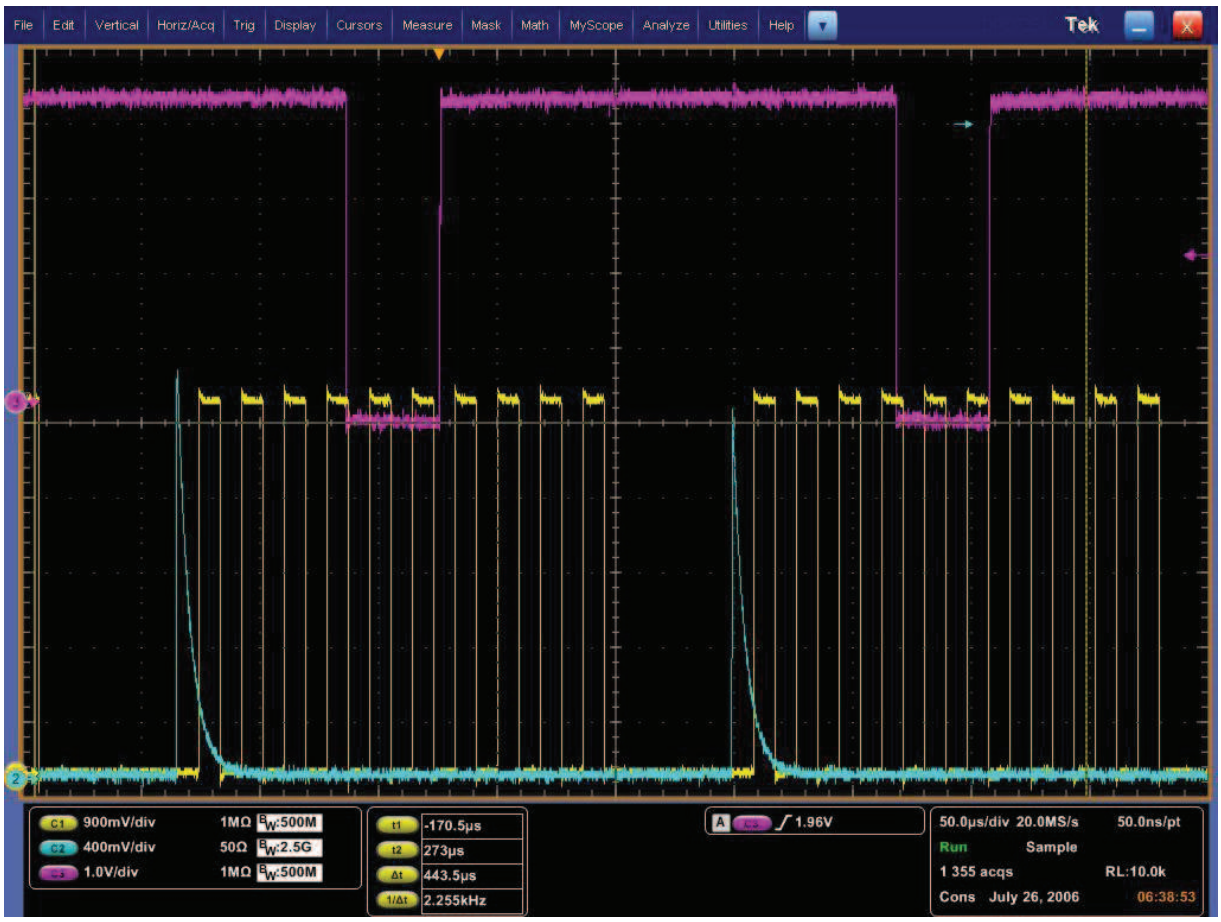

Figure II.19 Signals from the function generator (step pink signal), UV laser pulses (blue signal), signals from pulse generator (step yellow signal).

The pink plot is the signal delivered by the functions generator used to control the UV laser repetition rate. The photodiode PD1 detects the UV pulses at the output of the laser. The corresponding signal is represented in blue. This signal is used to trig a homemade pulse generator which delivers 10 pulses (yellow plot). These last are then used to trig the AC and ensure 10 measurements for each UV pulse.

We have developed a program in LabVIEW to control the registration of data by the acquisition card and to monitor the relevant signals during the experiment. The front panel interface is shown on the Figure II.20. On this interface the right graph corresponds to the signal measured on the photodiode PD2. Whereas left graph shows the UV power measured by the power meter (PM). A homemade control box allows the recording of the UV power only when the sample is irradiated.

For obtaining a zero level of this signal we have used a homemade reset box (RB on the Figure II.15). In each experiment the signals from PD 2 and UV detector have been transferred first to the RB and then to the AC.

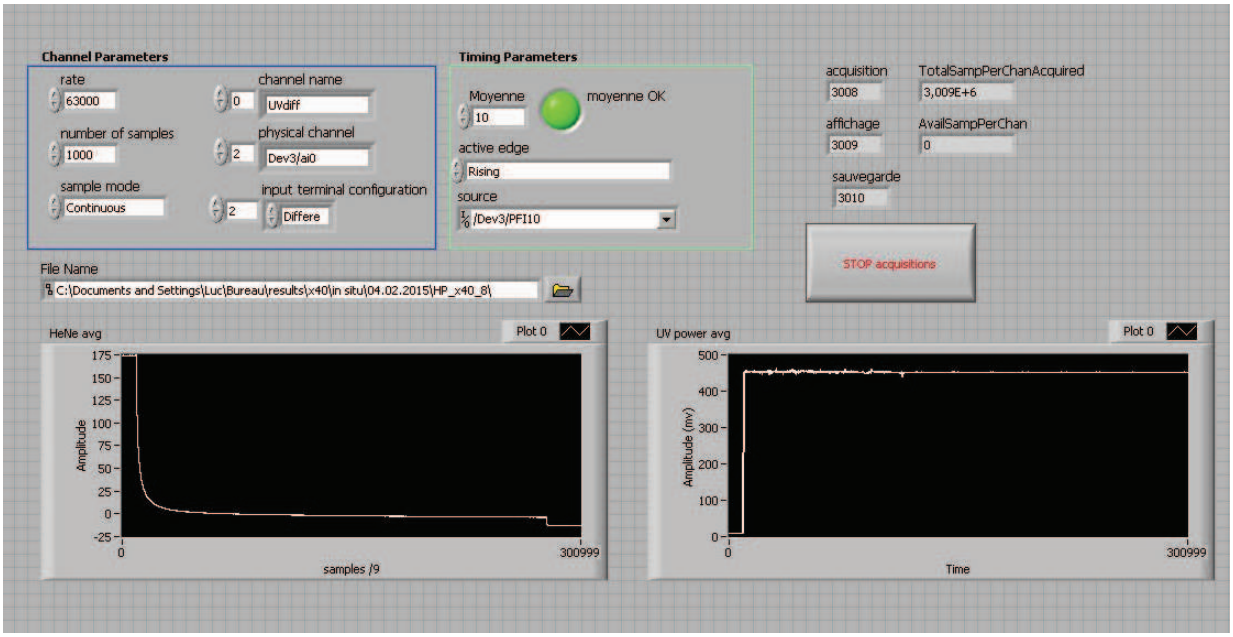

Figure II.20 Front panel of interface of the LabVIEW program.

II.3.3.6. Data post treatment

For treatment of the experimental data we have worked out MATLAB programs which allow calculating: (i) the average over 10 acquisitions, (ii) the UV irradiation dose received by the sample, (iii) the sample absorbance at 640 nm.

Chapter III: Laser assisted high pressure induced polymerization of 2-(hydroxyethyl)methacrylate.

III. Laser assisted high pressure induced polymerization of 2-(hydroxyethyl)methacrylate.

In this chapter we develop and demonstrate the successful room-temperature polymerization of 2-(hydroxyethyl)methacrylate (HEMA) under high pressure without use of any initiator. By means of Raman spectroscopy we characterize the HEMA at ambient pressure. All energies of Raman bands and their assignment in the range from 600 to 1800 cm^{-1} are presented. Then we also discuss the polymerization of HEMA at static pressure. The polymerization is observed in a limited range of pressures ranging from 0.1 to 1.6 GPa. Further, we consider laser assisted HP-induced polymerization of HEMA and show that laser irradiation of the compressed sample increases the reaction rate and improve the reaction efficiency. Finally, we explain the catalytic effect of light on polymerization process considering the one photon excitation of HEMA monomers in the triplet T_1 state.

III.1. Experimental techniques

III.1.1. Diamond Anvil Cell

The symmetric diamond anvil cell (DAC) used in these experiments, has been described in details in section II.2. Liquid HEMA (purity >99%, Aldrich) without further purification was loaded in a hole of 250 μm in diameter drilled in a preindented metallic gasket and compressed. The polymerization reaction has been probed in-situ by means of Raman spectroscopy using a HR800 spectrometer described in section II.3.2.

III.1.2. Laser systems

We used two different laser systems to activate the polymerization reaction under pressure. In the first configuration, the HEMA samples in the DAC were irradiated with the blue line of an Ar+ laser (Coherent, λ = 488 nm) through three different microscope objectives (10×, 40×, or 100×), providing various power densities on the sample. In the second configuration, a frequency-tripled Nd:YAG laser (CNI MPL-F-355, λ = 355 nm, 7 ns) with high repetition rate (7.6 kHz) and maximum average power of 10 mW was focused on the sample through a biconvex lens of 750 mm focal length. In both configurations the power density on samples was measured using a CCD beam-shape analyzer (Spiricon SP620U) and a power meter (PowerMax PS10Q Coherent).

III.2. Raman spectra of HEMA

Figure III.1 shows the Raman spectrum of liquid HEMA under ambient pressure. The energies of all observed Raman bands are reported in Table III.1, together with their assignment.

At ambient pressure four main vibrational bands are observed between 1380 and 1800 cm^{-1}: $C=CH_2$ stretching at 1404 cm^{-1}, the $C–CH_2$ deformation at 1455 cm^{-1}, the C=C aliphatic stretching at 1640 cm^{-1} and the C=O stretching at 1710 cm^{-1}. The assignment of bands observed between 1150 and 500 cm^{-1} is more controversial and based mainly on assignments proposed in compounds containing functional groups similar to those present in HEMA [125-128]. We note that the band at 947 cm^{-1} is not observed in acrylic or methacrylic compounds [126, 127]. It is only reported in pHEMA Raman spectra without any assignment [125]. Consequently, this band likely corresponds to a deformation localized on the OCH_2CH_2OH part of the HEMA molecule.

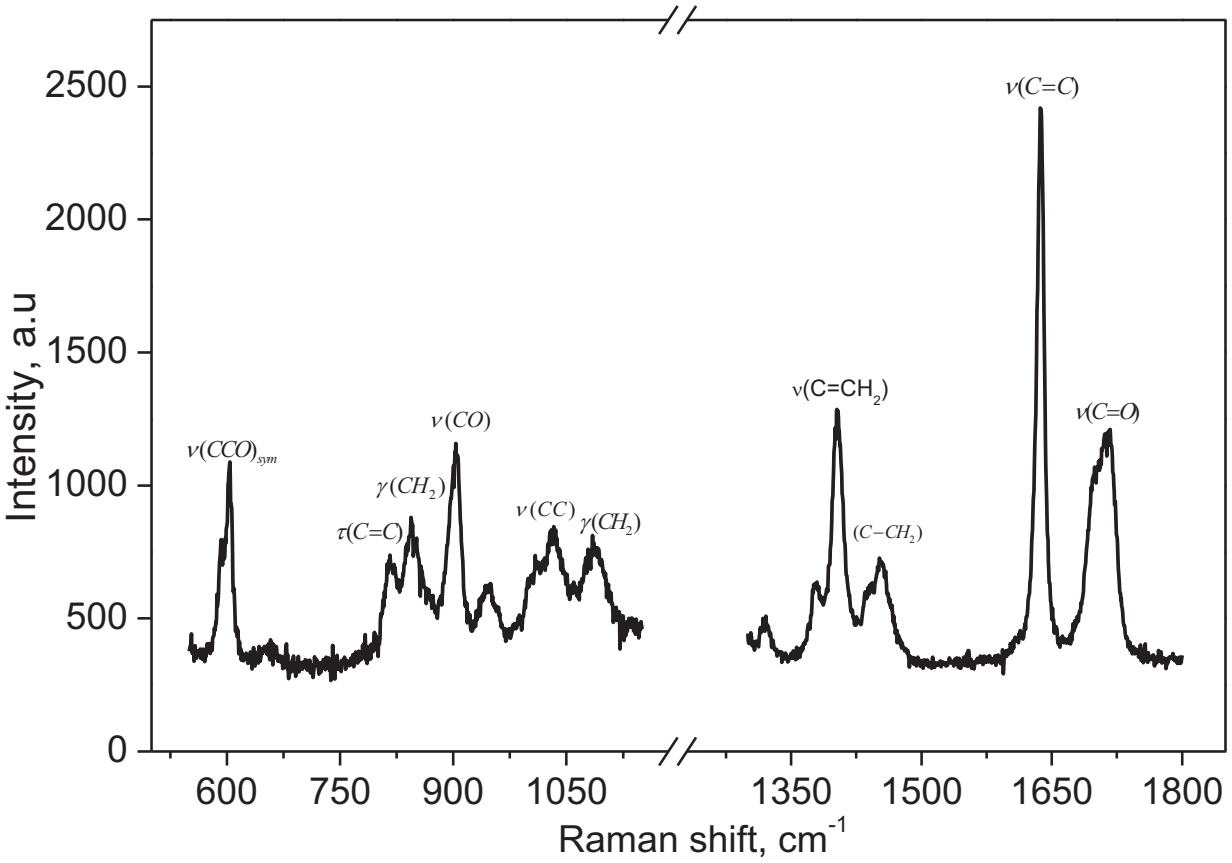

Figure III.1 Raman spectrum of liquid HEMA under ambient pressure.

Table III.1 Energies and assignment of the bands observed in the Raman spectra of HEMA at ambient pressure. Here ν is the bond stretching, δ the bending, ω the wagging, γ the rocking and τ the torsion

Raman shift (cm^{-1})	Assignment
600	$\nu(CCO)_{sym}$ [125] or $\delta(O-C=O)$ [126]
816	$\tau(C=C)$ [127], $\nu(COC)_{sym}$ [125], $\omega(C=O)$ [126] or $\nu(C-CH_3)$ [128]
845	$\gamma(CH_2)$ [125] or $\nu(C-C)$ [126, 127]
900	$\nu(CO)$ [125]
947	deformation localized on OCH_2CH_2OH part of the HEMA molecule
1023	$\nu(CC)$ [125]
1085	$\gamma(CH_2)$ [126, 127]
1404	$\nu(C=CH_2)$ [126, 127]
1455	$(C-CH_2)$ deformation [129, 130]
1640	$\nu(C=C)$ [125-127]
1705	$\nu(C=O)$ [125-127] free
1714	$\nu(C=O)$ [125-127] H-bounded

III.3. Measurement of the conversion yield of polymerization of HEMA

We have used in-situ Raman spectroscopy to monitor the kinetics of the polymerization reaction. Indeed, the characteristic bands of monomer and polymer change in intensity as the polymerization progresses. For example, in the polymerization of vinyl monomers, C=C double bonds are broken and C−C single bonds are formed [131, 132]. Figure III.2 shows Raman spectra of liquid HEMA and polymerized HEMA at atmospheric pressure in the spectral range between 1300 and 1800 cm^{-1}. As it can be seen form this figure the kinetics of the polymerization reaction can be monitored in situ by the decrease in intensity of vibrational bands associated with C=C double bonds in comparison with stretching bands associated with C=O bonds whose intensity do not change upon polymerization. In our experiments, the conversion yield (CY) of polymerization of HEMA at the time t, has been determined according to

$$CY(t) = 1 - \frac{(I_{C=C}/I_{C=O})_t}{(I_{C=C}/I_{C=O})_{t=0}}, \qquad (4.1)$$

where $I_{C=C}$ and $I_{C=O}$ are, respectively, the area of ν(C=C) and ν(C=O) Raman bands.

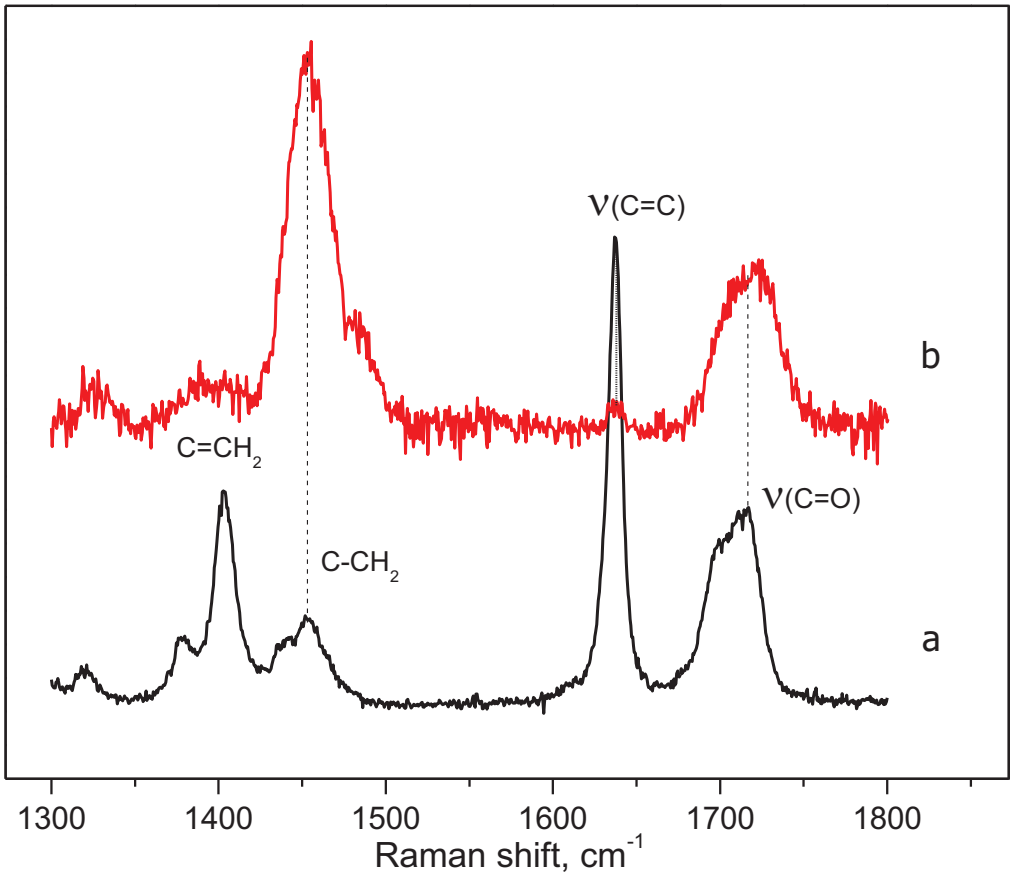

Figure III.2 Raman spectra of liquid HEMA (a) and polymerized HEMA (pHEMA) (b) at atmospheric pressure in the spectral range between 1300 and 1800 cm^{-1}.

III.4. Results and discussion

III.4.1. High pressure induced polymerization of HEMA

III.4.1.1. In situ observation of polymerization of HEMA

Figure III.3 shows Raman spectra of liquid HEMA and HEMA compressed at 0.7 GPa for different periods of time. The Raman spectra of recovered sample are also reported. Compared with the spectrum of liquid HEMA at atmospheric pressure (a), at HP (b−d) Raman bands are slightly broadened and blue-shifted indicating a stiffening of intramolecular bonds. The main effect of pressure is a progressive decrease in the C=C bands (1640 cm^{-1}) intensities together with a growing of the C−CH_2 (1455 cm^{-1}) band intensities. This behavior is characteristic of the polymerization process resulting from the double bond opening of the methacrylate group and propagation−elongation of polymer chains. This conclusion is supported by the observed pressure drop in the sample volume from 0.7 to 0.3 GPa, which reveals the formation of a higher density product.

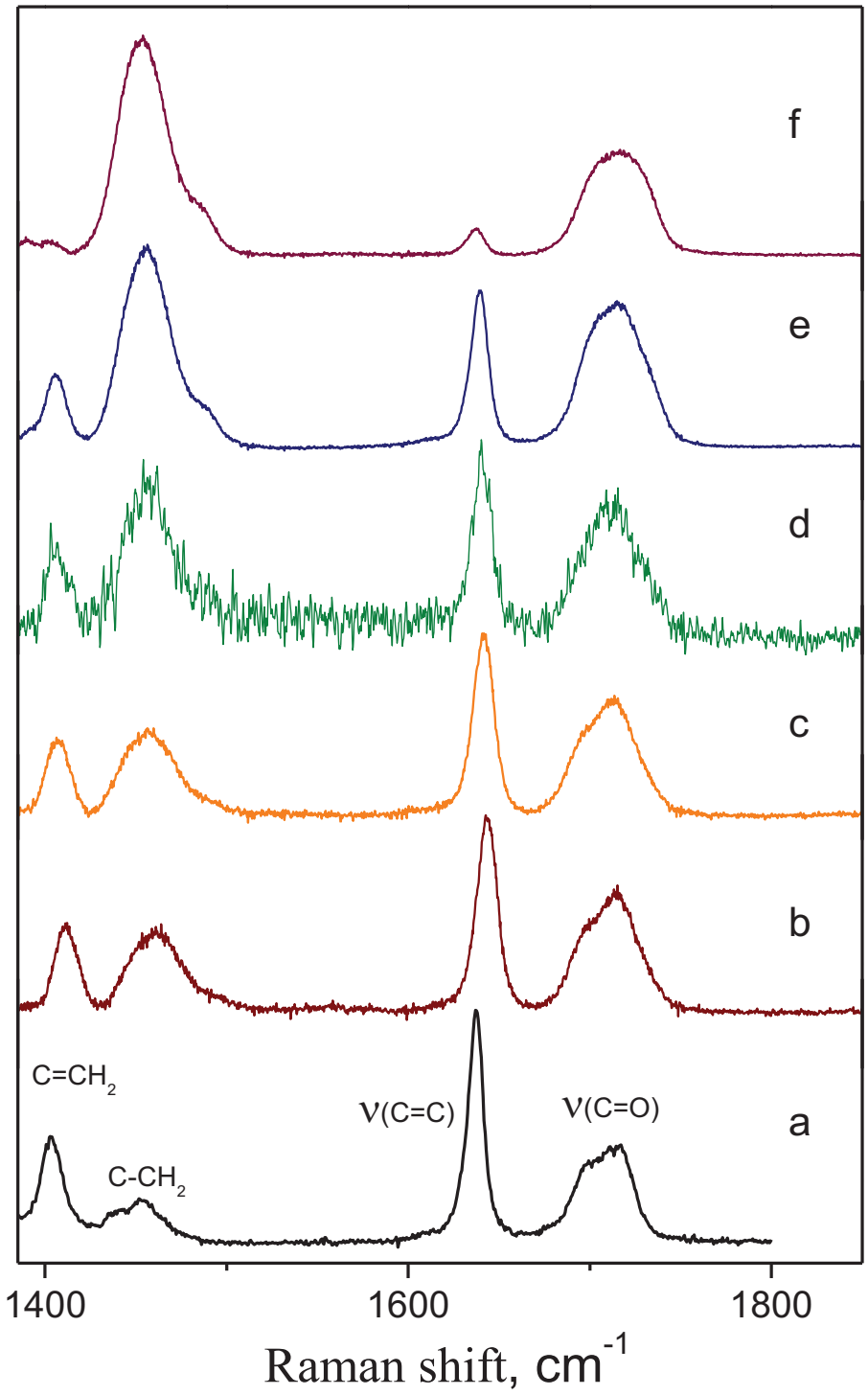

Figure III.3 Raman spectra of liquid HEMA at atmospheric pressure (a) and at 0.7 GPa and RT after 5 h (b), 6 days (c), and 41 days (d). Recovered sample after just a few minutes in air (e) and after 7 days (f).

The Raman spectra of the the recovered sample are shown in Figure III.3. Immediately after the opening of the DAC, the recovered sample retains the polymerization state before decompression (d), which evidences the permanent nature of the pressure-induced modification. It is worth remarking that after 1 week of exposure in air the recovered sample exhibits a

stronger attenuation of the double bond C=C bands (Figure III.3f), which was assigned to the natural sample purification owing to evaporation of the remaining HEMA monomers from the recovered sample.

III.4.1.2. Characterization of the recovered sample

The recovered product is similar to pHEMA synthesized by the usual radical polymerization process using thermal initiator. Indeed, apart from differences in the relative intensities of C=C (1640 cm^{-1}) and C−CH_2 (1455 cm^{-1}) bands, the Raman spectrum of the recovered product in the spectral range 700 to 1875 cm^{-1} is identical to the Raman spectrum measured on thermally polymerized HEMA (Figure III.4 and Figure III.5).

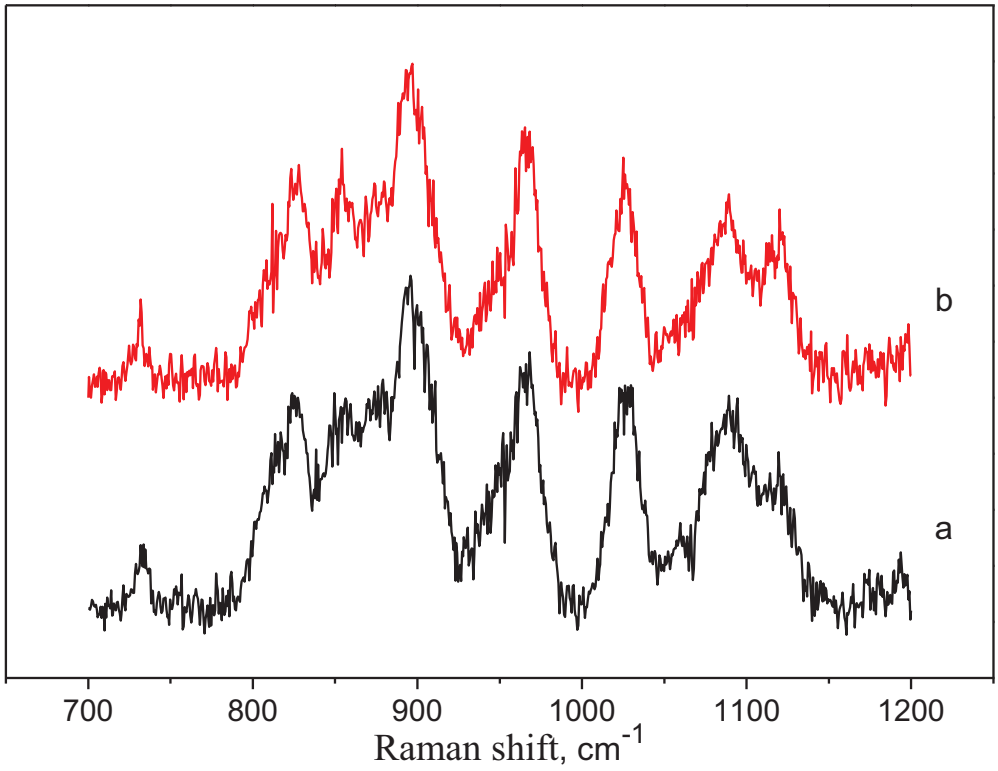

Figure III.4 Raman spectra of HP polymerized HEMA (a) and thermally polymerized HEMA (b) in the spectral range 700 to 1200 cm^{-1}.

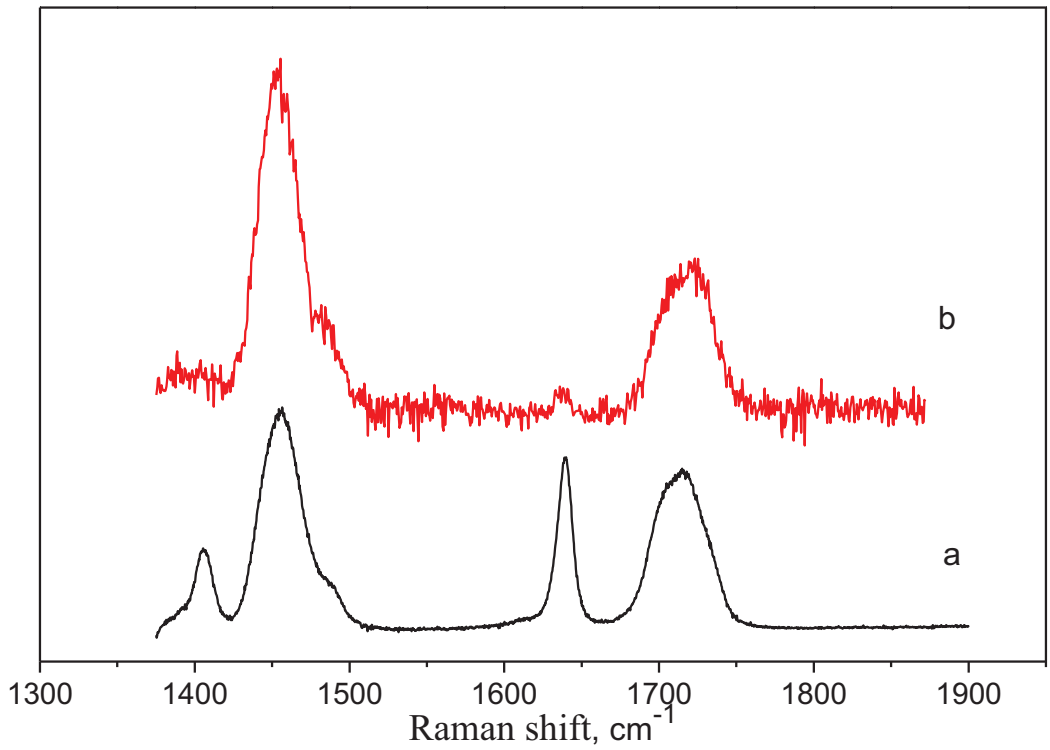

Figure III.5 Raman spectra of HP (0.7 GPa) polymerized HEMA (a) and thermally polymerized HEMA (b) in the spectral range 1375 to 1875 cm^{-1}.

Figure III.6 shows the photos of the recovered sample of pHEMA obtained by HP method: (a) freshly recovered sample of HP polymerized HEMA on the culet surface of the diamond, (b) top view of pHEMA recovered sample, (c) side view of pHEMA recovered sample.

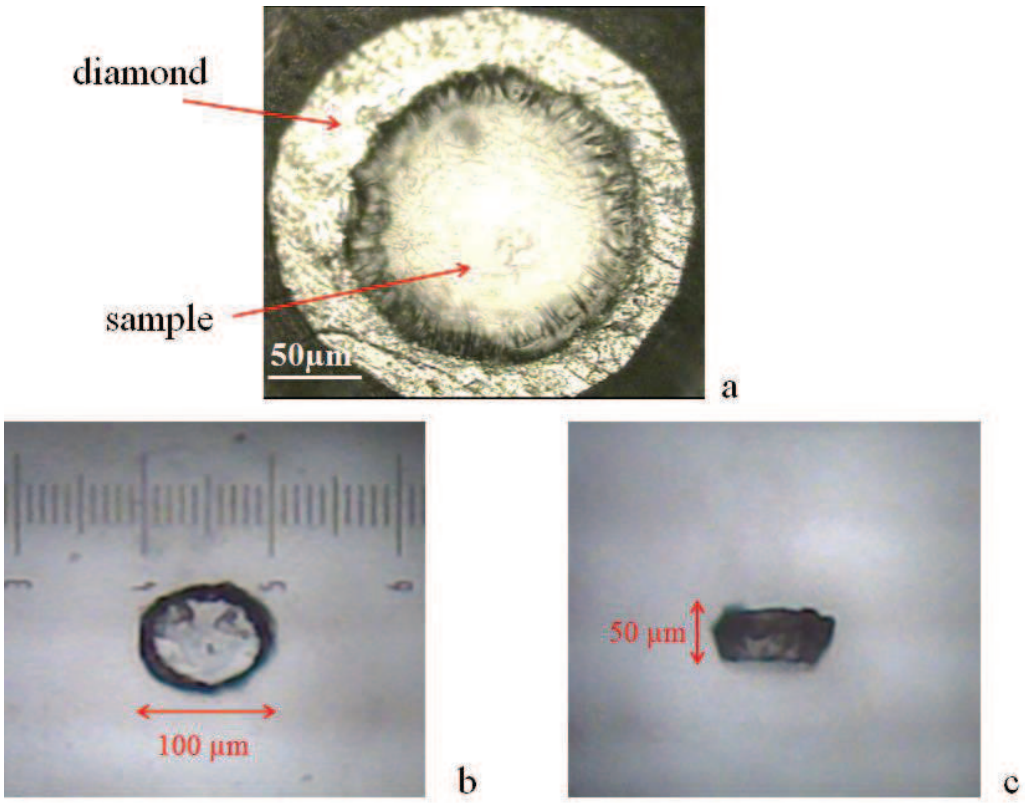

Figure III.6 Photos of the pHEMA sample obtained by HP method: (a) pHEMA sample on the surface of the diamond, (b) pHEMA sample top view, (c) pHEMA sample side view.

III.4.1.3. Efficiency of HP-induced polymerization of HEMA

The conversion yield measured in the recovered sample depends of at least two parameters: the value of the high pressure and the time during which the pressure is applied on the sample. We have analyzed separately these two factors.

Figure III.7 shows the in-situ measured CY as function of the time of compression at 0.7 GPa. The HP-induced polymerization process is slow and not completed even after 41 days, where the CY remains below 0.3.

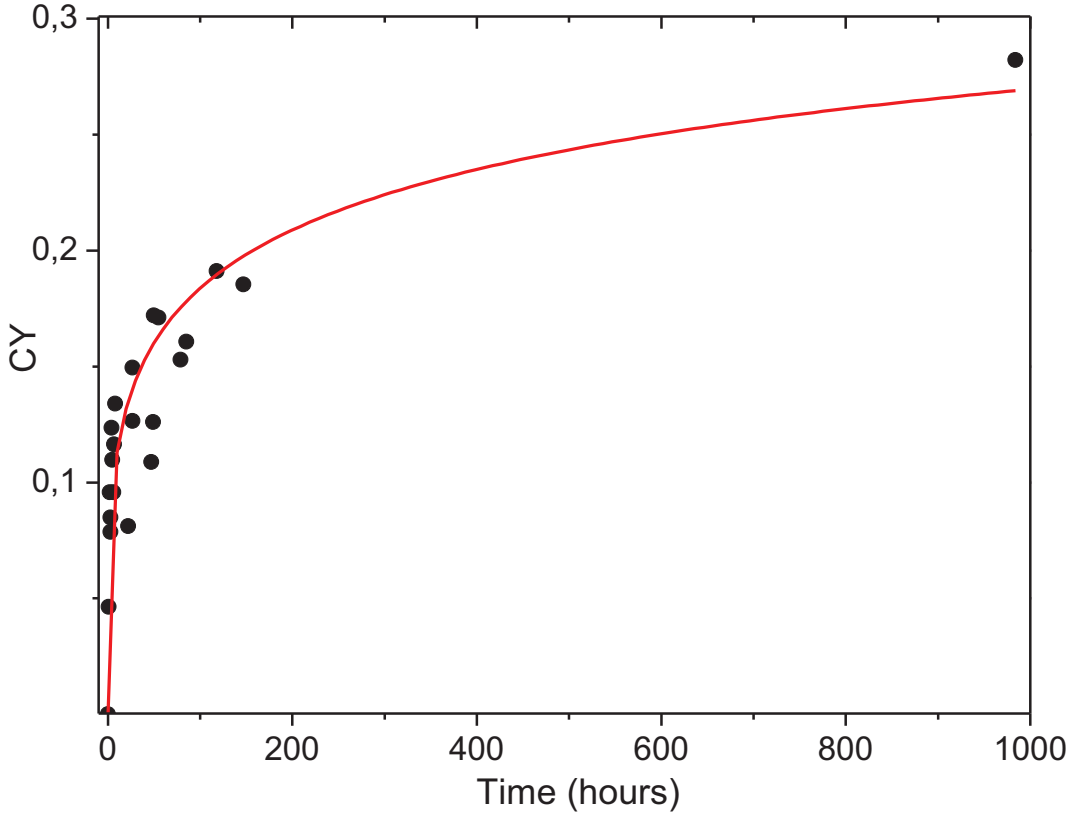

Figure III.7 Conversion kinetics of HEMA under 0.7 GPa static pressure. The solid line is a fit with the Avrami equation (See the text.).

Figure III.8 shows the CY of the recovered samples after 19 h of compression at different pressures. The CY attains the maximum at 0.35 GPa and progressively decreases when pressure increases. Above 1.6 GPa the CY becomes null even when samples are kept under pressure for several days. In the previously reported HP-induced polymerization experiments on simple unsaturated hydrocarbon molecules it has been shown that an increasing of pressure lead to an acceleration of the reaction [8, 82, 133, 134]. This picture is different in the case of HEMA. While the pressure threshold concerned the beginning of polymerization in previous studies, the present results evidence a pressure threshold $p^* \approx 1.6$ GPa, above which no polymerization occurs. We relate this to the growing influence of steric factors on the reaction mechanism resulting from the densification of the media.

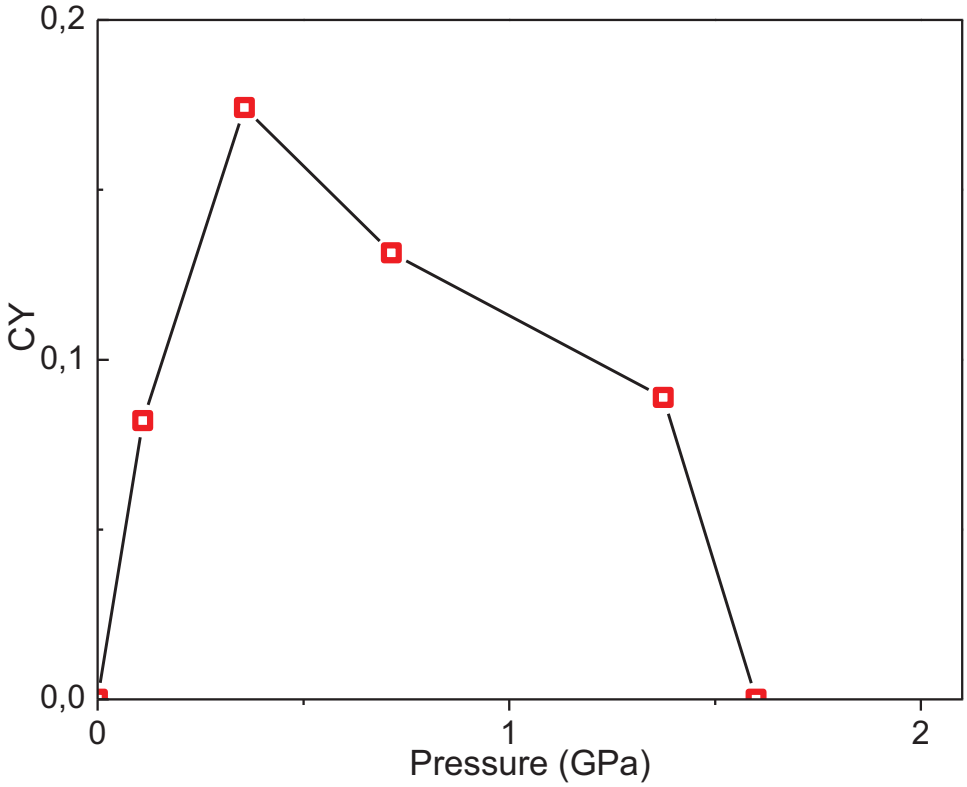

Figure III.8 Conversion yield (CY) of freshly recovered samples after 19 h under different pressures.

To check the variation of HEMA viscosity with pressure, we have loaded a copper sphere of 35 µm in diameter together with liquid HEMA into the DAC (Figure III.9). In the range of pressure between 0.1 and 0.9 GPa, we have observed that the sphere, attracted to gravitation, could move inside the DAC. Conversely, when the pressure exceeds 1.6 GPa, no movement of the sphere is observed. Because the characteristic time of polymerization is very long (several days), there is no possible confusion in differentiating the viscosity change due to an increase in pressure from that due to polymerization. We assign this finding to a glass transition above 1.6 GPa, leading to the molecular movement restriction. In any cases, the suppressed mobility and nonfavorable arrangement of monomers in the higher-pressure state above 1.6 GPa can restrict the formation of a polymeric chain.

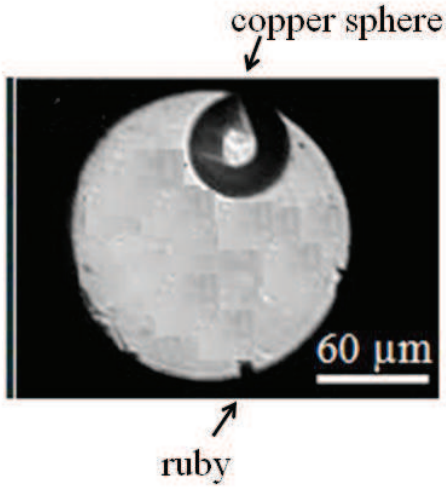

Figure III.9 Photo of the liquid HEMA loaded with a copper sphere in DAC.

III.4.2. Laser assisted high pressure induced polymerization of HEMA

III.4.2.1. In situ observation of polymerization

Acceleration of HP-polymerization reactions upon laser irradiation has been reported in literature for samples in liquid or solid states [7, 8, 79, 135]. Accordingly, we have studied the influence of laser irradiation on HEMA samples subjected to a pressure of 0.7 GPa. Two different laser systems were used to irradiate freshly loaded HEMA samples at 488 nm (12 kW/cm^2) or 355 nm (18 W/cm^2). Raman spectra recorded on these samples, after different irradiation times, are shown in Figure III.10. The obtained spectra clearly evidence the triggering of the polymerization reaction by light and acceleration of the reaction kinetics when the excitation wavelength is shifted to the UV.

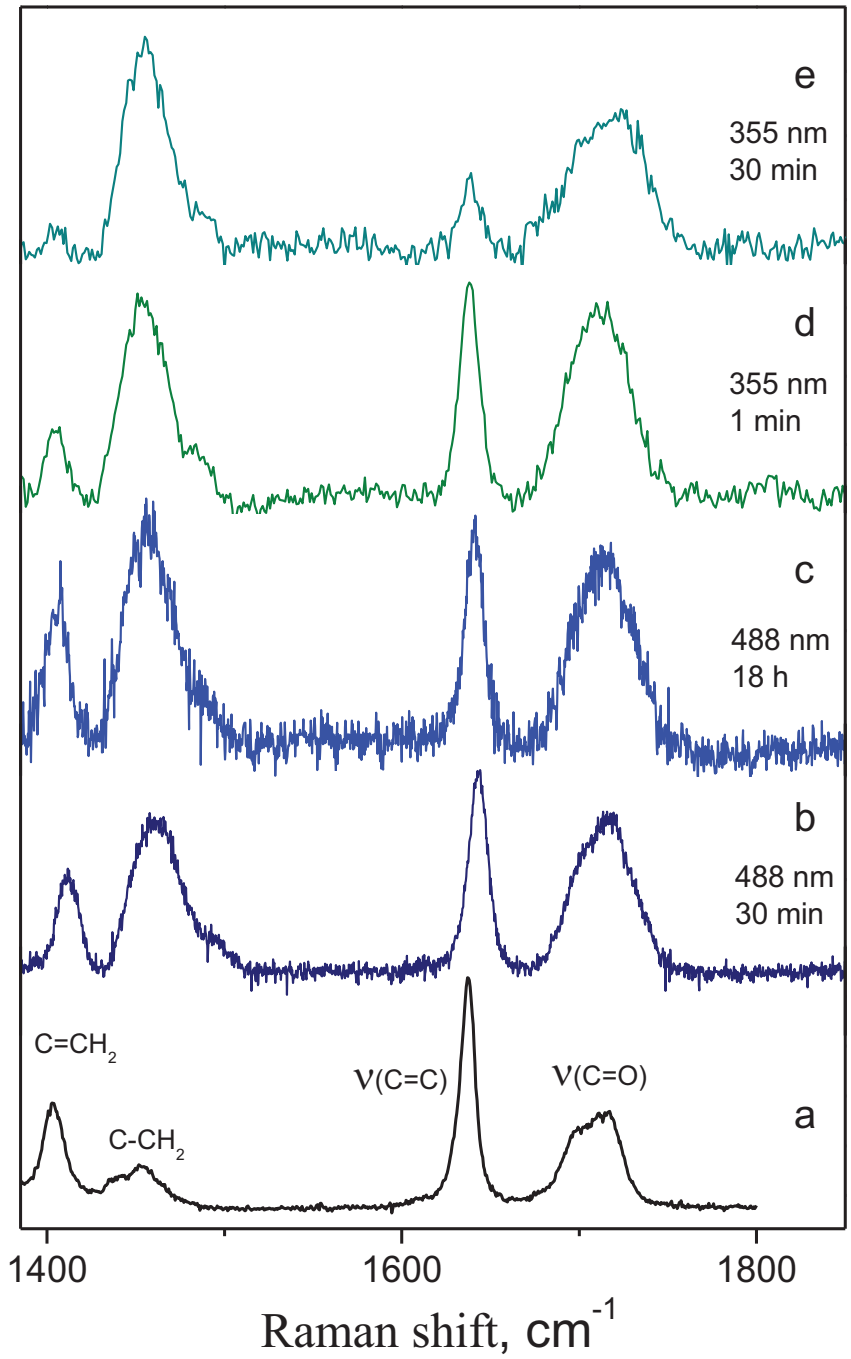

Figure III.10. Raman spectra of liquid HEMA before irradiation (a) and at 0.7 GPa after irradiation at 488 nm for 30 min (b), 488 nm for 18 h(c), 355 nm for 1 min (d), and 355 nm for 30 min (e).

III.4.2.2. Comparison of the static HP- and laser assisted HP-induced polymerization kinetics

The conversion yield CY(t) as a function of the irradiation time is shown in the Figure III.11 for both wavelengths. In the case of the irradiation at 488 nm (12 kW/cm^2), the polymerization progress is much faster compared with the nonirradiated sample in the

Figure III.7 and, after only 10 h, attains a plateau with CY ≈ 38 %. Acceleration of the process is even more pronounced with an irradiation at 355 nm because a plateau with CY ≈ 84 % is reached after only 30 min of irradiation. The observed effects are a net synergy of the HP and light treatments because at the atmospheric pressure the same laser irradiation does not produce any polymerization of HEMA even after 1 day of irradiation.

The HP compression of simple unsaturated hydrocarbons usually results in almost complete polymerization [7, 8, 78, 79, 82, 134, 135]. The partial polymerization of HEMA observed in our studies, with or without irradiation, could be explained by the presence of hydroxyl and carbonyl groups of the monomer molecule involved in intermolecular hydrogen bonds. Indeed, each HEMA molecule has only one C=C double bond and the polymer chains grow linearly without cross-linking (no branching of polymer chains). Consequently, the polymerization process requires a significant mobility of the monomers to fit the growing chain. Strengthening of hydrogen bonds at HP [136] can suppress this capacity of steric rearrangements by hindering the movement of HEMA monomers.

This hypothesis is supported by recent HP experiments with monomers containing hydroxyl or carbonyl groups. Murli *et al*. [66] have observed nonpermanent polymerization of acrylic acid with only short oligomers found in the recovered sample. Kaminski *et al*. [137] have reported on inefficient polymerization of tetraethylene glycol dimethacrylate at 1 GPa and room temperature.

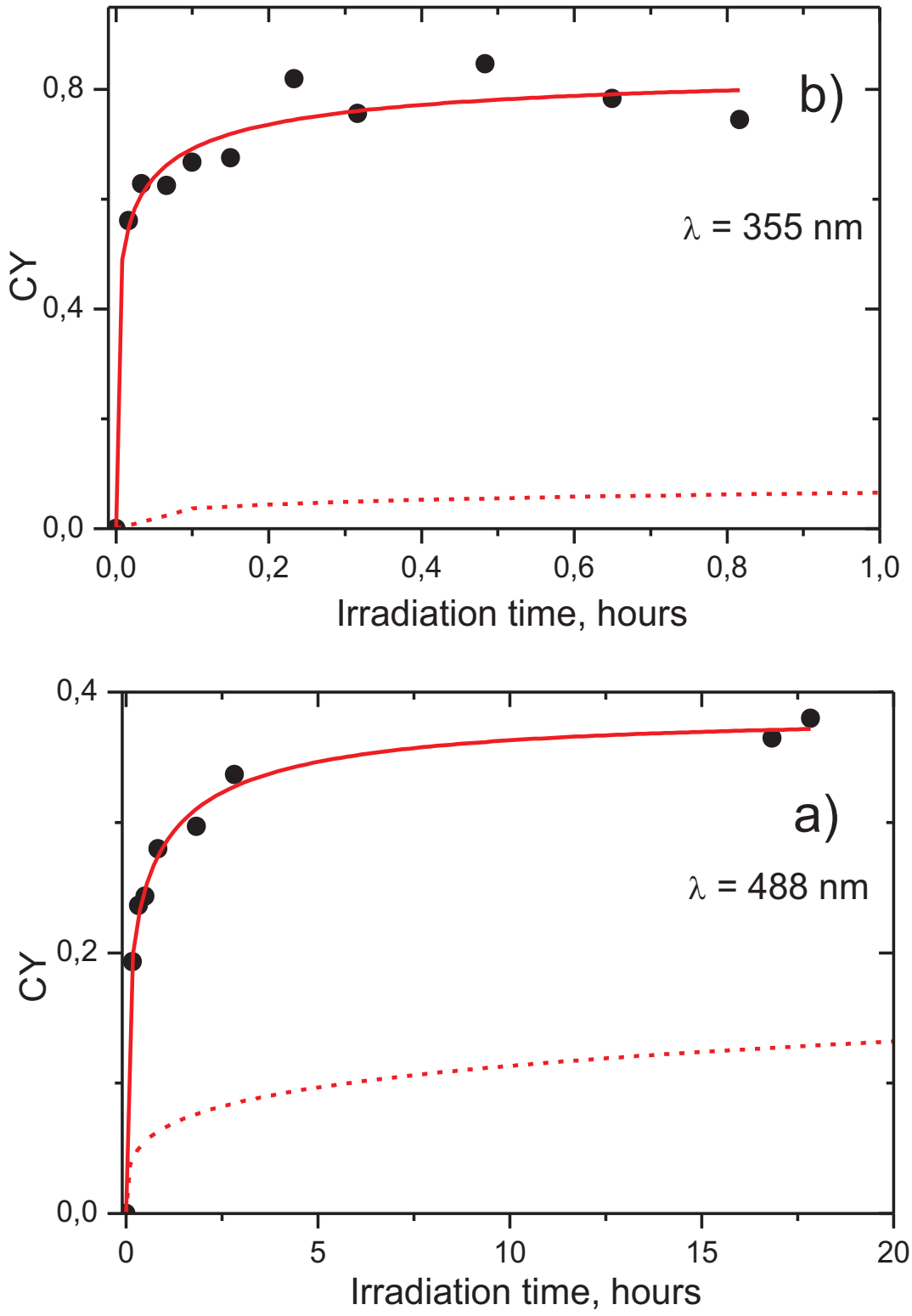

Figure III.11 Conversion kinetics of HEMA under 0.7 GPa pressure with laser irradiation at 488 nm (12 kW/cm^2) (a) and 355 nm (18 W/cm^2) (b). The solid lines are fits with Avrami equation. (See the text.) For a comparison with HP polymerization process without irradiation, the fit curve from Figure III.7 is shown as a dashed line.

Kinetics of the examined polymerization reactions can be analyzed in frame of the Avrami model [89]

$$CY(t) = CY_{\infty}(1 - \exp(-kt^{n})), \qquad (4.2)$$

where *CY(t)* and CY_{∞} are the polymer fractions at time t and at the end of the process, *k* is the rate constant, and *n* is a parameter, whose value depends on geometry of the growing polymer chains. Fits of *CY(t)* data with eq. 4.2 are shown in Figure III.7 and Figure III.11 by solid lines. The final conversion yield CY_{∞} is fixed at the value observed experimentally in Figure III.7 and Figure III.11 to reduce the number of free parameters in the fit procedure and improve the reliability of the fitted parameters. The obtained values of *k* and *n* are given in the Table III.2 together with the conversion yield CY_{∞} values chosen for the fit.

Table III.2 Avrami model parameters k and n obtained from the fit of HEMA polymerization kinetics measured at pressure of 0.7 GPa and different laser power densities and wavelengths.

wavelength	**power density**	**k (h^{-1})**	**n**	**CY_{∞}**
No irradiation	0	0.19 ± 0.02	0.27 ± 0.03	0.28
355 nm	18 W/cm^2	3.23 ± 0.5	0.27 ± 0.05	0.82
488 nm	12 kW/cm^2	1.37 ± 0.04	0.35 ± 0.04	0.38
488 nm	2 kW/cm^2	1.44 ± 0.08	0.34 ± 0.05	0.24
488 nm	0.2 kW/cm^2	1.41 ± 0.06	0.40 ± 0.05	0.24

The similar values of parameter n obtained in both experiments indicate that the growth geometry of the polymer chains is not strongly altered by the laser irradiation intensity and wavelength. Originally, the Avrami equation was proposed to model the crystal growth from a liquid phase [89, 138] and has been adapted later to polymerization processes [82, 134]. According to this model, the values of n are expected to increase with the dimensionality of the process, ranging from 1 to 2 in the case of linear growth. Nevertheless, in polymerization process involving a diffusion step where reactants are transported to reaction sites, values of n close to 0.5 ± 0.3 were found [7, 8, 79, 134], in agreement with model calculations showing that n is equal to 0.5 in the case of the diffusion-controlled 1D growth process [139]. The values of n reported in the Table III.2 suggest the diffusion-controlled linear growth of pHEMA chains. This diffusion step could be interpreted as a continuous modulation of relative orientations and

intermolecular distances, leading to instantaneous configuration allowing the polymerization reaction to occur.

III.4.2.3. Photochemical processes involved in the laser assisted HP-induced polymerization of HEMA

The obtained *k* values (Table III.2) evidence that the polymerization reaction of HEMA under HP is more than one order of magnitude faster under laser irradiation. The optical enhancement of the HP polymerization kinetics is usually explained by excitation of π* antibonding states. Under these conditions, the energy barrier hindering the system evolution toward the final state can be absent. We assign the acceleration of HP-induced polymerization under laser irradiation to triplet state mediated mechanisms.

There is no literature data about excited states of HEMA, nevertheless insights regarding the photochemical processes leading to polymer formation may be proposed based on the excited-state structure of acrylic and methacrylic acid containing the same chromophore backbone C=C−C=O. In these last two compounds, the available experimental and theoretical data are nevertheless restricted to ambient pressure range. A schematic representation of acrylic and methacrylic acid energy levels is given in the Figure III.12; we adopt this scheme for HEMA. Owing to the singlet−triplet intersystem crossing, optical excitation of singlet states $S_1(^1n\pi^*)$ and $S_2(^1\pi\pi^*)$ results in the efficient energy transfer to triplet $T_1(^3\pi\pi^*)$ state [140, 141]. The excited electron of the state in the π* orbital elongates the C=C double bond, delivering to it a single-bond character. Moreover, the rotational barrier around C−C bond is lowered in the T_1 state, and the CH_2 group can rearrange to minimize the steric repulsion with nearest molecules. Consequently, the long-lived excited T_1 monomer can initiate the polymerization reaction when it encounters an appropriate configuration with another ground-state monomer molecule. The previous observation of UV-induced polymerization of crystalline methacrylic acid [142] is consistent with this hypothesis.

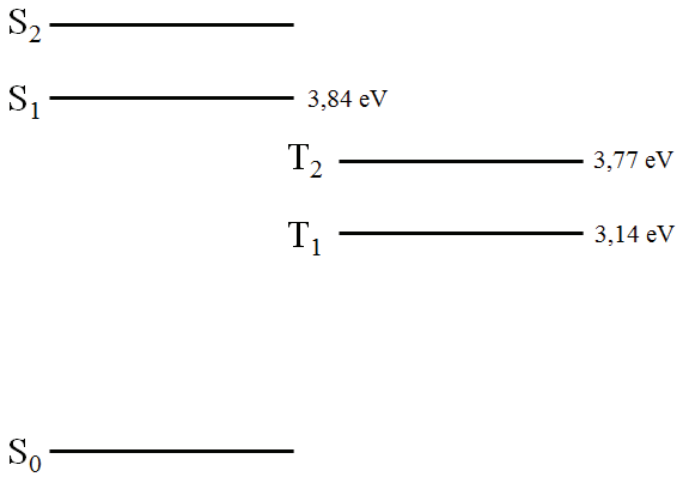

Figure III.12 Schematic energy levels of acrylic and methacrylic acids. The energy values are given for acrylic acid from ref [140].

In the case of the UV excitation, the photon energy (3.5 eV) seems not sufficient to excite the first singlet state (Figure III.12). On the other hand the two-photon excitation is strongly unlikely due to the low density of power used in the experiment (18 W/cm^2). Three factors may explain this disagreement. Figure III.13 shows schematic configuration coordinate diagram for HEMA. (1) The increasing overlap between electronic orbitals at HP induces a decrease in the energy gap between the occupied π (HOMO) and unoccupied π* (LUMO) orbitals (ΔE in Figure III.13) [32, 44]. (2) In addition to this vertical displacement of potential surfaces, there can be also a horizontal displacement along the configuration coordinate due to different compressibility of the ground and excited states (ΔQ in Figure III.13). Together, these two contributions may explain vanishing energy mismatch that allows one-photon excitation of HEMA S_1 state at 355 nm under high pressure. (3) Moreover, the low-energy forbidden $T_{1,2}$–S_0 transitions may become at least partially allowed at HP, which can promote the direct triplet states population (blue line in Figure III.13).

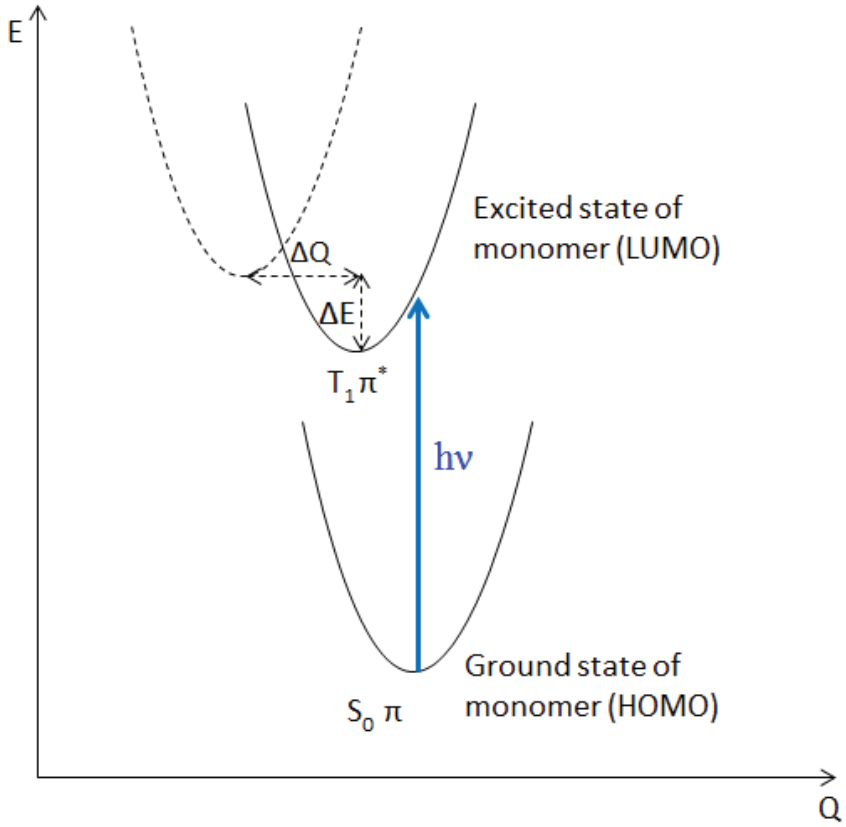

Figure III.13 Schematic configuration coordinate diagram (solids lines correspond to electronic orbitals of HEMA under pressure, dash line corresponds to the electronic orbital under atmospheric pressure).

More support to our assignment of the polymerization acceleration to one-photon transitions can be obtained in measurements conducted at different laser power densities. In these experiments, the overall photon flux was conserved and the intensity is varied according to the spot size by changing the microscope objective. The CY data are shown in Figure III.14 for two power densities of 2 and 0.12 kW/cm^2.

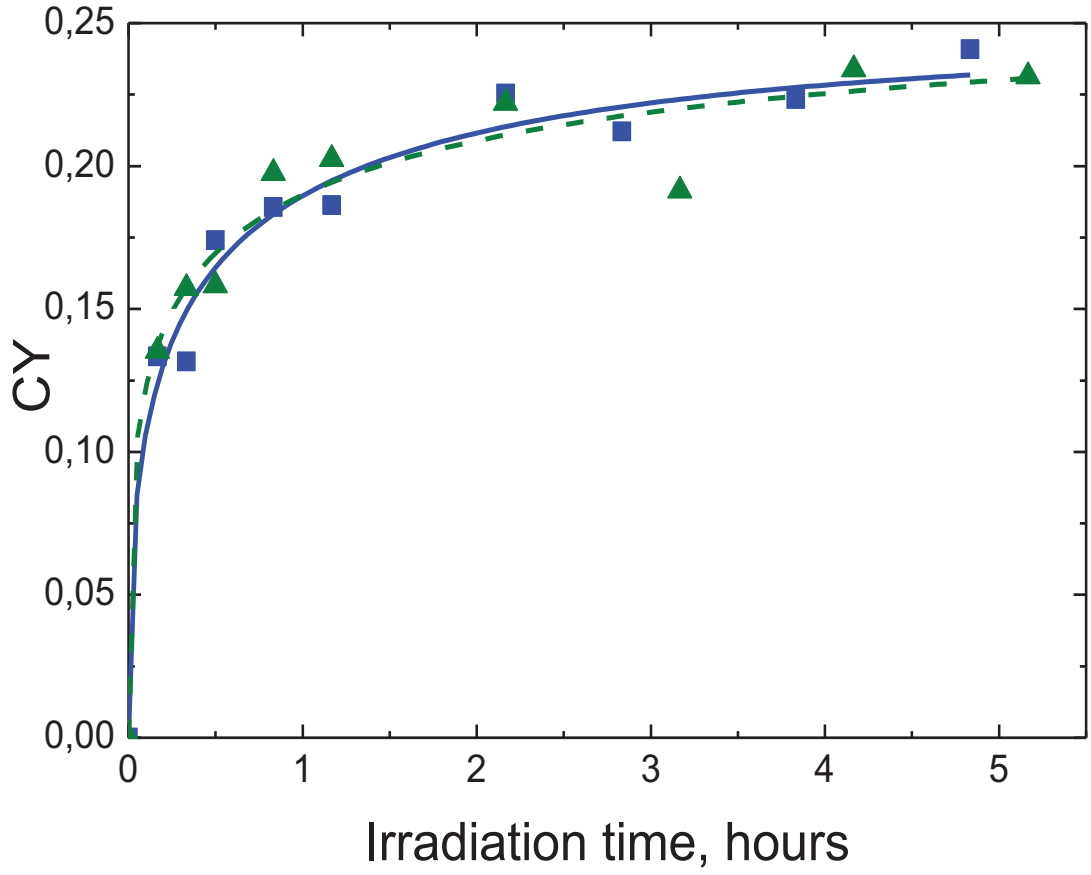

Figure III.14 Polymerization kinetics of HEMA at pressure of 0.7 GPa for laser intensities 0.12 (■) and 2 (▲) kW/cm^2 (λ = 488 nm). Fits of PY with Avrami equation for laser power densities 0.12 (solid line) and 2 kW/cm^2 (dashed line).

The experimental kinetics coincides, which reflect parameters of the Avrami model reported in Table III.2. This experiment shows that the rate constant, *k*, is independent of laser intensity, which is a strong indication of one-photon transitions.

III.5. Conclusions

In conclusion, we observed the HP-induced polymerization of 2-(hydroxyethyl)methacrylate at RT without the addition of any initiator. Firstly, the polymerization of HEMA at static pressure has been investigated. It has been found that HP induced polymerization process is extremely long (more than 41 days) and conversion yield of the final product does not exceed 38 %. The polymerization kinetics is diffusion-controlled and is explained by a decrease in the activation energy on compression. The HP induced polymerization of HEMA takes place at relatively low pressure (threshold pressure > 0.1 GPa) and ceases above p* ≈ 1.6 GPa. The HP limit p* can be explained by a sudden increase of

viscosity of HEMA leading to the molecular movement restriction. Secondly, we have investigated laser assisted HP-induced polymerization of HEMA. We found that polymerization process accelerates by ∼10 times under laser irradiation at 488 nm and by 30 times under irradiation at 355 nm. Considering the excited-state structure of acrylic and methacrylic acid containing the same chromophore backbone (C=C−C=O) as HEMA we have shown that both photoexcitation processes involve 1-photon transitions toward the low-lying excited states of HEMA molecules. The transitions at 488 nm most probably terminate on the T_1/T_2 triplet states that can be partially allowed at high pressures. At shorter wavelengths, participation of the singlet S_1/S_2 states cannot be excluded with subsequent energy conversion to the triplet states.

Chapter IV: Polymerization of 2-(hydroxyethyl)methacrylate by a high pressure ramp process

IV. Polymerization of 2-(hydroxyethyl)methacrylate by a high pressure ramp process

IV.1. Introduction

In previous chapter we have discussed the HP induced polymerization of HEMA at RT without addition of any initiator. Two different approaches of HP induced polymerization of HEMA were investigated. Firstly, the polymerization of HEMA at static pressure was found to be a very long process (more than 41 days) with low efficiency (conversion yield of the final product does not exceed 28 %) (section III.4.1). The polymerization was observed in a limited range of pressures ranging from 0.1 to 1.6 GPa. Above the pressure threshold value 1.6 GPa, no polymerization occurred possibly due to the glass transition of HEMA. Secondly, the laser-assisted HP induced polymerization of HEMA was also investigated. We found that the reaction rate of polymerization process was multiply by 10 times under laser irradiation at 488 nm and by 30 times under irradiation at 355 nm (section III.4.2). The polymerization of HEMA at static pressure and under irradiation at 355 nm appeared to be a very efficient (conversion yield of the final product after 30 min of irradiation is approximately 80 %). Both discussed approaches can be considered as appropriate methods for polymerization of HEMA. The situation is more complicate in the case of pHEMA-TiO_2 hybrid materials because these materials are photosensible under UV irradiation. Therefore, the laser-assisted HP induced polymerization cannot be applied for the fabrication of pHEMA-TiO_2 hybrids. For that reason one of the main tasks of our work was to find a pure HP alternative approach for fast elaboration of pHEMA-TiO_2 hybrid materials.

In this chapter we show that polymerization of HEMA is proceeded with the aid of a new High Pressure Ramp (HPR) process without photochemical or thermal activation of an initiator. The recovered product is similar to pHEMA synthesized by conventional processes. Besides its high efficiency, the main advantage of HPR polymerization is the creation of long polymer chains in a very short reaction time (few minutes). This is significantly faster compared to the polymerization process under static high pressure [7, 9, 45, 79, 135].

The presentation of the results is organized as follow. We first discuss the behavior of the initially liquid HEMA under increasing pressures from 0 to 12 GPa. From the evolution of their Raman spectra, we show that no phase transitions or polymerizations occur under these conditions. Then we evidence that under decompression from high to ambient pressure, the polymerization of HEMA occurs below a pressure threshold. We analyze the efficiency of this HP-induced reaction as a function of the pressure. The characterization of recovered samples by means of gel permeation chromatography is presented. In “discussion” part we present a possible

scheme of reaction pathway explaining the observed polymerization of HEMA under HPR process. We also compare this new approach with the laser assisted HP polymerization presented in Chapter III. Finally we explain why the HPR could extend the application field of HP induced reactions to a new class of monomers.

IV.2. Experimental details

IV.2.1. Diamond anvil cell

The symmetric diamond anvil cell (DAC) used in these experiments, has been described in details in section II.2. Liquid HEMA (purity >99%, Aldrich) without further purification was loaded in a hole of 150 µm in diameter drilled in a preindented metallic gasket and compressed in a symmetric diamond anvil cell (DAC). The polymerization reaction has been probed in-situ by means of Raman spectroscopy using a HR800 spectrometer described in section II.3.2.

IV.2.2. Bridgman anvil system

Sample analysis by chromatography requires about 1 mg of material which is well beyond what can reasonably be produced with a DAC. To produce bigger samples we used a Bridgman anvil system described in section II.2.2. Liquid HEMA was loaded in a hole of 1 mm in diameter drilled in a stainless steel gasket (thickness is 250 µm) and compressed in a symmetric opposed anvil system. The pressure to the opposed anvil system was applied by the commercial tensile and compression press (Instron 1195). Samples were compressed up to 7.5 GPa and immediately decompressed down to 0.5 GPa where they were kept for 10 minutes. As a result, the pHEMA solid samples with the diameter of 800 µm and a thickness of 120 µm were obtained.

The molecular weight and polydispersity of the polymeric chains were measured with Gel Permeation Chromatography (GPC) method discussed in section II.3.1.

IV.3. Evolution of HEMA under compression and decompression

In this section we discuss the behavior of the initially liquid HEMA under increasing pressures from 0 to 12 GPa. From the evolution of their Raman spectra, we show that no phase transitions or polymerizations occur under these conditions. Then we evidence that under decompression from high to ambient pressure, the polymerization of HEMA occurs below a pressure threshold. We analyze the efficiency of this HP-induced reaction as a function of the pressure.

IV.3.1. HEMA under compression from ambient pressure up to 12 GPa

The Figure IV.1 shows, the Raman spectra of HEMA upon compression from ambient pressure up to 12 GPa. All Raman vibration bands become stiffer and broaden with increased pressure. The energies shift of the observed Raman modes as function of pressure are shown in Figure IV.2 and the corresponding pressure dependence, i.e. dv/dP values, are listed in Table IV.1 which has been already presented in section III.2.

The progressive bands broadening and merging, as well as the depletion of most of the Raman modes, are an indication of a structural disorder induced by pressure in HEMA. Actually, except for bands at 947, 600 and 1710 cm^{-1}, all Raman bands undergo a linear stiffen, with a similar rate dv/dP, when the pressure is increased. This set of results, together with the absence of new vibrational bands in the whole range of pressures studied, suggests that HP does not induce any transition to a hypothetical crystalline solid phase of HEMA below 15 GPa. More probably, the increase of pressure results in a densification of HEMA, which leads to a liquid or solid amorphous state. The non-linear stiffen of both skeleton vibration modes at 600 cm^{-1} and 947 cm^{-1} below 6 GPa, could convey this progressive densification of the whole environment. The frequency evolution of the band at 1710 cm^{-1} is more delicate to discuss because it is indeed a doublet of lines assigned to the stretching vibrations of free and hydrogen-bounded carbonyl group (C=O). We notice that the pressure dependence factors dv/dP are of similar magnitude to those reported for acrylic acid under compression [66]. Nevertheless, in acrylic acid the variations were not uniformly linear because of the several phase transitions occurring in the range of pressures under consideration (1-10 GPa).

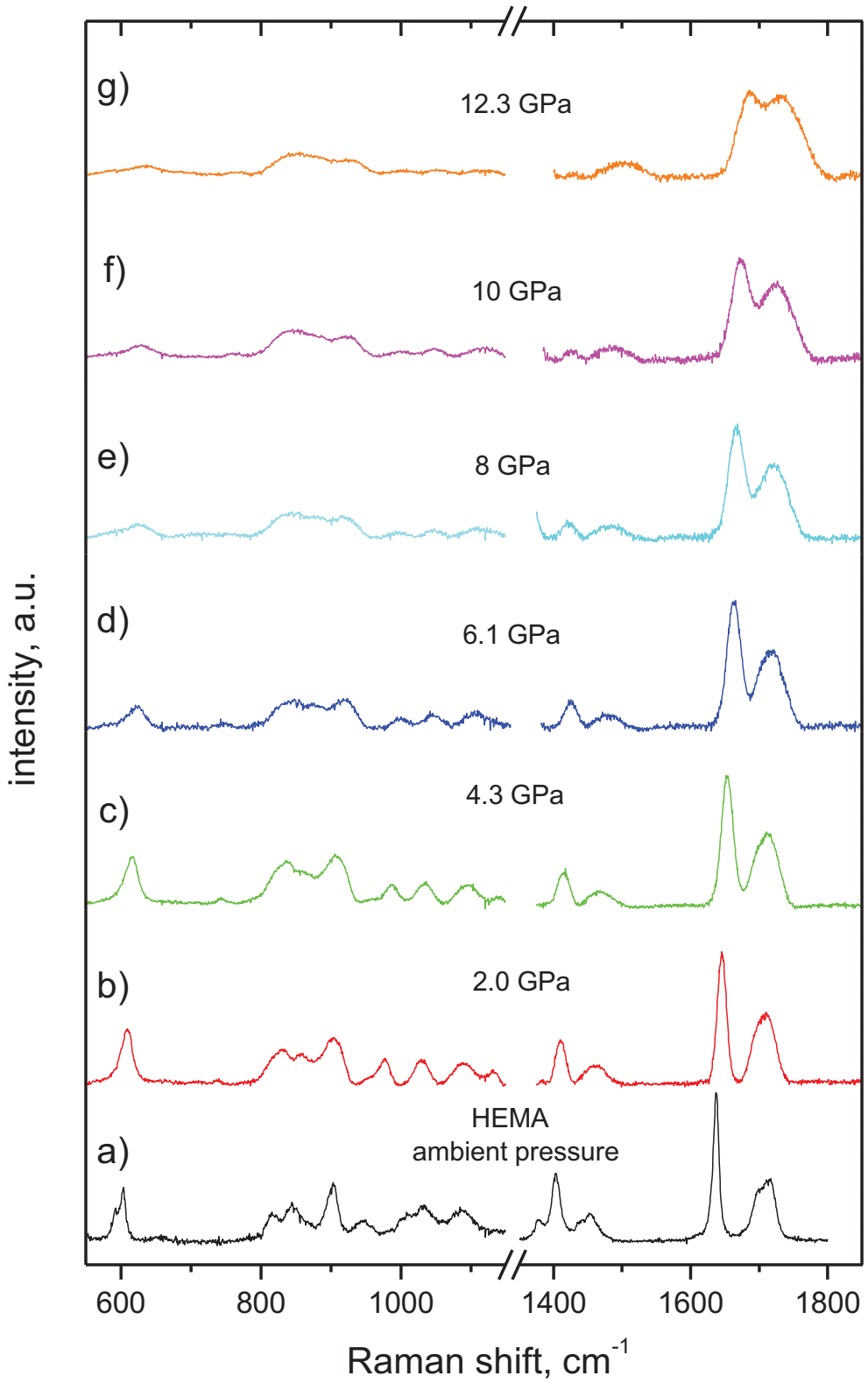

Figure IV.1 Raman spectra of HEMA at selected pressures upon compression from ambient pressure to 12 GPa.

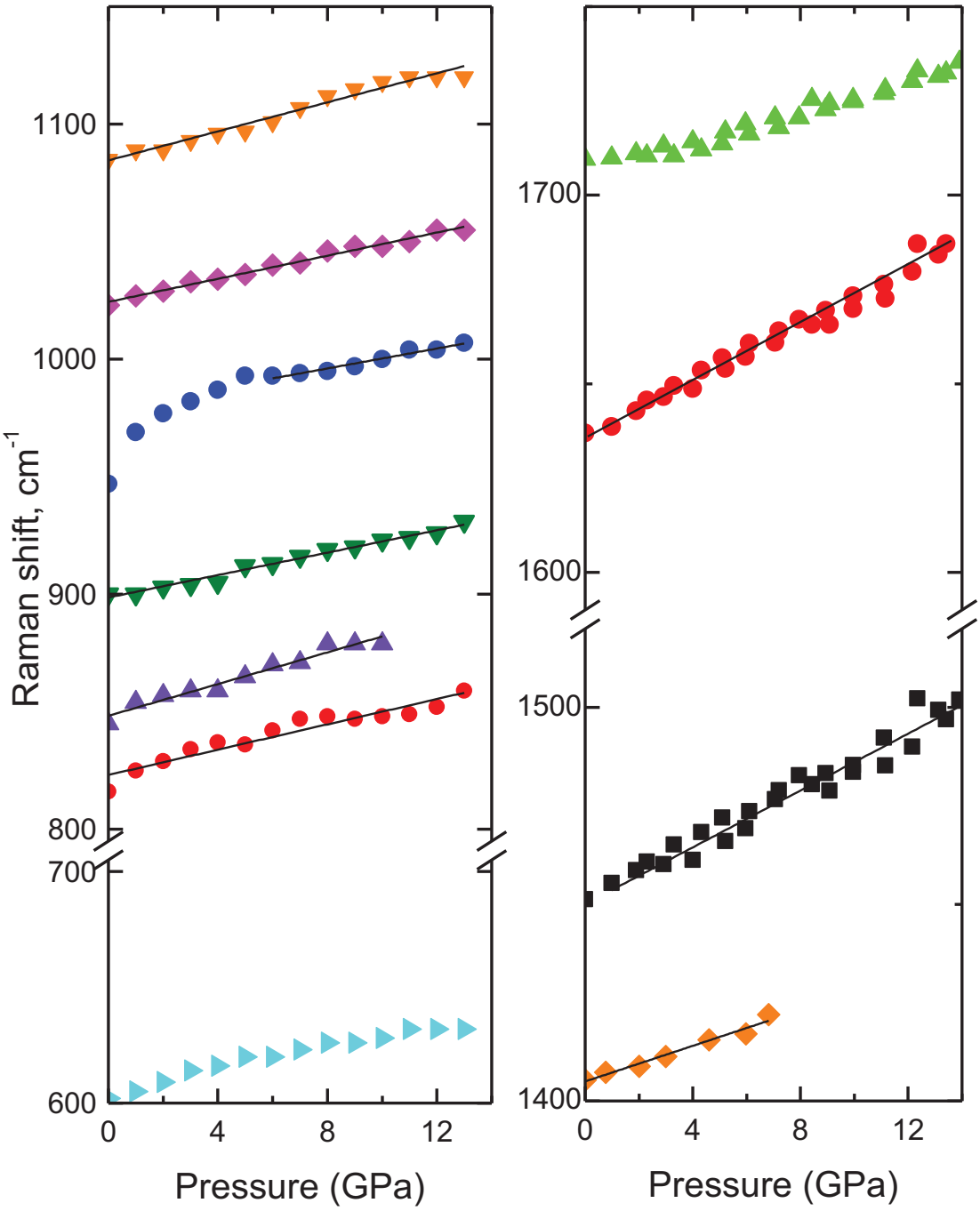

Figure IV.2 Raman shift of HEMA as a function of pressure on compression. Solid straight lines are linear fits of the data.

Table IV.1 Energies and assignments of the bands observed in Raman spectra of HEMA at ambient pressure. Here ν is the bond stretching, δ the bending, ω the wagging, γ the rocking and τ the torsion.

Raman shift (cm^{-1})	$d\nu / dP$ (cm^{-1}/GPa)	Assignment
600	Non linear	$\nu(CCO)_{sym}$ [125] or $\delta(O-C=O)$ [126]
816	2.7	$\tau(C=C)$ [127], $\nu(COC)_{sym}$ [125], $\omega(C=O)$ [126] or $\nu(C-CH_3)$ [128]
845	3.1	$\gamma(CH_2)$ [125] or $\nu(C-C)$ [126, 127]
900	2.4	$\nu(CO)$ [125]
947	Non linear	deformation localized on OCH_2CH_2OH part of the HEMA molecule
1023	2.5	$\nu(CC)$ [125]
1085	3.1	$\gamma(CH_2)$ [126, 127]
1404	2.3	$\nu(C=CH_2)$ [126, 127]
1455	3.6	$(C-CH_2)$ deformation [129, 130]
1640	3.6	$\nu(C=C)$ [125-127]
1705		$\nu(C=O)$ [125-127] free
1714		$\nu(C=O)$ [125-127] H-bounded

Raman spectra plotted in Figure IV.1 also indicate that no polymerization occurs during compression of HEMA. Indeed during the polymerization reaction of unsaturated monomers, C=C double bonds are broken while C-C single bonds are formed. Raman spectroscopy is therefore well suited for the in situ analysis of this kind of reactions by monitoring the decrease in the intensity of the bands of reactants or the increase in the intensity of new bands related to the products. As it has been discussed in Chapter III, in the case of HEMA, as the polymerization reaction progresses, the characteristic C=C vibrations of the monomer, at 1404 and 1640 cm^{-1}, decrease in intensity while the C–CH_2 band at 1452 cm^{-1} grows in intensity due to the growth of the polymer chain. This is not what we observed when we submit HEMA to increasing static pressures (Figure IV.1). It has been shown in Chapter III that C=O bond is not involved in the polymerization process, therefore the intensity of the C=O stretching band at 1710 cm^{-1} is used to normalize the intensities of other Raman bands. We actually observed a decrease in intensity of bands related to C=C vibrations (1404 and 1640 cm^{-1}). On the other hand, the relative intensity of the C–CH_2 band (1455 cm^{-1}) does not appear to grow with the increase of pressure. This remains true even if the sample is held under high pressure for several days. We therefore concluded that there is no HP-induced polymerization when HEMA is compressed in the range of pressures from 2 to 15 GPa. Moreover, if the sample under pressure is promptly decompressed to ambient pressure, the recovered sample is liquid and its Raman spectrum is similar to the spectra of HEMA recorded before compression.

We assign the decrease in intensity of the C=C vibration bands observed in Figure IV.1, to a HP-induced deformation of HEMA molecule and a modification of its electronic structure, leading to the thermal population of the triplet T_1 state. Indeed, with increasing pressure, the increasing overlap between electronic orbitals, gives rise to a mixing of the ground and excited states. The resulting interplay between energy surfaces makes the thermal excitation of excited electronic states feasible [32, 37, 44]. In section III.4.2 from the excited-state structure of acrylic and methacrylic acid based on the same chromophore backbone (C=C−C=O) as HEMA we have schemed the electronic structure of HEMA [140, 141]. At ambient pressure, the first excited state is a triplet state T_1 ($^3\pi\pi^*$) in which higher lying excited states efficiently relax due to strong intersystem crossing. In this triplet state the electron excited in the π^* orbital elongates the C=C double bond, conferring to it a single bond character. Thereby, the progressive decrease of the C=C vibration bands with the growth of pressure (Figure IV.1), could conveys the deformation of HEMA molecule in a configuration close to the T_1 state i.e. the population of the T_1 state.

IV.3.2. HEMA under decompression from 8 GPa down to ambient pressure

The previous results showed that the compression of HEMA up to 12 GPa does not lead to polymerization. Under HP, high energy barriers confine molecules in fixed positions and their residual mobility is limited to small vibrations whose amplitude depends on temperature. In these conditions the chemical reactivity must comply with the environment. Actually, we have discovered that HEMA can polymerize in a two-steps high pressure ramp (HPR) process. An example of this kind of experiments is presented in Figure IV.3. The sample is first compressed up 8.3 GPa and then decompressed step by step down to the atmospheric pressure. The corresponding Raman spectra in the energies range 1375 – 1850 cm^{-1} are shown in Figure IV.3. During the decompression process from 8.3 to 2.5 GPa the evolution of Raman spectra is rather smooth. All bands exhibit a softening. Moreover, the relative intensities of the bands related to the vibrations of the C = C double bond (1404 and 1640 cm^{-1}) slightly increase, reflecting a decrease in the proportion of HEMA molecules in the triplet T_1 excited state. In contrast at lower pressures, 0.52 and 0.3 GPa, the changes observed in Raman spectra are more striking. Compared to the reference band at 1710 cm^{-1} ($\nu(C=O)$), the relative intensities of bands associated with the C=C vibrations now decrease, while the band associated to C–CH_2 deformation (1455 cm^{-1}) grows in intensity. Both together, these observations are a clear signature that polymerization of HEMA monomers occurs during the decompression process. The transformation is irreversible and the Raman spectrum of the recovered sample (Figure IV.3g) is similar to that of pHEMA synthesized by free-radical polymerization.

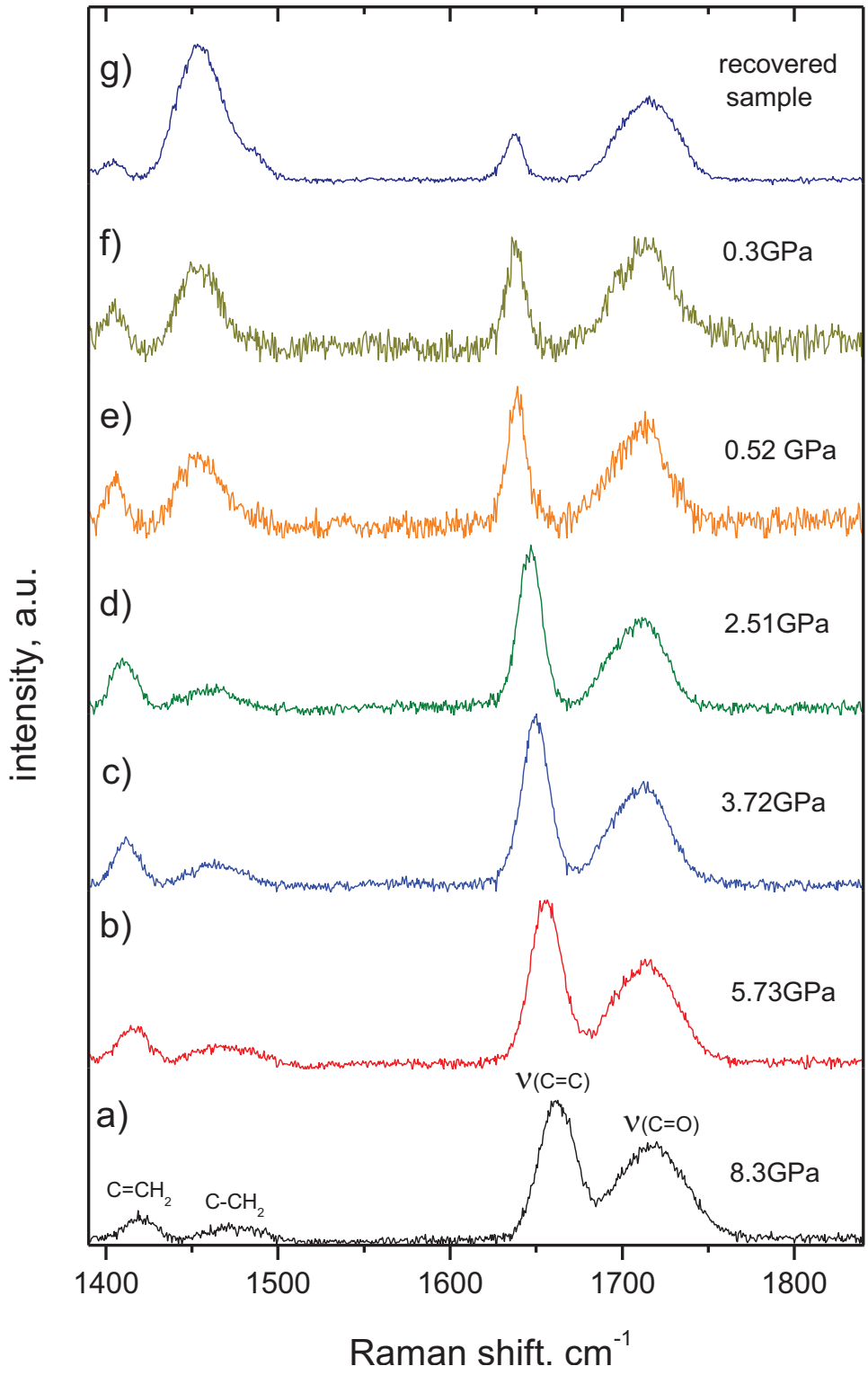

Figure IV.3 : Raman spectra of HEMA at selected pressures upon step by step decompression from 8 GPa to ambient pressure.

IV.4. High pressure ramp induced polymerization of HEMA

IV.4.1. Efficiency of polymerization process

We have analyzed in details the conditions in which the polymerization reaction occurs under decompression. It appears that the process is controlled by at least two important

parameters. The first one is the pressure p_1 at which the sample is initially compressed. The second is the pressure $p_2 < p_1$ at which the sample is decompressed. The influence of both parameters has been measured from the conversion yield (CY) of the recovered sample defined according to the expression given in section III.3:

$$CY(t) = 1 - \frac{(I_{C=C}/I_{C=O})_t}{(I_{C=C}/I_{C=O})_{t=0}}, \qquad (5.1)$$

where $I_{C=C}$ and $I_{C=O}$ are respectively the area of ν(C=C) and ν(C=O) Raman bands. In order to obtain a maximum of insights about the polymerization induced by HPR, we did different kind of experiments which are described below.

In a first series of experiments, the sample is compressed to pressures p_1 ranging from 2 to 13 GPa, before to be quickly decompressed down to the pressure p_2 = 0.5 GPa. The sample is kept at the pressure p_2 for 5 min and then is recovered at the ambient pressure. The CY of the recovered sample as function of the initial pressure p_1 is plotted in Figure IV.4.a. A new threshold is observed at the pressure p^*_1 = 6.5 GPa. Below this threshold, the CY of the recovered sample is less than 20 %. In contrast, if the sample is initially compressed above p^*_1 the CY of the recovered sample can reach 90 %. The star in Figure IV.4a, corresponds to a slightly different experiment: the sample is first compressed at 9.5 GPa then decompressed to 2.5 GPa and maintained at this pressure for 24h. After this time the sample is decompressed to 0.5 GPa for 5 min. The CY of the recovered sample reaches 89 %.

In a second kind of experiments, the initial pressure p_1 is fixed at 7 GPa, while the pressure p_2 of the decompression step, at which the samples are kept for 5 min, is changed from 2.4 to 0 GPa. The CY of the recovered samples as function of the pressure p_2 are plotted in Figure IV.4.b. The CY attains a maximum at $p_2 \sim$ 0.4 GPa and progressively decrease when the pressure increases. It is null at p^*_2 = 2 GPa and higher. Moreover if the sample is directly decompressed to the ambient pressure (p_2= 0 GPa) the recovered sample is liquid and non-polymerized.

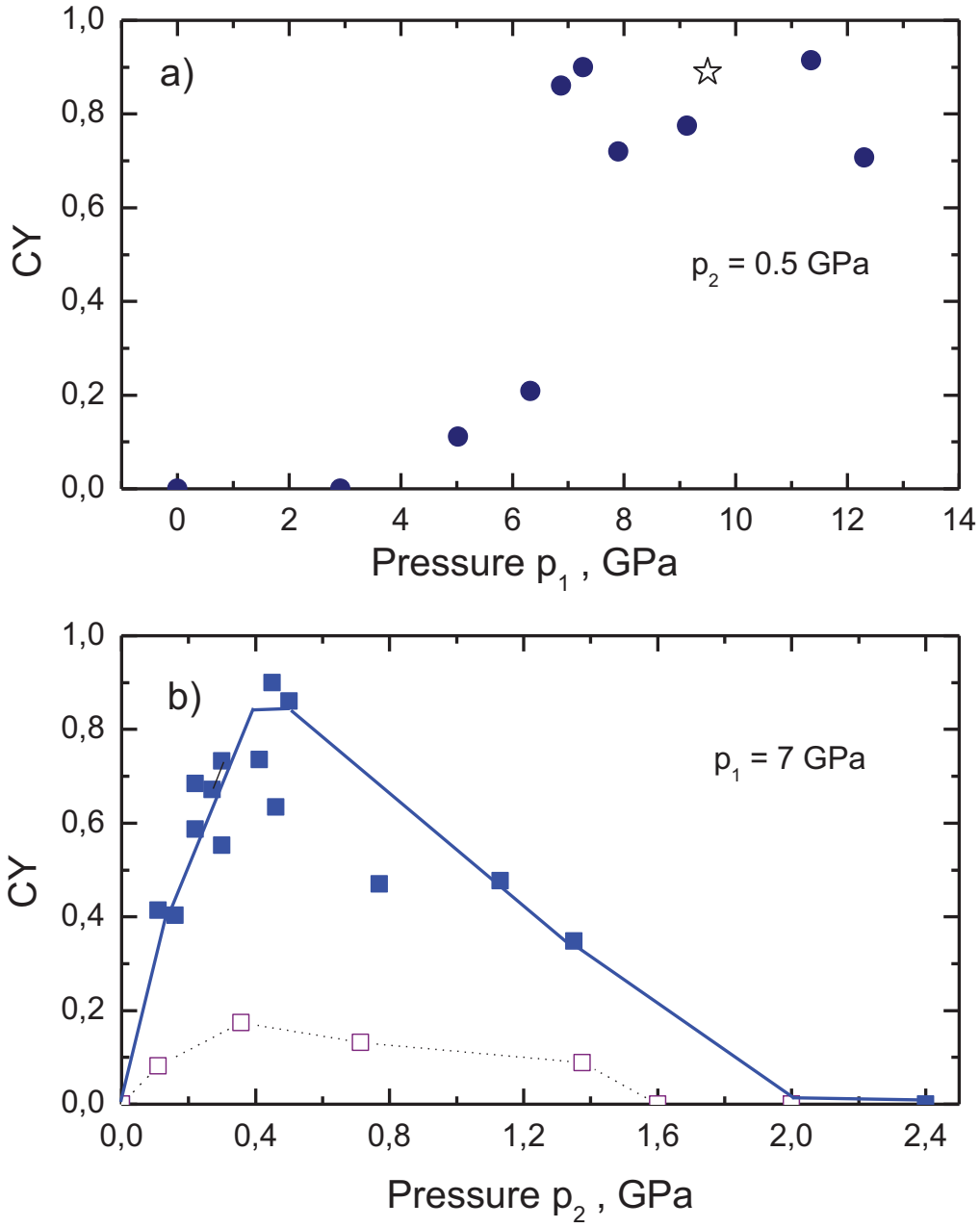

Figure IV.4 Evolution of pHEMA polymerization yield as function of the compression pressure (p_1) and decompression pressure (p_2) in which the sample is held for 5 min before to be recovered. (a) The decompression pressure is p_2 = 0.5 GPa. (b) The compression pressure is p_1 = 7 GPa. The open squares show the CY of freshly recovered samples after 19 hours under different static pressures (see section III.4.1).

We finally did a last kind of experiment. The sample is first compress up to 9 GPa then the DAC is open in order to quickly decompressed the sample to ambient pressure and finally the sample recompressed to 0.5 GPa for 5 min before to be recovered. If the experiment is conduct in air no polymerization is observed. On the other hand if the DAC is open and re-closed inside a

glove box to avoid contamination of the sample by air humidity, the recovered sample exhibit a CY of 70%.

This set of experimental results clearly evidence that (i) a compression above 6.5 GPa is a mandatory condition to initiate the polymerization, (ii) the polymerization occurs in a limited range of pressures, (iii) the initiators of polymerization created under compression above 6.5 GPa have a long lifetime inside the DAC, (iv) these initiators disappear in contact with air humidity. This seems to indicate that they are radical in nature and can be annihilated by H atoms abstraction from H_2O. Moreover, we have observed that the delay between the two steps of the HPR, does not influence on the CY of the recovered sample. Thereby, the HPR appears to be an efficient method of polymerization leading, with a high efficiency, to recovered products a priori similar to pHEMA synthesized by more conventional process based on thermal- or photo-initiators. Besides its high efficiency, a main advantage of the HPR is the very short time of the reaction. Indeed, the recovered samples are obtained in 5 minutes while reaction times ranging from few hours to several days are usually reported when the polymerization is induced under compression only [7-9, 79, 135].

IV.4.2. Characterization of HPR synthesized pHEMA by Gel Permeation Chromatography

In order to answer the question about the nature of active species that survive the pressure ramp and trig the polymerization we have analyzed recovered pHEMA samples with Gel Permeation Chromatography (GPC). Larger volume samples (mass ≈ 1 mg) have been obtained from the Bridgman anvil system. The liquid HEMA was compressed up to 7.5 GPa before being decompressed at p_2 = 0.5 GPa and kept at this pressure for 10 minutes. The Raman analysis of the recovered samples showed that their CY reaches 90 %, as already observed when using DAC equipment. It is worth to remark that although the volume of the samples is 100 times higher than those obtained with the DAC, the time the samples have to be maintained under decompression pressure p_2 is the same. These recovered samples have been dissolved in tetrahydrofuran (THF) in an ultrasonic bath for 2 hours. Despite this procedure, the dissolution was not total and some pieces of solid polymer were still present in the solution. This fact evidences the formation of long polymer chains with high molar mass. The measured chromatograms of liquid HEMA and that recovered after HPR process are shown in Figure IV.5. The HEMA monomers (130 g/mol) are observed at 9.96 min. The peaks of molecular weights 394, 545 and 676 g/mol were respectively assigned to oligomers formed of 3, 4 and 5 monomers. Because of the non-complete solubility of the recovered sample, relative intensities of the GPC peak of heavy oligomers and polymers underestimate their real populations. Most present are the shoulder at 7-8 min that corresponds to chains with the molecular weight of 2000-4000 g/mol

and the peak at 5 min due to heavy polymers with the weight 45000 g/mol. The GPC analysis demonstrates that HPR process results in the rapid polymerization of HEMA without sacrificing the polymer chain length.

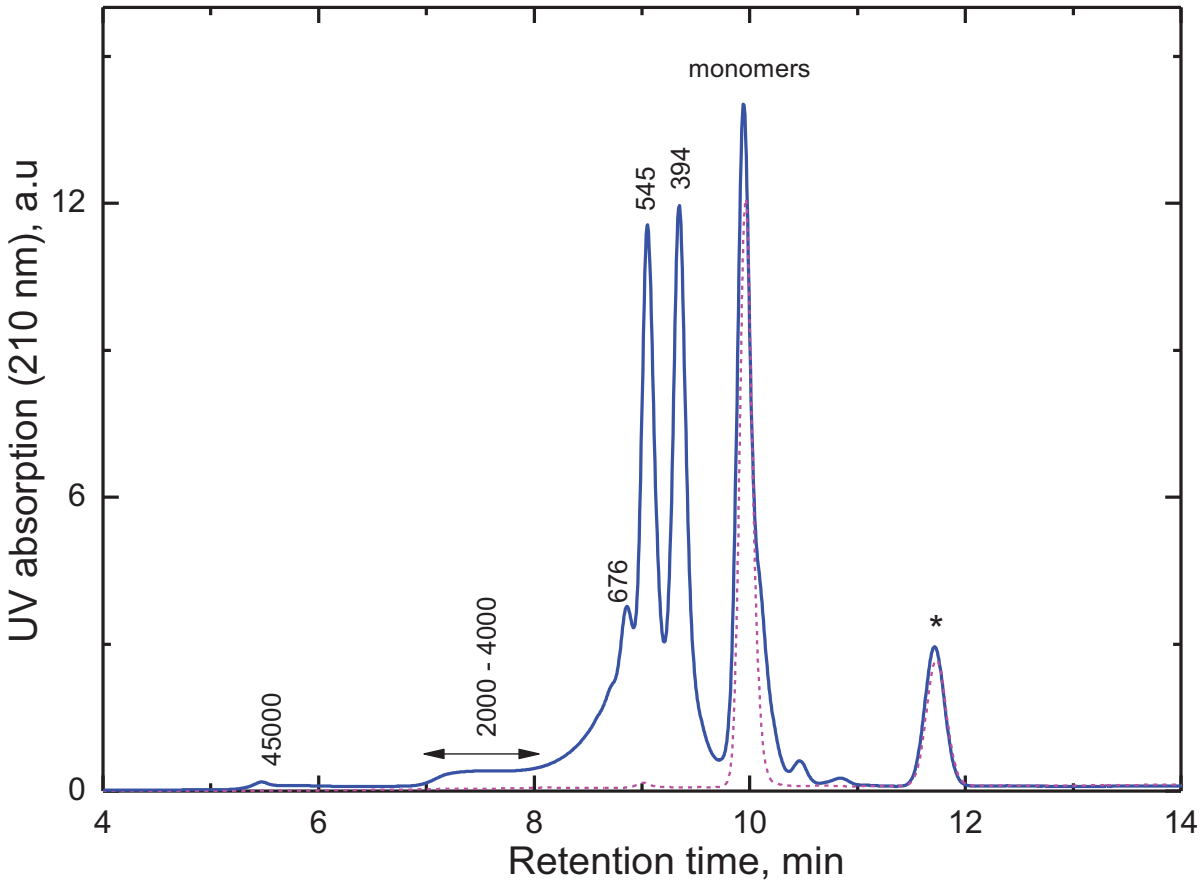

Figure IV.5 Gel permeation chromatogram of pHEMA synthesized by a HPR process. Molecular weights are indicated in g/mol. The chromatogram of liquid HEMA before HP treatment is shown by a dot line. The peak marked by symbol ∗ belongs to THF impurities.

The GPC analysis shows the remarkable absence of HEMA dimers in the recovered sample, which signifies their preferential consumption in course of the polymerization process. This is however only possible if these dimers are radical species that trigger the reaction. The biradicals $HEMA_2^{\bullet\bullet}$ can be spontaneously produced at the first step of compression at pressures above 2 GPa in the amorphous solid-like HEMA. These biradicals can react when they leave from the fixed positions at pressures below 2 GPa. As a consequence, the terminated species in the polymerized samples can be $HEMA_n$ species with $n > 2$. The formation of biradicals in excited triplet state as initiators of polymerization has been previously proposed by Lingnau *et al*. [143-146] and recently confirmed with quantum chemistry calculations [147], to explain the spontaneous polymerization of methyl methacrylate at high temperatures and

ambient pressure. The formation of excited biradical dimers has been also suggested to explain the polymerization of small hydrocarbon monomers under high pressures [81, 83].

IV.5. Discussion

In this section we present a possible scheme of reaction pathway explaining the observed polymerization of HEMA under HPR process. We also compare this new approach with the laser-assisted HP induced polymerization discussed in Chapter III. Finally we explain why the HPR could extend the application field of HP induced reactions to a new class of monomers.

IV.5.1. The mechanism of high pressure ramp induced polymerization of HEMA

The evolution of chemical reactions under HP is ruled both by the electronic structure of the reactants, and by the energetic and diffusive properties of the whole environment. This is why, when the density of the system is increased, a competition may happen between the different mechanisms involved in the chemical reaction. On the one hand, the energy brought to the system by the compression can be sufficient to initiate the reaction. On the other hand, the constraints induced by the environment can prevent the movements the molecules must undergo to react or even impedes the accommodation of the reaction products. These points are of particular importance when the reactions take place in amorphous solid or liquid states. Indeed, in these cases, the influence of environment on the diffusion of the reacting species is more delicate to understand than in crystalline solids phase where the positions and orientations of reactants are known and, in some specific cases, can promote the reaction.

The polymerization of HEMA proceeds via an addition reaction composed of three different steps: initiation, propagation and termination. The initiation stage usually requires the production of a free radical which subsequently reacts with the C=C double bond of a monomer to form a new radical specie. This active center reacts in turn with a new monomer, thereby allowing the propagation of the polymer chain. Moreover, since HEMA molecule has only one C=C double bond, the polymer chains grow linearly without cross-linking. Consequently, the polymerization process requires a significant mobility of the monomers in order to fit the growing chain. According to our results, it seems possible to completely dissociate and delay in time the first two stages of the polymerization reaction. In the first step, when the sample is compressed, initiators of polymerization are formed. In the second step, when the sample is decompressed, the molecules are free to undergo a steric rearrangement allowing the growing of the polymer chain. With this in mind, we now discuss a possible reaction pathway explaining the efficient polymerization of HEMA under the HPR.

The energetic scheme of HEMA modifications in course of HPR process is depicted in Figure IV.6 for the relevant pressures of the first ($p_1 \geq 6.5$ GPa) and second ($p_2 < 2$ GPa) stages.

The reaction pathway we propose, represented by an arrow, is based on the formation of an excited biradical $(HEMA)_2^{\bullet\bullet}$ at pressure p_1 and the subsequent propagation of the polymer chain at pressure p_2. The main features of this mechanism are the following:

1. The increase of pressure reduces the energy gap between the occupied π(HOMO) and unoccupied π^*(LUMO) allowing the population of the excited states [32, 36, 148]. Consequently, some HEMA molecules can be found in the T_1 ($^3\pi\pi^*$) triplet state, which is characterized by the double bond opening. The reversible decrease of the C=C bond intensity in Raman spectra validates this conclusion (Figure IV.1).

2. At pressures $p_1 \geq 6.5$ GPa, favorably oriented excited monomers HEMA(T_1) react with other monomers to form metastable activated biradical $(HEMA)_2^{\bullet\bullet}$, which are stables at any pressure but disappear in contact with atmospheric humidity. Dimerization occurs when the intermolecular distance becomes short enough to make the system unstable [81, 83, 148], which corresponds to the threshold pressure of 2 GPa, and completes at $p_1 \geq 6.5$ GPa, as validated experimentally. The reaction of the biradical is prohibited: (i) at pressures above 2 GPa by its steric confinement in the amorphous phase of HEMA and (ii) at low pressures below 0.1 GPa by its limited reactivity.

3. The liquid phase of HEMA is recovered at pressures p_2 below 2 GPa. The decrease of energy barriers (Figure IV.6) releases the biradicals from their fixed positions. Consequently the reactions of $(HEMA)_2^{\bullet\bullet}$ with monomers are no longer sterically hindered:

$$HEMA_2^{\bullet\bullet} + nHEMA \xrightarrow{0.1 \leq p_2 \leq 2\ GPa} HEMA_{n+2} \qquad (5.2)$$

As a result of (5.2), the formation of all oligomeric species except for $HEMA_2$ is allowed.

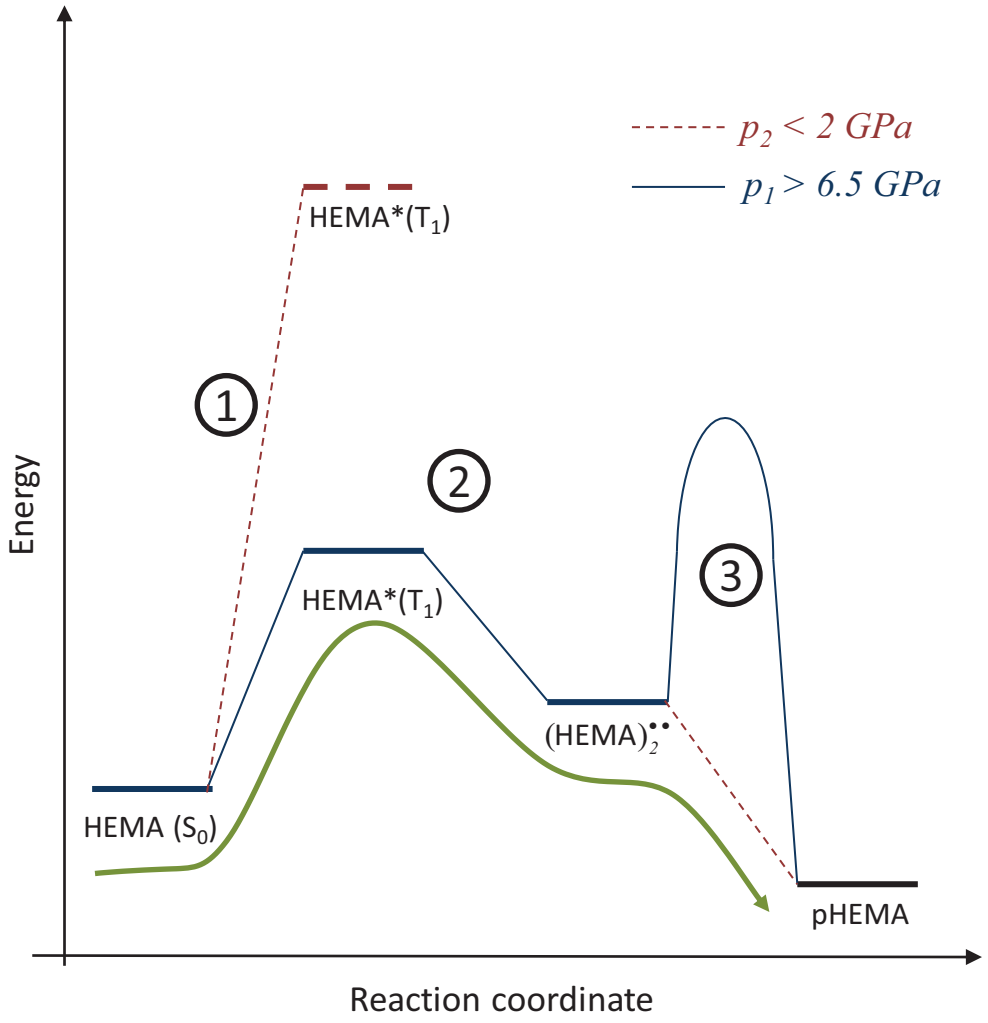

Figure IV.6 Energy diagram of HEMA in course of HPR polymerization process.

IV.5.2. Comparison of a high pressure ramp approach with static HP- and laser assisted HP-induced polymerization processes.

The model presented in Figure IV.6, in particular the formation of dimers as seeds for further polymerization and the influence of steric factors on the reaction mechanism, can be supported both by molecular dynamic simulations and previous experiments about polymerization of HEMA under static HP. Bernasconi *et al*. have analyzed the solid state polymerization of acetylene under HP [81]. They found that the reaction was initiated by molecules distorted in a geometry closely resembling to that of molecules in the T_1 triplet state, and showed that the first step of the reaction was the formation of a biradical dimer $(C_2H_2)_2$ when monomers are sufficiently close. More recently, Mugnai *et al*. have confirmed this general scheme in the cases of propene, ethylene and butadiene [83, 148, 149]. Moreover they underlined the efficiency of intramolecular charges separation processes under HP. They

concluded their analysis by ruling out the radical mechanism of polymerization and suggested that the polymerization results from an ionic collective mechanism leading to formation of dimers and further to oligomers. On the other hand Cittroni *et al.* proposed the formation of diradicals to explain the polymerization observed in butadiene crystal submitted to HP [88]. In the case of HEMA our results do not allow to conclude about the radical or ionic nature of the polymerization process under HP. Actually both polymerization mechanisms may happen. The charges separation is a common response of a molecular system to pressure since this ensure a closer packing of molecules [150]. Therefore the formation of $HEMA_2$ dimers which proceed at pressure $p_1 > 6.5$ GPa, could be ionic in nature. On the other hand, the subsequent growing of polymer chain at lower pressure $p_2 \approx 0.4$ GPa could results from radical reactions.

In chapter III we have reported the polymerization of HEMA under static compression without decompression step. The reaction was very slow, not completed even after a month, and poorly efficient since the polymerization yield of the recovered sample remained below 40 %. In addition, the process was only observed in a very limited range of pressures ranging from 0.1 to 1.6 GPa. These observations can be explained in the frame of the scheme described on Figure IV.6. For the sake of the discussion, the CY of recovered samples obtained after 19 hours under static compression at different pressures have been added in Figure IV.4 b (open squares). The series obtained after static HP and HPR process show the similar pressure dependence of CY with the maximum at about 0.5 GPa and vanishing at pressures lower that 0.1 GPa and higher than 1.5 GPa, which suggests similar activation process in both cases. The threshold pressures are respectively related to the energy activation and steric restriction of the reaction kinetics. On the other hand, the faster kinetics and high efficiency of the HPR process are related to the preformed $HEMA_2^{\bullet\bullet}$ biradicals. The high activation energy of HEMA (T_1) triplets makes their direct thermal population of low probability in this range of pressures p_2 (see Figure IV.6).
HP induced polymerization reactions proceed slowly and reaction times ranging from few hours to several days or even weeks are reported in literature. Two approaches are currently used to accelerate these reactions. The first consist in increasing the pressure. However, due to reduction of molecular mobility with the pressure, this approach is limited to monomers in ordered phases in which polymerization do not required strong molecular rearrangement [35, 151]. The photochemical activation is a second approach. It is generally considered as an unavoidable tool allowing to accelerate the reactions and to reduce the pressure threshold required for the reactions to occur [32]. The HPR process is actually an appealing alternative to the photoactivation.

In Chapter III we have also reported the laser assisted HP polymerization of HEMA. We observed that the UV (355 nm) irradiation of the compressed sample under 0.7 GPa improved

the CY of the recovered sample up to 80 % instead of 30 % without irradiation, and accelerated the reaction which proceeds in 30 min instead of a month. These results were explained by assuming that the polymerization of HEMA was mediated by monomers one photon excited in the T_1 triplet state. It is worth to compare these results with those presented in this chapter. Actually the polymerization processes are essentially the same, only the activation process of the reaction changes. The polymerization occurs at pressures below 2 GPa, but is activated by compression in one case and by light in the other. Nevertheless in both cases excited HEMA monomers are created but at different pressures. This explains why the polymerization proceeds more quickly by HPR process since the formation of $HEMA_2^{\bullet\bullet}$ biradicals from excited monomers HEMA* is more efficient at pressures $p_1 > 6.5$ GPa used in the HPR process, than at pressures $p < 2$ GPa required to induce the laser-assisted polymerization process. The HPR process is therefore an alternative to the usual photoactivation of HP-induced reactions and may open new perspectives for industrials applications particularly in the case of the numerous monomers which do not crystallize under HP.

The occurrence of polymerization reactions under HP are ruled by a complex interplay between several factors (i) the stresses induced by the environment (ii) the positions and orientations of molecules (iii) the nature of the intermolecular interactions (iv) the molecular electronic structure [59]. All these factors are pressure dependent and can be modified by thermal or electronic excitation. Therefore obtaining more insights about reaction mechanisms requires being able to separate the contributions of these different factors. This can be a delicate task since the photoactivation or the variations of pressure usually introduce some selectivity in the reaction pathways leading to different kind of recovered products. From this point of view, HEMA could be a model system. Indeed, whatever the polymerization method used, static compression, laser assisted HP induced polymerization [9] or HPR process, the recovered products are similar. They exhibit no crystalline structure and their Raman spectra are identical to the pHEMA obtain at ambient pressure by the usual radical polymerization. A detailed comparison of reaction mechanisms occurring in the different polymerization methods can be therefore envisaged.

IV.6. Conclusions

In conclusion, we have developed an efficient HP-induced polymerization of HEMA at room temperature without addition of any initiator. Firstly the behavior of the initially liquid HEMA under increasing pressures from 0 to 12 GPa has been investigated. Using Raman spectroscopic investigations it has been shown that no phase transitions or polymerizations occur at these conditions. After that we revealed that under decompression from high to ambient

pressure the polymerization of HEMA occurs below a pressure threshold. According to these observations we have proposed and realized a new two-step high-pressure ramp (HPR) induced polymerization process. In the first step the sample is compressed above 6.5 GPa without polymerization. Then during the second step, when the sample is decompressed and maintained below 2 GPa for 5 min, the polymerization takes place. Recovered samples with CY exceeding 90% are obtained and their analysis by the gel permeation chromatography evidences the formation of long polymer chains. In order to explain the polymerization process a theoretical scheme based on the influence of energetic and steric factors has been proposed. It was supposed that i) during the compression step polymerization seeds are formed by the dimerization of HEMA monomers; ii) however, the high pressures hinder the movement of monomers and prevent the growing of the polymer chains; iii) when the sample is decompressed, the geometrical and structural constraints are relaxed and the polymerization occurs.

Thus we consider that the HPR process developed and presented in this chapter is a powerful tool to activate and to control polymerization reactions. Realization of the pure HP process, without using catalysts or light activation, for efficient and fast polymerization opens new perspectives and possibilities for fabrication of pHEMA-TiO_2 hybrid materials with new optical and mechanical properties.

Chapter V: Optical properties of nanoparticulate pHEMA-TiO_2 hybrid materials elaborated using HPR polymerization

V. Optical properties of nanoparticulate pHEMA-TiO_2 hybrid materials elaborated using HPR polymerization

V.1. Introduction

In previous chapter we discussed the efficient polymerization of HEMA at room temperature without addition of any initiator by High Pressure Ramp (HPR) process. Here, we demonstrate that HPR polymerization can also be used for the efficient polymerization of nanoparticulate pHEMA-TiO_2 hybrid materials. After a description of the elaboration process, the first part of the chapter compares the polymerization yield of hybrids polymerized by HPR process or by conventional polymerization using a thermal initiator. The second part is devoted to the investigation of the optical properties of pHEMA-TiO_2 hybrids obtained by HPR polymerization from pump-probe experiments. We analyze the kinetics of the photo-induced darkening as function of the UV irradiation dose; we measure the quantum efficiency of charge separation process as well as the concentration of the trapped electrons on Ti^{3+} centers.

V.2. Experiment

Most of the information regarding the synthesis of liquid HEMA-TiO_2 hybrids and the photdarkening pump-probe experiment has been given in the Chapter II.

V.2.1. Preparation of pHEMA-TiO_2 hybrid materials

Liquid HEMA-TiO_2 hybrid samples are prepared in three steps (section II.1.2): (i) liquid HEMA (purity >99%, Aldrich) is purified by a vacuum distillation, (ii) TiO_2 nanoparticles are synthetized in a homemade reactor using micro-mixing of precursors, (iii) liquid HEMA-TiO_2 hybrid samples with different concentration of nanoparticles (see Table II.3) are finally obtained by solvent exchange.

The liquid HEMA-TiO_2 is then polymerized using the high pressure ramp process discussed in Chapter IV. In practice, liquid HEMA-TiO_2 hybrids is loaded in a hole of 150 µm in diameter drilled in a preindented metallic gasket and compressed above 6.5 GPa in a symmetric diamond anvil cell (DAC). Then the sample is quickly decompressed down to 0.5 GPa and kept for 5 min at this pressure stage before to be recovered at ambient pressure. The conversion yield of polymerization of the recovered pHEMA-TiO_2 hybrid samples is measured by means of Raman spectroscopy using a HR800 spectrometer described in section II.3.2.

V.2.2. Pump-probe photodarkening experiment

The optical properties of pHEMA-TiO_2 hybrids, mainly the UV photoinduced darkening, are analyzed using the pump-probe experiment described in details in section II.3.3. In order to

avoid any interaction between hybrid samples and oxygen (see section I.1.4.1) during each measurement the hybrid samples were kept inside DAC at pressure below 0.1 GPa. In the pump-probe experiment hybrid samples were irradiated by a pulsed UV laser (7 ns, 355 nm) under a fluence of 10 mJ/cm^2; the absorption of the UV irradiated hybrid samples is probed at 640 nm in situ by CW-laser as function of the UV irradiation dose. The experiment is schemed in Figure V.1.

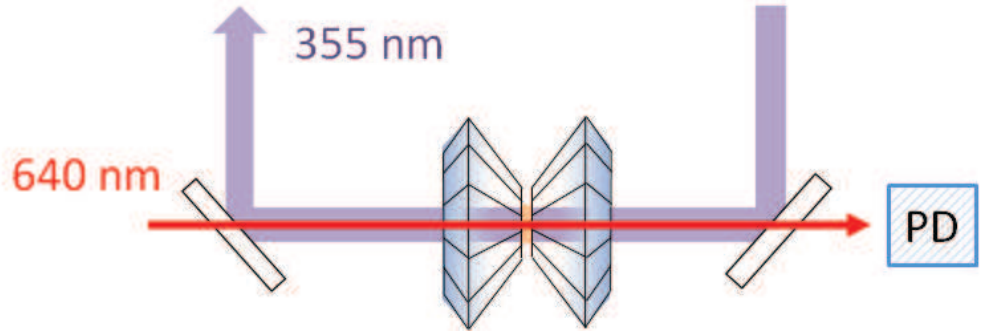

Figure V.1 Scheme of pump-probe photodarkening experiment.

V.3. Fabrication of pHEMA-TiO_2 hybrid materials using HPR polymerization process

V.3.1. Polymerization efficiency of pHEMA-TiO_2 hybrid materials.

The Figure V.2 shows Raman spectra of several samples in the energies range 1375 – 1850 cm^{-1}: the liquid HEMA at atmospheric pressure, the pHEMA obtained by HPR process and pHEMA-TiO_2 hybrid materials with different concentration of nanoparticles prepared by HPR process. The composition of samples under consideration is given in Table V.1. In Chapter III we have shown that the polymerization process can be monitored by the progressive decrease in intensity of the C=C stretching band (1640 cm^{-1}) together with a growing of the C−CH_2 (1455 cm^{-1}) band intensity. This behavior is a result of the double bond opening of the methacrylate group and propagation−elongation of polymer chains. The same behavior is observed in the case of pHEMA-TiO_2 hybrid materials. In Figure V.2 we note that intensities of the C=C and C−CH_2 bands are different according to the TiO_2 nanoparticles concentration in the samples. The conversion yield (CY) of polymerization in each sample is measured from the relation (see section III.3):

$$CY(t) = 1 - \frac{(I_{C=C}/I_{C=O})_t}{(I_{C=C}/I_{C=O})_{t=0}}, \qquad (6.1)$$

where $I_{C=C}$ and $I_{C=O}$ are respectively the area of ν(C=C) and ν(C=O) Raman bands. The calculated CY of polymerization of pHEMA-TiO_2 hybrid materials are also reported in Table V.1. The CY of polymerization decreases when the concentration in nanoparticles increases. In hybrids with smallest titanium concentration (hybrid x2) the CY is equal to ≈94 %. This value does not differ from the CY of pHEMA obtained by HPR process (see section IV.4). However for higher titanium concentrations ($C_{Ti} \geq 1.5$ M) the CY significantly decreases and reaches a minimum value of 11 % in hybrid samples with titanium concentration equal to 5.84 M (hybrid x40).

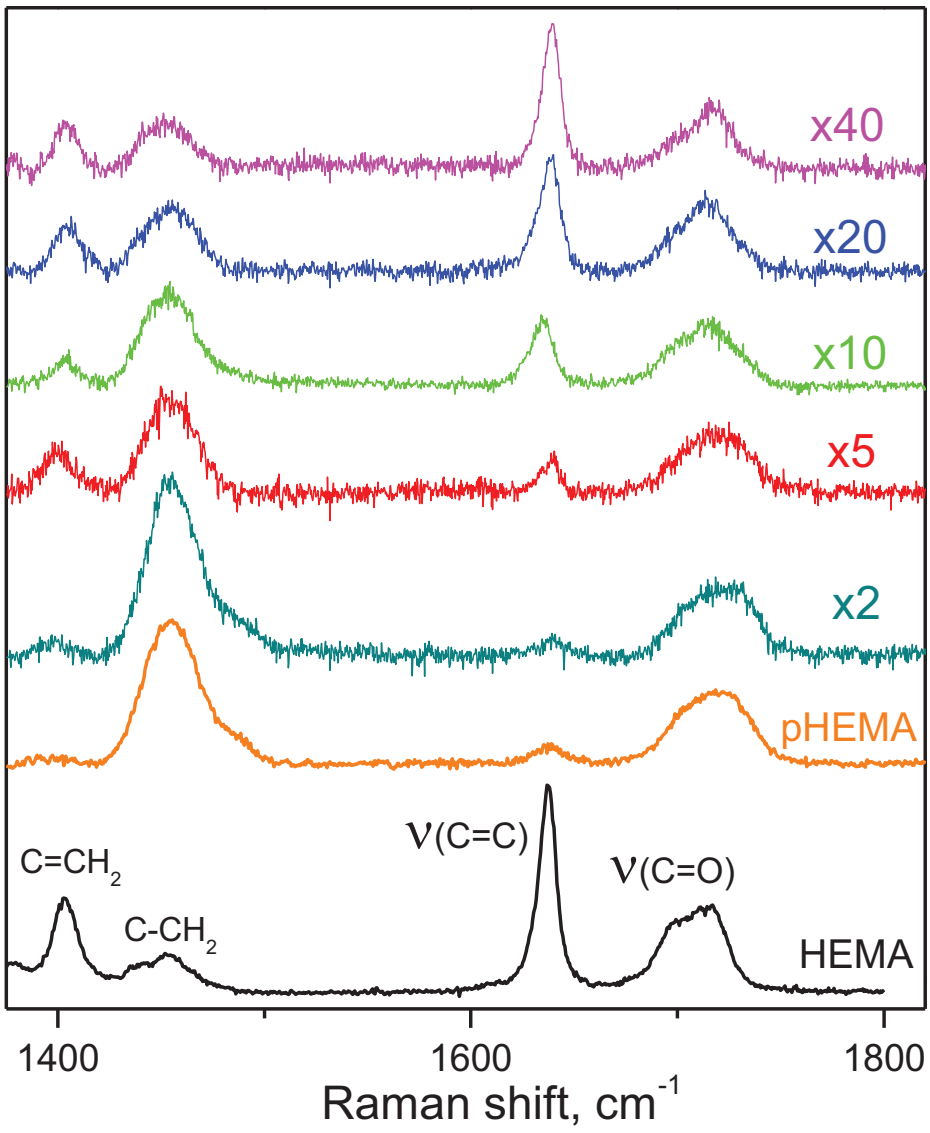

Figure V.2 Raman spectra of liquid HEMA at atmospheric pressure, pHEMA obtained by HPR process, and pHEMA-TiO_2 hybrid materials with different concentration of TiO_2 nanoparticles prepared by HPR process. Information related to components concentration in pHEMA-TiO_2 hybrid materials are reported in Table V.1.

Table V.1 Information about composition of pHEMA-TiO_2 hybrid materials

Name of the sample	Volume of initial TiO_2 suspension, used in synthesis*, ml	Titanium concentration in the final hybrid material, M	HEMA concentration in the final hybrid material, M	Conversion yield of polymerization, %
x2	10	0.292	8.0	94
x5	25	0.73	8.0	78
x10	50	1.46	8.0	63
x20	100	2.92	8.0	43
x40	200	5.84	8.0	11

*Initial volume of HEMA used in synthesis is 5 ml.

From the obtained results we conclude that presence of TiO_2 nanoparticles impedes the polymerization of HEMA in hybrid materials. A simple explanation of this effect could be proposed. Due to their fixed positions, monomer molecules grafted to the nanoparticle surfaces (grafted molecules on Figure V.3) exhibit a less probability to be involved in the formation of polymer chains (molecule chains on Figure V.3) in compared with free monomer molecules. Thereby, the higher concentration of nanoparticles, the higher concentration of grafted monomer molecules and consequently, the less amount of polymer chains in hybrids. However, this is only our assumption and further investigation of the polymer chains formation mechanism in pHEMA-TiO_2 hybrids is required.

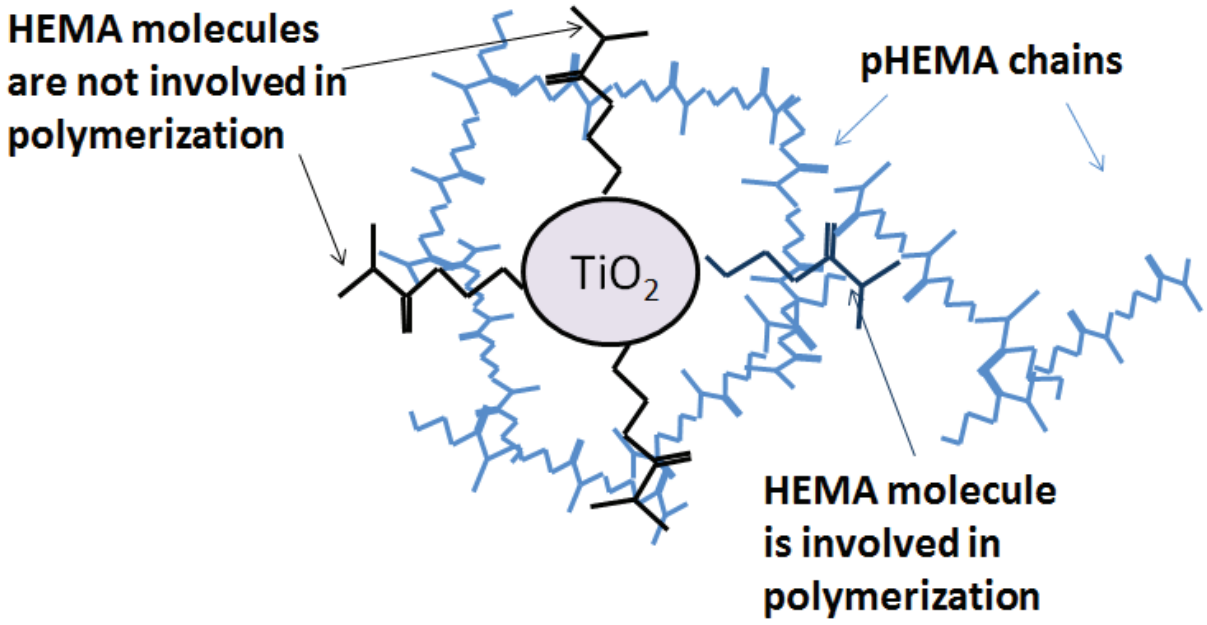

Figure V.3 The formation of polymer chains in pHEMA-TiO_2 hybrid materials.

V.3.2. Comparison of thermally and HPR polymerized pHEMA-TiO_2 hybrid materials

To demonstrate the advantages of the HPR induced polymerization in the fabrication of hybrid materials, we have compared the CY of pHEMA-TiO_2 samples obtained either by conventional thermally induced polymerization (at 90 °C during 12 hours with AIBN as initiator) or by HPR process. The optimal parameters for thermally induced polymerization of hybrid materials were chosen according to [6]. Here we consider hybrid samples with high titanium concentration ($C_{Ti} \geq 1.5$ M). The Raman spectra of the corresponding samples are presented in Figure V.4. Clearly, the CY of the polymerized hybrid samples obtained by HPR process is higher than that of thermally polymerized hybrids. So the CY of hybrids with C_{Ti} =1.5 M (samples x10) obtained by HPR process is two times bigger than the CY of thermally obtained hybrids with the same concentration C_{Ti} and three times bigger for hybrids with C_{Ti} = 3.0 M (samples x20).

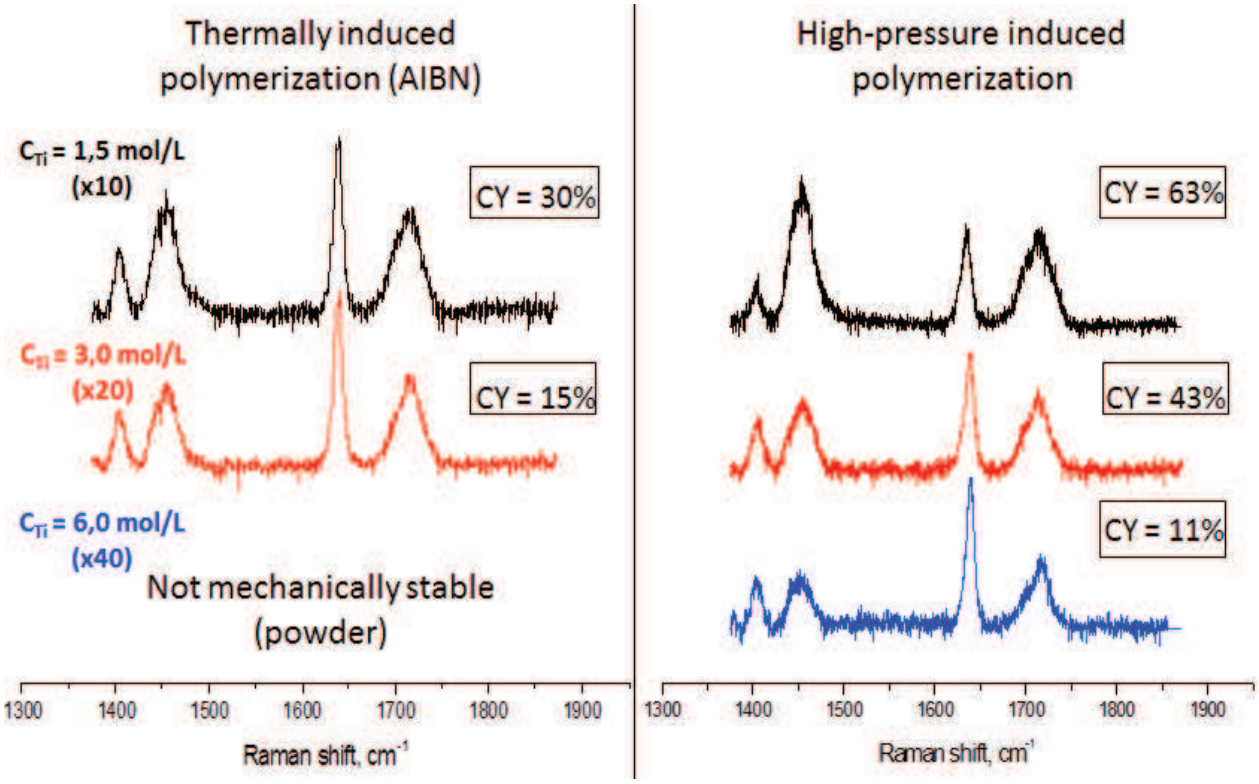

Figure V.4 Comparison of thermally and HPR polymerized hybrid samples.

The interest of the HPR induced polymerization with respect to the conventional thermally induced polymerization is even more pronounces in the case of hybrids with the highest titanium concentration (C_{Ti} = 6.0 M). Previous investigations [6] have shown that thermal approach allows to obtain mechanically stable pHEMA-TiO_2 hybrids only with titanium

concentration smaller than 3.0 M. Above this critical concentration the degradation of hybrid mechanical properties is significant and only crumbling samples are obtained. The HPR induced polymerization allows overcoming this problem. Indeed, hybrids samples with titanium concentration equal to 6.0 M can be obtained (see Figure V.4). These samples exhibit a solid form (not crumbling behavior) and an excellent transparency. For detailed analysis of their mechanical properties more precise measurements of elastic modulus, brittle, and plastic behavior, and hardness would be required. However the small size of hybrid samples produced by HP does not provide a possibility to use the standard techniques for these measurements. We nevertheless conclude on an improvement of mechanical properties of hybrids elaborated using the HPR process because of the increase of conversion yield of HEMA monomers which convey a better extend of the polymerization.

In conclusion, for a given TiO_2 concentration, the HPR process allows fabrication of pHEMA-TiO_2 hybrid materials with higher polymerization efficiency than conventional thermal approach (samples x10 and x20 in Figure V.4). Similarly, the HPR induced polymerization allows increasing at least 2 times the concentration of titanium in hybrid materials without changing the CY of polymerization.

It is interesting to compare the nanoparticles concentration in sample x40 with the maximal achievable concentration. To estimate this value we have considered a face-centered cubic (FCC) packing of spherical nanoparticles (see Figure V.5 (a)). The total number of particles within the unit cell can be calculated as follows: 8 particles on the cell corners (1 particle), 6 particles with half of their volumes within the cell (6 particles* 1/2 volume = 3 particles). This gives us a total of 4 particles. Therefore, the total volume of spheres in the unit cell is

$$V_{spheres\ in\ unit\ cell} = \frac{16}{3}\pi r^3, \qquad (6.1)$$

where *r* is the radius of a single nanoparticle.

The diagonal of the unit cell face is 4*r*, so each side is $2\sqrt{2}r$ (see Figure V.5 (b)). The volume of the unit cell is therefore:

$$V_{unit\ cell} = (2\sqrt{2}r)^3 = 16\sqrt{2}r^3. \qquad (6.2)$$

The packing density (the fraction of a volume filled by the particles in unit cell) is $\pi/(3\sqrt{2}) = 0.74$ is known to be the densest possible packings of equal spheres.

From the estimated maximal packaging density of nanoparticles (with r = 2.5 nm) we calculated the maximal value of titanium concentration in hybrid materials which is C_{Ti}=10.8 M (x70). This is larger than the concentration in our experiments (C_{Ti} = 6.0 M for sample x40). However the surface of nanoparticles in hybrids is covered by grafted HEMA molecules. We

have therefore estimated the maximal titanium concentration in hybrid materials assuming that HEMA monomer molecules (length of monomer molecule is ≈1 nm) are perpendicularly grafted on the surface of nanoparticles (grafted molecules on Figure V.3). The total radius of nanoparticles with grafted monomers is equal to 3.5 nm. The estimation gave us a value being equal to C_{Ti} = 4.0 M (x27). This is less than the titanium concentration in sample x40. We therefore conclude that under pressure nanoparticles are pushed one against the other and that grafted HEMA monomers are deformed and bend over the surface of nanoparticles. Nevertheless a more systematic series of experiments is required to determine the maximum titanium concentration achievable.

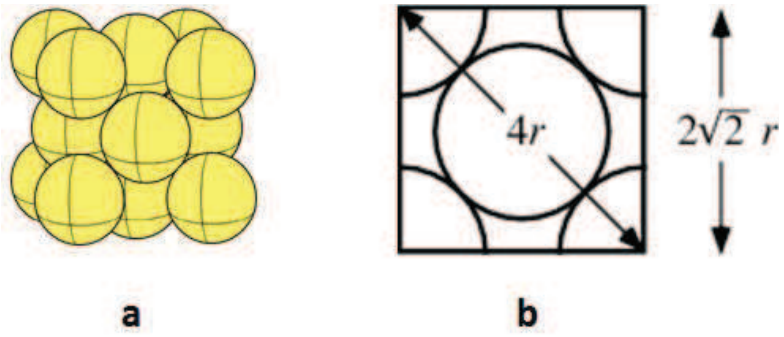

Figure V.5 Example of face-centered cubic (FCC) packaging of spherical nanoparticles (a) and the two-dimensional layer of FCC unit cell (b) (Redraw from ref. [152, 153]).

V.4. Laser-induced photodarkening of nanoparticulate (p)HEMA- and TiO_2-based hybrid materials

We now discuss the optical properties of hybrid materials obtained by HPR induced polymerization process.

V.4.1. Experimental results

In section II.3.3 we have presented in details the pump-probe photodarkening experiment. In each experiment two independent physical parameters are measured: (i) the UV irradiation dose on the sample and (ii) the power of the probe laser beam at 640 nm through the irradiated sample. The data processing is done in the following way. Firstly we calculate the UV irradiation dose. Details of this procedure have already been discussed in section II.3.3.4. Here we just remind the final equation for UV irradiation dose:

$$Dose = \frac{P}{S*Freq} * N_{pulses}\ , \qquad (6.3)$$

where P is the mean power of the UV laser, S is the area of the laser spot, and $Freq$ is the repetition rate of the UV laser, N_{pulses} is the laser pulses number.

Secondly, we measure the electrons trapped by Ti^{3+} centers concentration from the absorption of the probe beam at 640 nm [16] (see Figure V.6) according to Beer-Lambert law as:

$$[Ti^{3+}]L = -(1/\sigma_{640})Ln(I/I_0)\,, \qquad (6.4)$$

where $[Ti^{3+}]$ is the trapped electrons concentration by Ti^{3+} center which depends on the UV irradiation dose, L is the thickness of the samples, σ_{640} is the corresponding absorption cross-section of Ti^{3+} centers at laser wavelength λ=640 nm obtained in [16] and equal to 1.3×10^{-18} cm^2. I_0 is the intensity of incident light on the sample and I is the intensity of the transmitted light through the sample and depends on the UV irradiation dose.

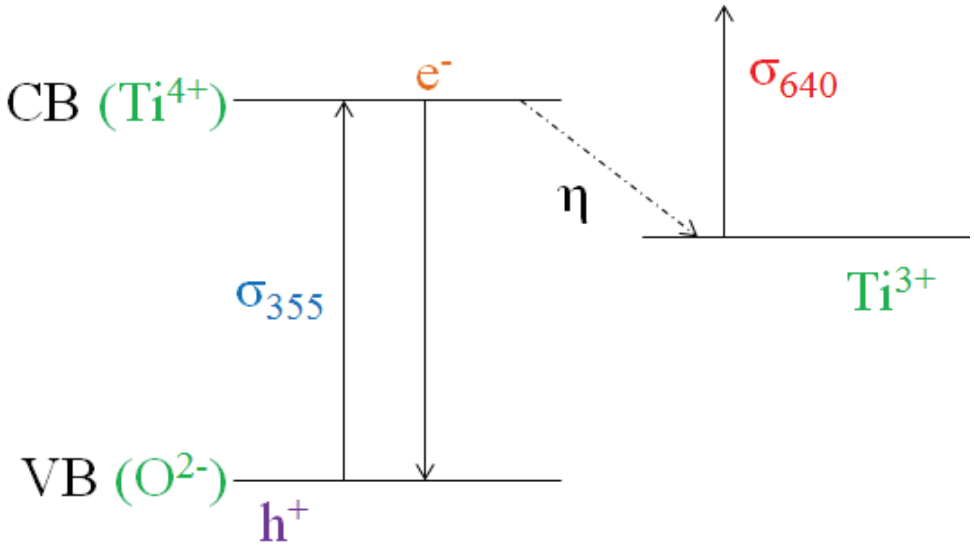

Figure V.6 The scheme of electrons transition in TiO_2 induced by UV irradiation (η is the quantum yield of charge separation). (Redraw from ref. [16]).

As a result of this processing we have obtained the laser-induced Ti^{3+} center kinetics in pHEMA-TiO_2 hybrid materials (Figure V.7) as well as in liquid (not polymerized) HEMA-TiO_2 hybrids (Figure V.8). These results are discussed in detail in the next sections.

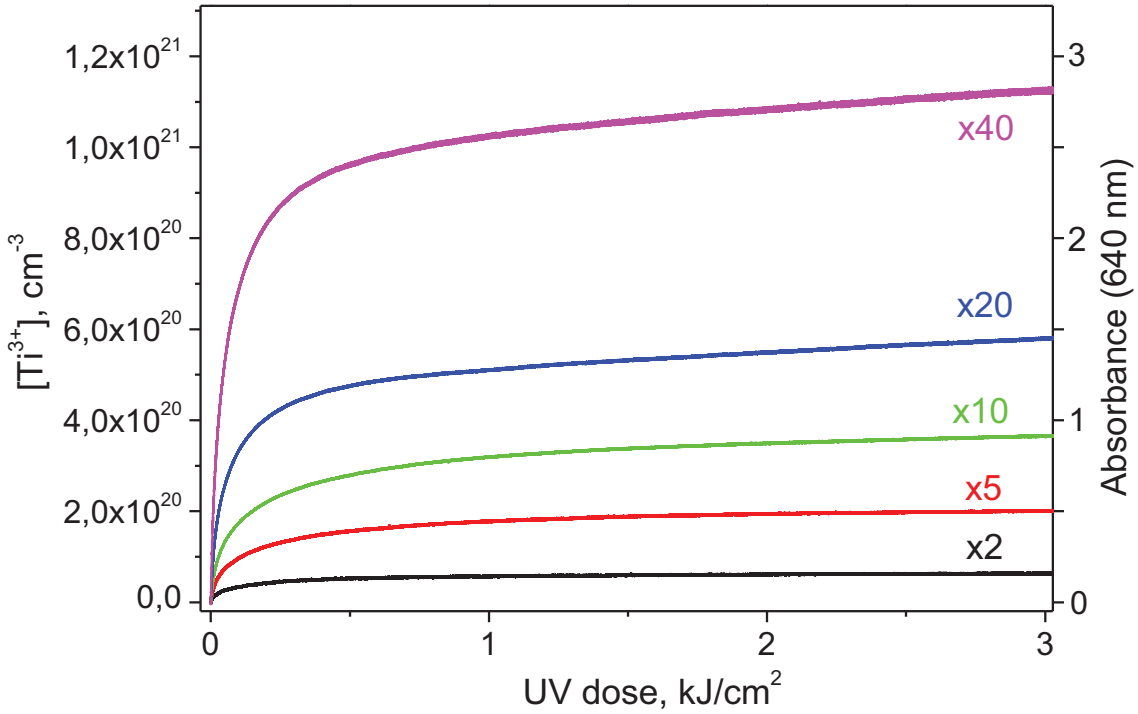

Figure V.7 Laser-induced Ti^{3+} center kinetics of pHEMA-TiO_2 hybrid materials obtained by HPR process (left vertical axis). The dependence of absorption at 640 nm laser irradiation from UV irradiation dose (right vertical axis). Information about hybrid samples is presented in Table V.1. The thicknesses of all samples are 20 μm.

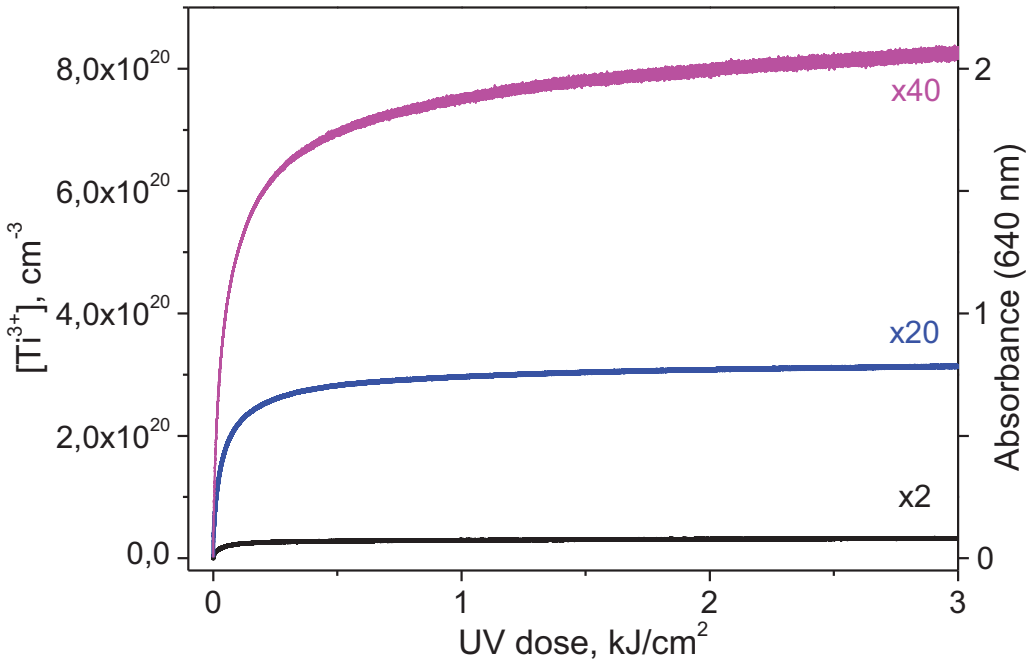

Figure V.8 Laser-induced photodarkening kinetics of liquid HEMA-TiO_2 hybrid materials. Thicknesses of the samples x2 and x40 are 40 μm, thickness of the sample x20 is 50 μm.

V.4.2. Results and discussions

The discussion of results is organized as follow. We consider first the efficiency of the photoinduced charges separation process under UV irradiation. Then we discuss the evolution of the laser-induced Ti^{3+} centers (trapped electrons concentration by Ti^{3+} center) of pHEMA-TiO_2 hybrid samples as function of the UV irradiation dose. Finally we test the validity of the theoretical model proposed by Kuznetsov *et al.* [16] to explain the main features of the laser-induced Ti^{+3} center kinetics in gel-based pHEMA-TiO_2 hybrids (see section I.1.4).

V.4.2.1. Charge separation process in hybrid materials based on TiO_2 nanoparticles

At the start of the UV irradiation process, when a fresh sample is irradiated, the concentration of Ti^{4+} centers can be considered as constant. In these conditions, the evolution of the Ti^{3+} concentration is given by:

$$\frac{\partial[Ti^{3+}]}{\partial t} = \eta\sigma_{355}[Ti^{4+}]_0 N_{ph.UV}, \qquad (6.5)$$

where $[Ti^{3+}]$ is the trapped electrons concentration by Ti^{3+} center during the action of the UV irradiation on the hybrid samples, η is the quantum yield of photoinduced charges separation process, σ_{355} is the absorption cross-section of Ti^{4+} inside the hybrid materials at laser wavelength λ = 355 nm, obtained in [16] and equal to 4.3 $\times 10^{-20}$ cm^2, $[Ti^{4+}]_0$ is the initial concentration of Ti^{4+} centers (see Table V.2), and $N_{ph.UV}$ is the number of incident UV photons per cm^2.

The solution of (6.5) is:

$$[Ti^{3+}] = \eta\sigma_{355}[Ti^{4+}]_0 \frac{Dose}{h\nu}. \qquad (6.6)$$

The Figure V.9 is a zoom at low UV irradiation dose of the photodarkening curves represented on Figure V.7 (samples x5, x10 and x40). The variation of Ti^{3+} centers concentration is linear and a fit with the expression 6.6 allows determining the quantum yield (η).We have applied the same procedure for liquid (not polymerized) HEMA-TiO_2 hybrid samples (Figure V.8).

.

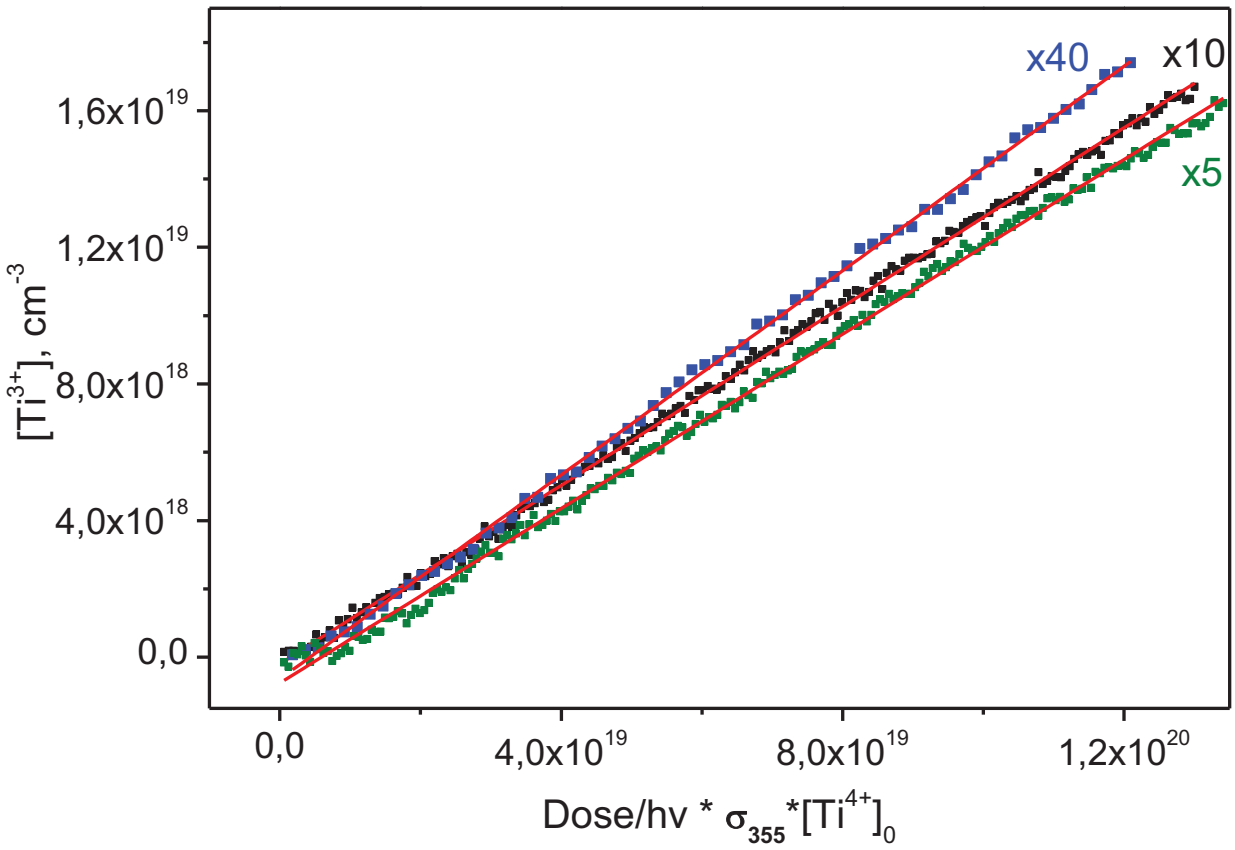

Figure V.9 Linear fitting of the results obtained by the equation (6.6) for pHEMA-TiO_2 hybrid sample x5, x10 and x40.

The obtained quantum efficiencies η for pHEMA-TiO_2 hybrid samples and liquid HEMA-TiO_2 hybrids are reported in Table V.2 and Table V.3, respectively. Whatever the sample the quantum efficiency seems constant and can be set to η ≈14±5 %. We therefore conclude that the process of charge separation is independent both of the nanoparticles concentration and of the polymerized or not polymerized environment of the nanoparticles. Moreover, the measured quantum efficiency of 14 % is close to the value (η ≈ 12 %) obtained by Kuznetsov *et al.* [17] in pHEMA-TiO_2 gel-based hybrid materials with various inorganic structure (see section I.1.4.1). These observations confirm that charge separation process in pHEMA-TiO_2 hybrids does not strongly dependent on the morphology of the interface between organic and inorganic components. However the measured quantum efficiency of nanoparticulate pHEMA-TiO_2 hybrid materials is higher than that earlier reported for colloidal nanoparticles in phosphate buffer solution (BDH) (η ≈ 4 %) [154] but is lower than that reported for wet TiO_2 alcogels (ethanol solution containing titanium tetraisopropoxide (TTIP), water, and acid (H^+)) (η ≈ 25 %) [12]. The organic component of hybrids seems to play an important role in the photoinduced charges separation process.

V.4.2.2. Laser-induced Ti^{3+} center kinetics of pHEMA-TiO_2 hybrid materials

The left vertical axis of Figure V.7 shows the concentration of Ti^{3+} centers as function of UV irradiation dose for five pHEMA-TiO_2 hybrid samples obtained by HPR process (see Table V.1). As it might be expected, for a given UV dose, the lowest concentration of Ti^{3+} centers is observed in the hybrid sample with smallest initial concentration of TiO_2 nanoparticles (sample x2). The higher concentration in nanoparticles, the higher Ti^{3+} centers concentration. Interestingly, the curves presented on Figure V.7 exhibits no saturation. The Ti^{3+} concentration continuously grows with the increase of UV irradiation dose. The measured electron loading capacities $[Ti^{3+}]/[Ti^{4+}]_0$ at an UV irradiation dose of 3 kJ/cm^2 are given in Table V.2 together with polymerization CY of each sample.

Table V.2 Electron loading ($[Ti^{3+}]/[Ti^{4+}]_0$) capacities of pHEMA-TiO_2 hybrid materials at UV irradiation dose equal to 3 kJ/cm^2, quantum yield of charge separation (η) and CY of polymerization.

Name of the sample	η, %	$[Ti^{4+}]_0\times10^{20}$, cm^{-3}	$[Ti^{3+}]/[Ti^{4+}]_0$, %	CY of polymerization, %
x2	14±5	1.76	37	94
x5		4.4	45	78
x10		8.8	41	63
x20		17.6	35	43
x40		32.5	36	11

Two conclusions can be drawn from these results. Foremost the electron loading capacity $[Ti^{3+}]/[Ti^{4+}]_0$ is similar in all samples indicating that each nanoparticles act independently to each other with respect to the trapping of electrons. At an irradiation dose of 3 kJ/cm^2 the electron loading is close to ≈40 %. Thus roughly one titanium atom over two stores an electron. This is not a limit value since no saturation is observed in curves presented in Figure V.7. Therefore higher concentration of trapped electrons can be expected if the irradiation dose exceeds 3 kJ/cm^2. For example, samples x10 and x5 at UV dose of 7 kJ/cm^2 exhibit an electron loading capacity equal to 45 % and 48 % respectively. The second conclusion concerns the CY of polymerization which seems to have no influence on the electron capacity storage of pHEMA-TiO_2 hybrid materials.

Furthermore, we compare the electron loading capacities of nanoparticulate pHEMA-TiO_2 hybrid materials with previously reported maximal electron loadings of gel-based pHEMA-TiO_2 hybrid materials [17] and of wet TiO_2 alcogel (ethanol solution containing

titanium tetraisopropoxide (TTIP), water, and acid (H^+)) [11]. The measured value in nanoparticulate pHEMA-TiO_2 hybrid materials (40 %) is four times higher than in gel-based pHEMA-TiO_2 hybrid materials (8-12 %) (see section I.1.4.1) and is 6 times higher than that reported for wet TiO_2 alcogel (7 %). We can therefore deduce that type of organic component as well as the microstructure of inorganic part, strongly influence on the electron loading capacity of hybrid materials.

V.4.2.3. Laser-induced Ti^{3+} center kinetics of liquid (not polymerized) HEMA-TiO_2 hybrid materials

The laser-induced Ti^{3+} center kinetics of liquid (not polymerized) HEMA-TiO_2 hybrid materials are shown in Figure V.8. As in the previous case, the similar dependence of laser-induced Ti^{3+} center concentration on the initial concentration of TiO_2 nanoparticles is observed. The liquid hybrid with smallest concentration of TiO_2 nanoparticles (sample x2) exhibits the lowest concentration of Ti^{3+} centers. The values of electron loading ($[Ti^{3+}]/[Ti^{4+}]_0$) capacity of liquid HEMA-TiO_2 hybrid materials at 3 kJ/cm^2 UV irradiation dose are reported in Table V.3.

Table V.3 Electron lading ($[Ti^{3+}]/[Ti^{4+}]_0$) capacities of HEMA-TiO_2 hybrid materials at UV irradiation dose equal to 3 kJ/cm^2 and quantum yield of charge separation (η).

Name of the sample	η, %	$[Ti^{4+}]_0\times10^{20}$, cm^{-3}	$[Ti^{3+}]/[Ti^{4+}]_0$, %
x2	14±5	1.76	18
x20*	-	17.6	18
x40	14±5	32.5	25

*For samples x20 it was not possible to calculate quantum yield of charge separation (η) because of the high noise and fluctuation in the obtained experimental data.

Whatever the sample the electron loading capacities at UV irradiation of 3 kJ/cm^2 are close to ≈ 20 %. These values are twice smaller than those measured in solid pHEMA-TiO_2 hybrid materials (≈ 40 %) at the same UV irradiation dose (see Table V.2). Apparently, the constituting components of hybrid materials play an important role in electron storage process. Even the small amount of the polymer in hybrid materials, for example pHEMA-TiO_2 hybrid sample x40 (CY ≈ 11 %), strongly influences on the charge separation process, thereby the electron loading capacity of solid pHEMA-TiO_2 hybrid materials are higher than of not polymerized hybrids.

V.4.2.4. Test of the theoretical model for pHEMA-TiO_2 hybrid optical properties

Kustnezov *et al*. have proposed a model to explain the evolution of the trapped electron concentration $[Ti^{3+}]$ as function of UV irradiation dose in gel-based pHEMA-TiO_2 hybrids. In

this section we propose to test the validity of this model on nanoparticulate pHEMA-TiO_2 hybrids elaborated by HPR process. With respect to the photodarkening experiment used by Kustnezov *et al*. [6, 12, 16], the pump-probe experiment built during this PhD presents some significant improvements both on the sample characterization, measurement of UV dose and signal to noise ratio. The mains improvements bring by the new pump-probe experiment are listed in the Table V.4.

Table V.4 Comparison of experimental conditions in ref. [6, 12, 16] and in the actual experiment.

Experimental conditions in ref. [6, 12, 16]	**Experimental conditions in the actual experiment**
In situ measurements – samples between two glass plates: not uniform shape of the samples, approximate measurement of the thicknesses	In situ measurements – samples in DAC: Uniform shape of the samples, accurate measurement of the thicknesses
The UV induced darkening of the sample is probed by a white lamp	The UV induced darkening of the sample is probed by a laser at 640 nm corresponding to the maximum of absorption (section II.3.3.2)
Measurement of UV irradiation dose from the time of irradiation	Control of the UV power during the experiment. Calculation of the dose from the fluence of each pulse. (section II.3.3.4)
Approximate measurements of the UV beam spot size using a ruler	Precise measurements of the UV beam spot size and shape by using a CCD camera (section II.3.3.3)
Experimental measurements limited to a small range of UV dose ($\leq$ 600 J/cm^2) (see inset in Figure V.10)	Irradiation on a large range of UV dose ($\leq$7000 J/cm^2) (see Figure V.10)
	Significant improvement of the signal to noise ratio

The Figure V.10 presents together the laser-induced Ti^{3+} centers concentration kinetics of nanoparticulate pHEMA-TiO_2 hybrid materials obtained by HPR process (x10) and of gel-based pHEMA-TiO_2 hybrid sample (sample #1, section I.1.4.1). The inset in Figure V.10 is a zoom on the range of dose < 600 J/cm^2. Both samples contain the same titanium concentration (C_{Ti}=1.5 M), but have slightly different microstructures. The sample #1 contains isolated or short

chains of TiO_2 nanoblocks poorly defined in size and shape. Conversely, the nanoparticles used to elaborate nanoparticulate pHEMA-TiO_2 samples are monodisperse in size (radius = 2.5 nm).

The electron loading capacity seems higher in hybrids composed of monodispersed nanoparticles than in gel-based hybrids. Indeed, at UV irradiation dose equal to 600 J/cm^2 the concentration of trapped electrons by Ti^{3+} center in nanoparticulate pHEMA-TiO_2 hybrid sample (x10) is three times bigger than in case of gel-based hybrid (sample #1) (inset in Figure V.10).

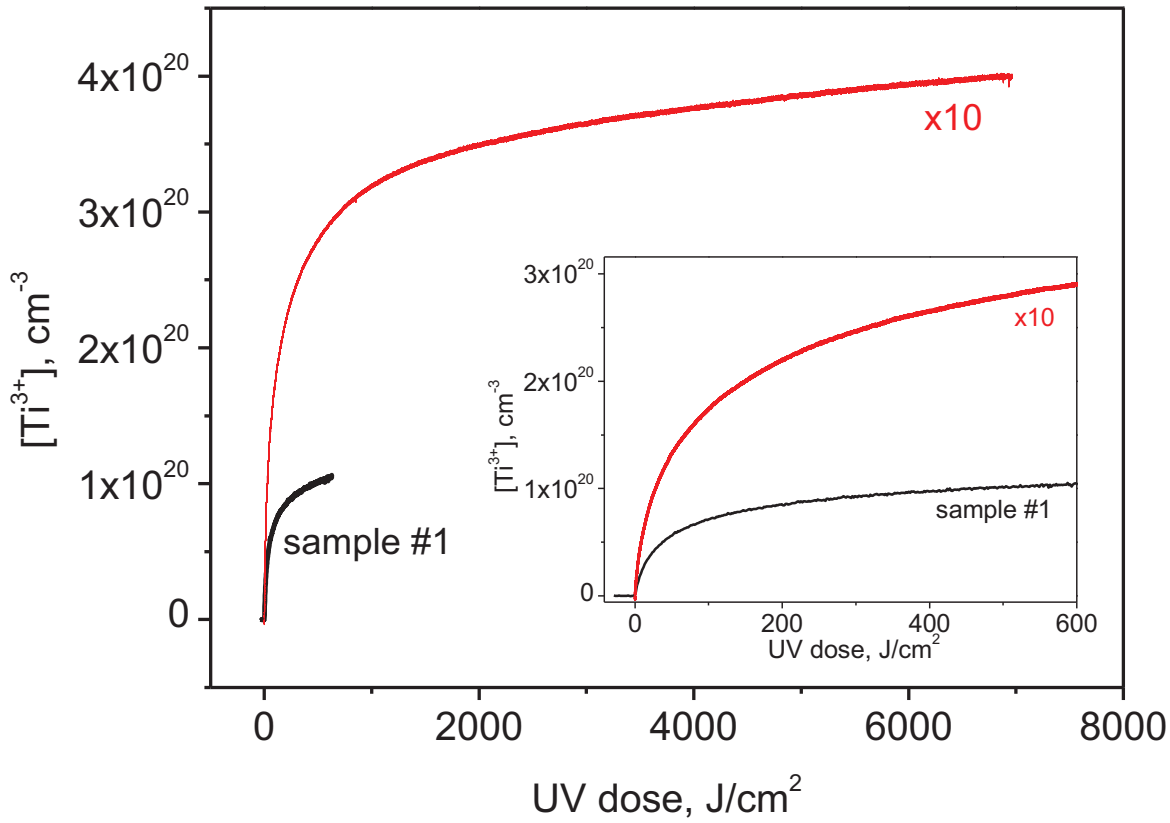

Figure V.10 Laser-induced Ti^{3+} center kinetics of nanoparticulate pHEMA-TiO_2 hybrid materials obtained by HPR process (x10) and gel-based pHEMA-TiO_2 hybrid samples (sample #1). The inset shows laser-induced Ti^{3+} center kinetics in dose range ≤ 600 J/cm^2. Information about samples x10 and #1 are presented in Table V.1 and Table I.1.5 respectively.

In section I.1.4.1 we have shown (see Figure I.1.17) that theoretical model proposed in [16] has been successfully applied to explain the UV photoinduced darkening of gel-based pHEMA-TiO_2 hybrid materials. The obtained fitting parameters are summarized Table I.1.6. The model is based on the following set of equations:

$$\partial[Ti^{3+}]/\partial t = \eta(1 + [Ti^{3+}]/b_c)^{-1}([Ti^{4+}]_0 - [Ti^{3+}])\sigma_a I - \eta_b[Ti^{3+}]\sigma_b I \qquad (6.7)$$

$$\partial I/\partial x = -(\sigma_a[Ti^{4+}] + \sigma_b[Ti^{3+}])I\,, \qquad (6.8)$$

where $[Ti^{4+}]_0$ is the initial concentration of titanium, η is the quantum yield of photoinduced charge separation process, η_b is the quantum yield of the so called inner photoeffect (the reexcitation of trapped electrons on Ti^{3+} centers by absorption of UV photons) and b_c is the critical concentration of Ti^{3+} centers. The UV laser intensity I on the sample is expressed in photons per cm^2 s and both absorption cross-sections σ_a and σ_b are referred to the same wavelength (λ_{laser} = 355 nm), the indexes a and b are related to Ti^{4+} and Ti^{3+} centers, respectively.

We have applied this model to nanoparticulate pHEMA-TiO_2 hybrid materials obtained by HPR process. We have considered hybrid samples with titanium concentration C_{Ti} = 1.5 M and tested the model in different ranges of UV irradiation dose.

a) Low irradiation doses: 0-25 J/cm²

The fit of experimental data for UV irradiation doses ranging from 0 to 25 J/cm^2 is shown in Figure V.11. A good agreement with the experiment is found for the following set of parameters: η = 0.135, η_q = 0, $b_c = [Ti^{4+}]_0 \times 0.021$. The quantum yield of charge separation η is similar to that determined by linear fitting in section V.4.2.1, moreover the critical concentration b_c compares well with values reported in gel based hybrids [17]. On the other hand the quantum yield η_b of the inner photoeffect is null whereas it is equal to 1.5 – 2 % in gel-based pHEMA-TiO^2 hybrids analyzed by Kuztnesov *et al*. [17].

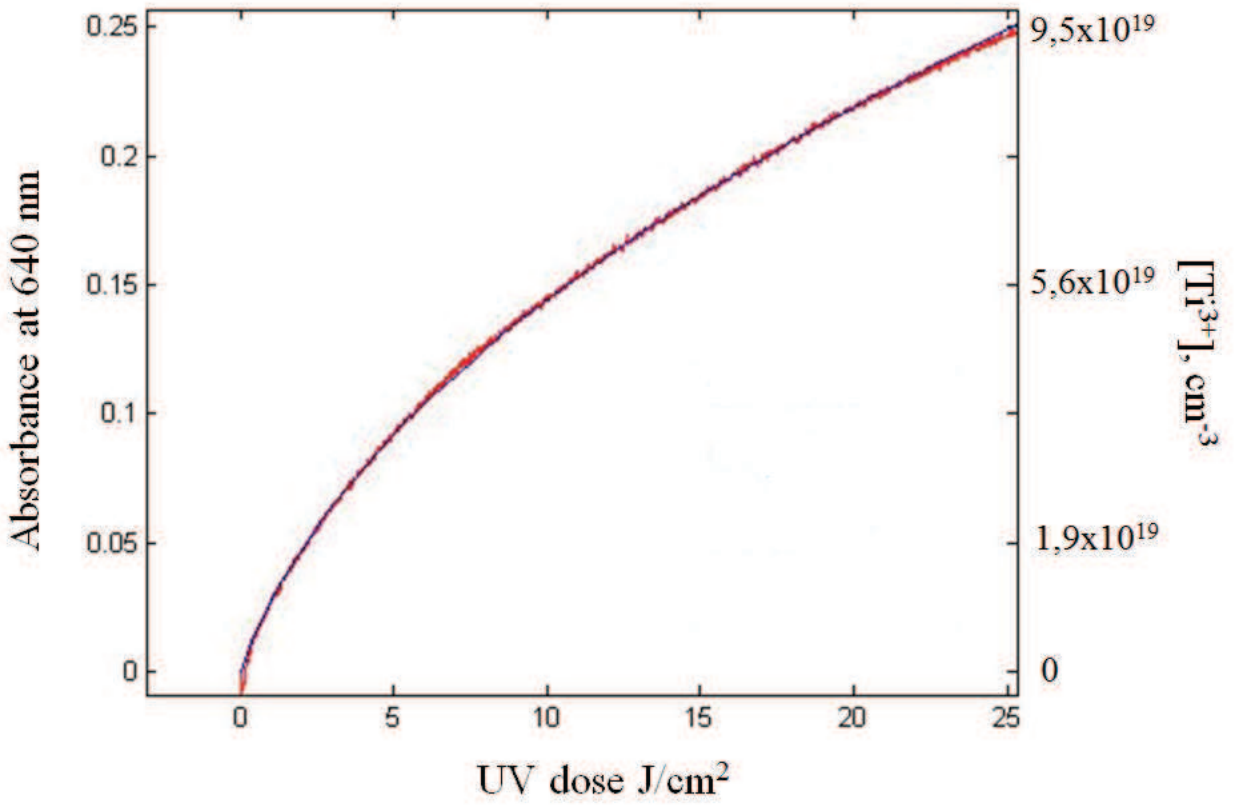

Figure V.11 Fitting of experimental data on dose (range 0-25 J/cm^2) dependence of laser-induced absorbance of pHEMA-TiO_2 hybrid sample with concentration of TiO_2 nanoparticles C_{Ti} = 1.5 M (sample x10).

b) High irradiation doses: 0-1 kJ/cm^2

When the UV irradiation dose is increased up to 1000 J/cm^2 , the fit of experimental data with the same set of parameters found before leads to a strong disagreement between experimental (solid line in Figure V.12) and theoretical curves when the UV dose is higher than 25 J/cm^2 (dash-dotted line in Figure V.12). The theoretical curve largely overestimates the absorbance, i.e. the concentration in trapped electrons, at high laser doses.

The absence of inner photoeffect could be responsible of this overestimation. Testing this possibility we have calculated the evolution of the absorbance with the following parameters $\eta = 0.135$, $\eta_b = 0.004$, $b_c = [Ti^{4+}]_0 \times 0.021$. Taking into account the inner photoeffect improves the agreement between experimental and theoretical curve (dashed line in Figure V.12) for doses lower than 200 J/cm^2, but leads to an underestimation of absorbance at higher dose. The obtained value of the quantum yield of the inner photoeffect , η_b = 0.4 %, is significantly lower than that reported for gel-based pHEMA-TiO_2 hybrids (η_b = 1.5 – 2 %).

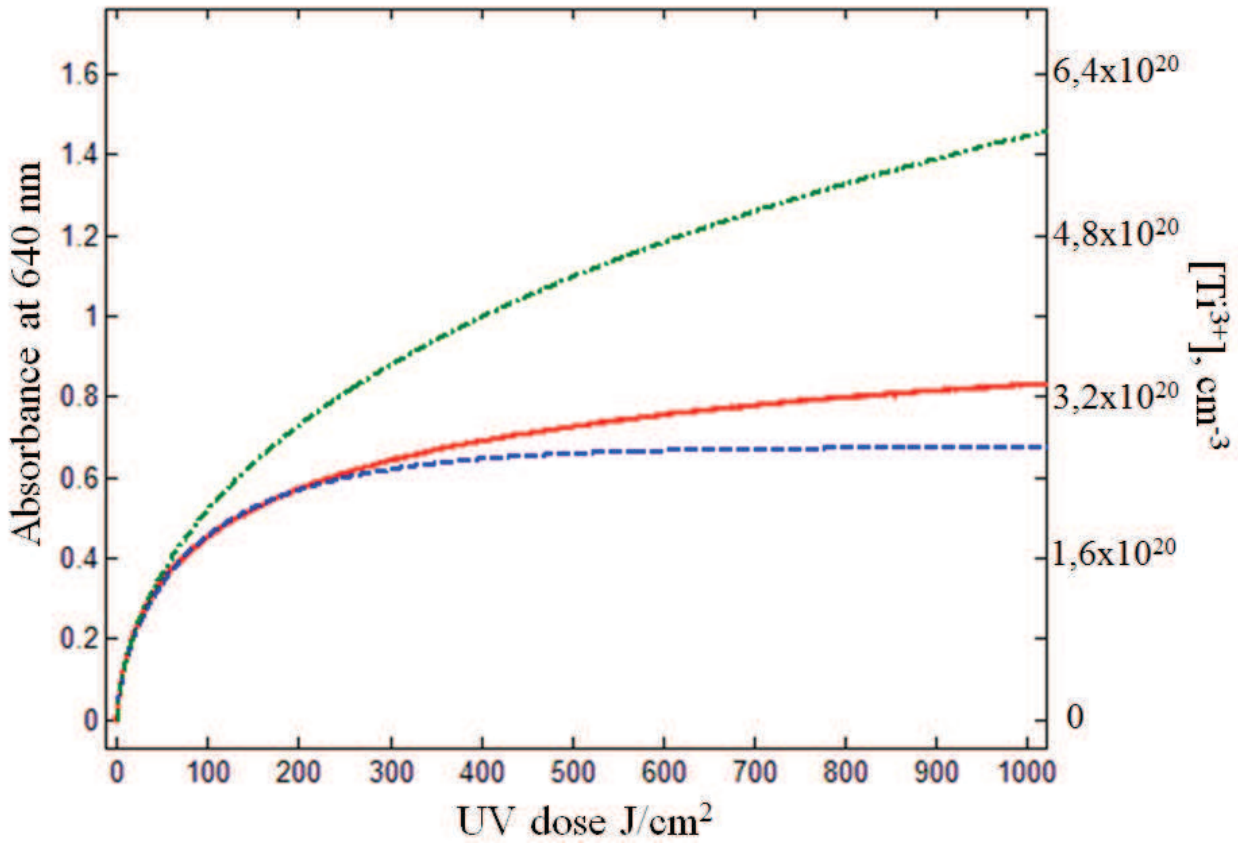

Figure V.12 Fitting (dash-dotted and dash lines (see text)) of experimental data (solid line) on dose (range 0-1000 J/cm^2) dependence of laser-induced absorbance of pHEMA-TiO_2 hybrid sample with concentration of TiO_2 nanoparticles C_{Ti} = 1.5 M (sample x10).

A better agreement with experimental data in UV irradiation doses ranging from 0 to 1000 J/cm^2 is obtained with the set of parameters: $\eta = 0.155$, $\eta_q = 0.0165$, $b_c = [Ti^{4+}]_0 \times 0.013$ (see Figure V.13). The obtained efficiency for the inner photoeffect is very low ($\eta_b = 0.165$ %) and the reliability of the measurement of a so small value is questionable.

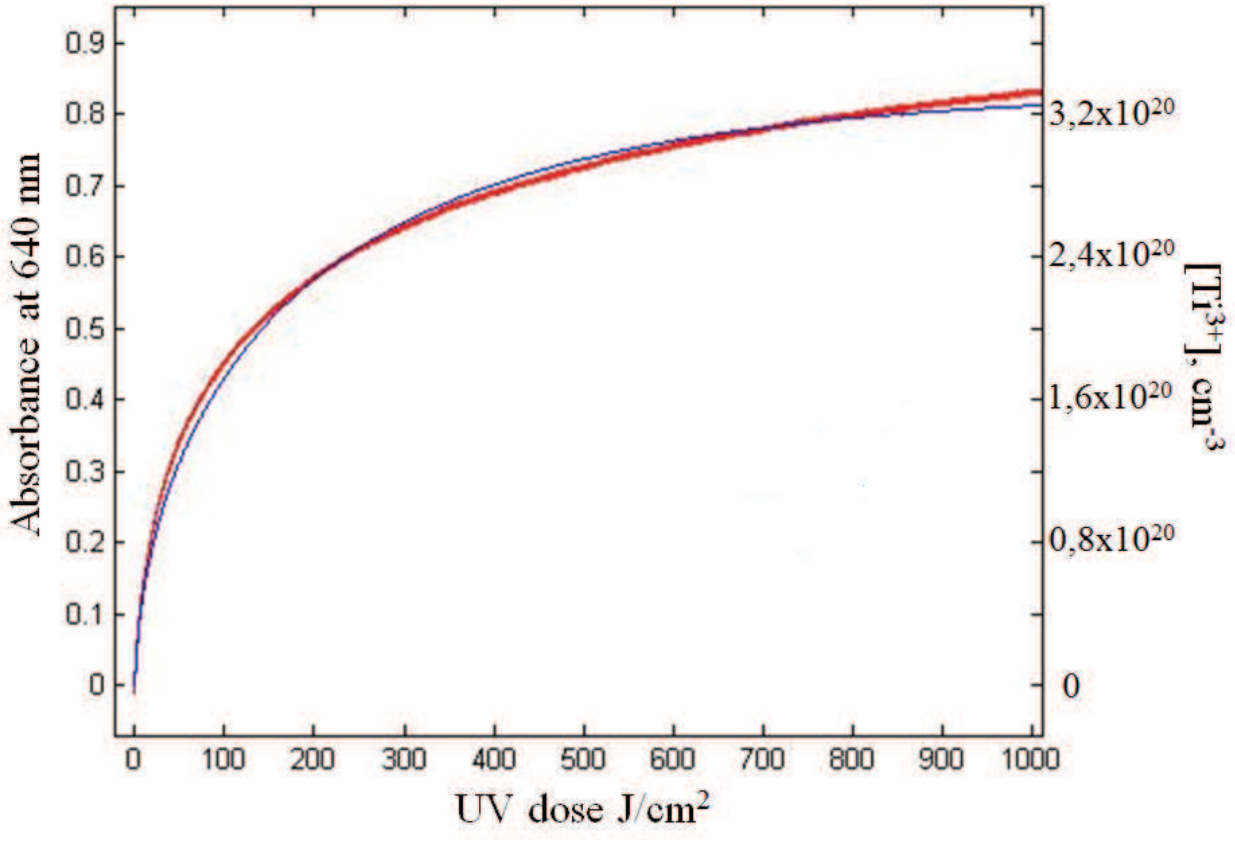

Figure V.13 Fitting of experimental data on dose (range 0-1000 J/cm^2) dependence of laser-induced absorbance of pHEMA-TiO_2 hybrid sample with concentration of TiO_2 nanoparticles C_{Ti} = 1.5 M (sample x10).

c) Very high irradiation doses: 0-7000 J/cm^2

If the previous set of parameters is used to calculate the absorbance as function of the UV dose, a strong disagreement is once again observed between experimental and theoretical curves (Figure V.14). At high dose the calculated absorbance is underestimated and saturates whereas, as we have already noted, the measured absorbance continuously grows. We did not find any set of parameters to reproduce correctly the experimental results.

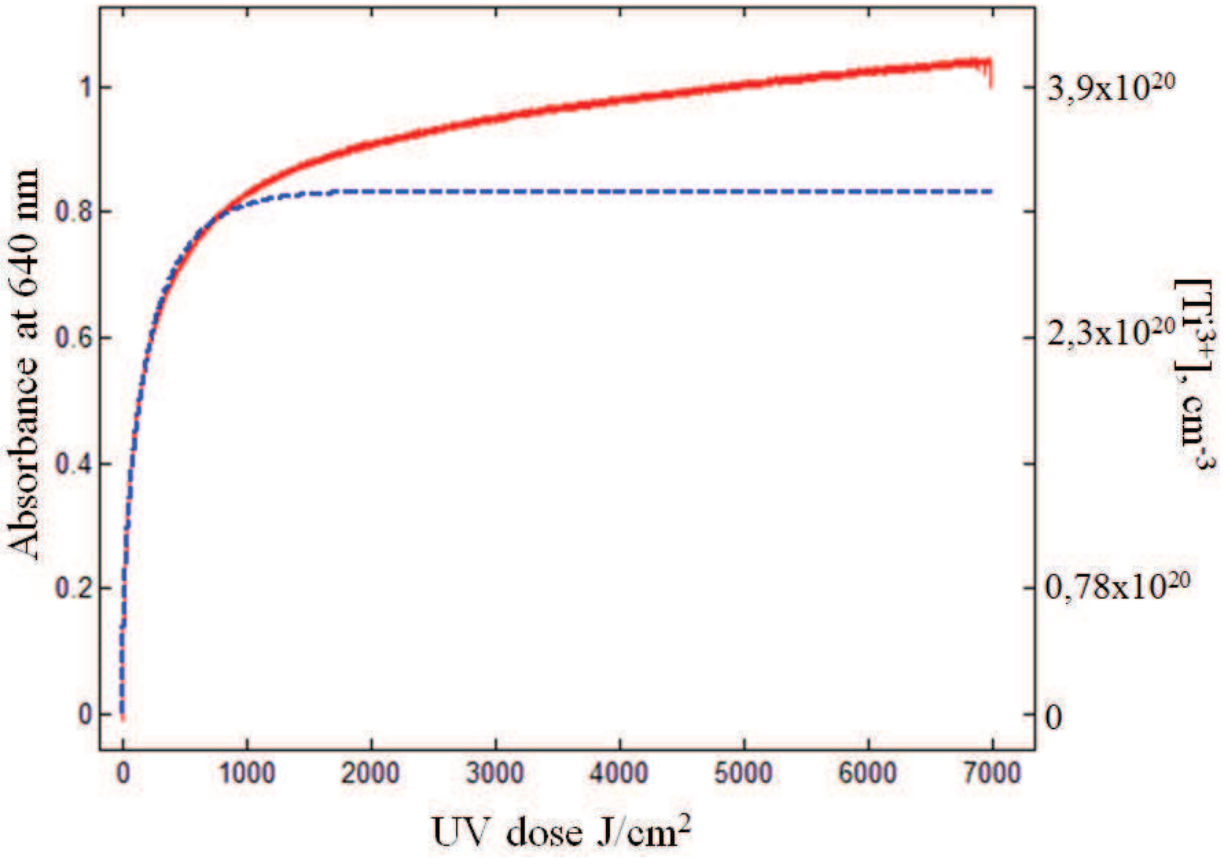

Figure V.14 Fitting (dash line) of experimental data (solid line) on dose (range 0-7000 J/cm^2) dependence of laser-induced absorbance of pHEMA-TiO_2 hybrid sample with concentration of TiO_2 nanoparticles C_{Ti} = 1.5 M (sample x10).

These results allow us concluding that the model proposed by Kustesnov *et al.* is not suitable to explain the kinetics of the photochromic effect observed in pHEMA-TiO_2 hybrid materials. At very low irradiation doses, the description of the initial absorption growth by the quantum yield η of photoinduced charges separation process is correct. The difficulties arise when the concentration of trapped electrons in Ti^{3+} center becomes significant. Two processes have been proposed to describe the recombination of trapped electrons:

- the inner photoeffect, i.e. the reexcitation of a trapped electron by absorption of a UV photon and its subsequent recombination with a trapped hole after to have migrated in the organic network (processes 7 and 9 in Figure I.1.16). The process is described by the term $\eta_b[Ti^{3+}]\sigma_b I$ in equation (6.7)
- the annihilation with freshly photoinduced light holes before they escape in the organic network (process 6 in Figure I.1.16). The process is described by the term $(1 + [Ti^{3+}]/b_c)^{-1}$ in equation (6.7) where b_c characterizes the critical concentration for

which the free hole as equal probability to recombine with a trapped electron or to escape in the organic network.

Our experimental results seem indicate that the inner photoeffect is not effective. Indeed, at low irradiation doses (0-25 J/cm^2) a correct agreement with experimental data is obtained without take into this inner photoeffect (η_b = 0), and at higher doses of the measured quantum yields are so low that their reliability is questionable. Moreover the inner photoeffect implies necessarily a saturation of the Ti^{3+} concentration when the amount of created electrons by absorption of UV photons becomes equal to the amount of electrons involved in the inner photoeffect. This is clearly in contradiction with our experimental results since we observe a continuous growing of the Ti^{3+} with the increase of the UV dose. On the other hand, the second process proposed to describe to recombination of trapped electrons, i.e. the annihilation with freshly photoinduced light holes, allows reproducing the evolution of Ti^{3+} concentration in the low range of irradiation (see Figure V.11). It nevertheless fails to provide a good fit of experimental data at higher doses. It could happen that the proposed model oversimplifies the description of the electron trapping mechanisms. Indeed, the quantum yield of the trapped electron formation could be effectively dependent on the density of filled traps. This could result from a specific interaction between the trapped electrons and the free electrons, which are attempting to be trapped into the empty site. Trapping may induce a distortion of the network near the filled trap reducing the probability for a following trapping event. In the vicinity of the occupied site, the interaction is expected to be strong [155], while it weakens considerably with increasing distance. If the concentration of the trapped electrons is smaller than the critical one, the effect of already trapped electrons on the trapping quantum efficiency of the newly created free electrons can be neglected. On the other hand, for $b > b_c$, the probability of trapping newly created free electrons decreases sharply because all the empty sites become distorted. This hypothesis is currently under consideration in the NINO team.

V.5. Conclusions

In conclusion, we have successfully fabricated nanoparticulate pHEMA-TiO_2 hybrid materials by a novel high pressure ramp (HPR) process. The polymerization efficiency of these hybrid materials have been characterized by means of Raman spectroscopy and compared with that of nanoparticulate pHEMA-TiO_2 hybrid elaborated using standard thermally activated polymerization. We have demonstrated that HPR polymerization allows increasing the concentration in nanoparticles without degrading the polymerization state of HEMA. For example, the conversion yield (CY) of polymerization of hybrids with C_{Ti} =1.5 M obtained by

HPR process is two times bigger than that of thermally polymerized hybrids with the same titanium concentration. The same is true for hybrids with titanium concentration of C_{Ti} = 3.0 M, for which the CY is multiply by 3. Moreover, we demonstrated that HPR process allows fabricating solid pHEMA-TiO_2 hybrids with titanium concentration up to 6.0 M close to the maximum possible concentration.

The optical properties of nanoparticulate pHEMA-TiO_2 hybrid materials prepared by HPR process were also examined. Using a pump-probe photodarkening experiment we have investigated the kinetics of the trapped electrons on Ti^{3+} centers as function of the UV irradiation dose in solid pHEMA-TiO_2 hybrid and in liquid (not polymerized) HEMA-TiO_2 hybrids. We have found that (i) the quantum yield of photo-induced charge separation process is equal to 14±5 % and independent the of the TiO_2 nanoparticles concentration and (ii) the electron loading capacity, $[Ti^{3+}]/[Ti^{4+}]_0$, is proportional to the TiO_2 nanoparticles concentration. The electron loading capacity exceeds 40 % far higher than capacities usually observed in other TiO_2 based materials.

Finally, we have tested the validity of the theoretical model proposed by Kuznetsov *et al.* [16] to explain the kinetics of Ti^{+3} centers concentration with the irradiation dose. We found that this model does not apply to our results for high doses of UV irradiation and that it will require significant modifications to account our observations.

Conclusions and prospects

Conclusions

This thesis was devoted to the development of an advance elaboration process allowing the increase of inorganic component concentration in hybrids materials without degrading their mechanical properties ensured by the polymerization of the organic component. We have demonstrated this new approach on photosensitive nanoparticulate pHEMA-TiO_2 hybrid materials and we have investigated the optical properties of these hybrids. The standard fabrication method of nanoparticulate pHEMA-TiO_2 hybrids, proposed by Gorboviy *et al.* [6] is composed of 3 stages (i) synthesize of size-selected nanoparticles, (ii) groups exchange at the surface of the nanoparticles and (iii) radical polymerization of the organic component using thermal initiators. The originality of the new process we propose in this PhD is to provoke the polymerization by applying high pressures on the sample.

We have foremost demonstrated the high-pressure induced bulk polymerization of 2-(hydroxyethyl) methacrylate (HEMA) at room temperature without addition of initiators. We found that the polymerization takes place in a limited range of pressures ranging from 0.1 to 1.6 GPa. Moreover, the polymerization processes very slowly and is poorly efficient. Indeed, after 41 days the conversion yield of polymerization, measured in recovered samples, did not exceed 30 %. The reaction can nevertheless be considerably accelerated by irradiating the compressed sample in the UV range. When the compressed sample is irradiated at 488 nm or 355 nm by a laser, the polymerization reaction rate is increased by a factor 10 or 30 respectively. Moreover, the shift of the laser wavelength to the UV improves the polymerization yield of the recovered sample up to 84 %. The catalysis of the polymerization process by light, results from a one-photon assisted electron transfer to π^* antibonding states of the monomer molecule.

The pHEMA-TiO_2 hybrids being highly photosensitive in the UV range, the laser assisted HP induced polymerization process presented above is not suitable for fabrication of this hybrid material. We have therefore developed a completely new HP process based on a two steps High Pressure Ramp (HPR) leading to an efficient and ultrafast polymerization of pure HEMA. The liquid sample is first activated by compression above 6.5 GPa. The polymerization only takes place in a second step after decompression down to 0.4 GPa. The conversion yield, monitored by Raman spectroscopy, exceeds 90 % in the recovered samples. The analysis of recovered products by Gel Permeation Chromatography evidences the major participation of the high pressure-activated biradicals $HEMA_2$•• in the formation of long polymer chains. In the first step the reactivity of radicals is hindered by the high-density solid-like environment. They react in the second step in the liquid environment at pressures below 2 GPa. The radicals are stable in inert atmosphere at the ambient pressure but disappear in contact with the ambient atmosphere. The

HPR polymerization process appears to be an appealing alternative to the usual photoactivation in high-pressure chemistry and permits an efficient synthesis of high-purity organic materials.

We have successfully applied the HPR polymerization to fabricate photosensitive nanoparticulate pHEMA-TiO_2 hybrid materials. By comparing the polymerization yield of hybrids polymerized by HPR process or by conventional polymerization using a thermal initiator, we have demonstrated that HPR polymerization allows multiplying by two the concentration in nanoparticles without degrading the polymerization state of HEMA. We have thus obtained solids hybrids with titanium concentration (C_{Ti} =6 M) close to the maximum possible, and not accessible with standard thermally initiated polymerization method. Finally, we have investigated the optical properties of nanoparticulate pHEMA-TiO_2 hybrid materials obtained by HPR process using a pump-probe photodarkening experiment. From the analysis of the trapped electrons concentration on Ti^{3+} centers as function of the UV irradiation dose, we have observed that (i) the quantum yield of photo-induced charge separation process is equal to 14±5 % and independent the of the TiO_2 nanoparticles concentration and (ii) the electron loading capacity, $[Ti^{3+}]/[Ti^{4+}]_0$, is proportional to the TiO_2 nanoparticles concentration. The electron loading capacity exceeds 40 % far higher than capacities usually observed in other TiO_2 based materials. In addition we have tested the validity of the theoretical model proposed by Kuznetsov *et al*. [16] to explain the kinetics of Ti^{+3} centers concentration with the UV irradiation dose. We have concluded this model requires major modifications to account our observations.

Prospects

In the frame of this PhD work we have demonstrated the efficient high-pressure induced bulk polymerization of 2-(hydroxyethyl) methacrylate (HEMA) at room temperature without addition of initiators. Moreover we have shown that HP approach can be used for synthesis of nanoparticulate pHEMA-TiO_2 hybrid materials. Nevertheless, the small size of the recovered products has restricted the possibility of using appropriate characterization methods. For example, characterization of molecular mass and molecular structure, morphology, thermal properties, and mechanical properties. For that reason the first prospect is to scale up the elaboration process for producing bigger samples thereby increasing the number of available characterization techniques.

In chapter IV we proposed a new high pressure ramp (HPR) ultrafast polymerization of HEMA. To investigate the universality of this method it is necessary to apply it to other types of polymers, thereby to understand the limits of its applicability.

In chapter V we compared two types of pHEMA-TiO_2 hybrid materials synthesized by thermal method of polymerization and HPR process as well. We showed that hybrids obtained by HPR process exhibit a higher conversion yield of polymerization than thermally prepared pHEMA-TiO_2 hybrids. Nevertheless, to get more insights about hybrid samples it would be useful to investigate their mechanical properties with more precise measurements of elastic modulus, brittle, and plastic behavior, and hardness.

In the last chapter we showed that theoretical model proposed by Kuznetsov *et al*. [16] to explain the kinetics of Ti^{+3} centers concentration with the UV irradiation does not apply (especially at high UV doses) in the case of nanoparticulate pHEMA-TiO_2 hybrid materials. Therefore, for a detailed understanding of the charge separation process of pHEMA-TiO_2 hybrids a new theoretical model should be proposed.

Finally, the investigation of two-photon polymerization of HEMA at high pressure without addition of photoinitiator would be highly interesting topic for further PhD works. The ability to build pure (no photoinitiators) 2D/3D microstructures can be highly valued for modern technologies and biomedicine.

References

1. Gómez-Romero, P. and C. Sanchez, *Hybrid Materials, Functional Applications.* 2003, Wiley-VCH Verlag GmbH & Co. KGaA.
2. Kickelbick, G., *Hybrid Materials*. 2006, Wiley-VCH Verlag GmbH & Co. KGaA.
3. Sanchez, C., et al., *Optical Properties of Functional Hybrid Organic–Inorganic Nanocomposites.* Advanced Materials, 2003. **15**(23): p. 1969-1994.
4. Escribano, P., et al., *Photonic and nanobiophotonic properties of luminescent lanthanide-doped hybrid organic-inorganic materials.* Journal of Materials Chemistry, 2008. **18**(1): p. 23-40.
5. Mammeri, F., et al., *Mechanical properties of hybrid organic-inorganic materials.* Journal of Materials Chemistry, 2005. **15**(35-36): p. 3787-3811.
6. Gorbovyi, P., *Elaboration des matériaux photosensibles organiques-inorganiques pour des applications en photonique*. 2012, Thèse de doctorat de l'Université Paris 13.
7. Chelazzi, D., et al., *High-pressure synthesis of crystalline polyethylene using optical catalysis.* Nat Mater, 2004. **3**(7): p. 470-475.
8. Chelazzi, D., et al., *Pressure-Induced Polymerization in Solid Ethylene.* The Journal of Physical Chemistry B, 2005. **109**(46): p. 21658-21663.
9. Evlyukhin, E., et al., *Laser-Assisted High-Pressure-Induced Polymerization of 2-(Hydroxyethyl)methacrylate.* The Journal of Physical Chemistry B, 2015. **119**(8): p. 3577-3582.
10. Bityurin, N., L. Znaidi, and A. Kanaev, *Laser-induced absorption in titanium oxide based gels.* Chemical Physics Letters, 2003. **374**(1–2): p. 95-99.
11. Kuznetsov, A.I., et al., *Light-induced charge separation and storage in titanium oxide gels.* Physical Review E, 2005. **71**(2): p. 021403.
12. Kuznetsov, A.I., et al., *Chemical Activity of Photoinduced Ti3+ Centers in Titanium Oxide Gels.* The Journal of Physical Chemistry B, 2006. **110**(1): p. 435-441.
13. Kuznetsov, A.I., A. Kanaev, and N. Bityurin, *Supercontinuum assisted trapped electron accumulation in titanium oxide gel by femtosecond laser pulses.* Optics Express, 2007. **15**(9): p. 5782-5788.
14. Kameneva, O., et al., *New photoactive hybrid organic-inorganic materials based on titanium-oxo-PHEMA nanocomposites exhibiting mixed valence properties.* Journal of Materials Chemistry, 2005. **15**(33): p. 3380-3383.
15. Kameneva, O.V., et al., *New hybrid organic-inorganic materials based on a poly(titanium oxide) gel with efficient UV-induced separation of charges.* Doklady Physics, 2006. **51**(3): p. 103-105.
16. Kuznetsov, *Laser processing of titanium oxide gels and gel-based hybrid materials*. 2006, Thèse de doctorat de l'Université Paris 13.
17. Kuznetsov, A.I., et al., *Laser-induced photopatterning of organic-inorganic TiO2-based hybrid materials with tunable interfacial electron transfer.* Physical Chemistry Chemical Physics, 2009. **11**(8): p. 1248-1257.
18. Kameneva, O., *MATERIAUX HYBRIDES ORGANIQUES-INORGANIQUES PHOTOCHROMES*. 2006, Thèse de doctorat de l'Université Paris 13.
19. Uklein, A., et al., *Photo-induced refraction of nanoparticulate organic-inorganic TiO2-pHEMA hybrids.* Optical Materials Express, 2013. **3**(5): p. 533-545.
20. Sanchez, C., et al., *Applications of hybrid organic-inorganic nanocomposites.* Journal of Materials Chemistry, 2005. **15**(35-36): p. 3559-3592.
21. Cottineau, T., et al., *Photosensitive Titanium Oxo-polymers: Synthesis and Structural Characterization.* Chemistry of Materials, 2008. **20**(4): p. 1421-1430.
22. Shannon. *TiO2 Photocatalys*. Available from: https://pavemaintenance.wikispaces.com/.
23. Daude, N., C. Gout, and C. Jouanin, *Electronic band structure of titanium dioxide.* Physical Review B, 1977. **15**(6): p. 3229-3235.
24. Filmon, R., et al., *Adherence of osteoblast-like cells on calcospherites developed on a biomaterial combining poly(2-hydroxyethyl) methacrylate and alkaline phosphatase.* Bone. **30**(1): p. 152-158.
25. Mabilleau, G., et al., *Effects of FGF-2 release from a hydrogel polymer on bone mass and microarchitecture.* Biomaterials, 2008. **29**(11): p. 1593-1600.

26. Montheard, J., P., J. Kahovec, and D. Chappard, *Desk Reference of Functional Polymers; Syntheses and Applications, Chap.5,*. 1997, Arshady R (ed). American Chemical Society: Washington, DC,. p. 699.
27. Nogueira, N., et al., *Characterization of poly(2-hydroxyethyl methacrylate) (PHEMA) contact lens using the Langmuir monolayer technique.* Journal of Colloid and Interface Science, 2012. **385**(1): p. 202-210.
28. Novak, B.M. and M.W. Ellsworth, *Mutually interpenetrating inorganic-organic networks. New routes into nonshrinking sol-gel composite materials.* Journal of the American Chemical Society, 1991. **113**(7): p. 2756-2758.
29. Trabelsi, S., et al., *Novel Organo-Functional Titanium–oxo-cluster-Based Hybrid Materials with Enhanced Thermomechanical and Thermal Properties.* Macromolecules, 2005. **38**(14): p. 6068-6078.
30. Howe, R.F. and M. Gratzel, *EPR observation of trapped electrons in colloidal titanium dioxide.* The Journal of Physical Chemistry, 1985. **89**(21): p. 4495-4499.
31. Scott, T.A., *Solid and liquid nitrogen.* Physics Reports, 1976. **27**(3): p. 89-157.
32. Bini, R., *Laser-Assisted High-Pressure Chemical Reactions.* Accounts of Chemical Research, 2004. **37**(2): p. 95-101.
33. McMillan, P.F., *New materials from high-pressure experiments.* Nat Mater, 2002. **1**(1): p. 19-25.
34. Hemley, R.J., *EFFECTS OF HIGH PRESSURE ON MOLECULES.* Annual Review of Physical Chemistry, 2000. **51**(1): p. 763-800.
35. Schettino, V. and R. Bini, *Molecules under extreme conditions: Chemical reactions at high pressure.* Physical Chemistry Chemical Physics, 2003. **5**(10): p. 1951-1965.
36. Drickamer, H.G. and C.W. Frank, *Electronic Structure, Electronic Transitions, and the High Pressure Chemistry and Physics of Solids.* Annual Review of Physical Chemistry, 1972. **23**(1): p. 39-64.
37. Drickamer, H.G., C.W. Frank, and C.P. Slichter, *Optical Versus Thermal Transitions in Solids at High Pressure.* Proceedings of the National Academy of Sciences of the United States of America, 1972. **69**(4): p. 933-937.
38. Lin, S.H., *Effect of high pressures on molecular electronic spectra and electronic relaxation.* The Journal of Chemical Physics, 1973. **59**(8): p. 4458-4467.
39. Tompkins, R.C., *Effects of high pressure on molecular electronic spectra.* The Journal of Chemical Physics, 1978. **69**(2): p. 579-583.
40. Tompkins, R.C., *Effects of high pressure on molecular electronic spectra. II. Morse potential formulation.* The Journal of Chemical Physics, 1980. **72**(6): p. 3449-3453.
41. Citroni, M., et al., *Role of excited electronic states in the high-pressure amorphization of benzene.* Proceedings of the National Academy of Sciences, 2008. **105**(22): p. 7658-7663.
42. Drickamer, H.G. and C.W. Frank *Electronic Transitions and the High Pressure Chemistry and Physics of Solids*. 1973: Chapman and Hall: London.
43. Feng, J., et al., *Erratum: Structures and Potential Superconductivity in ${\mathrm{SiH}}_{4}$ at High Pressure: En Route to ``Metallic Hydrogen'' [Phys. Rev. Lett. \textbf{96} , 017006 (2006)].* Physical Review Letters, 2006. **97**(11): p. 119901.
44. Grochala, W., et al., *The Chemical Imagination at Work in Very Tight Places.* Angewandte Chemie International Edition, 2007. **46**(20): p. 3620-3642.
45. Schettino, V., et al., *Chemical Reactions at Very High Pressure*, in *Advances in Chemical Physics*. 2005, John Wiley & Sons, Inc. p. 105-242.
46. Zigler, A., et al., *Laser-generated shock-wave velocity measurements using a visible backlighting technique.* Journal of Physics E: Scientific Instruments, 1986. **19**(4): p. 309.
47. Kuijpers, M.W.A., et al., *Cavitation-Induced Reactions in High-Pressure Carbon Dioxide.* Science, 2002. **298**(5600): p. 1969-1971.
48. Santoro, M. and F.A. Gorelli, *High pressure solid state chemistry of carbon dioxide.* Chemical Society Reviews, 2006. **35**(10): p. 918-931.
49. Yoo, C.S., et al., *Crystal Structure of Carbon Dioxide at High Pressure: ``Superhard'' Polymeric Carbon Dioxide.* Physical Review Letters, 1999. **83**(26): p. 5527-5530.

50. Iota, V., C.S. Yoo, and H. Cynn, *Quartzlike Carbon Dioxide: An Optically Nonlinear Extended Solid at High Pressures and Temperatures.* Science, 1999. **283**(5407): p. 1510-1513.
51. Santoro, M., et al., *In situ high P-T Raman spectroscopy and laser heating of carbon dioxide.* The Journal of Chemical Physics, 2004. **121**(6): p. 2780-2787.
52. Brazhkin, V.V. and A.G. Lyapin, *Metastable high-pressure phases of low-Z compounds: creation of a new chemistry or a prompt for old principles?* Nat Mater, 2004. **3**(8): p. 497-500.
53. Tschauner, O., H.-k. Mao, and R.J. Hemley, *New Transformations of ${\mathrm{CO}}_{2}$ at High Pressures and Temperatures.* Physical Review Letters, 2001. **87**(7): p. 075701.
54. Iota, V. and C.-S. Yoo, *Phase Diagram of Carbon Dioxide: Evidence for a New Associated Phase.* Physical Review Letters, 2001. **86**(26): p. 5922-5925.
55. Gorelli, F.A., et al., *Linear Carbon Dioxide in the High-Pressure High-Temperature Crystalline Phase IV.* Physical Review Letters, 2004. **93**(20): p. 205503.
56. Yoo, C.-S., V. Iota, and H. Cynn, *Nonlinear Carbon Dioxide at High Pressures and Temperatures.* Physical Review Letters, 2001. **86**(3): p. 444-447.
57. Nellis, W.J. and A.C. Mitchell, *Shock compression of liquid argon, nitrogen, and oxygen to 90 GPa (900 kbar).* The Journal of Chemical Physics, 1980. **73**(12): p. 6137-6145.
58. Nellis, W.J., et al., *Phase Transition in Fluid Nitrogen at High Densities and Temperatures.* Physical Review Letters, 1984. **53**(17): p. 1661-1664.
59. Bini, R., et al., *From simple to complex and backwards. Chemical reactions under very high pressure.* Chemical Physics, 2012. **398**(0): p. 262-268.
60. Reichlin, R., et al., *Optical Studies of Nitrogen to 130 GPa.* Physical Review Letters, 1985. **55**(14): p. 1464-1467.
61. Goncharov, A.F., et al., *Optical Evidence for a Nonmolecular Phase of Nitrogen above 150 GPa.* Physical Review Letters, 2000. **85**(6): p. 1262-1265.
62. Eremets, M.I., et al., *Semiconducting non-molecular nitrogen up to 240[thinsp]GPa and its low-pressure stability.* Nature, 2001. **411**(6834): p. 170-174.
63. Eremets, M.I., et al., *Single-bonded cubic form of nitrogen.* Nat Mater, 2004. **3**(8): p. 558-563.
64. Aoki, K., et al., *Solid state polymerization of cyanoacetylene into conjugated linear chains under pressure.* The Journal of Chemical Physics, 1989. **91**(2): p. 778-782.
65. Aoki, K., et al., *High-pressure Raman study of a one-dimensional hydrogen-bonded crystal of cyanoacetylene.* The Journal of Chemical Physics, 1989. **91**(5): p. 2814-2817.
66. Murli, C. and Y. Song, *Pressure-Induced Polymerization of Acrylic Acid: A Raman Spectroscopic Study*. The Journal of Physical Chemistry B, 2010. **114**(30): p. 9744-9750.
67. Conant, J.B. and C.O. Tongberg, *POLYMERIZATION REACTIONS UNDER HIGH PRESSURE. I. SOME EXPERIMENTS WITH ISOPRENE AND BUTYRALDEHYDE.* Journal of the American Chemical Society, 1930. **52**(4): p. 1659-1669.
68. Dick, R.D., *Shock compression data for liquids. I. Six hydrocarbon compounds.* The Journal of Chemical Physics, 1979. **71**(8): p. 3203-3212.
69. Wentorf, R.H., *The Behavior of Some Carbonaceous Materials at Very High Pressures and High Temperatures.* The Journal of Physical Chemistry, 1965. **69**(9): p. 3063-3069.
70. Warnes, R.H., *Shock Wave Compression of Three Polynuclear Aromatic Compounds.* The Journal of Chemical Physics, 1970. **53**(3): p. 1088-1094.
71. Pucci, R. and N.H. March, *Liquid crystal model for hydrocarbons under shock wave conditions.* The Journal of Chemical Physics, 1981. **74**(2): p. 1373-1378.
72. Bickham, S.R., J.D. Kress, and L.A. Collins, *Molecular dynamics simulations of shocked benzene.* The Journal of Chemical Physics, 2000. **112**(22): p. 9695-9698.
73. Citroni, M., et al., *Laser-Induced Selectivity for Dimerization Versus Polymerization of Butadiene Under Pressure.* Science, 2002. **295**(5562): p. 2058-2060.
74. Shirakawa, H., *Synthesis and characterization of highly conducting polyacetylene.* Synthetic Metals, 1995. **69**(1–3): p. 3-8.
75. Aoki, K., et al., *High-pressure Raman study of liquid and crystalline C2H2.* The Journal of Chemical Physics, 1988. **88**(8): p. 4565-4568.

76. LeSar, R., *Calculated high-pressure properties of solid acetylene and possible polymerization paths.* The Journal of Chemical Physics, 1987. **86**(3): p. 1485-1490.
77. Aoki, K., et al., *Raman study of the solid-state polymerization of acetylene at high pressure.* The Journal of Chemical Physics, 1988. **89**(1): p. 529-534.
78. Sakashita, M., H. Yamawaki, and K. Aoki, *FT-IR Study of the Solid State Polymerization of Acetylene under Pressure.* The Journal of Physical Chemistry, 1996. **100**(23): p. 9943-9947.
79. Ceppatelli, M., et al., *Fourier transform infrared study of the pressure and laser induced polymerization of solid acetylene.* The Journal of Chemical Physics, 2000. **113**(14): p. 5991-6000.
80. Moses, D., et al., *Pressure dependence of the photoabsorption of polyacetylene.* Physical Review B, 1982. **26**(6): p. 3361-3369.
81. Bernasconi, M., et al., *Solid-State Polymerization of Acetylene under Pressure: Ab Initio Simulation.* Physical Review Letters, 1997. **78**(10): p. 2008-2011.
82. Aoki, K., et al., *Raman study of the solid-state polymerization of acetylene at high pressure.* The Journal of Chemical Physics, 1988. **89**(1): p. 529-534.
83. Mugnai, M., et al., *Mechanism of the Ethylene Polymerization at Very High Pressure.* Journal of Chemical Theory and Computation, 2008. **4**(4): p. 646-651.
84. Benson, S.W., *Mechanism of the Diels—Alder Reactions of Butadiene.* The Journal of Chemical Physics, 1967. **46**(12): p. 4920-4926.
85. Miller, G.H., *Thermal polymerization of butadiene to solid polymer.* Journal of Polymer Science, 1960. **43**(142): p. 517-525.
86. Citroni, M., et al., *IR Study of the Pressure Induced Solid State DI- and Polymerization in 1,3-butadiene.* High Pressure Research, 2002. **22**(3-4): p. 507-510.
87. Citroni, M., et al., *Phase diagram and crystal phases of trans-1,3 butadiene probed by FTIR and Raman spectroscopy.* Chemical Physics Letters, 2003. **367**(1–2): p. 186-192.
88. Citroni, M., et al., *The high-pressure chemistry of butadiene crystal.* The Journal of Chemical Physics, 2003. **118**(4): p. 1815-1820.
89. Avrami, M., *Kinetics of Phase Change. II Transformation-Time Relations for Random Distribution of Nuclei.* The Journal of Chemical Physics, 1940. **8**(2): p. 212-224.
90. Dick, R.D., *Shock Wave Compression of Benzene, Carbon Disulfide, Carbon Tetrachloride, and Liquid Nitrogen.* The Journal of Chemical Physics, 1970. **52**(12): p. 6021-6032.
91. Mimura, K., *Synthesis of polycyclic aromatic hydrocarbons from benzene by impact shock: Its reaction mechanism and cosmochemical significance.* Geochimica et Cosmochimica Acta, 1995. **59**(3): p. 579-591.
92. Block, S., C.E. Weir, and G.J. Piermarini, *Polymorphism in Benzene, Naphthalene, and Anthracene at High Pressure.* Science, 1970. **169**(3945): p. 586-587.
93. Akella, J. and G.C. Kennedy, *Phase Diagram of Benzene to 35 kbar.* The Journal of Chemical Physics, 1971. **55**(2): p. 793-796.
94. Ciabini, L., et al., *High pressure reactivity of solid benzene probed by infrared spectroscopy.* The Journal of Chemical Physics, 2002. **116**(7): p. 2928-2935.
95. Pruzan, P., et al., *Transformation of benzene to a polymer after static pressurization to 30 GPa.* The Journal of Chemical Physics, 1990. **92**(11): p. 6910-6915.
96. Ciabini, L., et al., *High Pressure Photoinduced Ring Opening of Benzene.* Physical Review Letters, 2002. **88**(8): p. 085505.
97. Rivallin, M., *Evolution de sols nanométriques d'oxyde de titane durant l'inductiond'une précipitation de type sol-gel en réacteur à mélangeur rapide : Mesures granulométriques in-situ et modélisation*. 2003, Thèse de doctorat de l'Ecole des Mines de Paris.
98. Azouani, R., et al., *Elaboration of pure and doped TiO2 nanoparticles in sol–gel reactor with turbulent micromixing: Application to nanocoatings and photocatalysis.* Chemical Engineering Research and Design, 2010. **88**(9): p. 1123-1130.
99. T.Yagi, *Experimental overview of large volume techniques.* Proceedings of the International School of Physics Enrico Fermi, Course CXLVII High pressure Phenomena,Varenna on Como Lake (Italy) 3-13 July 2001, 2001: p. 41

100. Arthur L. Ruoff, H.X.a.Q.X., *The effect of a tapered aperture on x-ray diffraction from a sample with a pressure gradient: Studies on three samples with a maximum pressure of 560 GPa.* Rev. Sci. Instrum, 1992. **63**.
101. Eremets, M.I., et al., *Electrical Conductivity of Xenon at Megabar Pressures.* Physical Review Letters, 2000. **85**(13): p. 2797-2800.
102. R.K.W Haselwimmer, A.W.T., E.Pugh,, *Review of High pressure Science and THecnology, edited by M.Nakahara.* Japan Society of High Pressure Science and Technology, Kyoto, 1988. **7**: p. 481.
103. Boehler, R., *Temperatures in the Earth's core from melting-point measurements of iron at high static pressures.* Nature, 1993. **363**(6429): p. 534-536.
104. Eremets, M.E., *High Pressure Experimental Methods.* Oxford: Oxford Science, 1996: p. 408.
105. Pravica, M.G. and I.F. Silvera, *NMR Study of Ortho-Para Conversion at High Pressure in Hydrogen.* Physical Review Letters, 1998. **81**(19): p. 4180-4183.
106. *Type Ia Diamond Anvils*. Available from: https://www.diamondanvils.com/admin/uploaded/Product/.
107. *High Pressure.Types of Pressure Cells*. Available from: http://pd.chem.ucl.ac.uk.
108. D. L. Decker, W.A.B., L. Merrill, H. T. Hall and J. D. Barnett, *High-Pressure Calibration: A Critical Review.* J.Phys. and Chem. Ref. Data 1, 1972: p. 773.
109. G.J. Piermarini, S.B., *Ultrahigh pressure diamond-anvil cell and several semiconductor phase transition pressures in relation to the fixed point pressure scale.* Rev.sci.Instrum, 1975. **46**: p. 973.
110. Reinhard Boehler, G.C.K., *Thermal expansion of LiF at high pressures.* Journal of Physics and Chemistry of Solids, 1980. **41**(10): p. 1019–1022.
111. Mao, H.K., J. Xu, and P.M. Bell, *Calibration of the ruby pressure gauge to 800 kbar under quasi-hydrostatic conditions.* Journal of Geophysical Research: Solid Earth, 1986. **91**(B5): p. 4673-4676.
112. *Database of luminescent Minerals*. Available from: http://www.fluomin.org/spectrefluo/.
113. *Ruby Fluorescence*. Available from: https://geoweb.princeton.edu/research/MineralPhy/labtour/images/.
114. Bridgman, P.W., *Effects of High Shearing Stress Combined with High Hydrostatic Pressure.* Physical Review, 1935. **48**(10): p. 825-847.
115. Bridgman, P.W., *Shearing phenomena at high pressure of possible importance to geology.* The journal of Geology, 1936. **44**(6): p. 653.
116. Bridgman, P.W., *Shearing Phenomena at high pressures, particularly in inorganic compounds.* Proceedings of the American Academy of Arts and Sciences, 1937. **71**(9): p. 387.
117. Takayuki, O. and O. Masashi, *Precise electrical transport measurements by using Bridgman type pressure cell at low temperature.* Journal of Physics: Conference Series, 2010. **215**(1): p. 012180.
118. Zhai, S. and E. Ito, *Recent advances of high-pressure generation in a multianvil apparatus using sintered diamond anvils.* Geoscience Frontiers, 2011. **2**(1): p. 101-106.
119. Parlee, N.A.D., et al., *Metallurgy at high pressures and high temperatures: proceedings of a symposium*. Metallurgical Society conferences.v. 22. 1964, New York: Gordon and Breach Science Publishers. xii, 409 p.
120. Yousuf, M. and K. Rajan, *Principle of massive support in the opposed anvil high pressure apparatus.* Pramana, 1982. **18**(1): p. 1-15.
121. Kirk, R.S. and R.J. Vaišnys, *Electrical and Thermal Measurements with Bridgman Anvils.* Science, 1964. **143**(3613): p. 1436-1437.
122. *Raman spectroscopy*. Available from: http://chem.colorado.edu/chem4581_91/images/stories.
123. *A brief look at Raman scattering theory*. Available from: http://www.kosi.com/Raman_Spectroscopy/images/.
124. Schrader, B. Infrared and Raman spectroscopy : methods and applications. 1995, New York : VCH: Weinheim.
125. Bertoluzza, A., et al., *Applications of Raman spectroscopy to the ophthalmological field : Raman spectra of soft contact lenses made of poly-2-hydroxyethylmethacrylate (PHEMA).* Journal of Molecular Structure, 1986. **143**(0): p. 469-472.

126. Faria, M.D.G., J. Teixeira-Dias, and R. Fausto, *Conformational stability for methyl acrylate: a vibrational spectroscopic and ab initio MO study.* Vibrational spectroscopy, 1991. **2**(1): p. 43-60.
127. Kulbida, A., et al., *Rotational isomerism in acrylic acid. A combined matrix-isolated IR, Raman and ab initio molecular orbital study.* J. Chem. Soc., Faraday Trans., 1995. **91**(11): p. 1571-1585.
128. Arenas, J.F., et al., *SERS of acrylic acid and methyl derivatives on silver sols.* Journal of Raman Spectroscopy, 1998. **29**(7): p. 585-591.
129. Colthup, N., *Introduction to infrared and Raman spectroscopy*. 2012: Elsevier.
130. Lambert, J.B., et al., *Introduction to organic spectroscopy*. 1987: Macmillan Publishing Company.
131. Pallikari, F., et al., *Raman spectroscopy: A technique for estimating extent of polymerization in PMMA.* Material Research Innovations, 2001. **4**(2-3): p. 89-92.
132. Snively, C.M. and J.L. Koenig, *Polymer Applications of IR and Raman Spectroscopy*, in *Encyclopedia of Spectroscopy and Spectrometry*. 2000, Academic Press: San Diego. p. 1858.
133. Hamanoue, K., *Pressure Effect on the Kinetics of Polymerization I: Bulk Polymerization of Vinyl Chloride, Propylene and Butadiene.* Rev. Phys. Chem. Jpn., 1969. **38**: p. 103-119.
134. Yoo, C.S. and M. Nicol, *Kinetics of a pressure-induced polymerization reaction of cyanogen.* The Journal of Physical Chemistry, 1986. **90**(25): p. 6732-6736.
135. Citroni, M., et al., *Dimerization and Polymerization of Isoprene at High Pressures.* The Journal of Physical Chemistry B, 2007. **111**(15): p. 3910-3917.
136. Xie, S., Y. Song, and Z. Liu, *In situ high-pressure study of ammonia borane by Raman and IR spectroscopy.* Canadian Journal of Chemistry, 2009. **87**(9): p. 1235-1247.
137. Kaminski, K., et al., *Pressure-induced polymerization of tetraethylene glycol dimethacrylate.* Journal of Polymer Science Part A: Polymer Chemistry, 2008. **46**(11): p. 3795-3801.
138. Avrami, M., *Kinetics of Phase Change. I General Theory.* The Journal of Chemical Physics, 1939. **7**(12): p. 1103-1112.
139. Hulbert, S., *Models for Solid State Reaction in Powered Compacts: A Review.* J. Br. Ceram. Soc., 1969. **6**: p. 11-20.
140. Fang, W.-H. and R.-Z. Liu, *Photodissociation of Acrylic Acid in the Gas Phase: An ab Initio Study.* Journal of the American Chemical Society, 2000. **122**(44): p. 10886-10894.
141. Rosenfeld, R.N. and B.R. Weiner, *Photofragmentation of acrylic acid and methacrylic acid in the gas phase.* Journal of the American Chemical Society, 1983. **105**(20): p. 6233-6236.
142. Bamford, C.H., A.D. Jenkins, and J.C. Ward, *Polymerization of Crystalline Methacrylic Acid initiated by Ultra-violet Radiation.* Nature, 1960. **186**(4726): p. 713-714.
143. Lingnau, J. and G. Meyerhoff, *The spontaneous polymerization of methyl methacrylate, 7. External heavy atom effect on the initiation.* Die Makromolekulare Chemie, 1984. **185**(3): p. 587-600.
144. Lingnau, J. and G. Meyerhoff, *The spontaneous polymerization of methyl methacrylate: 6. Polymerization in solution: participation of transfer agents in the initiation reaction.* Polymer, 1983. **24**(11): p. 1473-1478.
145. Stickler, M. and G. Meyerhoff, *The spontaneous thermal polymerization of methyl methacrylate: 5. Experimental study and computer simulation of the high conversion reaction at 130° C.* Polymer, 1981. **22**(7): p. 928-933.
146. Lingnau, J., M. Stickler, and G. Meyerhoff, *The spontaneous polymerization of methyl methacrylate-IV: Formation of cyclic dimers and linear trimers.* European Polymer Journal, 1980. **16**(8): p. 785-791.
147. Srinivasan, S., et al., *Computational Evidence for Self-Initiation in Spontaneous High-Temperature Polymerization of Methyl Methacrylate.* The Journal of Physical Chemistry A, 2011. **115**(6): p. 1125-1132.
148. Mugnai, M., G. Cardini, and V. Schettino, *Charge separation and polymerization of hydrocarbons at an ultrahigh pressure.* Physical Review B, 2004. **70**(2): p. 020101.
149. Mugnai, M., G. Cardini, and V. Schettino, *High pressure reactivity of propene by first principles molecular dynamics calculations.* The Journal of Chemical Physics, 2004. **120**(11): p. 5327-5333.
150. Schettino, V., et al., *Activation and control of chemical reactions at very high pressure.* Physica Scripta, 2008. **78**(5): p. 058104.

151. Stickler, M. and G. Meyerhoff, *The spontaneous thermal polymerization of methyl methacrylate: 5. Experimental study and computer simulation of the high conversion reaction at 130°C.* Polymer, 1981. **22**(7): p. 928-933.
152. *Highest density of packing rigid spheres in a large box*. Available from: http://education.mrsec.wisc.edu/SlideShow/slides/unit_cells/.
153. *Cubic Close Packing*. Available from: http://mathworld.wolfram.com/.
154. Sun, L. and J.R. Bolton, *Determination of the Quantum Yield for the Photochemical Generation of Hydroxyl Radicals in TiO2 Suspensions.* The Journal of Physical Chemistry, 1996. **100**(10): p. 4127-4134.
155. Bityurin, N., A.I. Kuznetsov, and A. Kanaev, *Kinetics of UV-induced darkening of titanium-oxide gels.* Applied Surface Science, 2005. **248**(1–4): p. 86-90.